



Dissertation

On the formation of stratified surface layers associated to fatigue cracks on rail wheels

carried out for the purpose of obtaining the degree of
Doctor technicae (Dr. techn.),

submitted at TU Wien
Faculty of Mechanical and Industrial Engineering

by
Matthias FREISINGER

Mat.No.: 01035149

under the supervision of
Univ.Prof. Dipl.-Ing. Dr.mont. Paul H. Mayrhofer
Institute of Materials Science and Technology, E308

Reviewed by
Johan Ahlström
Chalmers University of Technology, Industrial & Materials Science; Gothenburg, Sweden
and
Carsten Gachot

Technische Universität Wien, TU Wien, Research Area Tribology; Vienna, Austria

Pottschach, August 2023

*Life is a mosaic,
a mosaic of moments, experiences, peoples, achievements and failures,
pieces vary in size, colour and arrangement,
some stay forever, some break away, some are temporarily behind others,
only together a steadily changing expression of bliss,
unique in its kind.*

This work has received funding from the Shift2Rail Joint Undertaking (JU) under grant agreement No 826255 and No 101012456. The JU receives support from the European Union's Horizon 2020 research and innovation programme and the Shift2Rail JU members other than the Union. In addition, this work was funded by the "Austrian COMETProgram" (project InTribology1, no. 872176) via the Austrian Research Promotion Agency (FFG) and the federal states of Niederösterreich and Vorarlberg and was carried out within the "Excellence Centre of Tribology" (AC2T research GmbH).

I confirm, that the printing of this thesis requires the approval of the examination board.

Affidavit

I declare in lieu of oath, that I wrote this thesis and carried out the associated research myself, using only the literature cited in this volume. If text passages from sources are used literally, they are marked as such.

I confirm that this work is original and has not been submitted for examination elsewhere, nor is it currently under consideration for a thesis elsewhere.

I acknowledge that the submitted work will be checked electronically-technically using suitable and state-of-the-art means (plagiarism detection software). On the one hand, this ensures that the submitted work was prepared according to the high-quality standards within the applicable rules to ensure good scientific practice "Code of Conduct" at the TU Wien. On the other hand, a comparison with other student theses avoids violations of my personal copyright.

Kalymnos, 22.08.2023

Place and Date

Signature

Acknowledgements

To begin with, I want to express my gratitude to the CEO, Prof. Dipl.-Ing. Dr.techn. **Andreas Pauschitz**, and the scientific board, Priv.-Doz. Dipl.-Ing. Dr.techn. **Nicole Dörr** and Dipl.-Ing. Dr.mont. **Ewald Badisch**, of *AC2T research GmbH* for providing me the opportunity to focus my work on near-surface microstructures in wheel-rail contacts – paving the way to the scientific contributions presented in this thesis. In line, I owe special gratitude to my supervisor Prof. Dipl.-Ing. Dr.mont. **Paul Heinz Mayrhofer** from *TU Wien* who supported my scientific work and resulting publications in combination with great personal freedom within my PhD journey. Thank you, I appreciate your time as I know there are numerous tasks of higher priority you must encounter in your position.

I want to thank DI(FH) DI DI Dr.mont. **Andreas Trausmuth** for enabling and promoting my PhD studies within the IN2TRACK3 project. I would like to express special gratitude to the collaborating researchers from *Virtual Vehicle GmbH*, Dipl.-Ing. Dr.techn. **Gerald Trummer** and Dipl.-Ing. Dr.techn. **Klaus Six**. Gerald, Klaus, I highly appreciate our lively discussions, your valuable inputs and fruitful feedback over the last years! This thesis wouldn't be so extensive without your worthwhile participation.

Moreover, I would like to thank two fundamental colleges without those this thesis would have never been accomplished, MSc. **Kurt Pichelbauer** and Dipl.-Ing **Balazs Jakab**. Big thanks Kurt, besides rocking the diode laser you supported me significantly by your accompanying thoughts and critical remarks throughout my PhD studies. The same applies to you Balasz, thank you for managing the twin disc tribometer and your constructive feedback. Further, I want to express my gratitude to my office buddies **Hari** and **Markus**, as well as other colleagues at *AC2T* – **Karin, Lea, Tetyana, Arpi, Norbert, Luki, Martin, Hasi, Manuel, Tobi, Jürgen, Manel** – supporting my work over the last 3 years.

In line, I want to express my gratitude to **Rainer** and **Lukas** from *TU Wien* for promoting the micro-mechanical testing included in this thesis. **Rainer**, you accompanied my micro-testing journey and gave me valuable hints – looking forward to future joint research activities!

Finally, and most importantly I would like to express my deepest gratitude to my **family** and **friends** for their unconditional love and support in every aspect of my life. **Papa**, without your encouragement I would never have had these opportunities. In the hardest time you gave everything for us kids, we are so proud of you – and Mama would be too!

To my fiancée, **Sara**, thank you for your love, balancing my life whatever comes around. You are my anchor, my soulmate – this is going to be a sensational mosaic of life with you!

Table of Contents

Table of Contents	V
Abstract	VI
Kurzfassung.....	VII
List of Figures	VIII
List of Symbols & Abbreviations	IX
1 Introduction and Motivation	1
2 Wheel-rail contact	4
2.1. Evolution of near-surface microstructures.....	6
2.1.1 Severe plastic deformation	6
2.1.2 White Etching Layer	8
2.1.3 Brown Etching Layer.....	11
2.2 Rolling-contact fatigue	12
3 Laboratory methodologies to imitate near-surface microstructure in wheel-rail contacts.....	15
3.1 Twin disc tribometer.....	15
3.2 Laser surface treatment	17
4 Bibliography.....	19
5 Scientific Contribution	28
5.1 Microstructural and micro-mechanical properties of evolved near- surface microstructures of rail wheels	28
5.2 Thermally induced surface layers by laser surface treatments.....	33
5.2 Participations at national and international conferences	38
6 Concluding Remarks & Outlook	39
Publication I.....	41
Publication II.....	55
Publication III.....	63
Publication IV.....	74
Publication V.....	88
Publication VI.....	100
Publication VII.....	110
Publication VIII.....	122

Abstract

To reduce global greenhouse gas emissions, rail transportation offers enormous potential as one of the lowest CO₂-emitting modes of transportation. The expansion in passenger mobility and freight transportation on current rail networks however leads to increasing mechanical and thermal loads in the wheel-rail contact due to higher train speeds, shorter train intervals, and higher axle loads. This affects rails and wheels in terms of wear and rolling contact fatigue damage. To ensure reliability and safety, and improve maintenance procedures and costs, the understanding of microstructural changes in the near-surface of rails and wheels is vital. While research has strived to unravel the formation of brittle surface layers, limited information has been gathered on the stratification of formed surface layers, often observed in the presence of cracks on rail wheels. Hence, this thesis contributes to a fundamental understanding of the microstructural and micro-mechanical characteristics of stratified surface layers (SSLs) on rail wheels and their contribution to rolling-contact fatigue (RCF). The framework ranges from extensive analyses of wheel samples from the field, to the development of a novel laboratory approach to imitate realistic SSLs with defined loading history to enable systematic studies.

Wheel samples from service are analysed by in-depth microstructural characterisation methods, revealing insights into evolved near-surface microstructures such as severe plastic deformed (SPD) zones, white etching layers (WELs), brown etching layers (BELs) – and their combination, the so-called stratified surface layer. To evaluate its fracture behaviour – crucial in terms of RCF crack initiation – the *in situ* micro bending method is applied, bringing light into the micro-mechanical behaviour of evolved near-surface regions in addition to common hardness measurement techniques. Finding the impetus in the results, the relevance of SSLs on RCF crack initiation is pointed out. However, the indefinite loading history of samples from the field hinders a systematic study. To address this, a novel laboratory approach is developed by combining a twin disc tribometer (defined mechanical loads) and laser surface treatments (specific thermal loads) to imitate realistic and reproducible SSLs. Finally, this novel approach is used to generate defined samples for one of the first systematic studies on the RCF crack initiation in the presence of SSLs of different wheel materials. The laboratory approach in combination with in-depth microstructural and micro-mechanical analysis methods contributes to an improved understanding of evolved near-surface microstructures on wheels and helps to ensure the reliability of rail transportation.

Kurzfassung

Zur Reduzierung der weltweiten Treibhausgasemissionen bietet der Schienenverkehr mit geringen CO₂-Emissionen ein enormes Potenzial. Die Verstärkung des Personen- und Güterverkehrs führt jedoch aufgrund höherer Zuggeschwindigkeiten, kürzerer Intervalle und höherer Achslasten zu steigenden mechanischen und thermischen Belastungen im Rad-Schiene-Kontakt. Dies wirkt sich auf Schienen und Räder aus und führt häufig zu mehr Verschleiß und Schädigungen. Um die Zuverlässigkeit zu gewährleisten und die Wartungsstrategien zu optimieren, ist das Wissen über mikrostrukturelle Veränderungen von Schienen und Rädern von entscheidender Bedeutung. Auf Eisenbahnradern wird Rissinitiierung häufig in der Umgebung von geschichteten Oberflächenschichten, so genannten *Stratified Surface Layers (SSLs)* beobachtet, welche während des Betriebes entstehen. Diese Doktorarbeit hat daher das Ziel, das grundlegende Verständnis der mikrostrukturellen und mikro-mechanischen Eigenschaften von SSLs auf Rädern, sowie deren Beitrag zur Rollkontaktermüdung zu erweitern. Die Arbeit umfasst sowohl umfangreiche Analysen von Rädern aus dem Feld, als auch die Entwicklung eines neuartigen Laboransatzes zur Nachbildung realistischer SSLs mit definierter Belastungsgeschichte um systematische Studien zu ermöglichen.

Radproben aus dem Betrieb werden durch detaillierte mikrostrukturelle Charakterisierungsmethoden analysiert, welche Einblicke in die Charakteristiken von oberflächennahen Mikrostrukturen, wie zum Beispiel stark plastisch verformten Zonen, weiße – und braune Ättschichten und geschichteten Oberflächenschichten (SSLs) ermöglichen. Zur Bewertung mikro-mechanischer Eigenschaften, entscheidend für Rissinitiierung und -wachstum, wird die *in situ* Mikrobiegebalken Methode angewandt. Die Ergebnisse zeigen eindrücklich die Relevanz von SSLs für die Rissbildung bei Rollkontaktermüdung auf. Die unbestimmte Belastungsgeschichte der Proben aus dem Feld behindert jedoch eine systematische Untersuchung. Um dieses Problem zu lösen, wird ein neuartiger Laboransatz entwickelt, bei dem ein Zwei-Scheiben-Tribometer (mechanische Belastung) und Laseroberflächenbehandlungen (thermische Belastung) kombiniert werden, um realistische SSLs zu imitieren. Im letzten Teil der Arbeit wird dieser Ansatz verwendet, um definierte Proben für eine systematische Studie über die Rissinitiierung bei SSLs zu generieren. Die vorgestellte Methodik trägt zu einem besseren Verständnis der entstandenen oberflächennahen Mikrostrukturen an Rädern bei und kann helfen, die Lebensdauer von Eisenbahnradern in Zukunft zu steigern.

List of Figures

Figure 1: Several tons of wheel load and an open system tribology within ~1 cm² of contact zone, the outstanding complexity of the wheel-rail contact results in a wide variety of evolving near-surface microstructures during service. [58], [59]..... 2

Figure 2: Different possible regions of the wheel-rail contact (image adapted from [59])..... 4

Figure 3: Microstructural evolution of SPD microstructure based on a cross-sectional cut of a rail from service: Different zones represent the evolution of the near-surface microstructure undergoing continuous dynamic recrystallization. (Own unpublished work) 7

Figure 4: a) Fe–C phase diagram, coloured region demonstrate carbon content range of common wheel and rail steels in Europe (adapted from [107]). The kinetics of phase transformation is described by b) TTA (heating) and c) TTT (cooling) diagrams are used, shown for a Ck45 steel comparable to common wheel steel [104]. 10

Figure 5: Exemplary RCF related material defect on rails: a) severe squat formation [119], b) spalled-out stud defect [35], c) squat defect [115], and wheels: tread surface after d) ~40,000 km and e) 140,000 km [120], f) RCF cluster [110] 13

Figure 6: Fundamental principle of a twin disc configuration (Image adapted from [121]) 15

Figure 7: Self-constructed twin disc tribometer at AC2T research GmbH..... 16

Figure 8: a) Laser system at AC2T research GmbH [159]; b) Schematic illustration of the laser surface treatment in *feed mode*. 18

List of Abbreviations and Symbols

α	Optical absorption coefficient
a	Length of laser spot
A_1	Minimum temperature for austenite (Fe-C phase diagram)
A_3	Boundary temperature austenite – austenite/ferrite (Fe-C phase diagram)
bcc	Body centred cubic crystal structure
BE	Backscattered electron
BEL	Brown etching layer
E	Young's modulus
EBSD	Electron backscatter diffraction
ED	Energy density
FIB	Focused ion beam
HAGB	High angle grain boundary
IPCC	Intergovernmental panel on climate change
K_{I0}	Local fracture toughness
LAGB	Low angle grain boundary
LDQ	Laser dispersed quenching / Laser discrete quenching
LOM	Light optical microscopy
LSP	Laser shock peening
NI	Nanoindentation
p	Pressure
P	Normal load
PD	Power density
P_{Laser}	Laser power
R_1, R_2	Radii of the wheel and the rail
ROI	Region of interest
SE	Secondary electron
SEM	Scanning electron microscopy
SPD	Severe plastic deformation
SRR	Sliding rotation ratio
TEM	Transmission electron microscopy
TTA	Time-Temperature-Austenitization
TTT	Time-Temperature-Transformation

v_1, v_2 Rotational speeds of the discs
 v_{Laser} Moving speed of the laser
wt%Mass fraction

1 Introduction and Motivation

The latest report of the Intergovernmental Panel on Climate Change (IPCC) published in 2021 points out far-reaching and rapid consequences for the atmosphere, oceans, cryosphere, and biosphere due to global warming. In 2019 the atmospheric CO₂ concentration – a key factor in climate change – was higher than at any time in at least 2 million years. Limiting human-induced global warming to a certain level requires limiting cumulative CO₂ emissions. In this regard, the transport sector shows a huge potential underlined by a cost-benefit calculation for climate protection up to 2030 in the IPCC report, showing that an expansion of public transportation can reduce CO₂ emissions in a significantly cheaper way compared to other activities. [1]

Rail transportation is one of the lowest CO₂-emitting modes of transportation worldwide and can make a valuable contribution to the fight against climate change, in both passenger mobility and freight transport. However, its expansion leads to advanced challenges for the railroad infrastructure due to increasing train speeds and shorter train intervals for passenger trains, and higher axle loads for freight trains. [2]

The increasing loading conditions significantly influence the materials in the wheel-rail contact. High mechanical and thermal loads lead to a change of the near-surface microstructure on rails and wheels [3]–[16]. Besides gradual wear and severe plastic deformation (SPD) of the microstructure, a brittle layer is commonly observed, the so-called *White Etching Layers* (WELs), named after its appearance in light optical microscopy after etching with diluted nitric acid [7], [17]–[24]. Recently, an underlying so-called *Brown Etching Layer* (BEL) attracted research interest, the combination of WEL and BEL is called *Stratified Surface Layer* (SSL) [25]–[29]. Various possible formation mechanisms are discussed in the literature (mechanically, thermally, or a combination), however, analyses of samples from the field indicate the relation of SSLs to rolling contact fatigue (RCF) damage [14], [25], [30]–[36]. Hence, to understand RCF crack initiation, knowledge of the near-surface microstructure is crucial. To remove surface defects and ensure good operating conditions periodic grinding is executed on rails [37]–[42], on the wheel side re-turning is done in certain intervals [43]–[45]. Nevertheless, RCF and tread damage are the main reasons for premature wheel removal. Despite increasing demands and new wheel material developments [46]–[52], the effects on microstructural changes of wheels are less well studied compared to rails up to now, showing a need to catch up. Several studies

present in-depth analyses of the microstructural characteristics of evolved near-surface microstructures of rail wheels, but micro-mechanical properties are barely addressed due to the small scale of these microstructural regions. Until recently, nanoindentation hardness seemed to be the only tool to evaluate mechanical properties in the micrometre scale. However, recent developments in focused ion beam (FIB) technique enable the preparation of specimens in the micrometre range, facilitating the execution of small-scale mechanical testing methods such as bending, tensile, or compression tests [53], [54]. This allows the evaluation of mechanical properties with high spatial resolution. Micro-bending studies can give insights into material behaviour in distinctive regions, and – under certain conditions – can be used to calculate the local fracture toughness, which is recently shown for WELs and BELs on rails [54]–[57]. However, an insurmountable handicap of samples from the field is the unknown loading history. Even though certain parameters are known (e.g. kilometrage, axle load, running speed), the complex loading situation in combination with several environmental influences leads to almost unlimited variations of WELs, BELs, and SSLs. This hinders a systematic and reproducible study of its formation mechanism and its relation to RCF.



Figure 1: Several tons of wheel load and an open system tribology within $\sim 1 \text{ cm}^2$ of contact zone, the outstanding complexity of the wheel-rail contact results in a wide variety of evolving near-surface microstructures during service. [58], [59]

To overcome this issue, efforts have been made to imitate near-surface microstructures evolving in wheel-rail contacts under defined parameters in the laboratory. Mechanical loads are applied by e.g. twin disc tribometers or “full-scale” wheel-rail test benches, while thermal loads are imitated by e.g. inductive heating. Moreover, laser surface treatments demonstrate a promising method to create thermal-induced near-surface layers, since numerous parameters can be varied such as laser energy, lens geometry, traveling speed, or frequency. By adjusting the parameters applied in the laboratory, different reproducible variations of WELs, BELs, and SSLs can be created with defined loading history. Combining mechanical and thermal loads in different sequences can allow imitation of a chronological evolution of near-surface microstructures in wheel-rail contacts. This enables a systematic study of the formation mechanisms and their influencing parameters. Moreover, lab-induced samples can serve for further testing such as wear or fatigue tests. However, reasonable studies are always based on the comparability of the lab-induced microstructures to the microstructures observed in the field.

This thesis aims to improve the knowledge about the evolution of near-surface microstructures on rail wheel treads with a focus on microstructural layers (WELs, BELs, and SSLs) susceptible to RCF crack initiation.

Extensive studies are conducted on wheel microstructures from field samples, where *in situ* micro-bending studies are implemented to complement the analysis of microstructural characteristics with micro-mechanical characteristics. Based on these findings, a method to imitate realistic WELs on rail wheel materials under defined parameters is presented by laser surface treatments. Lab-induced samples are benchmarked against samples from the field in terms of microstructure and micro-mechanical properties to demonstrate reasonable comparability. Finally, an approach to imitate realistic and reproducible SSLs on rail wheel materials for systematic studies on RCF crack initiation is presented. This is accomplished by combining laser surface treatments (representing thermal loads) and twin disc tribometer tests (mechanical load). A methodological model of RCF crack initiation in the presence of SSLs is described, whereat a huge potential of the testing method in terms of variations of formation and testing parameters is shown.

2 Wheel-rail contact

The wheel-rail contact reveals an enormous complexity due to the interaction of several variables such as high mechanical loads (static and dynamic), thermal influences, as well as constantly changing environmental conditions and wheel/rail profiles. Compared to the component dimensions the contact zone is small ($\sim 1 \text{ cm}^2$), whereas its position varies continuously depending on the current wheel and rail profiles, whether it is a straight or curved track, and on the type of wheelset (leading or trailing). [3], [60]

Three regions of the possible location of the wheel-rail contact can be defined (Figure 2):

- Region A: Wheel tread – Rail head
- Region B: Wheel flange – Rail gauge corner
- Region C: Wheel field side – Rail field side

Region A represents the main contact region – most common for straight or large curved tracks – revealing low contact stresses. Longitudinal creep forces are larger in comparison to side creep forces. When the wheel-rail contact occurs in region B, the contact zone is smaller coming up with high contact stresses. This can lead to significant fatigue of the inner side of the rail and wear at the wheel flange. The latter can lead to changing contact mode, a two-point contact is possible (Wheel tread and flange – Rail gauge corner). Lubrication can reduce the wear rate in this region. Contact situated in region C is quite rare, but if this case occurs induced contact stresses are high with significant tangential forces toward the wheel tread. [3], [11], [61]



Figure 2: Different possible regions of the wheel-rail contact (image adapted from [59])

To understand and model the contact mechanics in wheel-rail contacts several theories have been introduced, divided into normal contact and tangential contact theories [62]. Regarding normal contact theories, Hertz presented a theory in the 19th century to calculate the contact area and the normal pressure distribution [63]. In this approach, two cylinders (wheel and rail) are in contact perpendicular to each other resulting in elliptical contact zones, pressure p is calculated as follows:

$$p = \sqrt[3]{\frac{3 P E^2}{2 \pi^3 R^2 (1-\nu^2)^2}} \quad (1)$$

The material constants (Young's modulus E and Poisson's ratio ν) are assumed equal for wheel and rail material, P represents the normal load, and R the equivalent radius. The latter is calculated by

$$\frac{1}{R} = \frac{1}{R_1} + \frac{1}{R_2} \quad (2)$$

where the radii of the wheel and rail are represented by R_1 and R_2 . For this approach, linear elastic material behaviour, no friction, smooth contacting surfaces, and further geometrical limitations are assumed. Besides significant restrictions, Hertzian theory is still widely used for wheel-rail contact mechanics and dynamics, and maximum contact pressures in the range of 600 MPa and 2.7 GPa are calculated. [3], [11], [60], [62], [64]

Accelerating, braking, or steering of the wheel induces slip between the wheel and the rail resulting in longitudinal creep forces, while sideslip events lead to lateral creep forces. To address this – in particular to study the tangential shear stress distribution over the contact patch area – several tangential contact theories are developed and presented in a comprehensive review article by Meymand et al. [62]. However, the need for further research to address the complex wheel-rail contact mechanics is pointed out, even though much time elapsed since Hertzian theory back in 1881.

In addition to mechanical loads, wheels and rails are subjected to thermal loads in service [65]–[68]. For instance, tread breaking (without wheel sliding) can induce temperatures of ~500 °C for durations up to 0.5 h in the wheel-rail contact during regular freight operations [69], [70]. Moreover, braking and traction processes can result in relative wheel sliding, potentially inducing even higher local temperatures [69]. Full-scale tests conducted by Ahlström et al. [4] show possible temperatures up to 1000 °C. Since there is no possibility to measure the current temperature within the wheel-rail contact zone, efforts have been

done on modelling [23], [71]–[73]. Bernsteiner et al. [23] combined a simulation model with full-scale tests, where results show possible maximum temperatures of 1050 °C under certain creepage conditions.

In summary, thermal loads are supposed to significantly influence the near-surface microstructure in the wheel-rail contact, additionally to the mechanical loading situation. Consequent microstructural changes are therefore presented in the following section.

2.1. Evolution of near-surface microstructures

Upon the first day in service, the near-surface microstructure of wheels and rails is affected by mechanical and thermal loads. Microstructural evolution in service is substantially influencing the mechanical properties of the materials in contact and bias material behaviour such as wear, crack initiation, and rolling contact fatigue. Therefore, understanding the evolution of rail and wheel microstructures is crucial to ensure rail infrastructure reliability and safety. Due to their combination of good strength and wear properties, steel grades with carbon contents in the range of 0.5–1.1 wt% for rails [74] and ~ 0.55 wt% for wheels [75] are commonly used in European rail networks. Variations in the as-manufactured microstructure are based on additional heat treatments, affecting the grain size, pro-eutectoid ferrite content, and lamellae spacing in the pearlite. However, some specific microstructures evolving in the wheel-rail contact are observed on samples from the field over the last decades.

2.1.1 Severe plastic deformation

In general, common wheel and rail materials show elastic limits above the expected stress level in the wheel-rail contact. But, in operation, surface stresses often exceed the elastic limit in the near-surface region due to interfacial shear and slip (curving, traction, braking), hence, introducing plastic flow and residual stresses. This increases the elastic limit of the material, known as “shakedown” or “strain hardening” effect. Further, if the limit of possible hardening increase of the material is reached (“shakedown limit”), repeated plastic deformation occurs at every load cycle. [8], [65], [66], [76]–[78]

Hence, a massive change of the near-surface microstructure is observed [5], [15], [76], [79]–[81], resulting in SPD microstructure in the outermost layer of wheels and rails. The evolved microstructure can be divided into three zones – SPD zone, transition zone, and bulk zone – whereat the zones can also be seen as the microstructural evolution over time (Figure 3).

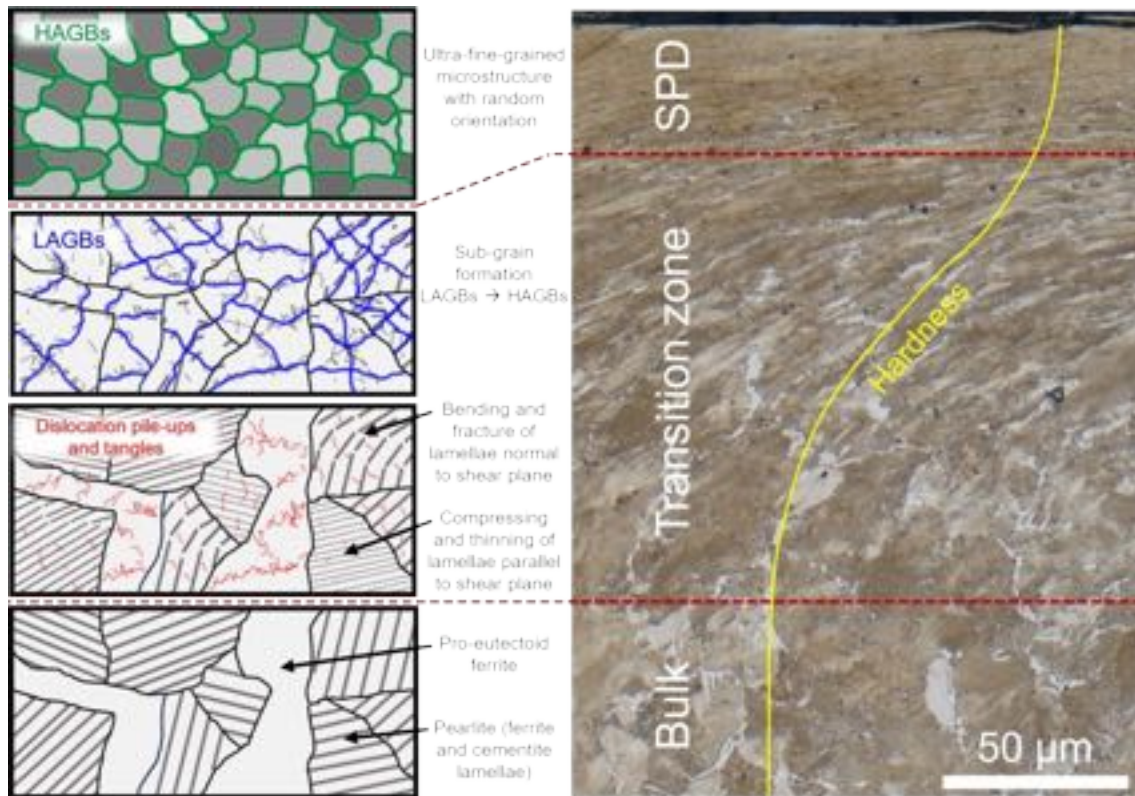


Figure 3: Microstructural evolution of SPD microstructure based on a cross-sectional cut of a rail from service: Different zones represent the evolution of the near-surface microstructure undergoing continuous dynamic recrystallization. (own unpublished work)

For a common ferritic-pearlitic rail wheel (~ 0.55 wt% C), the bulk zone represents the strain-free microstructure, with unaffected lamellar structure and random orientation of the lamellae in the pearlite and pro-eutectoid ferrite. In the transition zone, the microstructure is affected by the normal forces and induced shear stresses. Hence, grains are compressed and further stretched in shear stress direction. Pearlite colonies with lamellae parallel to the shear plane tend to exhibit decreased lamellar spacing, while lamellae normal to the shear plane start to bend and fracture, while a large number of dislocations are formed in the ferrite. This leads to the formation of low angle grain boundaries (LAGBs) resulting in sub-grain formation with a preferred orientation in the direction of the shear stress. With increased strain the orientation of the sub-grains becomes random, and the microstructure is transforming into an ultra-fine-grained microstructure with high angle grain boundaries (HAGBs). The simultaneous increase of HAGBs and refinement of grains indicates dynamic recrystallization, which is usually observed at elevated temperatures ($400\text{--}600^\circ\text{C}$). However, in rolling-sliding contacts, this can be completed at lower temperatures due to SPD, referred as to continuous dynamic recrystallization. The cementite fragmentation segues into a dissolution until reaching a saturation concentration. The SPD zone pictures the most advanced microstructural

evolution in terms of plastic deformation. Pearlite colonies are severely fragmented and a fibrous structure almost parallel to the surface is observed. Finally, the grain refinement ceases due to the balance of dislocation accumulation rate and dislocation annihilation. [15], [80], [82]

Although normal force and shear stress in the wheel-rail contact are the main drivers in the formation of SPD microstructures on wheels and rails, elevated temperatures from friction are suggested to affect its evolution [5]. However, it is clear that the evolved SPD microstructure comes up with different mechanical properties – e.g. increased hardness – in comparison to the “virgin” rail/wheel material [83]–[85] (Figure 3). Moreover, SPD disrupts the thermodynamic equilibrium and can promote subsequent phase transformations such as the formation of WEL.

2.1.2 White Etching Layer

Probably more than 100 years passed since the first mention of the term *White Layer* by Stead [86] in 1912 in the course of studying steel wire ropes. Investigations concerning microstructural evolutions in wheel-rail contacts gained momentum around 1950 [87]–[90] due to their high relevance for railway safety and reliability. In general, the term *White Layer* or *White Etching Layer* is originating from the resistance to etching in contrast to the bulk material, revealing a featureless white appearance under optical microscopes. The WEL usually represents a hard and brittle layer broadly observed at the surfaces of materials in sliding or rolling-sliding contacts, however, this section will focus on the wheel-rail contact.

Over the years the formation mechanism of WEL is controversially discussed due to the complex contact situation in the wheel-rail contact and its open system tribology [3], [91]. The formation was stated mechanically, thermally, and thermo-mechanically. It is clear, that the influences of stresses and temperature act simultaneously in the wheel-rail, therefore the question is more likely what the main driving force of the formation is. Within the last decades, tremendous advances in microstructural analysis methodologies enabled in-depth studies on WEL microstructures and shed more light on their formation mechanism. Summarizing around 100 years of research on WELs, the current state of knowledge includes two main categories of WELs:

- *WEL predominantly formed by severe deformation*

In literature, this category of WEL is also referred to as “SD-WEL” (severe deformation) [7], [92] and “T-WEL” (tribological) [18], [93].

- *WEL induced by temperatures above austenitization temperature*

The terminology in literature includes “TP-WEL” (thermal produced) [14] / (temperature and pressure) [7], “thermally-induced WEL” [17], [94], and “M-WEL” (martensite) [95].

The broad variety of terms used in literature in combination with innumerable WEL varieties observed on samples from the field does not make it easier for researchers to systematically study the phenomena of WEL in wheel-rail contacts. However, both categories reveal increased hardness and brittleness, and commonly cracks are observed in the presence of WELs. These changes in mechanical properties are based on the microstructural characteristics developed in the wake of their formation.

In the case of the *WEL predominantly formed by severe deformation*, the formation mechanism is proposed as a follow-up to SPD (described in the previous section), where uniform and equiaxed grains with random orientation in the nanometre scale evolve in the final stage. Further, the dissolution of cementite progresses, and the volume factor of the cementite decreases constantly until an almost single-phase equiaxed nano-grained ferritic microstructure evolves in the outermost layer of the wheel or rail. This process is equivalent to mechanical alloying, where the dissolution of cementite is possible below the austenitization temperature. WELs formed primarily by plastic deformation reveal high hardness (>800 HV) and minor layer thickness in the range of 10 – 20 μm . [9], [10], [18], [22], [92], [93], [96]–[100]

The other category, *WEL induced by temperatures above austenitization temperature*, presumably starts its formation based on a deformed wheel/rail microstructure as well but is mainly driven by high thermal loading. This is especially the case when the wheel slides along the rail due to braking and traction processes, or when rails get ground in the course of maintenance works. Moreover, arcing due to electrical current leaking is proposed as a source of high local temperatures. [38], [101]–[103]

Since rail and wheel materials are usually low-alloy steels, the Fe–C phase diagram can be used to roughly evaluate phase transformation temperatures (Figure 4a). For ferritic-pearlitic wheel steels, a temperature rise above A_1 temperature leads to the destabilization of the pearlite. With the diffusion of C, austenite nucleates at the cementite/ferrite interfaces. For further austenite growth C diffusion from the cementite through the austenite to the austenite/ferrite interfaces is necessary, which is a limiting factor due to lower diffusion rate compared to through the ferrite. Therefore, for a single wheel-rail contact cycle complete austenitization is not considered. However, the temperature rise

above A_3 can last several seconds during massive braking events. Time-Temperature-Austenitization (TTA) diagrams are used to describe the kinetics of phase transformation in the course of temperature increase, shown for a Ck45 steel (comparable to common wheel steel) (Figure 4b). It shows that high heating rates shift the transformation temperatures A_1 and A_3 to higher levels. Another influence on phase transformation is multiaxial compression, which can lower the transformation temperatures and therefore supports austenitization in the near-surface wheel and rail microstructure. Time-Temperature-Transformation (TTT) diagrams describe the subsequent phase transformations during cooling. Even though they are influenced by various parameters – e.g. chemical composition, grain size distribution, and degree of deformation – the diagram of Ck45 can give a good estimation for common wheel and rail materials (Figure 4c). Due to the rapid cooling within the wheel/rail, a certain fraction of the austenite transforms to martensite. The microstructure of WELs induced by temperatures above austenitization temperature is therefore reported as martensitic with some amount of retained austenite. [23], [26], [28], [32], [69], [97], [104]–[106]

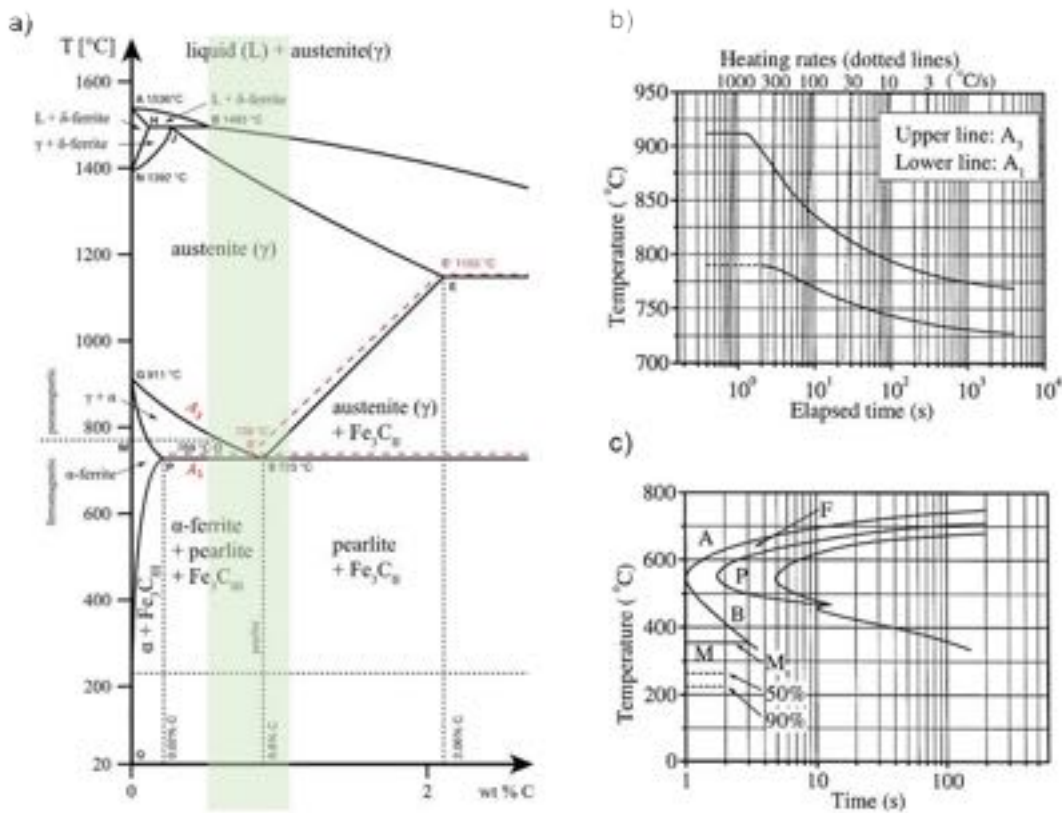


Figure 4: a) Fe-C phase diagram, coloured region demonstrates the range of common wheel and rail steels in Europe (adapted from [107]). The kinetics of phase transformation is described by b) TTA (heating) and c) TTT (cooling) diagrams are used, shown for a Ck45 steel comparable to common wheel steel [104].

2.1.3 Brown Etching Layer

In addition to the WEL, another characteristic layer is observed on wheels and rails in service, the so-called *Brown Etching Layer* (BEL). As for the WEL, the BEL is named after its appearance under light optical microscopy after etching, in the case of the BEL featureless and brownish. BELs are not as well studied as WELs, but increasing research is done in the last years since it is supposed to play a crucial role on fatigue cracking.

Based on the lack of systematic studies no common formation mechanism of BEL is known at this time, its formation is discussed controversially. It is suggested that several observations have already been made prior using the terminology BEL.

In 1999 Ahlström and Karlsson [104] observed distinctive layers underneath martensite plugs (referring to WEL) when conducting full-scale experiments on wheel flats. They termed these layers primary- and secondary martensite plugs and stated, that the heat from the second contact tempered the martensite below. Observations of BELs on rails were presented in the following years, proposing mechanical cold working as its formation [10], [36], even though the observation of BELs was not the main objective of these works. The first focused study on BEL was done by Li et al. [25] in 2016. The authors proposed repeated martensite-austenite-martensite transformations as the formation mechanism of the BEL, resulting in a tempered martensitic microstructure. Two years later, Messaadi and Steenbergen [29] identified a globular bainitic microstructure for the BEL by studying rails from the field. They introduced the term *Stratified Surface Layer* (SSL) for the combination of WEL and underlying BEL and claimed the difference in the cooling rate at the surface and the subsurface as the origin of the formation of WEL and BEL.

In contrast, in 2019 Kumar et al. [26] studied the formation mechanisms for BELs based on investigating a curved rail track and concluded that multiple cycles of mechanical and thermal loads cause a modification of the pearlitic microstructure in near-surface regions where the temperature was too low for austenitization. The cementite laths of pearlite are fragmented and partially dissolved, as a finer microstructure allows for a higher C content in the alpha regions. Further, other regions experiencing a temperature sufficient for austenitization contain a high fraction of martensite, which under certain wheel-rail contact conditions or for certain temperature-profiles are tempered to precipitate secondary carbides, forming the BEL. In the same year, Al-Juboori et al [108] observed BELs on worn rails and suggested their formation either mechanically by repeated plastic deformation and/or thermally due to tempering of the initial martensitic microstructure. In a study by Tung et al. [27] in 2022, BEL on rails is identified as lath martensite, proposing

temperatures above austenitization. However, the definition of BEL and WEL in this study is not precise and fails a clear differentiation.

The latest study on this topic is presented by Gao et al. [28] investigating a heterogeneous WEL/BEL structure observed in bainitic rail steels from the field. The authors analysed the BEL microstructure as a composite of nanocrystalline martensite or ferrite, austenite, cementite, and oxide. Further, in contrast to all conducted studies on WELs and BELs for pearlitic steels, the BEL was supposed to be harder and more brittle in contrast to the WEL. However, this observed multiple stratification layers are suggested as a unique phenomenon of bainitic rails and are presumably not occurring for common (ferritic-) pearlitic wheel and rail steels.

In summary, the formation of BEL is a quite new topic of research and studies stated controversial mechanisms based on observations on samples from the field. However, the evolution of BELs and therefore SSLs change the mechanical properties in the near-surface microstructure and is assumed to be affecting wear and rolling contact fatigue.

2.2 Rolling-contact fatigue

Rolling contact fatigue (RCF) is defined as a failure or material removal driven by crack propagation caused by the near-surface alternating stress field [109] and is an important factor in rail transportation efficiency and safety. Accidents caused by RCF can lead to personal injuries and economical costs due to unplanned maintenance and further possible train delays and decreased capacities. Numerous studies of material failures on rails and wheels related to RCF are published over the last decades and a more sophisticated terminology is developed. [34], [66], [110]–[113]

Two types of apparently similar-looking material defects on rails are very prominent in literature, namely the *squat defect* and the *stud defect* [35], [110], [114], [115]. The *squat defect* is associated with plastic deformation [116]. Traction, curving, and braking lead to extensive plastic deformation of the near-surface microstructure with distinctive orientation and alignment based on the dominant rolling direction. Consequently, when the accumulation of plastic strains exceeds the fracture strain, cracks are initiated at the surface. This phenomenon is called ratcheting. In the case of alternating directions – thus plastic deformation in both directions – failure is caused by low-cycle fatigue. Cracks initiated at the surface propagate under a shallow angle along the alignment of the

plastically deformed microstructure. In a certain depth branching of the crack towards the surface is followed and results in a break-out of material fragments. In contrast, the RCF crack initiation in case of *stud defects* is associated to presence of brittle surface layers, more precisely WELs [117]. Their low fracture toughness and residual stress promote crack initiation and growth. Moreover, this relation is also indicated for RCF clusters in the centre of wheel treads, since they show parallels to stud defects on rails. [3], [34], [35], [66], [115], [115], [118]

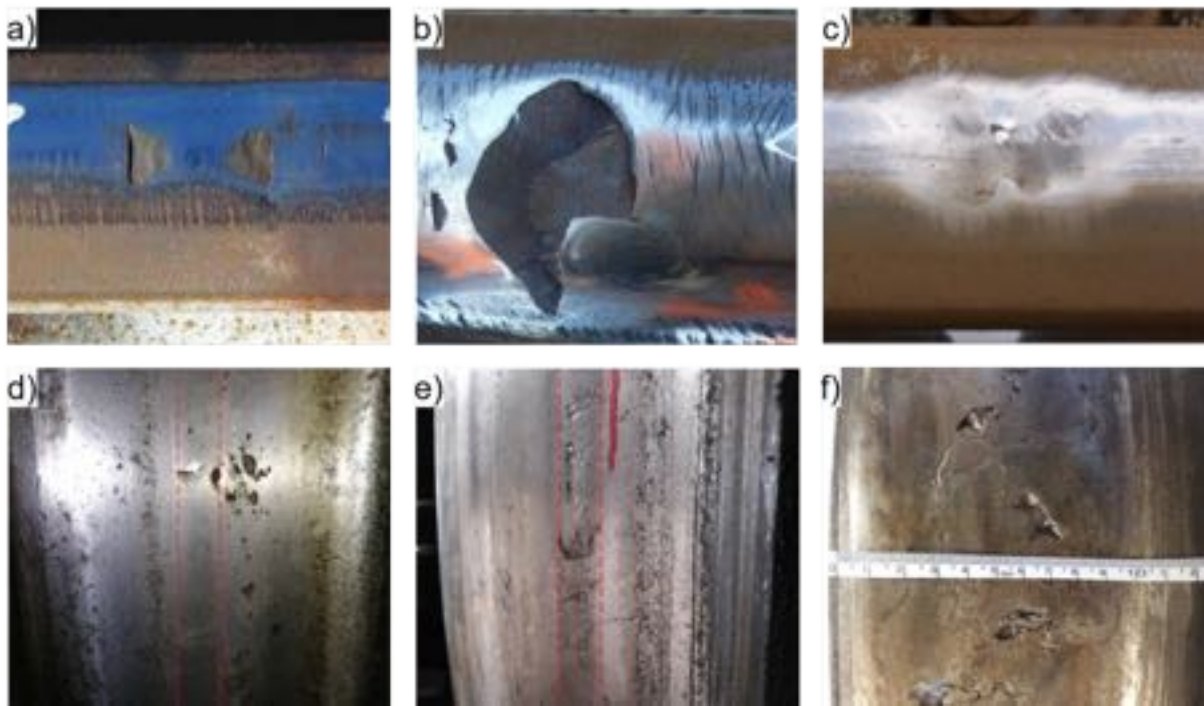


Figure 5: Exemplary RCF-related material defect on rails: a) severe squat formation [119], b) spalled-out stud defect [35], c) squat defect [115], and wheels: tread surface after d) ~40,000 km and e) 140,000 km [120], f) RCF cluster [110]

Besides extensive studies, a common terminology on RCF-related defects is still not well developed since RCF crack initiation and propagation are influenced by numerous parameters due to the open tribology system of the wheel-rail contact and its complex loading situation with additional dynamic effects. Further, thermal loading highly influences surface cracking since a temperature rise decreases the fatigue strength of the material and potentially induces residual tensile stresses.

Rail wheels run at moderate surface friction can show subsurface crack initiation, whereat material defects can cause high localized stresses and fatigue crack initiation in considerable depths. This is promoted due to material hardening and residual compressive stresses at the wheel surface. Subsurface crack initiation on rails is observed in heavy haul

lines, where cracks are initiated in depths where large tensile stresses – often in combination with material defects – occur. [3], [34], [35], [66], [115], [115], [118]

The wheel-rail contact is one of the most complex contact situations in engineering accompanied by an open tribology system, hence, this results in innumerable influencing parameters on the RCF. In addition to valuable observations from the field and advanced modelling, systematic studies are needed with defined and reproducible parameters to improve the knowledge of microstructural changes and related failures in wheel-rail contacts.

3 Laboratory methodologies to imitate near-surface microstructure in wheel-rail contacts

To study the wheel-rail contact – more specifically the evolving near-surface microstructures and related wear, crack initiation, and fatigue failure – extensive analyses of rail and wheel samples from the field are conducted. This is fundamental for understanding ongoing mechanisms, however, the main drawback remains the unknown loading history of the samples. Even though estimations of axle loads, speeds, or kilometrages are known, the definite experienced mechanical and thermal loads are never recorded exactly. Therefore, laboratory approaches with defined samples tested under well-known loading parameters are crucial to enable systematic studies of phenomena in the wheel-rail contact.

3.1 Twin disc tribometer

Since the first development of twin disc equipment by Amsler in 1922, test rigs based on the principle of two rotating discs are widely used in investigating rolling- and rolling-sliding contacts. Basically, three main variables can be controlled in this setup: The rotation speed, the contact pressure (by applying an external force), and the slip (by varying the disc speeds). In most cases, the latter is managed by two independent motors for the discs, although numerous other constructive configurations have been developed over the last decades. Twin disc tribometers are nowadays often used for evaluating rolling-sliding contacts with high Hertzian contact stresses, for instance bearings, gears, or railway components. [121]

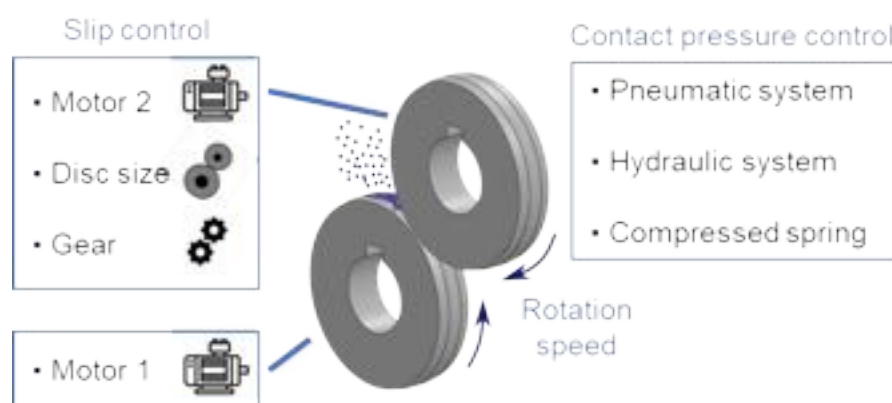


Figure 6: Fundamental principle of a twin disc configuration (Image adapted from [121])

In railway research, the twin disc tribometer is very popular due to relatively low costs and a good transferability of operational conditions to the small-scale test setup. Besides contact pressure, slippage, and speed [122]–[126], environmental influences can be studied due to an open construction in most configurations [127]–[132]. Probably most studies using twin disc tribometers in railway research are focused on wear, investigating different influences, rail and wheel materials, and surface treatments [48], [133]–[142]. Further, studies on crack initiation and RCF are presented [143]–[148]. However, the small-scale test setup also reveals some weak points such as potential misalignment of the discs or different heat dissipation in the contact due to smaller component volumes compared to the field, which has to be taken into account [147], [149]–[152].

The twin disc tribometer used in this thesis (*Publication VIII*) is a self-constructed test rig at AC2T research GmbH (Figure 7) with possible disc diameters from 45 – 150 mm, normal forces from 50 – 800 N, and rotation speeds in the range of 0 – 3,000 rpm. The discs are driven by separate motors which enables a continuous variation of the relative speed difference to ensure the set sliding rotation ratio *SRR* based on

$$SRR = 2 * \frac{(v_1 - v_2)}{(v_1 + v_2)} * 100 \quad (\%) \quad (3)$$

where v_1 and v_2 represent the rotational speeds of the discs. On the one hand, the twin disc tribometer is used to develop a deformation state in the near-surface microstructure of the samples under defined mechanical loading parameters. This enables reproducible samples for further experiments. On the other hand, the test rig was used to conduct fatigue tests of prior deformed samples affected by thermal loadings by laser surface treatments.

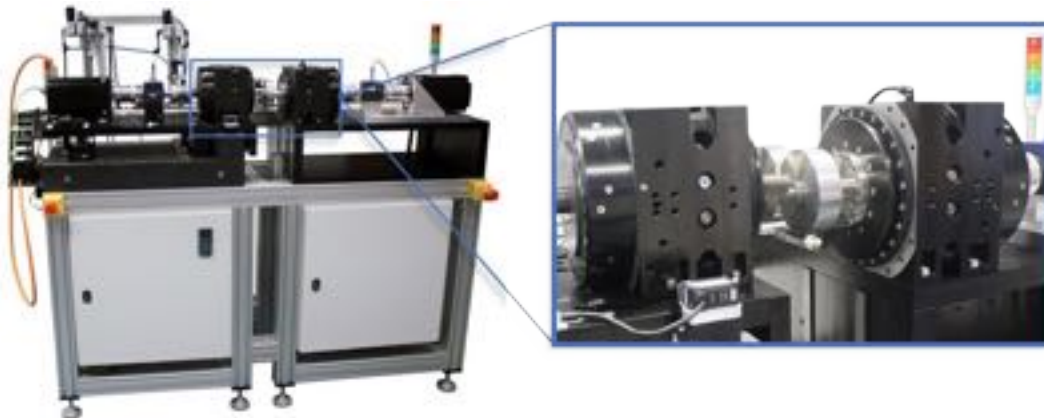


Figure 7: Self-constructed twin disc tribometer at AC2T research GmbH.

3.2 Laser surface treatment

Frequently used in the field of surface engineering, laser surface treatments are conducted to harden the surface layer and to improve the wear resistance of components in different applications. Various technologies are studied for wheel and rail materials, with broad terminology such as laser hardening, laser melting, laser shock peening (LSP), laser discrete quenching and laser dispersed quenching (LDQ). However, the basic principle is the increase of the surface temperature by high local laser power input above the critical transformation temperature A_1 and subsequent rapid cooling, resulting in a self-quenching of the near-surface region. For ferrous alloys such as wheel and rail steels, the quenching leads to a martensitic transformation forming a hard surface layer (referred to as WEL). Besides the material characteristics of the sample before laser treatment (chemical composition, grain size distribution,...) the phase transformation during laser surface treatment depends on the laser processing parameters, such as laser power, beam shape and geometry, and moving speed of the laser. [95], [138], [139], [153]–[157]

Hence, by varying these parameters defined and reproducible thermal loads can be applied. This reveals a promising approach to using laser surface treatments to imitate high local thermal loads – occurring in the wheel-rail contact zone at e.g., braking or slippage events – for systematic studies on WELs without the critical factor of an unknown (thermal) loading history as for samples from the field.

The laser system used in this thesis (*Publication V – VIII*) is a *Direct Diode Laser System* (HighLight 8000D, Coherent, U.S.) at AC2T research GmbH (Figure 8a). The laser source, a beam shape cartridge, generates a line beam which is combined with a negative lens for expanding the line beam to produce different rectangular focus sizes. For most of our experiments, a beam shape cartridge emitting a 24 mm wide line beam was used in combination with a negative lens for expanding the line beam to 3 mm. The nominal continuous power output of the system is 8 kW at a wavelength of 975 nm, whereby different laser powers were used for the experiments. In addition, a *pulse-mode* is available with a repetition rate of up to 300 Hz. The moving and positioning of the laser spot is done by the installation of the laser system on a 6-axis robot arm (IRB 4600-60/2.05, ABB, Austria) with a range of 2.05 m.

Laser surface treatments are conducted in *feed-mode* and *pulse-mode*. In *feed-mode* the laser spot is moving at a constant travel speed along the surface. In contrast, the laser spot

is positioned at the same place during the treatment duration for the *pulse-mode*, applying repetitive laser treatments.

The power density PD (in *feed-mode*) for a rectangular laser spot (a , b) at a certain laser power P_{Laser} can be calculated based on:

$$PD = \frac{P_{Laser}}{a*b} * \alpha \left(\frac{W}{mm^2} \right) \quad (4)$$

The optical absorption coefficient α is depending on the surface quality of the treated samples [158]. Further, the energy density ED can be calculated:

$$ED = PD * \frac{b}{v_{Laser}} \left(\frac{Ws}{mm^2} \right) \quad (5)$$

The power density PD is calculated above, b represents the length of the rectangular laser spot in the travel direction and v_{Laser} the travel speed of the laser (Figure 8b).

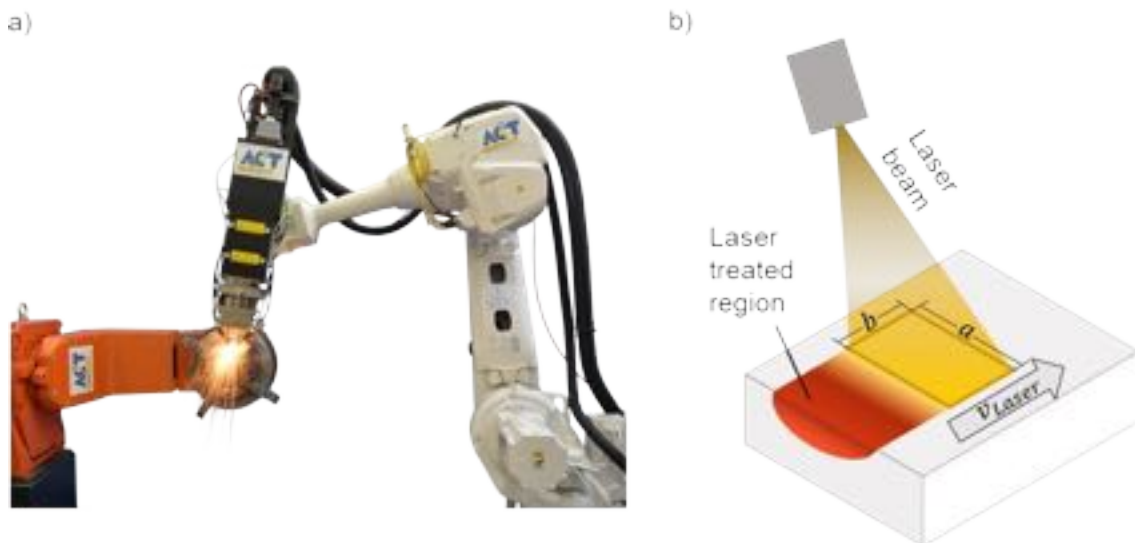


Figure 8: a) Laser system at AC2T research GmbH [159]; b) Schematic illustration of the laser surface treatment in *feed-mode*.

To conclude it can be stated that by varying the laser parameters different thermal loads can be imitated and, most importantly, reproduced due to defined settings. By combining defined mechanical loads (twin disc tribometer) and thermal loads by laser surface treatments a reproducible laboratory approach can be executed for systematic studies of evolving near-surface microstructure in wheel-rail contacts during service.

4 Bibliography

- [1] UN IPCC, “Sixth Assessment Report (AR6),” *Intergovernmental Panel on Climate Change*, 2023 2021.
- [2] IEA, “The Future of Rail: Opportunities for energy and the environment,” *IEA*, 2019, doi: 10.1787/9789264312821-en.
- [3] R. Lewis and U. Olofsson, *Wheel—rail interface handbook*. Woodhead Publishing Limited, 2009. doi: 10.1533/9781845696788.
- [4] J. Ahlstrom and B. Karlsson, “Microstructural evaluation and interpretation of the mechanically and thermally affected zone under railway wheel flats,” *Wear*, vol. 232, p. 1–14, 1999.
- [5] K. Cvetkovski and J. Ahlström, “Characterisation of plastic deformation and thermal softening of the surface layer of railway passenger wheel treads,” *Wear*, vol. 300, no. 1–2, pp. 200–204, 2013, doi: 10.1016/j.wear.2013.01.094.
- [6] J. Hua *et al.*, “EBSD Study on Proeutectoid Ferrite and Eutectoid Ferrite Refinement Mechanism of D2 Wheel Steel Under a Rolling Condition,” *Tribol Lett*, vol. 69, no. 4, p. 148, 2021, doi: 10.1007/s11249-021-01527-6.
- [7] A. Al-Juboori *et al.*, “Characterisation of White Etching Layers formed on rails subjected to different traffic conditions,” *Wear*, vol. 436–437, p. 202998, 2019, doi: 10.1016/j.wear.2019.202998.
- [8] J. Tunna, J. Sinclair, and J. Perez, “A Review of wheel wear and rolling contact fatigue,” *Proceedings of the Institution of Mechanical Engineers, Part F: Journal of Rail and Rapid Transit*, vol. 221, no. 2, pp. 271–289, 2007, doi: 10.1243/0954409JRRT72.
- [9] A. Pyzalla, L. Wang, E. Wild, and T. Wroblewski, “Changes in microstructure, texture and residual stresses on the surface of a rail resulting from friction and wear,” *Wear*, vol. 251, no. 1–12, pp. 901–907, 2001, doi: 10.1016/S0043-1648(01)00748-7.
- [10] W. Lojkowski, M. Djahanbakhsh, G. Bürkle, S. Gierlotka, W. Zielinski, and H.-J. Fecht, “Nanostructure formation on the surface of railway tracks,” *Materials Science and Engineering: A*, vol. 303, no. 1–2, pp. 197–208, 2001, doi: 10.1016/S0921-5093(00)01947-X.
- [11] P. Molyneux-Berry, C. Davis, and A. Bevan, “The Influence of Wheel/Rail Contact Conditions on the Microstructure and Hardness of Railway Wheels,” *The Scientific World Journal*, 209752, 2014, doi: 10.1155/2014/209752.
- [12] G. Donzella, A. Mazzù, and C. Petrogalli, “Competition between wear and rolling contact fatigue at the wheel—rail interface: some experimental evidence on rail steel,” *Proceedings of the Institution of Mechanical Engineers, Part F: Journal of Rail and Rapid Transit*, vol. 223, no. 1, pp. 31–44, 2009, doi: 10.1243/09544097JRRT161.
- [13] R. Pan, Y. Chen, H. Lan, S. E, and R. Ren, “Investigation into the microstructure evolution and damage on rail at curved tracks,” *Wear*, vol. 504–505, p. 204420, 2022, doi: 10.1016/j.wear.2022.204420.
- [14] J. I. Pereira, G. Tressia, E. J. Kina, A. Sinatora, and R. M. Souza, “Analysis of subsurface layer formation on a pearlitic rail under heavy haul conditions: Spalling characterization,” *Engineering Failure Analysis*, vol. 130, p. 105549, 2021, doi: 10.1016/j.engfailanal.2021.105549.
- [15] Y. Hu *et al.*, “Microstructure evolution of railway pearlitic wheel steels under rolling-sliding contact loading,” *Tribology International*, vol. 154, p. 106685, 2021, doi: 10.1016/j.triboint.2020.106685.
- [16] D. Peng and R. Jones, “The development of combination mechanical contact and thermal braking loads for railway wheel fatigue analysis,” *Theoretical and Applied Fracture Mechanics*, vol. 60, no. 1, pp. 10–14, 2012, doi: 10.1016/j.tafmec.2012.06.002.

- [17] B. Hieu Nguyen, A. Al-Juboori, H. Zhu, Q. Zhu, H. Li, and K. Tieu, “Formation Mechanism and Evolution of White Etching Layers on Different Rail Grades,” *International Journal of Fatigue*, p. 107100, 2022, doi: 10.1016/j.ijfatigue.2022.107100.
- [18] R. Pan, Y. Chen, H. Lan, S. E, and R. Ren, “Investigation into the evolution of tribological white etching layers,” *Materials Characterization*, vol. 190, p. 112076, 2022, doi: 10.1016/j.matchar.2022.112076.
- [19] R. Pan, R. Ren, C. Chen, and X. Zhao, “The microstructure analysis of white etching layer on treads of rails,” *Engineering Failure Analysis*, vol. 82, pp. 39–46, 2017, doi: 10.1016/j.engfailanal.2017.06.018.
- [20] C. Liu *et al.*, “Formation mechanism for the white etching microstructure in the subsurface of the failure pearlite wheel steel,” *Wear*, vol. 494–495, p. 204243, 2022, doi: 10.1016/j.wear.2022.204243.
- [21] Q. Lian *et al.*, “Evolution of thermally induced white etching layer at rail surface during multiple wheel/train passages,” *International Journal of Fatigue*, vol. 159, p. 106799, 2022, doi: 10.1016/j.ijfatigue.2022.106799.
- [22] G. Baumann, H. J. Fecht, and S. Liebelt, “Formation of white-etching layers on rail treads,” *Wear*, vol. 191, no. 1–2, pp. 133–140, 1996, doi: 10.1016/0043-1648(95)06733-7.
- [23] C. Bernsteiner, G. Müller, A. Meierhofer, K. Six, D. Künstner, and P. Dietmaier, “Development of white etching layers on rails: simulations and experiments,” *Wear*, vol. 366–367, pp. 116–122, 2016, doi: 10.1016/j.wear.2016.03.028.
- [24] W. Österle, H. Rooch, A. Pyzalla, and L. Wang, “Investigation of white etching layers on rails by optical microscopy, electron microscopy, X-ray and synchrotron X-ray diffraction,” *Materials Science and Engineering: A*, vol. 303, no. 1–2, pp. 150–157, 2001, doi: 10.1016/S0921-5093(00)01842-6.
- [25] S. Li, J. Wu, R. H. Petrov, Z. Li, R. Dollevoet, and J. Sietsma, “‘Brown etching layer’: A possible new insight into the crack initiation of rolling contact fatigue in rail steels?,” *Engineering Failure Analysis*, vol. 66, pp. 8–18, 2016, doi: 10.1016/j.engfailanal.2016.03.019.
- [26] A. Kumar, G. Agarwal, R. Petrov, S. Goto, J. Sietsma, and M. Herbig, “Microstructural evolution of white and brown etching layers in pearlitic rail steels,” *Acta Materialia*, vol. 171, pp. 48–64, 2019, doi: 10.1016/j.actamat.2019.04.012.
- [27] P.-Y. Tung, X. Zhou, L. Morsdorf, and M. Herbig, “Formation mechanism of brown etching layers in pearlitic rail steel,” *Materialia*, vol. 26, p. 101625, 2022, doi: 10.1016/j.mtla.2022.101625.
- [28] G. Gao *et al.*, “Heterogenous structure and formation mechanism of white and brown etching layers in bainitic rail steel,” *Acta Materialia*, vol. 250, p. 118887, 2023, doi: 10.1016/j.actamat.2023.118887.
- [29] M. Messaadi and M. Steenbergen, “Stratified surface layers on rails,” *Wear*, vol. 414–415, pp. 151–162, 2018, doi: 10.1016/j.wear.2018.07.019.
- [30] Q. Lian, G. Deng, H. Zhu, H. Li, X. Wang, and Z. Liu, “Influence of white etching layer on rolling contact behavior at wheel-rail interface,” *Friction*, vol. 8, no. 6, pp. 1178–1196, 2020, doi: 10.1007/s40544-020-0388-x.
- [31] S. Pal, W. J. T. Daniel, and M. Farjoo, “Early stages of rail squat formation and the role of a white etching layer,” *International Journal of Fatigue*, vol. 52, pp. 144–156, 2013, doi: 10.1016/j.ijfatigue.2013.02.016.
- [32] A. Al-Juboori *et al.*, “Squat formation and the occurrence of two distinct classes of white etching layer on the surface of rail steel,” *International Journal of Fatigue*, vol. 104, pp. 52–60, 2017, doi: 10.1016/j.ijfatigue.2017.07.005.
- [33] N. Chandak, “Analysis of railway wheel to study crack initiation due to thermal loading and calculating life cycle,” *Materials Today y: Proceedings*, vol. 4, 2017.

- [34] A. Ekberg and E. Kabo, “Fatigue of railway wheels and rails under rolling contact and thermal loading—an overview,” *Wear*, vol. 258, no. 7–8, pp. 1288–1300, 2005, doi: 10.1016/j.wear.2004.03.039.
- [35] S. L. Grassie, “Studs and squats: The evolving story,” *Wear*, vol. 366–367, pp. 194–199, 2016, doi: 10.1016/j.wear.2016.03.021.
- [36] M. Steenbergen and R. Dollevoet, “On the mechanism of squat formation on train rails – Part I: Origination,” *International Journal of Fatigue*, vol. 47, pp. 361–372, 2013, doi: 10.1016/j.ijfatigue.2012.04.023.
- [37] E. Magel, M. Roney, J. Kalousek, and P. Sroba, “The blending of theory and practice in modern rail grinding,” *Fatigue & Fracture of Engineering Materials & Structures*, vol. 26, no. 10, pp. 921–929, 2003, doi: 10.1046/j.1460-2695.2003.00669.x.
- [38] B. Lin, K. Zhou, J. Guo, Q. Y. Liu, and W. J. Wang, “Influence of grinding parameters on surface temperature and burn behaviors of grinding rail,” *Tribology International*, vol. 122, pp. 151–162, 2018, doi: 10.1016/j.triboint.2018.02.017.
- [39] K. Zhou *et al.*, “Experimental investigation on material removal mechanism during rail grinding at different forward speeds,” *Tribology International*, vol. 143, p. 106040, 2020, doi: 10.1016/j.triboint.2019.106040.
- [40] E. Uhlmann, P. Lypovka, L. Hochschild, and N. Schröer, “Influence of rail grinding process parameters on rail surface roughness and surface layer hardness,” *Wear*, vol. 366–367, pp. 287–293, 2016, doi: 10.1016/j.wear.2016.03.023.
- [41] M. Mesaritis *et al.*, “A laboratory demonstration of rail grinding and analysis of running roughness and wear,” *Wear*, vol. 456–457, p. 203379, 2020, doi: 10.1016/j.wear.2020.203379.
- [42] K. Zhou, H. Ding, M. Steenbergen, W. Wang, J. Guo, and Q. Liu, “Temperature field and material response as a function of rail grinding parameters,” *International Journal of Heat and Mass Transfer*, vol. 175, p. 121366, 2021, doi: 10.1016/j.ijheatmasstransfer.2021.121366.
- [43] A. R. Andrade and J. Stow, “Assessing the potential cost savings of introducing the maintenance option of ‘Economic Tyre Turning’ in Great Britain railway wheelsets,” *Reliability Engineering & System Safety*, vol. 168, pp. 317–325, 2017, doi: 10.1016/j.ress.2017.05.033.
- [44] Y. Muhamedsalih, J. Stow, and A. Bevan, “Use of railway wheel wear and damage prediction tools to improve maintenance efficiency through the use of economic tyre turning,” *Proceedings of the Institution of Mechanical Engineers, Part F: Journal of Rail and Rapid Transit*, vol. 233, no. 1, pp. 103–117, 2019, doi: 10.1177/0954409718781127.
- [45] G. Tao, Z. Wen, X. Jin, and X. Yang, “Polygonisation of railway wheels: a critical review,” *Rail. Eng. Science*, vol. 28, no. 4, pp. 317–345, 2020, doi: 10.1007/s40534-020-00222-x.
- [46] M. Faccoli, C. Petrogalli, and A. Ghidini, “On Mechanical Properties of New Railway Wheel Steels for Desert Environments and Sand Caused Wheel Damage Mechanisms,” *J. of Materi Eng and Perform*, vol. 28, no. 5, pp. 2946–2953, 2019, doi: 10.1007/s11665-019-04049-4.
- [47] A. Kapito, R. J. Mostert, W. E. Stumpf, and C. W. Siyasiya, “Carbide-free bainitic steels for rail wheel applications,” *IOP Conf. Ser.: Mater. Sci. Eng.*, vol. 655, p. 012012, 2019, doi: 10.1088/1757-899X/655/1/012012.
- [48] A. B. Rezende *et al.*, “Wear behavior of bainitic and pearlitic microstructures from microalloyed railway wheel steel,” *Wear*, vol. 456–457, p. 203377, 2020, doi: 10.1016/j.wear.2020.203377.

- [49] S. Ya. Shipitsyn, Yu. Z. Babaskin, I. F. Kirchu, L. G. Smolyakova, and N. Ya. Zolotar, “Microalloyed steel for railroad wheels,” *Steel Transl.*, vol. 38, no. 9, pp. 782–785, 2008, doi: 10.3103/S0967091208090222.
- [50] Si Wu, Xiu-Cheng Li, Juan Zhang, Cheng-jia Shang, and Raja Devesh Kumar Misra, “Microstructural Refinement and Mechanical Properties of High-Speed,” *Steel Research International*, vol. 86, no. 7, 2015, doi: 10.1002/srin.201400236.
- [51] U. P. Singh, A. M. Popli, D. K. Jain, B. Roy, and S. Jha, “Influence of Microalloying on Mechanical and Metallurgical Properties of Wear Resistant Coach and Wagon Wheel Steel,” *Journal of Materials Engineering and Performance*, vol. 12, no. 5, pp. 573–580, 2003, doi: 10.1361/105994903100277085.
- [52] D. Zeng, L. Lu, Y. Gong, N. Zhang, and Y. Gong, “Optimization of strength and toughness of railway wheel steel by alloy design,” *Materials & Design*, vol. 92, pp. 998–1006, 2016, doi: 10.1016/j.matdes.2015.12.096.
- [53] R. Pippan, S. Wurster, and D. Kiener, “Fracture mechanics of micro samples: Fundamental considerations,” *Materials & Design*, vol. 159, pp. 252–267, 2018, doi: 10.1016/j.matdes.2018.09.004.
- [54] A. K. Saxena, A. Kumar, M. Herbig, S. Brinckmann, G. Dehm, and C. Kirchlechner, “Micro fracture investigations of white etching layers,” *Materials & Design*, vol. 180, p. 107892, 2019, doi: 10.1016/j.matdes.2019.107892.
- [55] A. Kumar *et al.*, “In situ study on fracture behaviour of white etching layers formed on rails,” *Acta Materialia*, vol. 180, pp. 60–72, 2019, doi: 10.1016/j.actamat.2019.08.060.
- [56] M. Alfreider, S. Kolitsch, S. Wurster, and D. Kiener, “An analytical solution for the correct determination of crack lengths via cantilever stiffness - SUPP,” *Materials & Design*, vol. 194, p. 108914, 2020, doi: 10.1016/j.matdes.2020.108914.
- [57] M. Alfreider, D. Kozic, O. Kolednik, and D. Kiener, “In-situ elastic-plastic fracture mechanics on the microscale by means of continuous dynamical testing,” *Materials & Design*, vol. 148, pp. 177–187, 2018, doi: 10.1016/j.matdes.2018.03.051.
- [58] “https://de.m.wikipedia.org/wiki/Datei:C3%96BB_Railjet_1116-236_on_Krauselklause-Viaduct.jpg,” Jul. 21, 2023.
- [59] “<https://9gag.com/gag/aWZqjzA>,” Jul. 21, 2023.
- [60] S. Iwnicki, *Handbook of Railway Vehicle Dynamics*. CRC Press, 2006.
- [61] H. Soleimani and M. Moavenian, “Tribological Aspects of Wheel–Rail Contact: A Review of Wear Mechanisms and Effective Factors on Rolling Contact Fatigue,” *Urban Rail Transit*, vol. 3, no. 4, pp. 227–237, 2017, doi: 10.1007/s40864-017-0072-2.
- [62] S. Z. Meymand, A. Keylin, and M. Ahmadian, “A survey of wheel–rail contact models for rail vehicles,” *Vehicle System Dynamics*, vol. 54, no. 3, pp. 386–428, 2016, doi: 10.1080/00423114.2015.1137956.
- [63] H. Hertz, “Über die Berührung fester elastischer Körper,” *J Reine Angewandte Mathematik*, vol. 92, pp. 156–171, 1881.
- [64] K. Knothe, “History of wheel/rail contact mechanics: from Redtenbacher to Kalker,” *Vehicle System Dynamics*, vol. 46, no. 1–2, pp. 9–26, 2008, doi: 10.1080/00423110701586469.
- [65] M. Ertz and K. Knothe, “Thermal stresses and shakedown in wheel/rail contact,” *Archive of Applied Mechanics (Ingenieur Archiv)*, vol. 72, no. 10, pp. 715–729, 2003, doi: 10.1007/s00419-002-0255-4.
- [67] T. Vernesson and R. Lundén, “Temperatures at railway tread braking. Part 3: wheel and block temperatures and the influence of rail chill,” *Proceedings of the Institution of Mechanical Engineers, Part F: Journal of Rail and Rapid Transit*, vol. 221, no. 4, 2007, doi: 10.1243/09544097JRRT91.

- [68] J. P. Srivastava, P. K. Sarkar, and V. Ranjan, “Effects of thermal load on wheel–rail contacts: A review,” *Journal of Thermal Stresses*, vol. 39, no. 11, pp. 1389–1418, 2016, doi: 10.1080/01495739.2016.1216060.
- [69] A. Esmaili, J. Ahlström, B. Andersson, and M. Ekh, “Modelling of cyclic plasticity and phase transformations during repeated local heating events in rail and wheel steels,” *International Journal of Fatigue*, vol. 151, p. 106361, 2021, doi: 10.1016/j.ijfatigue.2021.106361.
- [70] J. Ahlström, E. Kabo, and A. Ekberg, “Temperature-dependent evolution of the cyclic yield stress of railway wheel steels,” *Wear*, vol. 366–367, pp. 378–382, 2016, doi: 10.1016/j.wear.2016.04.002.
- [71] J. Ahlström and B. Karlsson, “Modelling of heat conduction and phase transformations during sliding of railway wheels,” *Wear*, vol. 253, no. 1–2, pp. 291–300, 2002, doi: 10.1016/S0043-1648(02)00119-9.
- [72] M. Naeimi *et al.*, “Thermomechanical analysis of the wheel-rail contact using a coupled modelling procedure,” *Tribology International*, vol. 117, pp. 250–260, 2018, doi: 10.1016/j.triboint.2017.09.010.
- [73] K. J. Sawley, “Calculation of temperatures in a sliding wheel/rail system and implications for wheel steel development,” *Proceedings of the Institution of Mechanical Engineers, Part F: Journal of Rail and Rapid Transit*, vol. 221, no. 4, pp. 455–464, 2007, doi: 10.1243/09544097JRRT120.
- [74] “EN 13674-1:2011+A1:2017; Railway applications. Track. Rail Vignole railway rails 46 kg/m and above.” 2017.
- [75] “EN 13262:2020; Railway application. Wheelsets and bogies. Wheels. Product requirements.” 2020.
- [76] M. Linz, U. Cihak-Bayr, A. Trausmuth, S. Scheriau, D. Künstner, and E. Badisch, “EBSD study of early-damaging phenomena in wheel–rail model test,” *Wear*, vol. 342–343, pp. 13–21, 2015, doi: 10.1016/j.wear.2015.08.004.
- [77] Z. Lawrynowicz, “Plastic Deformation and Softening of the Surface Layer of Railway Wheel,” *Advances in Materials Science*, vol. 15, no. 4, pp. 5–13, 2015, doi: 10.1515/adms-2015-0018.
- [78] J. E. Garnham and C. L. Davis, “The role of deformed rail microstructure on rolling contact fatigue initiation,” *Wear*, vol. 265, no. 9–10, pp. 1363–1372, 2008, doi: 10.1016/j.wear.2008.02.042.
- [79] L. Ma *et al.*, “Study on wear and rolling contact fatigue behaviors of wheel/rail materials under different slip ratio conditions,” *Wear*, vol. 366–367, pp. 13–26, 2016, doi: 10.1016/j.wear.2016.04.028.
- [80] C. G. He *et al.*, “On the microstructure evolution and nanocrystalline formation of pearlitic wheel material in a rolling-sliding contact,” *Materials Characterization*, vol. 164, p. 110333, 2020, doi: 10.1016/j.matchar.2020.110333.
- [81] B. Dylewski, M. Risbet, and S. Bouvier, “The tridimensional gradient of microstructure in worn rails – Experimental characterization of plastic deformation accumulated by RCF,” *Wear*, vol. 392–393, pp. 50–59, 2017, doi: 10.1016/j.wear.2017.09.001.
- [82] T. Sakai, A. Belyakov, R. Kaibyshev, H. Miura, and J. J. Jonas, “Dynamic and post-dynamic recrystallization under hot, cold and severe plastic deformation conditions,” *Progress in Materials Science*, vol. 60, pp. 130–207, 2014, doi: 10.1016/j.pmatsci.2013.09.002.
- [83] Y. Cao, S. Ni, X. Liao, M. Song, and Y. Zhu, “Structural evolutions of metallic materials processed by severe plastic deformation,” *Materials Science and Engineering: R: Reports*, vol. 133, pp. 1–59, 2018, doi: 10.1016/j.mser.2018.06.001.

- [84] X. Sauvage, A. Chbihi, and X. Queleuennec, “Severe plastic deformation and phase transformations,” *J. Phys.: Conf. Ser.*, vol. 240, p. 012003, 2010, doi: 10.1088/1742-6596/240/1/012003.
- [85] F. Wetscher, R. Stock, and R. Pippan, “Changes in the mechanical properties of a pearlitic steel due to large shear deformation,” *Materials Science and Engineering: A*, vol. 445–446, pp. 237–243, 2007, doi: 10.1016/j.msea.2006.09.026.
- [86] J. W. Stead, “Micro-Metallography & its Practical Application,” *West. Scot. Iron & Steel Inst.*, vol. 19, pp. 169–204, 1912.
- [87] R. G. Bhatwadekar and S. Ramanujam, “Service Failures of Railway Materials,” 1953.
- [88] R. N. Datta, “The Defects in Rail and In Rail Steel,” *Colorado School of Mines*, 1948.
- [89] J. Dearden, “The wear of steel rails and tyres in railway service,” *Wear*, vol. 3, no. 1, pp. 43–59, 1960, doi: 10.1016/0043-1648(60)90174-5.
- [90] J. Dearden, “The wear of steel rails: A review of the factors involved,” *Proceedings of the Institution of Civil Engineers*, vol. 3, no. 5, pp. 456–481, 1954.
- [91] U. Olofsson and Y. Lyu, “Open System Tribology in the Wheel–Rail Contact—A Literature Review,” *Applied Mechanics Reviews*, vol. 69, no. 6, p. 060803, 2017, doi: 10.1115/1.4038229.
- [92] B. Hieu Nguyen, A. Al-Juboori, H. Zhu, A. A. Gazder, H. Li, and K. Tieu, “Fracture mechanisms in rails with mechanically and thermomechanically-induced white etching layers under three-point bending,” *Engineering Failure Analysis*, vol. 131, p. 105813, 2022, doi: 10.1016/j.engfailanal.2021.105813.
- [93] R. Pan, Y. Chen, H. Lan, S. E, and R. Ren, “Investigation into the microstructure evolution and damage on rail at curved tracks,” *Wear*, vol. 504–505, p. 204420, 2022, doi: 10.1016/j.wear.2022.204420.
- [94] Q. Lian *et al.*, “Evolution of thermally induced white etching layer at rail surface during multiple wheel/train passages,” *International Journal of Fatigue*, vol. 159, p. 106799, 2022, doi: 10.1016/j.ijfatigue.2022.106799.
- [95] Y. Chen, X. Zhao, P. Liu, R. Pan, and R. Ren, “Influences of local laser quenching on wear performance of D1 wheel steel,” *Wear*, vol. 414–415, pp. 243–250, 2018, doi: 10.1016/j.wear.2018.07.016.
- [96] S. B. Newcomb and W. M. Stobbs, “A transmission electron microscopy study of the white-etching layer on a rail head,” *Materials Science and Engineering*, vol. 66, no. 2, pp. 195–204, 1984, doi: 10.1016/0025-5416(84)90180-0.
- [98] C. Liu *et al.*, “Formation mechanism for the white etching microstructure in the subsurface of the failure pearlite wheel steel,” *Wear*, vol. 494–495, p. 204243, 2022, doi: 10.1016/j.wear.2022.204243.
- [99] L. Wang, A. Pyzalla, W. Stadlbauer, and E. A. Werner, “Microstructure features on rolling surfaces of railway rails subjected to heavy loading,” *Materials Science and Engineering: A*, vol. 359, no. 1–2, pp. 31–43, 2003, doi: 10.1016/S0921-5093(03)00327-7.
- [101] A. Al-Juboori *et al.*, “Microstructural changes on railway track surfaces caused by electrical leakage between wheel and rail,” *Tribology International*, vol. 140, p. 105875, 2019, doi: 10.1016/j.triboint.2019.105875.
- [102] A. D. Bedoya-Zapata *et al.*, “White Etching Layer (WEL) formation in different rail grades after grinding operations in the field,” *Wear*, vol. 502–503, p. 204371, 2022, doi: 10.1016/j.wear.2022.204371.
- [103] C. J. Rasmussen, S. Fæster, S. Dhar, J. V. Quaade, M. Bini, and H. K. Danielsen, “Surface crack formation on rails at grinding induced martensite white etching layers,” *Wear*, vol. 384–385, pp. 8–14, 2017, doi: 10.1016/j.wear.2017.04.014.

- [104] J. Ahlström and B. Karlsson, “Microstructural evaluation and interpretation of the mechanically and thermally affected zone under railway wheel flats,” *Wear*, vol. 232, no. 1, pp. 1–14, 1999, doi: 10.1016/S0043-1648(99)00166-0.
- [105] Y. Z. Chen, C. G. He, X. J. Zhao, L. B. Shi, Q. Y. Liu, and W. J. Wang, “The influence of wheel flats formed from different braking conditions on rolling contact fatigue of railway wheel,” *Engineering Failure Analysis*, vol. 93, pp. 183–199, 2018, doi: 10.1016/j.engfailanal.2018.07.006.
- [106] D. I. Fletcher and S. H. Sanusi, “The potential for suppressing rail defect growth through tailoring rail thermo-mechanical properties,” *Wear*, vol. 366–367, pp. 401–406, 2016, doi: 10.1016/j.wear.2016.06.022.
- [107] “<https://mechanicalcheat.wordpress.com/metallurgy/iron-and-carbon/>,” Jul. 21, 2023.
- [108] A. Al-Juboori *et al.*, “Evolution of rail surface degradation in the tunnel: The role of water on squat growth under service conditions,” *Engineering Fracture Mechanics*, vol. 209, pp. 32–47, 2019, doi: 10.1016/j.engfracmech.2019.01.018.
- [109] “Rolling Contact Fatigue - tribonet.org,” [https://www.tribonet.org/wiki/rolling-contact-fatigue/#:~:text=Rolling%2Dcontact%20fatigue%20\(RCF\),due%20to%20RCF%20%5B1%5D.](https://www.tribonet.org/wiki/rolling-contact-fatigue/#:~:text=Rolling%2Dcontact%20fatigue%20(RCF),due%20to%20RCF%20%5B1%5D.), Jul. 21, 2023.
- [119] M. Kerr, A. Wilson, and S. Marich, “The epidemiology of squats and related rail defects,” *Conference On Railway Engineering*, 2008.
- [120] K. Lyu *et al.*, “Analysis on the features and potential causes of wheel surface damage for heavy-haul locomotives,” *Engineering Failure Analysis*, vol. 109, p. 104292, 2020, doi: 10.1016/j.engfailanal.2019.104292.
- [121] R. C. Rocha, H. Ewald, A. B. Rezende, S. T. Fonseca, and P. R. Mei, “Using twin disc for applications in the railway: a systematic review,” *J Braz. Soc. Mech. Sci. Eng.*, vol. 45, no. 4, p. 191, 2023, doi: 10.1007/s40430-023-04104-1.
- [122] Y. Zhou, J. F. Peng, W. J. Wang, X. S. Jin, and M. H. Zhu, “Slippage effect on rolling contact wear and damage behavior of pearlitic steels,” *Wear*, vol. 362–363, pp. 78–86, 2016, doi: 10.1016/j.wear.2016.05.001.
- [123] H. Chen, A. Namura, M. Ishida, and T. Nakahara, “Influence of axle load on wheel/rail adhesion under wet conditions in consideration of running speed and surface roughness,” *Wear*, vol. 366–367, pp. 303–309, 2016, doi: 10.1016/j.wear.2016.05.012.
- [124] W. J. Wang, S. R. Lewis, R. Lewis, A. Beagles, C. G. He, and Q. Y. Liu, “The role of slip ratio in rolling contact fatigue of rail materials under wet conditions,” *Wear*, vol. 376–377, pp. 1892–1900, 2017, doi: 10.1016/j.wear.2016.12.049.
- [125] C. G. He, J. Guo, Q. Y. Liu, and W. J. Wang, “Experimental investigation on the effect of operating speeds on wear and rolling contact fatigue damage of wheel materials,” *Wear*, vol. 364–365, pp. 257–269, 2016, doi: 10.1016/j.wear.2016.08.006.
- [126] H. Lee, H.-G. Namgung, and S.-B. Kwon, “Effect of train velocity on the amount of airborne wear particles generated from wheel–rail contacts,” *Wear*, vol. 414–415, pp. 296–302, 2018, doi: 10.1016/j.wear.2018.08.023.
- [127] M. Faccoli, C. Petrogalli, M. Lancini, A. Ghidini, and A. Mazzù, “Effect of desert sand on wear and rolling contact fatigue behaviour of various railway wheel steels,” *Wear*, vol. 396–397, pp. 146–161, 2018, doi: 10.1016/j.wear.2017.05.012.
- [128] W. J. Wang *et al.*, “Sub-scale simulation and measurement of railroad wheel/rail adhesion under dry and wet conditions,” *Wear*, vol. 302, no. 1–2, pp. 1461–1467, 2013, doi: 10.1016/j.wear.2012.12.014.
- [129] O. Arias-Cuevas, Z. Li, and R. Lewis, “A laboratory investigation on the influence of the particle size and slip during sanding on the adhesion and wear in the wheel–rail contact,” *Wear*, vol. 271, no. 1–2, pp. 14–24, 2011, doi: 10.1016/j.wear.2010.10.050.

- [130] W. J. Wang, T. F. Liu, H. Y. Wang, Q. Y. Liu, M. H. Zhu, and X. S. Jin, "Influence of friction modifiers on improving adhesion and surface damage of wheel/rail under low adhesion conditions," *Tribology International*, vol. 75, pp. 16–23, 2014, doi: 10.1016/j.triboint.2014.03.008.
- [131] W. J. Wang, P. Shen, J. H. Song, J. Guo, Q. Y. Liu, and X. S. Jin, "Experimental study on adhesion behavior of wheel/rail under dry and water conditions," *Wear*, vol. 271, no. 9–10, pp. 2699–2705, 2011, doi: 10.1016/j.wear.2011.01.070.
- [132] W. J. Wang, H. F. Zhang, H. Y. Wang, Q. Y. Liu, and M. H. Zhu, "Study on the adhesion behavior of wheel/rail under oil, water and sanding conditions," *Wear*, vol. 271, no. 9–10, pp. 2693–2698, 2011, doi: 10.1016/j.wear.2010.12.019.
- [133] J. W. Ringsberg, A. Skyttebol, and B. L. Josefson, "Investigation of the rolling contact fatigue resistance of laser clad twin-disc specimens: FE simulation of laser cladding, grinding and a twin-disc test," *International Journal of Fatigue*, vol. 27, no. 6, pp. 702–714, 2005, doi: 10.1016/j.ijfatigue.2004.10.006.
- [134] L. Zhou, Y. Hu, H. H. Ding, Q. Y. Liu, J. Guo, and W. J. Wang, "Experimental study on the wear and damage of wheel-rail steels under alternating temperature conditions," *Wear*, vol. 477, p. 203829, 2021, doi: 10.1016/j.wear.2021.203829.
- [135] G. Vasić, F. J. Franklin, and D. I. Fletcher, "Influence of partial slip and direction of traction on wear rate in wheel-rail contact," *Wear*, vol. 270, no. 3–4, pp. 163–171, 2011, doi: 10.1016/j.wear.2010.10.012.
- [136] R. Pan, Y. Chen, H. Lan, S. E. and R. Ren, "Investigation into the evolution of the microcosmic surface of bainitic wheel steel material suffering polygonal wear," *Wear*, vol. 504–505, p. 204430, 2022, doi: 10.1016/j.wear.2022.204430.
- [137] B. Rodríguez-Arana, A. San Emeterio, M. Panera, A. Montes, and D. Álvarez, "Investigation of a relationship between twin-disc wear rates and the slipping contact area on R260 grade rail," *Tribology International*, vol. 168, p. 107456, 2022, doi: 10.1016/j.triboint.2022.107456.
- [138] H. H. Ding *et al.*, "Investigation on the rolling wear and damage properties of laser discrete quenched rail material with different quenching shapes and patterns," *Surface and Coatings Technology*, vol. 378, p. 124991, 2019, doi: 10.1016/j.surfcoat.2019.124991.
- [139] D. Zeng, L. Lu, Z. Li, J. Zhang, X. Jin, and M. Zhu, "Influence of laser dispersed treatment on rolling contact wear and fatigue behavior of railway wheel steel," *Materials & Design (1980-2015)*, vol. 54, pp. 137–143, 2014, doi: 10.1016/j.matdes.2013.08.041.
- [140] S. R. Lewis *et al.*, "Improving rail wear and RCF performance using laser cladding," *Wear*, vol. 366–367, pp. 268–278, 2016, doi: 10.1016/j.wear.2016.05.011.
- [141] S. R. Lewis, R. Lewis, and D. I. Fletcher, "Assessment of laser cladding as an option for repairing/enhancing rails," *Wear*, vol. 330–331, pp. 581–591, 2015, doi: 10.1016/j.wear.2015.02.027.
- [142] J.-W. Seo, H.-K. Jun, S.-J. Kwon, and D.-H. Lee, "Rolling contact fatigue and wear of two different rail steels under rolling–sliding contact," *International Journal of Fatigue*, vol. 83, pp. 184–194, 2016, doi: 10.1016/j.ijfatigue.2015.10.012.
- [143] J.-W. Seo, S.-J. Kwon, D.-H. Lee, and H.-Y. Choi, "Analysis of contact fatigue crack growth using twin-disc tests and numerical evaluations," *International Journal of Fatigue*, vol. 55, pp. 54–63, 2013, doi: 10.1016/j.ijfatigue.2013.05.005.
- [144] M. Kráčalík, G. Trummer, and W. Daves, "Application of 2D finite element analysis to compare cracking behaviour in twin-disc tests and full scale wheel/rail experiments," *Wear*, vol. 346–347, pp. 140–147, 2016, doi: 10.1016/j.wear.2015.11.013.
- [146] R. S. Miranda, A. B. Rezende, S. T. Fonseca, F. M. Fernandes, A. Sinatora, and P. R. Mei, "Fatigue and wear behavior of pearlitic and bainitic microstructures with the same

chemical composition and hardness using twin-disc tests,” *Wear*, vol. 494–495, p. 204253, 2022, doi: 10.1016/j.wear.2022.204253.

- [147] E. Kabo, A. Ekberg, P. T. Torstensson, and T. Vernersson, “Rolling contact fatigue prediction for rails and comparisons with test rig results,” *Proceedings of the Institution of Mechanical Engineers, Part F: Journal of Rail and Rapid Transit*, vol. 224, no. 4, pp. 303–317, 2010, doi: 10.1243/09544097JRRT343.
- [148] G. Y. Zhou, J. H. Liu, W. J. Wang, G. Wen, and Q. Y. Liu, “Study on the fatigue and wear characteristics of four wheel materials,” *J. Mod. Transport.*, vol. 21, no. 3, pp. 182–193, 2013, doi: 10.1007/s40534-013-0021-z.
- [149] M. Vandenbussche, J. Sukumaran, W. Ost, and Á. Horváth, “Conceptualization of Test Configuration for Tribological Characterization of the Rail-wheel Contact,” 2016.
- [150] R. Lewis *et al.*, “Towards a standard approach for the wear testing of wheel and rail materials,” *Proceedings of the Institution of Mechanical Engineers, Part F: Journal of Rail and Rapid Transit*, vol. 231, no. 7, pp. 760–774, 2017, doi: 10.1177/0954409717700531.
- [151] E. A. Gallardo-Hernandez, R. Lewis, and R. S. Dwyer-Joyce, “Temperature in a twin-disc wheel/rail contact simulation,” *Tribology International*, vol. 39, no. 12, pp. 1653–1663, 2006, doi: 10.1016/j.triboint.2006.01.028.
- [152] Y. Hu *et al.*, “Wear of driving versus driven discs in a twin disc rolling-sliding test,” *Wear*, vol. 512–513, p. 204528, 2023, doi: 10.1016/j.wear.2022.204528.
- [153] J.-H. Lee, J.-H. Jang, B.-D. Joo, Y.-M. Son, and Y.-H. Moon, “Laser surface hardening of AISI H13 tool steel,” *Transactions of Nonferrous Metals Society of China*, vol. 19, no. 4, pp. 917–920, 2009, doi: 10.1016/S1003-6326(08)60377-5.
- [154] D. I. Pantelis, E. Bouyiouri, N. Kouloumbi, P. Vassiliou, and A. Koutsomichalis, “Wear and corrosion resistance of laser surface hardened structural steel,” *Surface and Coatings Technology*, vol. 161, no. 2–3, pp. 125–134, 2002, doi: 10.1016/S0257-8972(02)00495-4.
- [155] J. S. Selvan, K. Subramanian, and A. K. Nath, “Effect of laser surface hardening on En18 (AISI 5135) steel,” *Journal of Materials Processing Technology*, vol. 91, no. 1–3, pp. 29–36, 1999, doi: 10.1016/S0924-0136(98)00430-0.
- [156] Y. Xiong *et al.*, “Microstructure and microhardness of pearlitic steel after laser shock processing and annealing,” *Materials Science and Technology*, vol. 31, no. 15, pp. 1825–1831, 2015, doi: 10.1179/1743284715Y.0000000020.
- [157] A. Buling, H. Sändker, J. Stollenwerk, U. Krupp, and A. Hamann-Steinmeier, “Laser surface pretreatment of 100Cr6 bearing steel – Hardening effects and white etching zones,” *Applied Surface Science*, vol. 378, pp. 564–571, 2016, doi: 10.1016/j.apsusc.2016.03.088.
- [158] I. Jordanova and V. Antonov, “Surface oxidation of low carbon steel during laser treatment, its dependence on the initial microstructure and influence on the laser energy absorption,” *Thin Solid Films*, vol. 516, no. 21, pp. 7475–7481, 2008, doi: 10.1016/j.tsf.2008.03.031.
- [159] “<https://www.ac2t.at/services/laserauftrag/>,” Jul. 26, 2023.

5 Scientific Contribution

Within this chapter, an overview of all publications that originated in the framework of this thesis is presented, summarized into two parts: *Publications I to IV* contribute to the knowledge of microstructural changes in the near-surface region of rail wheels during service and the related micro-mechanical properties. *Publications V to VIII* subsequently deal with a systematic laboratory approach to imitate thermally induced stratified surface layers formed on rail wheels, their micro-mechanical properties, and their relation to fatigue crack initiation. The chapter concludes with an overview of contributions to national and international conferences.

5.1 Microstructural and micro-mechanical properties of evolved near-surface microstructures of rail wheels

Publication I

Severe plastic deformed zones and white etching layers formed during service of railway wheels

M. Freisinger, H. Rojacz, A. Trausmuth, P.H. Mayrhofer
Metallography, Microstructure, and Analysis, vol. 12, no. 3 (2023)
DOI: 10.1007/s13632-023-00967-x

The complex loading situation in wheel-rail contacts and its environmental influences lead to a significant change in the near-surface microstructure during service. Although the material properties of the wheels and rails are well known before service, the evolving microstructure and its mechanical properties determine the wear, surface crack initiation, and potential subsequent RCF failure during service. Therefore, an understanding of the microstructural evolution is vital. However, in literature the overwhelming majority of studies are conducted on rails. Significantly less attention is paid to wheels, even though their microstructural changes are as important as on the rails since surface crack initiation and RCF damage highly affect the maintenance strategy and the component lifetime.

Addressing this issue, the work presented in *Publication I* shows extensive studies on the near-surface microstructure evolved for a wheel in service for ~200,000 km provided by the Austrian Federal Railways (OEBB). Different zones along the wheel tread are investigated by LOM, SEM, as well as Vickers hardness measurements, and NI. Further, detailed analyses of microstructural characteristics in various depths from the surface are conducted by high-magnification SEM imaging and EBSD analysis in the different zones. Results show a broad variation of microstructures along the wheel tread and give hints

about the mechanical and thermal loads experienced during service. The zone at the field side exhibits an SPD microstructure down to $\sim 300 \mu\text{m}$ and numerous RCF cracks at the surface. The deformed microstructure is evident upon $600 \mu\text{m}$ from the surface, with a gradual hardness increase starting from $\sim 350 \text{HV}0.05$ in the bulk to $\sim 450 \text{HV}0.05$ in a depth of $50 \mu\text{m}$. The results of the region at the wheel flange indicate higher mechanical loads since deformation in increased depths ($1,500 \mu\text{m}$ from the surface) and pronounced grain elongation and alignment in $\sim 45^\circ$ to the tread surface plane are observed. Further, high hardness ($\sim 550 \text{HV}0.05$) is measured next to the tread surface. The zone in the middle of the wheel tread shows significant spheroidized cementite which indicates more severe thermal loads. Moreover, a fine-grained microstructure with a low degree of misorientation and a high fraction of HAGBs can be identified, underlining the major thermo-mechanical loading situation in the middle of the wheel tread. In addition to the deformed near-surface microstructure, variations of phase-transformed surface layers are observed. More precisely, a thin WEL with mesh-like martensitic microstructure and high hardness ($\sim 6 \text{GPa}$) and an SSL combining a WEL with a more flawed microstructure ($\sim 4.6 \text{GPa}$) with an underlying BEL ($\sim 3.6 \text{GPa}$). The microstructural analysis of the BEL indicates high thermal loads presumably generated due to massive slippage events. The study contributes to the fundamental knowledge of evolving microstructures and the mechanical properties of wheels. The importance of changes in the near-surface microstructures on crack initiation and RCF failures is pointed out, especially when it comes to the formation of WELs and/or SSLs.

Publication II

Influence of the evolution of near-surface rail wheel microstructure on crack initiation by micro-bending investigations

M. Freisinger, A. Trausmuth, R. Hahn, E. Badisch
Journal of Rail and Rapid Transit, published online (2023)
DOI: 10.1177/09544097231191550

To further study evolved near-surface wheel microstructures discussed in *Publication I*, this work introduces the *in situ* micro-bending method to evaluate its micro-mechanical properties. In current literature, low-load hardness measurement techniques (including NI) are the common tools to evaluate mechanical properties in small-scale regions of wheels and rails. In addition, the determination of fracture toughness seems to be crucial in terms of RCF crack initiation during service. However, this is unfortunately not possible with

established testing methods due to the size limitations of the samples. Therefore, the micro-bending method – well established in the field of thin films – is recently applied on WELs of rails. This method can give valuable insights into crack initiation, deformation, and fracture behaviour with high spatial resolution. The work in *Publication II* presents the first *in situ* micro-bending experiments in near-surface regions of rail wheels from service.

Within the study, two distinctive regions in the near-surface microstructure of a wheel in service for ~200,000 km are investigated: (a) SPD region, and (b) corrosion-affected region. Results of the *in situ* micro-bending experiments in the SPD region demonstrate pronounced plastic behaviour without crack initiation at the notch. Cantilevers with notch direction in the rolling direction and perpendicular to the rolling direction show no differences in deformation behaviour. In contrast, cantilevers with notches situated in corroded zones show crack initiation and fracture, with maximum stress levels of 10–15 MPa (contra ~70 MPa for cantilevers in the SPD zone). Results indicate a minor crack initiation probability in evolved SPD microstructures of rail wheels and underline the relevance of brittle surface layers (WEL, BEL, SSL) to fatigue crack initiation. Additionally, corrosion-affected regions are proved to be prone to crack initiation as shown within the presented micro-bending studies.

The work within *Publication II* gives insights into the material behaviour of microstructures evolved in wheel-rail contacts with a novel micro-mechanical testing procedure for wheel and rail materials. Further, the applicability of *in situ* micro-bending experiments is demonstrated, showing a great potential to broaden the understanding of changed mechanical properties of near-surface wheel and rail microstructures during service.

Publication III

Microstructural characterization of near-surface microstructures on rail wheels in service – an insight into “stratified surface layers”

M. Freisinger, A. Trausmuth

Open Research Europe, vol. 3, no. 73 (2023)

DOI: 10.12688/openreseurope.15881.2

As indicated in *Publication I* and *II*, surface layers such as WELs and BELs are suggested to play a key role in fatigue crack initiation of rail wheels. Besides extensive studies on WELs in the last decades, the BEL – often observed underneath a WEL – is barely studied. This is particularly the case for wheels. On top of this, the broad variety of these layers demands further comprehensive studies. Hence, in the presented work of *Publication III*

variations of WELs, BELs, and SSLs formed on a wheel during service are investigated by LOM, SEM, and Vickers hardness measurements.

In ROI-1, a BEL is observed by LOM, further, higher magnification shows a thin WEL (~20 µm) on top – representing an SSL. The BEL reveals an aligned microstructure with globular cementite particles randomly distributed and a hardness of ~540 HV0.01. Within ROI-2, another SSL (~30 µm WEL and ~50 µm BEL) is identified in the presence of macroscopic RCF cracking. The WEL features a fine mesh-like microstructure with some nanometre-sized globular particles, moreover, a hardness of ~1180 HV0.01 is measured. In contrast, the BEL comes up with a coarser grain size and a fibrous microstructure aligned under an angle of ~30° to the surface. The measured hardness within the BEL is ~500 HV0.01. The observed BEL in ROI-3 represents once more an SSL detected by higher magnification, where a thin WEL is observed on top of the BEL. Crack propagation within the BEL is observed, and the microstructure shows a flawed mesh-like microstructure with spheroidized particles and a hardness of ~510 HV0.01. In ROI-4, a ~50 µm thick surface layer with several cracks is observed, but no stratification can be seen. Terminology is questionable since this layer reveals a fine-grained mesh-like microstructure and high hardness (~980 HV0.01), indicating a WEL, but a brownish appearance under LOM suggesting a BEL. However, it can be concluded that many variations are evident due to the indefinite loading history of the wheel during service. Moreover, even though it is not obvious by minor magnification, most layers show stratification with BEL underneath the WEL with a closer look. Small cracks seem to be common in WELs (resulting in micro-spalling), while pronounced cracks propagate into the material in the presence of BELs. The study points out the broad variety of surface layers evolving on wheels, and their relation to RCF crack initiation. Due to the missing knowledge of the loading history of wheel and rail samples from the field, more studies can pave the way toward a common classification and understanding of evolved near-surface microstructures. Besides ongoing research on this topic for several decades, this can further be promoted by advanced analysis techniques developed in recent times.

Publication IV

Microstructural characteristics of stratified surface layers affecting crack propagation in rail wheel near-surface regions

M. Freisinger, S. Fellner, C. Gammer, H. Riedl, R. Hahn
submitted to *Materials Characterization* (19.09.2023)

The relevance of SSLs – especially the microstructural characteristics in the BEL – to the RCF crack initiation and propagation on wheel treads is clearly apparent in *Publication III*. Hence, an in-depth analysis of microstructural and micro-mechanical characteristics in BEL regions within an SSL on a wheel from service is conducted and results are presented in *Publication IV*.

Within this work, LOM and SEM investigations are executed in different depths within the SSL. Microstructural features are identified by SE and BE imaging, EBSD analysis and TEM investigations. To obtain micro-mechanical properties low load Vickers hardness measurements and NI is performed, as well as *in situ* micro-bending underneath the WEL-BEL transition zone.

The results explicitly show an RCF crack initiating in the WEL and propagating – with changes in the crack growth angle – through the BEL down into the underlying deformed ferritic-pearlitic microstructure of the wheel. SEM analyses confirm a fine-grained martensitic microstructure with a mesh-like appearance in higher magnification for the WEL, while hardness measurements reveal ~830 HV0.05 and ~7.2 GPa. More interestingly, a certain microstructural gradient is observed within the BEL, and a relation to the changing crack growth direction is indicated. In the upper part, the grain size is coarser, large globular cementite particles are identified, and the hardness is in the order of 5 GPa. With increasing depth from the surface, the lower part of the BEL shows a decreasing grain size, mesh-like microstructure, and increasing hardness (~6.5 GPa). More detailed analyses (TEM and micro-bending investigations) are done with a focus on the BEL region just underneath the WEL-BEL transition zone, where the RCF crack propagates in the BEL and changes its direction. TEM analysis reveals a distorted *bcc* lattice and microstructural features such as high dislocation density and globular particles, proposing the presence of tempered martensite. *In situ* micro-bending experiments in this region show a predominant plastic material behaviour and maximum stresses of 60–90 MPa, however, the lack of crack initiation at the notch hinders a calculation of fracture toughness.

This work constitutes a further contribution to the understanding of evolved near-surface microstructures on wheels, notably in respect of SSLs. Based on advanced microstructural

and micro-mechanical analysis methods, a microstructural gradient within the BEL is discovered – not yet discussed in the literature. Its influence on RCF crack propagation appears obvious, however, a systematic study is hindered by the indefinite loading history of samples from the field. Thereof, the following publications attempt to develop a laboratory approach to create defined and reproducible samples for further systematic studies.

5.2 Thermally induced surface layers by laser surface treatments

Publication V

Comparative study on the influence of initial deformation and temperature of thermally induced white etching layers on rail wheels

M. Freisinger, H. Rojacz, K. Pichelbauer, A. Trausmuth, G. Trummer, K. Six, P.H. Mayrhofer
Tribology International, vol. 177 (2023)
DOI: 10.1016/j.triboint.2022.107990

Concluding *Publications I–IV*, it can be seen that phase-transformed regions such as WELs are prone to RCF crack initiation. Furthermore, extensive analyses demonstrate the limits of systematic studies on samples from the field due to their unknown mechanical and thermal loading history. This asks for laboratory approaches to imitate such layers under defined parameters, enabling in-depth systematic studies. Hence, *Publication V* represents an approach to reproducibly create thermally induced WELs by laser surface treatments, whereas influencing variables such as the initial deformation state of the microstructure and the induced temperature based on the laser power are studied.

To picture different initial deformation states, a tread surface of an ER7 wheel from service (deformed microstructure) and a sample extracted from the middle of the wheel (undeformed microstructure) is laser treated. Two different laser surface treatment modes are applied: *Feed-mode* (constant moving speed of the laser spot over the sample), and *pulse-mode* (fixed location of the laser spot, repetitive laser power inputs). Variations of laser energies and surface temperatures, respectively, are conducted. Induced surface temperatures are measured by a pyrometer and evaluated by finite element simulations. Laser-treated samples are analysed by LOM, SEM, and EBSD, as well as low-load Vickers hardness measurements. Further, results are compared to a WEL formed on a wheel during service to validate a realistic laboratory imitation.

The results show the formation of a WEL by laser treatment in *feed-mode* at laser powers of 2.1–2.3 kW with the first WEL formation at a surface temperature of ~640 °C (~ 25 μm).

Pulse-mode induced WELs at laser powers of 2.8–3.3 kW and higher surface temperatures (starting with a WEL of 80 μm at $\sim 740^\circ\text{C}$). The initial deformation state results in increased layer thicknesses at the same surface temperatures in the case of the deformed material. Further, differences in microstructural characteristics are evident besides comparable hardness (750–850 HV0.05): Pronounced proeutectoid ferrite is evident in the WEL formed on the initial undeformed material, hence, EBSD results show better comparability of the laser-induced WEL on the deformed microstructure to the field-WEL.

The work presented in *Publication V* shows the possibility to imitate realistic and reproducible WELs on wheel materials by defined thermal loadings and explains various influencing parameters. It points out, that the initial deformation state of the microstructure significantly affects the resulting WEL and must be considered in future studies. Moreover, the presented results of different laser surface treatment modes and the relation of laser power and induced surface temperature on the formation and thicknesses of the WELs contribute to advanced knowledge of the imitation of near-surface microstructures occurring in the wheel-rail contact by laboratory methods.

Publication VI

In-situ micro-cantilever bending studies of a white etching layer thermally induced on rail wheels

M. Freisinger, L. Zauner, R. Hahn, H. Riedl, P.H. Mayrhofer
Materials Science & Engineering A, 869 (2023)
DOI: 10.1016/j.msea.2023.144805

Introduced in *Publications II* and *IV*, the micro bending method extends the possibility of evaluating micro-mechanical properties beyond common hardness measurement techniques. These properties are crucially affecting crack initiation and subsequent RCF failure, therefore, should be known when imitating WELs by laboratory approaches to confirm reasonable comparability to the field. To address this, a thermally induced WEL by laser surface treatment (presented in *Publication V*) is studied by *in situ* micro bending studies – on top of LOM, SEM, EBSD, Vickers hardness, and NI investigations – to enable a broad insight into the microstructural and micro-mechanical properties.

Results show a fine-grained, randomly orientated acicular martensitic microstructure with an increasing fraction of ferrite into depth and a hardness of ~ 740 HV0.05 respectively ~ 7 GPa. Upon 30–40 μm from the surface, a transition layer is identified with decreased hardness (~ 520 HV0.05 / ~ 5 GPa). The *in situ* V-notched micro-cantilever experiments show elastic-plastic material behaviour under applied loading with crack initiation in the

notch area at 70–100 MPa. By continuous stiffness measurement and therefore continuous calculation of the crack extension, the J -integral for the calculation of the local fracture toughness through the elastic-plastic fracture mechanics can be determined. The calculated local fracture toughness K_{IQ} of the thermally induced WEL reveals $\sim 16 \text{ MPam}^{1/2}$. Post-testing SEM investigations of the cantilevers demonstrate the elastic-plastic material behaviour and give insights into the crack propagation in the presence of WEL microstructures.

It is concluded that micro bending experiments provide a valuable complementary testing method to understand the material behaviour in small scales, such as WELs on wheel treads. Obtained results are validated by comparing to studies from literature done on WELs on rails, hence, proving the comparability of WELs imitated by the presented laboratory approach to WELs from the field. Moreover, this work underlines the susceptibility of WELs to RCF crack initiation and propagation by a novel high spatial resolution testing method in this research field.

Publication VII

Influence of thermal loading parameters and microstructure on the formation of stratified surface layers on railway wheels

M. Freisinger, K. Pichelbauer, G. Trummer, K. Six
under review at *Journal of Rail and Rapid Transit* (17.07.2023)

In *Publications I, III, and IV* a layer underneath the WEL – the BEL – is discussed and its importance to RCF fatigue crack propagation is pointed out. Hence, based on the laboratory approach to imitate WELs presented in *Publication V*, a development is needed to address SSLs with BEL underneath the WEL. This will enable further systematic studies, however, influential parameters on the formation process must be understood as well. To address this, *Publication VII* presents a laboratory approach based on the findings from *Publication V* to imitate SSLs under defined thermal loading history and studies various influential parameters.

Different sequences of two consecutive thermal loads are applied by laser surface treatments in *feed-mode*, whereat results show the formation of an SSL in the case of a primary higher laser energy (forming a WEL) and a subsequent applied minor laser energy (forming the BEL). Further, changes in the thermal loading parameters influence the induced thicknesses of the layers: A higher laser power for the first treatment with the same difference to the second minor treatment results in an increased SSL layer thickness with

the same amount of BEL. In contrast, with equal SSL layer thickness, an increase in the power difference between the first and the second thermal loading leads to a larger BEL region. Besides the parameters of the laser surface treatment, the initial microstructure affects the SSL formation: With decreasing grain size, the SSL thickness is increasing. Furthermore, different chemical compositions of the wheel steel affect the SSL formation, demonstrated by applying laser surface treatments on a common ER7 wheel steel and a micro-alloyed ER7 wheel steel sample. Comparable grain size distribution is ensured by prior equal heat treatments of the samples. Results show decreased SSL thickness for the micro-alloyed wheel steel sample, with significantly lower hardness (WEL_{ER7} : ~900 HV0.01, $WEL_{ER7\text{micro-alloyed}}$: ~700 HV0.01).

The presented work adds a fundamental study on the formation mechanism of BEL respectively SSL on rails and wheels by defined laser surface treatments, contributing to the few existing literature with controversial hypotheses. Moreover, the development of a laboratory method to imitate reproducible SSLs with defined thermal loading history opens new possibilities for systematic studies in future works.

Publication VIII

Fatigue crack initiation in the presence of stratified surface layers on rail wheels

M. Freisinger, B. Jakab, K. Pichelbauer, G. Trummer, K. Six, P.H. Mayrhofer
International Journal of Fatigue, accepted (19.09.2023)

Based on in-depth investigations of *Publications I–IV* and the developed laboratory approach presented in *Publications V* and *VII*, this work presents the first systematic study on RCF crack initiation in the presence of SSLs under defined and reproducible mechanical and thermal loadings. Two different wheel materials (ER7, ER9) with imitated SSLs are fatigue tested by twin disc tribometer experiments, and an explanatory model of RCF crack initiation is introduced.

To ensure good comparability to SSLs observed in the field, the influence of the initial deformation state (pointed out in *Publication V* and *VII*) is addressed by applying a defined mechanical load in a twin disc tribometer (100,000 cycles, 800 N normal force, 1% slip). This leads to a reproducible deformation state of the near-surface microstructure. Then, the surface of the twin disc sample is treated by the laser in three sectors. Two consecutive thermal loadings are applied under controlled conditions (Laser power 1: 4.0 kW; Laser power 2: 3.2 kW), creating an SSL with distinctive WEL and BEL fractions. Finally, the samples are tested in the twin disc tribometer (100,000 cycles, 800 N normal force,

1% slip) and investigated by focus-variation microscopy, LOM, SEM, and hardness measurements.

Results clearly show the trend of RCF crack initiation next to the transition zones of the SSLs to the base material, whereby massive cracking is observed at the side where the tangential force directs toward the base material. In contrast, the other side reveals no RCF crack initiation, neither for the ER7 samples nor for the ER9 samples. In terms of severity of crack initiation and growth, the ER9 material seems more critical, explained by the higher hardness of the formed WEL and BEL, hence, lower fracture toughness. The results are summarized by introducing an explanatory model of RCF crack initiation in the transition zone of SSLs, divided into 4 stages: *Stage 1* represents the wear-dominated state, where shallow micro-cracks are initiated along the surface leading to detachments of particles especially in the WEL. In *Stage 2*, a surface crack is initiated at a certain distance from the WEL-BEL transition, first propagating along the alignment of the deformed martensitic microstructure, followed by a crack growth $\sim 90^\circ$ to the surface through the WEL. *Stage 3* is described by multiple cracks initiating and propagating vertically through the WEL next to the transition zone of the SSL and the base material, with characteristic crack branching at the WEL/BEL interface. The crack branch growing in tangential force direction is propagating along the WEL/BEL interface, while the crack branch in the other direction propagates deeper into the BEL. In the final stage, *Stage 4*, cracks are merging, hence, leading to break-outs of several WEL fragments. This results in a significant geometrical deviation of the wheel surface.

This conclusive publication of the thesis demonstrates a systematic approach to create and test near-surface microstructures evolving in the wheel-rail contact during service by defined and reproducible mechanical and thermal loadings. Paving the way not only to a better understanding of the formation mechanism of SSLs and the influential parameters, but this work also allows a discussion on RCF damage of rail and wheel materials without the uncertainty of field sample loading histories.

5.2 Participations at national and international conferences

ÖTG Symposium 2022

Wiener Neustadt, Austria

Talk: *History-dependent microstructure on railway wheels – lab imitation by combined mechanical and thermal loadings*

M. Freisinger, B. Jakab, K. Pichelbauer, A. Trausmuth

International Conference on Railway Technology 2022

Montpellier, France

Talk: *On the variations of white etching layers on railway wheels and the possibilities of imitation in a laboratory*

M. Freisinger, H. Rojacz, K. Pichelbauer, A. Trausmuth, G. Trummer, K. Six, P.H. Mayrhofer

19. Internationale Schienenfahrzeugtagung 2023

Dresden, Germany

Poster: *Nachbildung von „White Etching Layer“ mittels Lasertechnologie auf Rad und Schienenmaterialien*

M. Freisinger, K. Pichelbauer, K.Six

Ecotrib 2023

Bari, Italy

Talk 1: *Stratified surface layer – a potential fatigue crack initiation site on rail wheels*

M. Freisinger, K. Pichelbauer, B. Jakab, A. Trausmuth, K. Six

Talk 2: *Case study research on the applicability of the micro-bending method in the field of tribology*

M. Freisinger, R. Hahn, I. Delic, M. Rodriguez Ripoll

Euromat 2023

Frankfurt, Germany

Talk 1: *Rolling contact fatigue of stratified surface layers on rail wheel materials*

M. Freisinger, B. Jakab, K. Pichelbauer, G. Trummer, K. Six

Talk 2: *Micro-bending investigations of stratified surface layers on rail wheel materials*

M. Freisinger, R. Hahn, L. Zauner, P.H. Mayrhofer

6 Concluding Remarks & Outlook

This thesis broaches the issue of the formation of near-surface layers on rail wheels during service and their relation to RCF crack initiation. Focus was placed on studying the microstructural characteristics in combination with its micro-mechanical properties. This extends the fundamental knowledge and gives hints to the experienced mechanical and thermal loadings. However, to overcome the unknown loading histories of samples from the field, the thesis presents a framework to imitate realistic and reproducible surface layers under defined parameters on rail wheel materials by combining a twin disc tribometer and laser surface treatments, enabling systematic studies in the future.

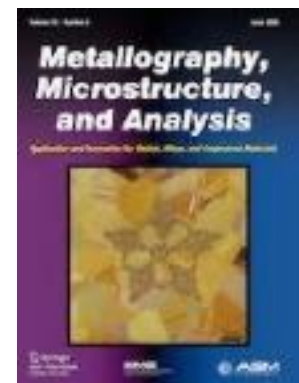
In *Publications I–IV* a wheel sample from the field after ~200,000 km in service was investigated. It must be clearly stated that no further information on the experienced mechanical and thermal loads is known due to the complex wheel-rail contact situation, numerous environmental influences, and additional dynamic effects during service. Results displayed a vast variety of near-surface microstructures differing by location along the wheel tread, with *Publication I* indicating the SPD microstructure as a preliminary stage to the formation of phase-transformed surface layers such as WELs and BELs. Besides numerous existing literatures on the microstructure of evolving surface layers on wheels and rails, there is a research gap on the micro-mechanical behaviour of these layers concerning fracture toughness. Given the overall limited number of publications addressing small-scale fracture toughness evaluation of steel materials, the work in *Publication II* aims to establish the *in situ* micro-bending method in railway research. Based on remarkable improvements in the FIB technique and advanced small-scale testing devices, this methodology surely holds further interesting use cases in the near future, especially for the field of tribology. In tribological contacts, mechanical and thermal loads often lead to a change in the near-surface microstructures with limited size in the contact zone. Outside the framework of this thesis, the micro-bending experiments were conducted on near-surface regions evolving in roller bearings. Further, due to the high spatial resolution of this testing method for focused fracture experiments were done in the matrix region and selective sulphide regions within self-lubricated laser claddings.

Publications III and IV investigated the phenomena of stratification of evolved near-surface layers on rail wheels. The BEL underneath the WEL gained increasing interest in research recently, but the formation mechanism is discussed controversially. With respect to the

diversified loading history of samples from the field – resulting in a vast variety of evolved SSLs – the presented works contribute to the fundamental knowledge about the microstructural characteristics of SSLs. Even though advanced analysis methods revealed results that gave hints to its formation mechanisms, the works did not conclude in a general description, but rather led to new potential research focuses for instance the observed microstructural gradient within the BEL (*Publication IV*). The relation of SSL affecting RCF crack initiation and growth was additionally pointed out by complementary micro-mechanical investigations. Further advanced analysis methods will help unravelling the formation of SSLs on wheels during service, however, the significant uncertainty of the unique mechanical and thermal loading history of samples from the field will always hinder profound studies on its formation mechanisms and systematic studies on the effects of SSL on RCF crack initiation in the wheel-rail contact. This leaves a desire for a laboratory approach to imitate realistic and reproducible near-surface microstructures under defined loading parameters.

In *Publication V* an approach for thermally induce WELs is presented, where microstructural characteristics were further compared to WELs from the field. A reasonable correlation could be shown under certain laser parameters, which was also approved by *in situ* micro-bending experiments in *Publication VI*. Often missing in the literature, the importance of the materials' deformation state prior to laser surface treatment could be demonstrated. To focus on the formation of SSLs, the laser surface treatment approach was enhanced to create a combination of WEL and BEL, see *Publication VII*. The study once again underlines the importance of various influencing parameters. Finally, *Publication VIII* brought together gained knowledge from *Publication I – VII* and presents an innovative laboratory approach to imitate defined mechanical loads (twin disc tribometer) and thermal loads (laser surface treatments) to create realistic and reproducible SSLs on wheel materials. In terms of scientific directions, the developed laboratory approach opens the door for systematic studies not only on the origin of SSLs but also on related material behaviour such as wear and RCF failure. This is demonstrated in *Publication VIII* by the first systematic study on the RCF crack initiation in the presence of SSLs for different wheel materials. In combination with in-depth microstructural and micro-mechanical analysis methods, this approach surely holds further interesting results in the near future and will contribute to the research on evolved microstructures in wheel-rail contacts.

Publication I



Severe plastic deformed zones and white etching layers formed during
service of railway wheels

M. Freisinger, H. Rojacz, A. Trausmuth, P.H. Mayrhofer
Metallography, Microstructure, and Analysis, vol. 12, no. 3 (2023)
DOI: 10.1007/s13632-023-00967-x



Severe Plastic Deformed Zones and White Etching Layers Formed During Service of Railway Wheels

M. Freisinger^{1,2} · H. Rojacz¹ · A. Trausmuth¹ · P. H. Mayrhofer²

Received: 9 February 2023 / Revised: 31 March 2023 / Accepted: 10 April 2023
© The Author(s) 2023

Abstract

The near-surface regions of rail wheels experience a complex thermo-mechanical loading, which varies along the location of the tread and causes severe changes to the microstructure. Occasionally, brittle white etching layers (WEL) are formed, representing a high risk of wheel damage. Therefore, we studied the depth-evolution of the surface-near microstructure along different regions of the tread of a wheel being ~200,000 km in service. The microstructural variations point toward a higher thermal loading history in the middle of the tread and predominant mechanical loading in the neighboring regions, where a severe plastic deformed microstructure with rolling contact fatigue cracks is present. Varieties of WEL-like microstructures were investigated, the presented analysis contributes to the knowledge of their microstructural characteristics and outpoints these regions in terms of potential crack initiation sites on railway wheels.

Keywords Rail-wheel contact · Severe plastic deformation · White etching layer · Brown etching layer · Stratified surface layer

Introduction

Medium carbon steels are commonly used for railway wheels due to a good balance of hardness and fracture toughness, as well as solid wear properties. Among rail wheel steels, the grade ER7 is one of the most used grades on freight trains in Europe. During service, the contact surface is affected by a complex mechanical loading situation in terms of vertical, tangential, and longitudinal loads [1]. High shear stresses can cause rolling contact fatigue (RCF) damage [2–5], and cracks propagating into the material can lead to catastrophic failure [6]. Besides the mechanical loads, the wheel tread surface is additionally affected by high thermal loads due to frictional heating during curving, braking, short slippage events when acceleration, or even occasional full slippage events. Temperatures can exceed 500 °C in slip zones on wheel tread surfaces [7] leading to a massive influence on microstructure and mechanical properties [8,

9]. Even though modern trains are equipped with wheel slide protection systems [10, 11] thermally induced damage is still an issue [10, 12, 13]. Additionally important are mechanical loads, which in combination with temperature heavily affect the near-surface microstructure [9, 14–16]. Besides the loading history, the microstructural evolution also varies on the location along the wheel tread surface [17, 18].

The formation of a white etching layer (WEL) can initiate cracks and promote their propagation [19–27], since the evolved microstructure of the WEL comes up with higher hardness and lower fracture toughness. Most studies are performed for railheads, but the comparable materials and rolling-sliding contact situation may allow transferring the gained know-how about the relevant mechanisms to railway wheels as well. The formation process is still under discussion, some studies predict heating above austenitization temperature followed by rapid cooling [21, 22, 25, 28] is the major cause, while others claim heavy plastic deformation [23, 24, 29], and further ones their combination [30, 31]. However, WEL can form in several variations—a common and consistent classification is still missing—on railway wheel tread surfaces [13, 32–34]. Recently, the terms brown etching layer (BEL) and stratified surface layer (SSL) are introduced [35–38], outpointing the diversity of the evolved microstructures.

✉ M. Freisinger
matthias.freisinger@ac2t.at

¹ AC2T research GmbH, 2700 Wiener Neustadt, Austria

² Institute of Materials Science and Technology, TU Wien, 1060 Vienna, Austria

The different variations are further summarized as WEL-like microstructures within this work.

The aim of this study is to study the evolved microstructure on railway wheels in greater detail, since this is the initial microstructural state before a possible formation of WEL-like microstructures (WEL, BEL, SSL). For this, the three main zones along a railway wheel tread after service are investigated. We concentrated on the microstructural evolution in transversal and rolling directions—in different depths from the surface—using light optical microscopy (LOM) as well as high magnification scanning electron microscopy (SEM) and electron backscatter diffraction (EBSD) measurements. Our studies also reveal different variations of WEL-like microstructures, characterized by different microstructures and hardness.

Experimental

A railway wheel of the wheel steel grade ER7 (EN13262 [39]) with a diameter of 0.95 m and after nearly 200,000 km in service was provided by the Austrian Federal Railways. Table 1 summarizes the chemical composition of this material, which typically shows an upper yield strength of $R_{eH} \geq 520$ MPa, a tensile strength R_m between 820 and 940 MPa, and an elongation at break A_5 of $\geq 14\%$. Brinell hardness is above 235 HB and a fracture toughness between 40 and 80 MPa $m^{1/2}$ is standardized [40], when treated and tested according to EN13262.

The samples for our investigations were prepared with a laboratory cutting device (Struers Secotom-50; Struers ApS, Denmark) out of three different zones of the railway wheel. These zones are named according to [41] as zone 1 (being taken from the peripheral tread region, at the field side), zone 2 (taken from the tread surface close to the wheel flange), and the middle zone 3 (major wheel tread) (Fig. 1a).

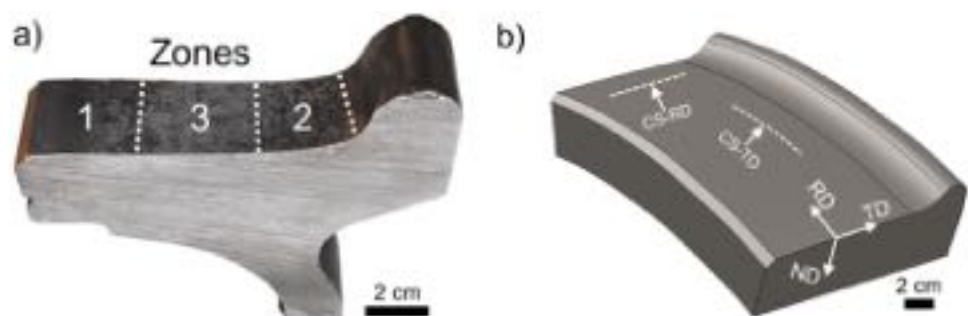
For each zone, multiple cross sections in transversal direction (CS-TD) and in rolling direction (CS-RD) are analyzed (Fig. 1b).

Samples taken from these zones are embedded in conductive compounds and prepared by coarse grinding, 1 μm diamond fine polishing, and etching with ethanolic nitric acid (3% HNO_3 , 97% ethanol). The microstructure is studied LOM (Axio Imager M2m, Carl Zeiss AG, Germany) and SEM (Jeol JIB 4700F, Jeol Ltd., Japan) equipped with a Schottky field emission gun, secondary and backscattered electron detectors, and an electron backscatter diffraction (EBSD) detector (Bruker e-Flash HR, USA). SEM investigations were performed at 15 kV acceleration voltage. To gain optimal results at the EBSD measurements, additional finish polishing for 10 min with colloidal Silica ($< 0.25 \mu\text{m}$) was carried out. EBSD measurements were performed in the SEM with optimized electron beam conditions at 15 kV acceleration voltage and a probe current of 3.6 nA. The working distance of the SEM was set to 16 mm, and the EBSD detector distance to 18 mm. Kikuchi patterns were acquired at 200×150 px with an exposure time of 20 ms. Setup and analysis were performed via the Bruker Esprit 2.2 software package, whereas the American Mineralogist Crystal Structure Database (AMCSD) database was used for phase identification. The inverse pole figure (IPF) maps, the grain average misorientation (GAM) maps, and the grain boundaries (GB) maps are presented in this work to describe the evolved microstructure in more detail. The IPF map is used to describe the grain structure in general, possible preferred orientations, and the grain size distribution. The GAM maps show the calculated misorientation between each neighboring pair of points within the grain and therefore give information about the orientation changes inside the grains. The GB maps are useful to evaluate the fraction of small angle grain boundaries, defined in this study with GB angles up to 10° , and large angle grain boundaries ($> 10^\circ$).

Table 1 Maximum percentages of elements for ER7 according to the standard EN13262 [39]

C	Si	Mn	P	S	Cr	Cu	Mo	Ni	V
0.52	0.40	0.80	0.020	0.015	0.30	0.30	0.08	0.30	0.06

Fig. 1 (a) Designated zones along the tread surface of the ER7 railway wheel after ~200,000 km in service. (b) Schematic illustration of the cross sections prepared in transversal direction (CS-TD) and rolling direction (CS-RD)



Hardness was investigated by low load Vickers hardness depth profiles (load of 0.05 kp (0.49 N)) indenting the cross sections at increasing distances from the surface with a Future-Tech FM-700 hardness tester. The diagonals of the indents are measured with a LOM. Furthermore, nanoindentation measurements of individual regions within the samples were performed with a Bruker Hysitron Triboindenter TI980–Performech II (equipped with a Berkovich diamond tip) to characterize their indentation hardness as well as moduli. The load–displacement curves (with a peak load of 5 mN) were evaluated and the hardness was deduced via the load/area ratio, whereby the reduced Young’s modulus was evaluated via the Oliver and Pharr method [42].

Results

Out of each zone, several cross sections in transversal direction and rolling direction were prepared and analyzed. The presented images indicate that there is no preferred rolling direction, this is because this study is based on a railway wheel from the field where the running direction was changing over the service.

Characteristic Microstructural Evolution in Different Wheel Tread Zones

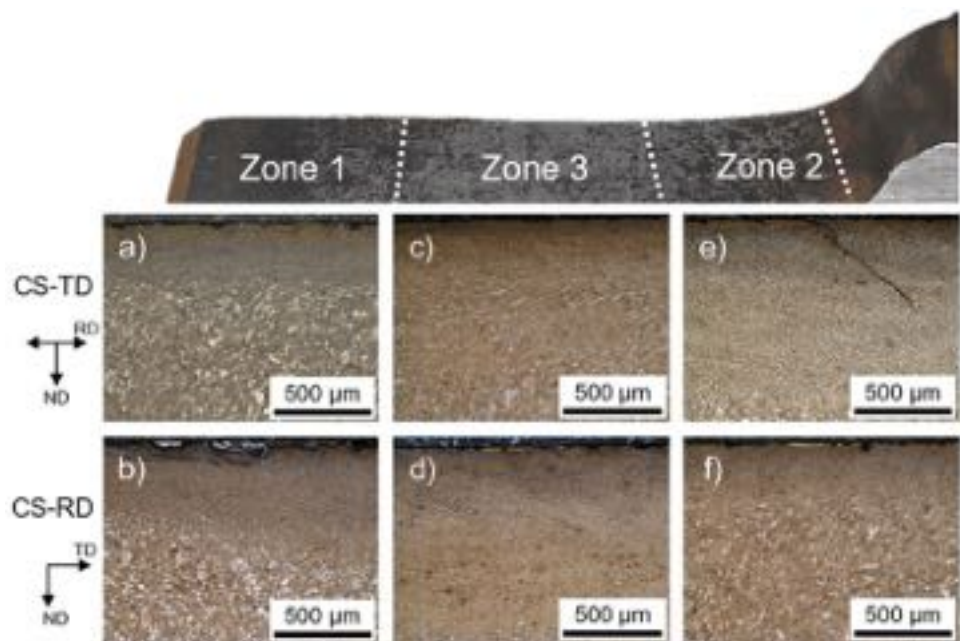
In the peripheral tread region (field side) of the wheel, zone 1, the cross section CS-TD (Fig. 2a) shows numerous cracks with depths of $\sim 100\ \mu\text{m}$ propagating in a severely plastically deformed (SPD) microstructure, which expands

down to $\sim 300\ \mu\text{m}$ from the surface. Some of the cracks are wide opened and/or changing crack growth direction leading to multiple spalling of the material, hence, resulting in a rough surface. In a depth of $300\text{--}600\ \mu\text{m}$ from the surface the microstructure gradually changes from a fine-grained SPD microstructure with random orientation to a ferritic-pearlitic microstructure (with elongated grains in rolling direction, aligned with about $30\text{--}45^\circ$ to the surface). The elongation, alignment, and grain size decrease with increasing distance from the surface, featuring a ferritic-pearlitic bulk microstructure without preferred orientation upon $\sim 600\ \mu\text{m}$ from surface.

For the cross section CS-RD in zone 1 (Fig. 2b) a rough surface can be seen as described for CS-TD due to numerous spallation. But this cross section in rolling direction additionally shows long cracks propagating almost parallel to the tread surface in depths of about $100\ \mu\text{m}$. These cracks are branching or merging at certain stages, which leads to large spallation. The evolution of the sub-surface microstructure is in general comparable to that shown for the cross section CS-TD: A gradual change from a fine-grained and randomly orientated SPD microstructure at $\sim 300\ \mu\text{m}$ from surface to a ferritic-pearlitic microstructure. The latter is aligned parallel to the surface with increasing grain size from 300 to $600\ \mu\text{m}$ with increasing distance from the surface. At $\geq 600\ \mu\text{m}$ below the surface, the original bulk microstructure is present.

In the middle of the wheel tread, designated as zone 3, the cross section CS-TD (Fig. 2c) shows that the fine-grained microstructure reaches deeper into the material than for zone 1, although, the depth is varying widely between 300 and $700\ \mu\text{m}$ from the surface. Below that

Fig. 2 Sub-surface microstructure LOM images of the ER7 railway wheel after $\sim 200,000$ km in service. The first column shows the cross-sections in zone 1: (a) in transversal direction (CS-TD) and (b) in rolling direction (CS-RD). The second column shows the middle zone 3: (c) CS-TD and (d) CS-RD, and the third column the zone 2: (e) CS-TD, (f) CS-RD



region, the microstructure changes gradually to an aligned SPD microstructure with decreasing deformation degree with increasing depth. Within zone 3, the thickness of the influenced microstructure varies widely within a maximum of $\sim 1,000 \mu\text{m}$. Also in rolling direction, the microstructure is comparable (Fig. 2d). Here, a formation of a thin WEL can be detected with a thickness of about $30 \mu\text{m}$.

The cross-sectional LOM image of the region close to the wheel flange (zone 2, Fig. 2e) clearly shows massive cracks, which mainly originate from regions where a WEL is present. These cracks typically propagate down to depths of $\sim 600 \mu\text{m}$ with an angle of about 45° from surface. Some cracks branch within the WEL and/or grow along the interface between WEL and underlying material, leading to spallation. A fine-grained microstructure is present down to almost $900 \mu\text{m}$ from surface. Below this uniform microstructure, there is immediately the original microstructure.

Microstructural investigations of the material in rolling direction (Fig. 2f) exhibit similar features as perpendicular to it. Below the fine-grained microstructure, there is directly the original microstructure, without the presence of an aligned SPD microstructure as within the other two zones.

Detailed investigations of zone 1 (Fig. 2a) by higher magnification SEM and EBSD measurements on cross sections perpendicular to the rolling direction in different depths from the surface are presented in Fig. 3. At a depth of $50 \mu\text{m}$ (Fig. 3a) a fragmentation (and possible dissolution) of the cementite is evident and the spherical cementite particles are randomly distributed. At a depth of $100 \mu\text{m}$ (Fig. 3b) and $150 \mu\text{m}$ (Fig. 3c) the microstructural features are comparable, with a slightly less dense arrangement. For the regions at distances of $\sim 150 \mu\text{m}$ (Fig. 3c), $300 \mu\text{m}$ (Fig. 3d), $600 \mu\text{m}$ (Fig. 3e), and $1500 \mu\text{m}$ (Fig. 3f) below the surface detailed EBSD measurements were conducted and evaluated for their IPFs, GAM, GBs. The IPF map for the region at $\sim 150 \mu\text{m}$ from the surface shows a fine-grained microstructure with slightly elongated grains and no preferred orientation. The fraction of large angle grain boundaries (with misorientation angles between adjacent grains of $\geq 10^\circ$) is relatively high (Fig. 3c). At a depth of $300 \mu\text{m}$, the SEM investigations suggest for larger grains (Fig. 3d), bent and broken cementite lamellae (next to spheroidized particles), and proeutectoid ferrite. EBSD investigations of this region prove the larger grains, which seem to be elongated along the rolling direction (Fig. 3h). The GAM map analysis shows a wider GAM angle distribution than the region closer to the surface.

At a depth of $600 \mu\text{m}$ from the surface, the microstructure is comparable to the original condition with clearly present pearlite and ferrite grains (Fig. 3e). The original microstructure is essentially present at a distance of $1500 \mu\text{m}$ from the surface (Fig. 3f). The GAM analysis of the EBSD measurements (Fig. 3i) show that the highest misorientation angles

are at the lamellar structures of pearlite, and the respective GB analysis yield only a fraction of 25–18% of small angle GB (angle below 10°).

Detailed analysis of zone 3 (Fig. 2c) by SEM (Fig. 4) show spheroidized cementite (Fig. 4a) down to $100 \mu\text{m}$ (Fig. 4b) and even $150 \mu\text{m}$ from the surface (Fig. 4c). With increasing distance from the surface, the overall microstructure gradually changes toward the original one (Fig. 4d, e, and f). EBSD analyzes of the region $150 \mu\text{m}$ below the surface (Fig. 4g) show a fine-grained microstructure with slightly elongated grains. The GAM angle map pictures low misorientation angles and the fraction of large angle grain boundaries (angles $> 10^\circ$) is high with $\sim 86\%$. At a distance of $300 \mu\text{m}$ from the surface (Fig. 4h), the microstructure is still very similar with slightly more pronounced elongated grains (represented by the IPF map) and a smaller fraction of large angle grain boundaries.

With further distance from the surface, ($300 \mu\text{m}$, Fig. 4d) the fraction of spheroidized cementite decreases and that of cementite lamellae increases, suggesting less broken and annealed cementite lamellae upon this depth. However, even at $600 \mu\text{m}$ from the surface (Fig. 4e), spheroidized particles are present. The corresponding IPF map (Fig. 4i) shows a mixture of elongated grains (orientated in rolling direction) and polygonal grains. At this distance from the surface there are more areas with larger GAM angles than closer to the surface and the fraction of small angle grain boundaries ($< 10^\circ$ misorientation) increased to almost 17%. Contrary to zone 1, here, even at a depth of $1500 \mu\text{m}$ (Fig. 4f), broken and bent cementite lamellae are present within the pearlite grains. Further, the EBSD investigations do not represent an unaffected bulk microstructure like in zone 1 at this depth. Clearly, a sub-grain microstructure is present.

Detailed SEM investigations of zone 2 (Fig. 2e), $50 \mu\text{m}$ below the surface perpendicular to the rolling direction, show fine globular particles (Fig. 5a). Although generally, the overall microstructure is similar to that of zone 1 and zone 3 at this depth (compare with Fig. 3 and Fig. 4), still some cementite lamellae are present here. At distances of $100 \mu\text{m}$ (Fig. 5b) and $150 \mu\text{m}$ (Fig. 5c) from the surface, the overall microstructure is very similar to that at $50 \mu\text{m}$, with tendencies of an increased fraction of cementite lamellar. This tendency continues with increasing distance from the surface ($300 \mu\text{m}$, Fig. 5d), and at a distance of $600 \mu\text{m}$ (Fig. 5e) the grains are already more globular with cementite lamellae fragments and proeutectoid ferrite. At a distance of $1500 \mu\text{m}$ the original pearlitic microstructure is present (Fig. 5f).

EBSD measurements clearly show elongated grains aligned parallel to the rolling direction at a distance of $150 \mu\text{m}$ from the surface (Fig. 5g). Compared with the other zones, the grain size is larger. With increasing distance (Fig. 5h and i), the grain size further increases while

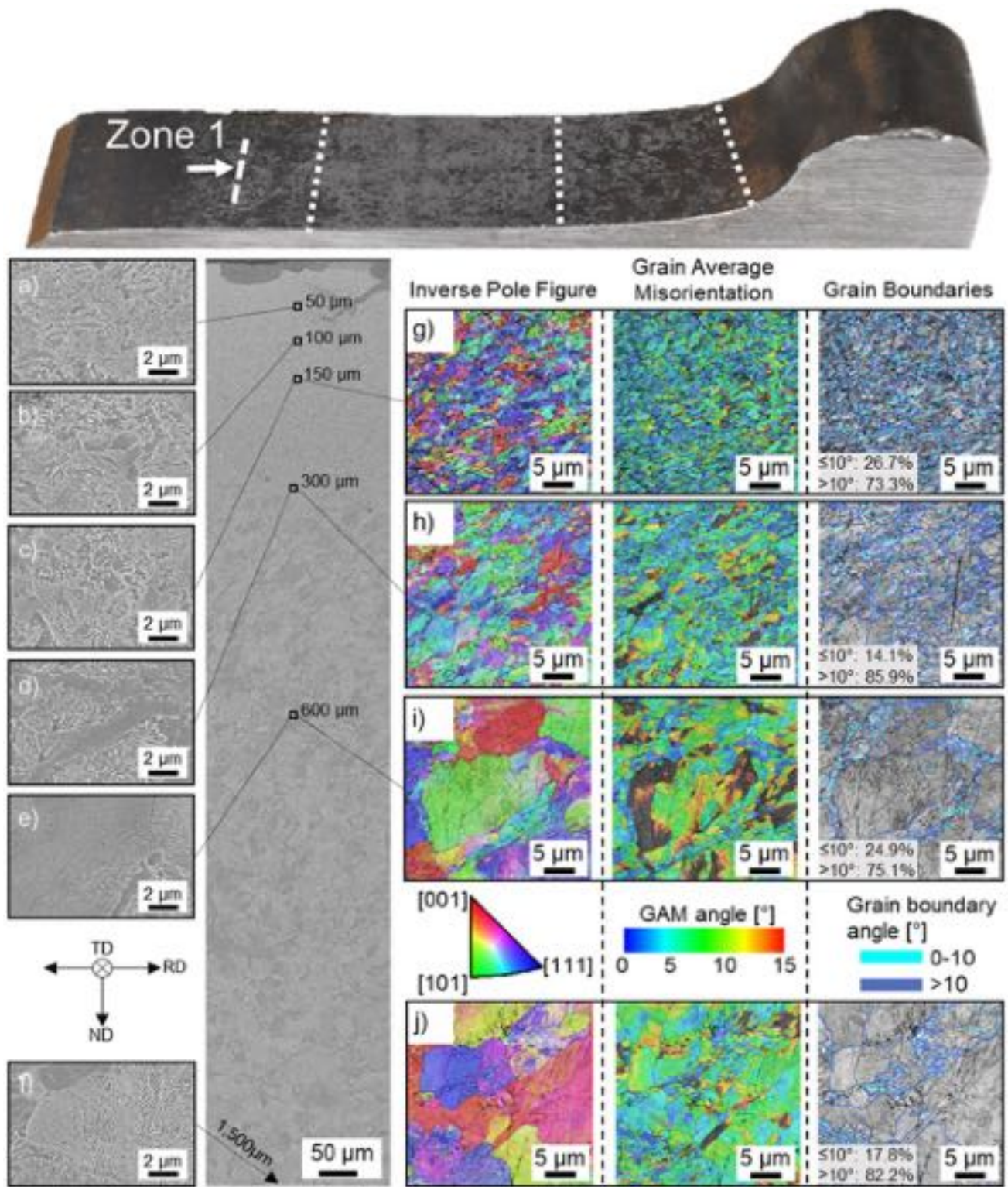


Fig. 3 Detailed SEM investigations of the zone 1 in transversal direction (CS-TD): Micrographs with a magnification of 35,000× are presented in various depths in the first column: (a) 50 μm, (b) 100 μm, (c) 150 μm, (d) 300 μm, (e) 600 μm, and (f) 1500 μm.

Inverse pole figure, grain average misorientation and grain boundary maps from EBSD measurements are shown for selected depths on the right side: (g) 150 μm, (h) 300 μm, (i) 600 μm, and (j) 1500 μm

Die approbierte gedruckte Originalversion dieser Dissertation ist an der TU Wien Bibliothek verfügbar. The approved original version of this doctoral thesis is available in print at TU Wien Bibliothek.

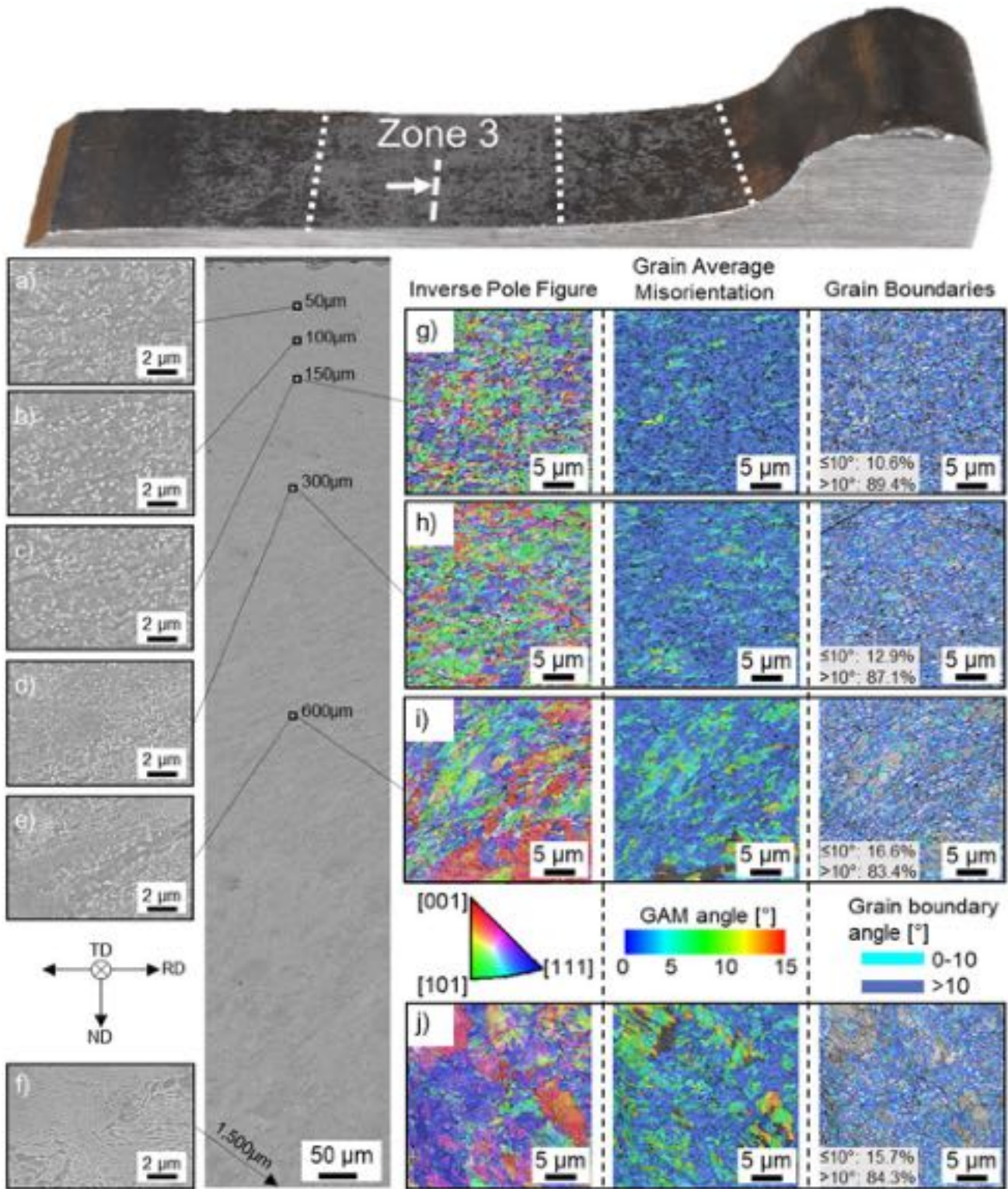


Fig. 4 Detailed SEM investigations of the zone 3 in transversal direction (CS-TD): Micrographs with a magnification of 35,000× are presented in various depths in the first column: (a) 50 μm, (b) 100 μm, (c) 150 μm, (d) 300 μm, (e) 600 μm, and (f) 1500 μm.

Inverse pole figure, grain average misorientation and grain boundaries maps from EBSD measurements are shown for selected depths on the right side: (g) 150 μm, (h) 300 μm, (i) 600 μm, and (j) 1500 μm

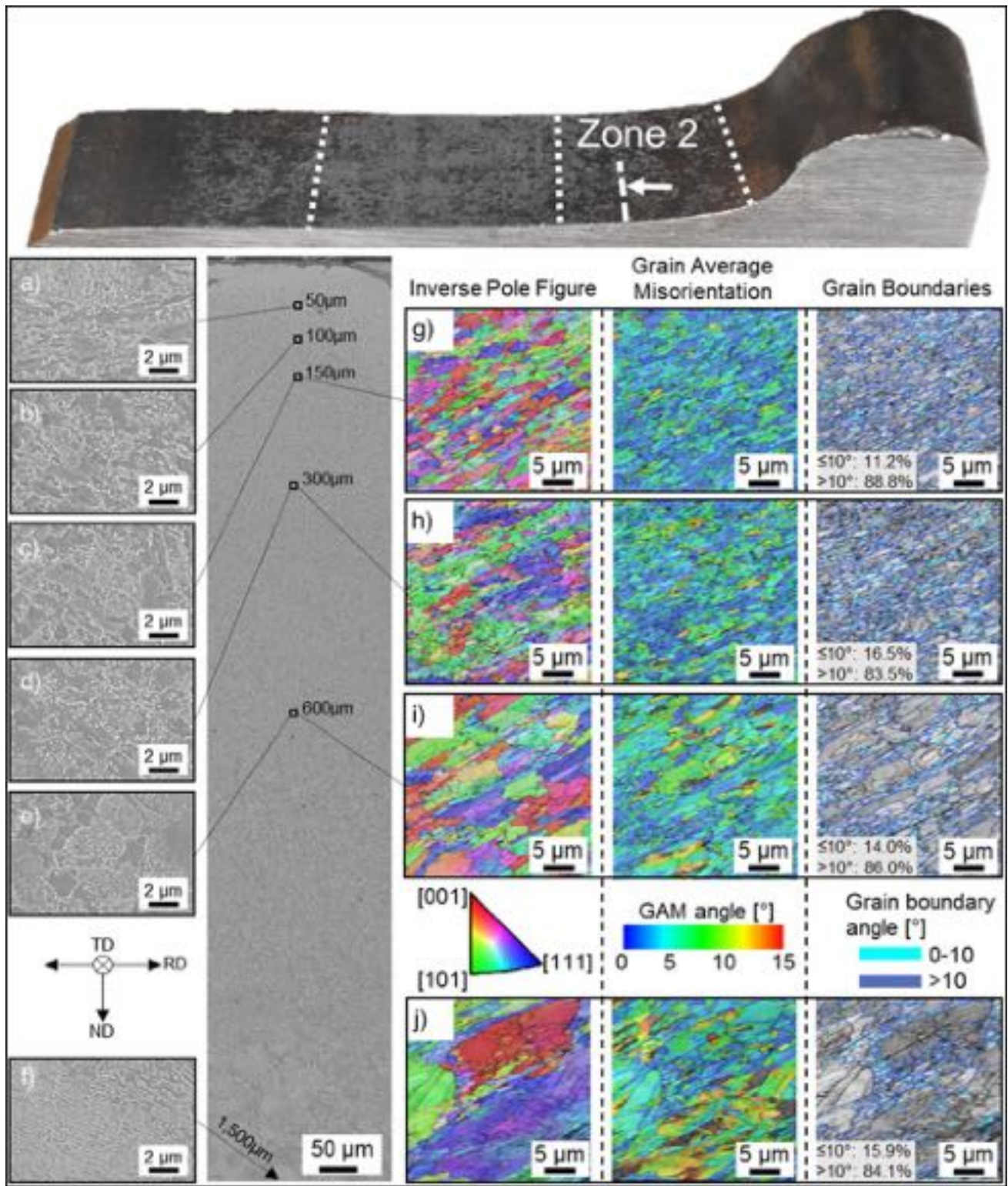


Fig. 5 Detailed SEM investigations of the zone 2 in transversal direction (CS-TD): Micrographs with a magnification of 35,000× are presented for various distances from the surface: (a) 50 μm, (b) 100 μm, (c) 150 μm, (d) 300 μm, (e) 600 μm, and (f) 1500 μm.

Inverse pole figure, grain average misorientation, and grain boundary maps from EBSD measurements are shown for (g) 150 μm, (h) 300 μm, (i) 600 μm, and (j) 1500 μm distances from the surface

still being aligned in rolling direction. Areas with larger GAM angles increase and the fraction of large angle grain boundaries decreases. Even at a distance of 1500 μm from the surface, the EBSD investigations (Fig. 5j) hint toward a modified microstructure with elongated ferrite and pearlite grains aligned in rolling direction.

Microhardness is determined by Vickers hardness measurements, the results show an increase within 200 μm from surface for zone 1 and zone 2, in contrast to no significant change in zone 3 (Fig. 6a). Below ~ 300 μm from surface the hardness values are constant in each zone, differences are supposed to be evident due to the thermal treatment when manufacturing the wheel. An attempt to evaluate nanoindentation hardness (Fig. 6b) is done at various depths from surface, referring to the depths of the detailed SEM investigations. An increase in hardness can be seen within the outermost 100 μm from surface in all zones, however, scattering is very pronounced.

Various WEL-Like Microstructures on the Wheels

Various WEL-like microstructures are identified by etching the cross-sectional samples, with variations in appearance (bright shining to brownish), thicknesses (20–600 μm) as well as microstructure (Fig. 7).

The white appearing layer pictured in Fig. 7a is present on the tread surface in the region between zone 2 and 3. It comes up with a thickness of ~ 30 μm , formed top of an SPD aligned microstructure and numerous cracks originate within this layer (defined as WEL1 in this work). Figure 7b shows different WEL-like microstructures, more precisely a stratification of different layers. A large brownish appearing region extends down to 500 μm below the surface of zone 3. On top of this brownish region (defined as BEL) a brighter, more

homogenous and thinner layer is present, which is defined as WEL2. The combination can be designated as SSL. Some cracks stop at the interface of WEL2 and BEL, but at the margin of the SSL a crack propagates through both layers, arresting at the interface to the underlying microstructure. In some areas, the underlying material (below the SSL) is an SPD microstructure and in others an almost original coarse ferritic-pearlitic microstructure.

Detailed high-magnification SEM investigations of selected regions highlight the typical microstructure of the formed WEL-like microstructures (Fig. 7a and b). The thin and homogenous WEL1 has a uniform microstructure (Fig. 7c). Further increasing the magnification highlights a fine mesh-like structure with some evenly distributed sub-micron globular particles < 100 nm (Fig. 7d). The underlying SPD region exhibits a coarser and more aligned microstructure (Fig. 7e and f), corresponding to that presented earlier for a distance of ~ 50 μm below the wheel tread surface.

In general, WEL2 exhibits a comparable microstructure to WEL1 but the mesh-like structure tends to be demolished, compare Fig. 7c and d (WEL2) with Fig. 7g and h. Moreover, differences can be seen regarding hardness, where WEL1 reveals the highest values of 6.09 ± 0.43 GPa followed by WEL2 with 4.61 ± 0.46 GPa. The high-magnification SEM micrographs of the BEL (Fig. 7i and j) show a dissolved microstructure with spheroidized cementite and the hardness significantly decreased to 3.57 ± 0.50 GPa.

Discussion

When comparing individual studies about wear and fatigue phenomena of railway wheels, it is of utmost importance to know the loading history and whether there is a preferred

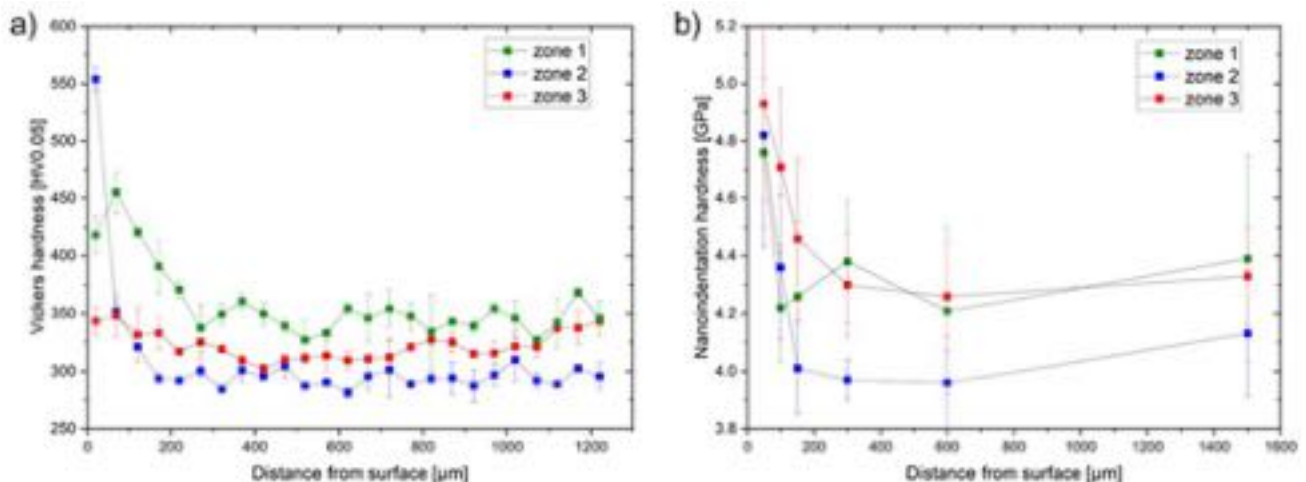


Fig. 6 Low-load Vickers hardness measurements (a) and nanoindentation hardness (b) graphs for the different zones

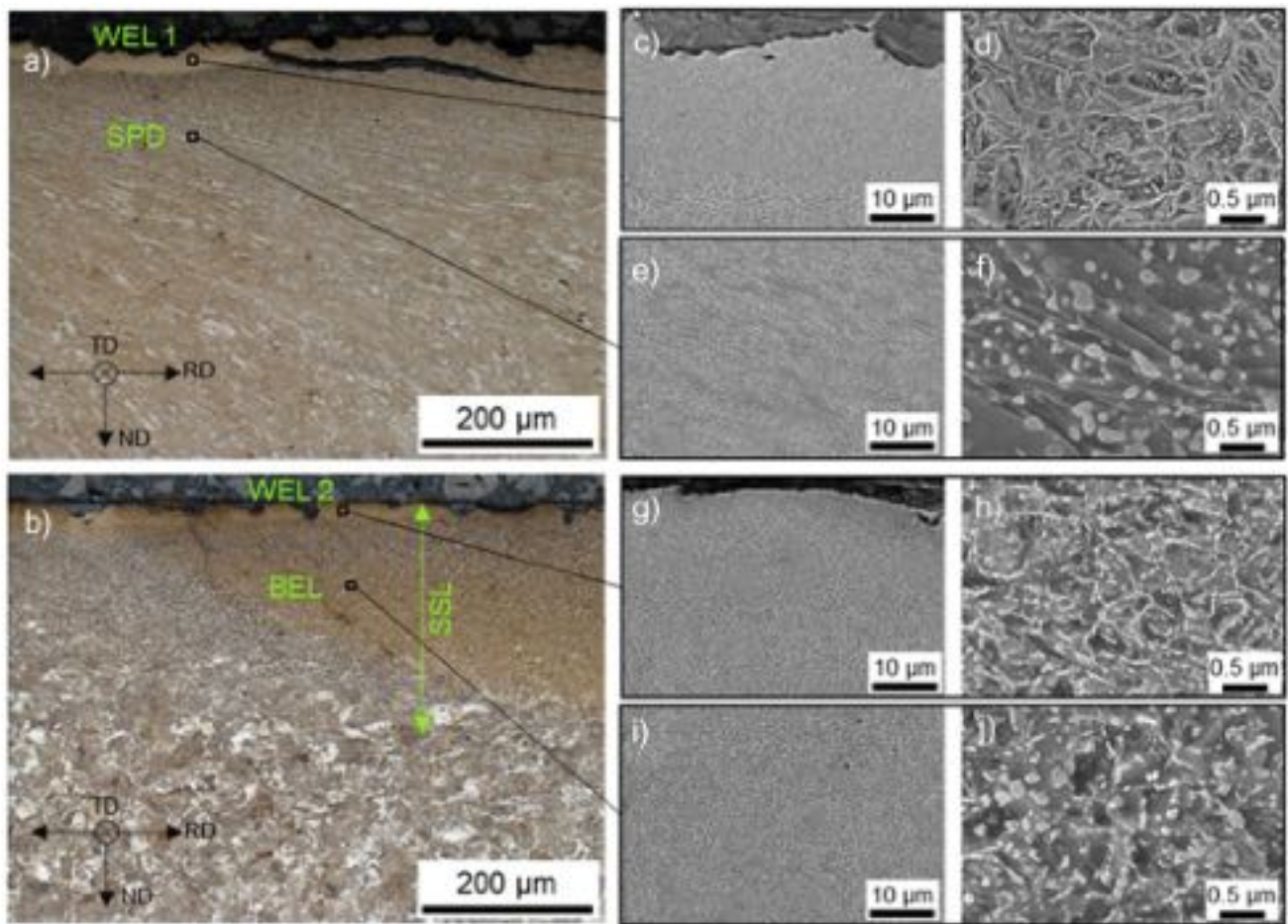


Fig. 7 (a) and (b) show overview micrographs of the investigated WEL-like microstructures. Detailed SEM investigations of the regions marked in (a) and (b) are presented in (c–j) with different

magnifications: WEL1 (c) and (d), aligned SPD microstructure (e) and (f), WEL2 (g) and (h), and BEL (i) and (j)

rolling direction, or this changed periodically throughout the service like for the wheel studied in the current work. Whereas most of the studies focus on a certain zone along the railway wheel tread [43–45], we compared the microstructural evolution in the near-surface regions for different locations of the railway wheel tread. A corresponding study was conducted by Molyneux-Berry et al. [17] for a railway wheel being in service for ~280,000 km. For the region corresponding to our zone 1 (named region E in [17]) they report that there are few contacts (with the rail) but high tangential forces toward the middle of the tread, causing rolling contact fatigue (RCF) cracking. Our microstructural results are comparable (Fig. 2a and b, Fig. 3) exhibiting an about 300–500 μm deep deformed region with numerous small RCF cracks along the surface and some long but shallow cracks propagating toward the middle of the railway wheel tread. For this middle region, moderate normal stresses and circumferential tangential forces are present [17]. Due to various characteristics (e.g., traction, braking),

the peak loading tends to be in the near sub-surface region. Corresponding to the results reported in [17], our microstructural studies indicate a weaker line structure in transversal direction of this middle region (Fig. 2d) than for the cross section in rolling direction (Fig. 2c, Fig. 4). This low shear strain values with minor deformed microstructure and practically featureless appearance for the middle sector of the railway wheel tread is also reported by Cvetkovski and Ahlstrom [18]. Important to mention is also that for this middle region—being the main contact zone between wheel and rail—traction and braking will lead to significant temperature influence on the railway wheel [17]. This thermal loading is sufficient to initiate spheroidization of broken cementite lamellae (due to the mechanical loading) [13, 16, 46], (Fig. 4a and b). Nikas et al. [9] studied different railway wheel materials and found comparable microstructures in this middle region of the railway wheel tread.

For the region of our zone 2, Molyneux-Berry et al. [17] proposed that significant normal and tangential stresses

lead to the formation of fine surface cracks, which tend to propagate not deep into the material. While in general, our microstructural observations are similar for this region, we do observe also cracks that propagate almost 500 μm deep into the material (Fig. 2e). This might be affected by the formation of a different WEL-like microstructures, which easily results in a different fracture toughness [1, 2, 4, 6, 7, 19, 20, 47, 48].

Corresponding detailed EBSD studies at different regions of the railway wheel to ours are so far mainly conducted for wheel materials loaded via a twin-disc setup [33, 49–60]. These lab-tests do have their advantages as the loading conditions are controlled, but a direct comparison of the thereby obtained microstructural changes with those present in railway wheels after service is difficult. Nevertheless, the deformation of ferrite and cementite lamella, their fragmentation and the subsequent formation of a sub-grain structure and fine-grained microstructure—as reported for materials tested with the twin disc setup [51]—was also observed for our wheel after service (Figs. 3, 4 and 5). Differences for our ex-service wheel are that in zone 1 an SPD microstructure with high GAM angles is present, resulting from high tangential forces [17] and that the fraction of small angle GB is higher for the measurement depth of 150 μm (Fig. 3g). Also for the other zones, 2 (Figs. 3, 4g–j) and 3 (Fig. 5 g–j), the fraction of large angle GB is highest directly below the surface. The GAM is lowest in the middle region of the railway wheel treat (zone 3), where the highest thermal loading is present as discussed above, promoting dynamic recrystallization [52] and spheroidization of fragmented cementite lamellae. This leads to no significant hardness increase within zone 3 (Fig. 6a), in contrast to an increase for the other zones. Some studies measured an increase in hardness in the middle zone of an used rail wheel with values up to 300–400 HV1 [17, 61], however, the wheel grade and the loading history are different. In general, plastic deformed regions and fine-grained layers near the surface come up with hardness increases [51, 57] but due to local inhomogeneities of rail wheels from service the variation is large. This is also the issue for the presented nanoindentation measurement results (Fig. 6b), which were performed in the same depths as the detailed SEM investigations. A trend toward a hardness increase up to 5 GPa can be seen for all zones, but especially below 300 μm the coarse microstructure led to a large scattering of the nanoindentation results.

Our results clearly show the variety of WEL-like microstructures, whereby its formation depends on the different loading conditions present at the different zones of the railway wheel. Further, the initial local microstructure along the wheel tread potentially influences the formation [28]. Most characteristically the WEL-like microstructures lead to different colors during LOM investigations (Fig. 7a, b) and exhibit a different microstructure (during SEM

investigations), as well as mechanical properties. The brightest WEL (WEL1 Fig. 7a, c, d) is thin and formed on top of an otherwise heavily deformed material, suggesting that short but intense slipping events are primarily responsible for their formation. A comparable microstructure and general appearance are reported by Handa et al. [11] for a wheel from service, and by Zhu et al. [50] for a wheel tested via a twin-disc setup with a 25% slip ratio. The large brownish (during LOM) appearing area (named here BEL, Fig. 7h) suggests a massive thermal influence (like present during heavy braking) because microstructural investigations after brake dynamometer experiments yield a comparable result [11]. The microstructure is almost featureless with larger spheroidized cementite particles, which can be ascribed as BEL or tempered WEL, discussed in detail by Kumar et al. [35] for rails. Corresponding variations of WEL-like microstructures at the same location along the tread wheel surface are also reported by others [13, 32–34], but a different classification is still missing and most likely not meaningful due to the complex loading situation during service.

Conclusions

The near-surface regions of a railway wheel after almost 200,000 km in service exhibit huge variations in their microstructural evolution from the field side of the wheel treat to its flange, due to variations in loading situations.

The field side (named here zone 1) reveals numerous RCF cracks, indicative of high tangential forces toward the middle of the tread. A severe plastic deformed microstructure extends down to a depth of ~ 300 μm from the surface, with cementite fragmentation and even spheroidization. EBSD investigations show that the microstructure exhibits signs of deformation even down to 600 μm and a relatively high grain average misorientation. The corresponding hardness variation—which increases from the core value to the surface by only $\sim 8\%$ —is less pronounced than for the other zones along the surface tread. The microstructural changes in the region next to the wheel flange (named here zone 2) extend deeper into the material than for the field side. The microstructural features—like more pronounced elongation in rolling direction as well as alignment $\sim 45^\circ$ to the tread surface—indicate a comparably lower thermal loading history. The hardness at the surface is $\sim 15\%$ above the core value. The region between these, being the major tread surface (named here as zone 3), exhibits a microstructure with spheroidized cementite down to deeper regions as for the field side. This suggests that the thermal loading history was more severe. Furthermore, the region is characteristic of its fine-grained microstructure with minor preferred alignment,

low misorientation, and a higher fraction of large angle GBs near the surface.

In addition to these different microstructural evolutions and characteristics, variations of WEL-like microstructures are present, acting as potential crack initiation sites. The thin ($\sim 3 \mu\text{m}$) and brightest appearing (after metallographic sample preparation) WEL (classified as WEL1) reveals a fine mesh-like structure and the highest hardness of $6.09 \pm 0.43 \text{ GPa}$. The overall morphology of this WEL suggests a minor loading since formation, hence being relatively “young”. This is in contrast to the other variation identified (classified as WEL2), which is up to $50 \mu\text{m}$ thick and exhibits a more flawed mesh-like microstructure suggesting severe loading since formation. This WEL appears more brownish-like during light optical microscopy and has a lower hardness with $4.61 \pm 0.46 \text{ GPa}$. The third majorly different variation (classified as BEL) is softest ($3.57 \pm 0.50 \text{ GPa}$) and $500 \mu\text{m}$ thick. Its microstructure shows small spheroidized cementite particles and suggests even for their dissolution; hence, the ferrite would be supersaturated in C. Several reports indicate that such a BEL resulted from severe thermal loads generated during hard wheel braking and massive slippage events. The presented analysis shows the diversity of WEL-like microstructures in the field and can contribute to the knowledge of potential fatigue crack initiation sites. The highest tendency for crack-formation was found for the WEL1 and in its vicinity. Therefore, we classify WEL1 as more dangerous than WEL2 or BEL in terms of cracking risk. Knowledge of microstructural characteristics and mechanical properties, especially crack initiation and fracture behavior, is crucial for further improvement of railroad safety.

Acknowledgements This project has received funding from the Shift2Rail Joint Undertaking (JU) under grant agreement No 826255 and No 101012456. The JU receives support from the European Union’s Horizon 2020 research and innovation programme and the Shift2Rail JU members other than the Union. In addition, this work was funded by the “Austrian COMET-Program” (project InTribology1, no. 872176) via the Austrian Research Promotion Agency (FFG) and the federal states of Niederösterreich and Vorarlberg and was carried out within the “Excellence Center of Tribology” (AC2T research GmbH). The authors acknowledge the TU Wien Bibliothek for financial support through its Open Access Funding Program. We thank DI Roman Schmid and Andreas Schachner from the Austrian Federal Railways Holding Stock Company for providing ex-service material and their help in this work. We are also thankful to Iñigo Sarries (CAF, Construcciones y Auxiliar de Ferrocarriles) for useful discussion and the supply of rail wheel materials.

Funding Open access funding provided by TU Wien (TUW).

Conflict of interest On behalf of all authors, the corresponding author states that there is no conflict of interest.

Open Access This article is licensed under a Creative Commons Attribution 4.0 International License, which permits use, sharing, adaptation, distribution and reproduction in any medium or format, as long as you give appropriate credit to the original author(s) and the source,

provide a link to the Creative Commons licence, and indicate if changes were made. The images or other third party material in this article are included in the article’s Creative Commons licence, unless indicated otherwise in a credit line to the material. If material is not included in the article’s Creative Commons licence and your intended use is not permitted by statutory regulation or exceeds the permitted use, you will need to obtain permission directly from the copyright holder. To view a copy of this licence, visit <http://creativecommons.org/licenses/by/4.0/>.

References

1. X. Sauvage, A. Chbihi, X. Queleu, Severe plastic deformation and phase transformations. *J. Phys. Conf. Ser.* **240**, 012003 (2010). <https://doi.org/10.1088/1742-6596/240/1/012003>
2. A. Ekberg, B. Åkesson, E. Kabo, Wheel/rail rolling contact fatigue—Probe, predict, prevent. *Wear.* **314**(1–2), 2–12 (2014). <https://doi.org/10.1016/j.wear.2013.12.004>
3. A. Ekberg, E. Kabo, H. Andersson, An engineering model for prediction of rolling contact fatigue of railway wheels. *Fat. Frac. Eng. Mat. Struct.* **25**(10), 899–909 (2002). <https://doi.org/10.1046/j.1460-2695.2002.00535.x>
4. J. Tunna, J. Sinclair, J. Perez, A review of wheel wear and rolling contact fatigue. *Proc. Inst. Mech. Eng. Part F J. Rail Rapid Trans.* **221**(2), 271–289 (2007). <https://doi.org/10.1243/0954409JRRT72>
5. A. Hohenwarter, A. Taylor, R. Stock, R. Pippan, Effect of large shear deformations on the fracture behavior of a fully pearlitic steel. *Metall. Mat. Trans. A.* **42**(6), 1609–1618 (2011). <https://doi.org/10.1007/s11661-010-0541-7>
6. S.J. Kwon, D.H. Lee, S.T. Kwon, B.C. Goo, Failure analysis of railway wheel tread. *KEM.* **321–323**, 649–653 (2006). <https://doi.org/10.4028/www.scientific.net/KEM.321-323.649>
7. F. Walther, D. Eifler, Fatigue behaviour of railway wheels at different temperatures: Interrelation of the microstructure and the fatigue behaviour of railway wheels at ambient and elevated temperatures. *Mater. Test.* **46**(4), 158–162 (2004). <https://doi.org/10.3139/120.100576>
8. M. Faccoli, A. Ghidini, A. Mazzù, Experimental and numerical investigation of the thermal effects on railway wheels for shoe-braked high-speed train applications. *Metall. Mat. Trans. A.* **49**(10), 4544–4554 (2018). <https://doi.org/10.1007/s11661-018-4749-2>
9. D. Nikas, J. Ahlström, A. Malakizadi, Mechanical properties and fatigue behaviour of railway wheel steels as influenced by mechanical and thermal loadings. *Wear.* **366–367**, 407–415 (2016). <https://doi.org/10.1016/j.wear.2016.04.009>
10. K. Knothe, S. Liebelt, Determination of temperatures for sliding contact with applications for wheel-rail systems. *Wear.* **189**(1–2), 91–99 (1995). [https://doi.org/10.1016/0043-1648\(95\)06666-7](https://doi.org/10.1016/0043-1648(95)06666-7)
11. K. Handa, Y. Kimura, Y. Mishima, Ferrite and spheroidized cementite ultrafine microstructure formation in an Fe-0.67 Pct C steel for railway wheels under simulated service conditions. *Metall. Mat. Trans. A.* **40**(12), 2901–2908 (2009). <https://doi.org/10.1007/s11661-009-0015-y>
12. K.J. Sawley, Calculation of temperatures in a sliding wheel/rail system and implications for wheel steel development. *Proc. Inst. Mech. Eng. Part F J. Rail Rapid Trans.* **221**(4), 455–464 (2007). <https://doi.org/10.1243/0954409JRRT120>
13. J. Ahlstrom, B. Karlsson, Microstructural evaluation and interpretation of the mechanically and thermally affected zone under railway wheel flats. *Wear.* **232**(1), 1–4 (1999). [https://doi.org/10.1016/S0043-1648\(99\)00166-0](https://doi.org/10.1016/S0043-1648(99)00166-0)

14. M. Faccoli, A. Ghidini, A. Mazzù, Changes in the microstructure and mechanical properties of railway wheel steels as a result of the thermal load caused by shoe braking. *Metall. Mat. Trans. A.* **50**(4), 1701–1714 (2019). <https://doi.org/10.1007/s11661-019-05135-x>
15. O. Hajizad, A. Kumar, Z. Li, R.H. Petrov, J. Sietsma, R. Dollevoet, Influence of microstructure on mechanical properties of bainitic steels in railway applications. *Metals.* **9**(7), 778 (2019). <https://doi.org/10.3390/met9070778>
16. K. Cvetkovski, J. Ahlström, B. Karlsson, Thermal degradation of pearlitic steels: influence on mechanical properties including fatigue behaviour. *Mater. Sci. Technol.* **27**(3), 648–654 (2011). <https://doi.org/10.1179/026708310X520538>
17. P. Molyneux-Berry, C. Davis, A. Bevan, The influence of wheel/rail contact conditions on the microstructure and hardness of railway wheels. *Sci. World J.* (2014). <https://doi.org/10.1155/2014/209752>
18. K. Cvetkovski, J. Ahlström, Characterisation of plastic deformation and thermal softening of the surface layer of railway passenger wheel treads. *Wear.* **300**(1–2), 200–204 (2013). <https://doi.org/10.1016/j.wear.2013.01.094>
19. A. Al-Juboori et al., Characterisation of White Etching Layers formed on rails subjected to different traffic conditions. *Wear.* **436–437**, 202998 (2019). <https://doi.org/10.1016/j.wear.2019.202998>
20. M. Kerr, A. Wilson, S. Marich, ‘The epidemiology of squats and related rail defects’, CORE 2008: Rail; the core of integrated transport: rail. *Core Integr. Transp. Perth Railw. Tech. Soc. Australas. Eng. Aust.* (2008). <https://doi.org/10.3316/informit.564088292893778>
21. J. Takahashi, K. Kawakami, M. Ueda, Atom probe tomography analysis of the white etching layer in a rail track surface. *Acta Mater.* **58**(10), 3602–3612 (2010). <https://doi.org/10.1016/j.actamat.2010.02.030>
22. J. Wu et al., Micro and nanoscale characterization of complex multilayer-structured white etching layer in rails. *Metals.* **8**(10), 749 (2018). <https://doi.org/10.3390/met8100749>
23. S.B. Newcomb, W.M. Stobbs, A transmission electron microscopy study of the white-etching layer on a rail head. *Mater. Sci. Eng.* **66**(2), 195–204 (1984). [https://doi.org/10.1016/0025-5416\(84\)90180-0](https://doi.org/10.1016/0025-5416(84)90180-0)
24. G. Baumann, H.J. Fecht, S. Liebelt, Formation of white-etching layers on rail treads. *Wear.* **191**(1–2), 133–140 (1996). [https://doi.org/10.1016/0043-1648\(95\)06733-7](https://doi.org/10.1016/0043-1648(95)06733-7)
25. W. Österle, H. Rooch, A. Pyzalla, L. Wang, Investigation of white etching layers on rails by optical microscopy, electron microscopy, X-ray and synchrotron X-ray diffraction. *Mater. Sci. Eng., A.* **303**(1–2), 150–157 (2001). [https://doi.org/10.1016/S0921-5093\(00\)01842-6](https://doi.org/10.1016/S0921-5093(00)01842-6)
26. H.W. Zhang, S. Ohsaki, S. Mitao, M. Ohnuma, K. Hono, Microstructural investigation of white etching layer on pearlite steel rail. *Mater. Sci. Eng., A.* **421**(1–2), 191–199 (2006). <https://doi.org/10.1016/j.msea.2006.01.033>
27. A. Al-Juboori et al., Squat formation and the occurrence of two distinct classes of white etching layer on the surface of rail steel. *Int. J. Fatigue.* **104**, 52–60 (2017). <https://doi.org/10.1016/j.ijfatigue.2017.07.005>
28. M. Freisinger et al., Comparative study on the influence of initial deformation and temperature of thermally induced white etching layers on rail wheels. *Tribol. Int.* **177**, 107990 (2023). <https://doi.org/10.1016/j.triboint.2022.107990>
29. W. Lojkowski, M. Djahanbakhsh, G. Bürkle, S. Gierlotka, W. Zielinski, H.-J. Fecht, Nanostructure formation on the surface of railway tracks. *Mater. Sci. Eng., A.* **303**(1–2), 197–208 (2001). [https://doi.org/10.1016/S0921-5093\(00\)01947-X](https://doi.org/10.1016/S0921-5093(00)01947-X)
30. L. Wang, A. Pyzalla, W. Stadlbauer, E.A. Werner, Microstructure features on rolling surfaces of railway rails subjected to heavy loading. *Mater. Sci. Eng., A.* **359**(1–2), 31–43 (2003). [https://doi.org/10.1016/S0921-5093\(03\)00327-7](https://doi.org/10.1016/S0921-5093(03)00327-7)
31. A. Pyzalla, L. Wang, E. Wild, T. Wroblewski, Changes in microstructure, texture and residual stresses on the surface of a rail resulting from friction and wear. *Wear.* **251**(1–12), 901–907 (2001). [https://doi.org/10.1016/S0043-1648\(01\)00748-7](https://doi.org/10.1016/S0043-1648(01)00748-7)
32. R. Lewis et al., Mapping railway wheel material wear mechanisms and transitions. *Proc. Inst. Mech. Eng. Part F J. Rail Rapid Trans.* **224**(3), 125–137 (2010). <https://doi.org/10.1243/09544097JRR328>
33. D. Zeng, L. Lu, Y. Gong, Y. Zhang, J. Zhang, Influence of solid solution strengthening on spalling behavior of railway wheel steel. *Wear.* **372–373**, 158–168 (2017). <https://doi.org/10.1016/j.wear.2016.12.025>
34. J. Jergéus, C. Odenmarck, R. Lundén, P. Sotkovszki, B. Karlsson, P. Gullers, Full-scale railway wheel flat experiments. *Proc. Inst. Mech. Eng. Part F J. Rail Rapid Trans.* **213**(1), 1–13 (1999). <https://doi.org/10.1243/0954409991530985>
35. A. Kumar, G. Agarwal, R. Petrov, S. Goto, J. Sietsma, M. Herbig, Microstructural evolution of white and brown etching layers in pearlitic rail steels. *Acta Mater.* **171**, 48–64 (2019). <https://doi.org/10.1016/j.actamat.2019.04.012>
36. S. Li, J. Wu, R.H. Petrov, Z. Li, R. Dollevoet, J. Sietsma, Brown etching layer: a possible new insight into the crack initiation of rolling contact fatigue in rail steels? *Eng. Fail. Anal.* **66**, 8–18 (2016). <https://doi.org/10.1016/j.engfailanal.2016.03.019>
37. M. Messaadi, M. Steenbergen, Stratified surface layers on rails. *Wear.* **414–415**, 151–162 (2018). <https://doi.org/10.1016/j.wear.2018.07.019>
38. P.-Y. Tung, X. Zhou, L. Morsdorf, M. Herbig, Formation mechanism of brown etching layers in pearlitic rail steel. *Materialia.* **26**, 101625 (2022). <https://doi.org/10.1016/j.mtla.2022.101625>
39. ‘EN 13262:2004+A2:2011: Railway applications - Wheelsets and bogies-Wheels-Product requirements
40. M. Diener, A. Ghidini, Fracture toughness: a quality index for railway solid wheels. *Mats. Perf. Charact.* **3**(3), 20130047 (2014). <https://doi.org/10.1520/MPC20130047>
41. R. Deuce, Wheel tread damage-an elementary guide, Bombardier Transportation GmbH, Netphen, Germany, Technical Report, (2007)
42. W.C. Oliver, G.M. Pharr, An improved technique for determining hardness and elastic modulus using load and displacement sensing indentation experiments. *J. Mater. Res.* **7**(6), 1564–1583 (1992). <https://doi.org/10.1557/JMR.1992.1564>
43. J. Dearden, The wear of steel rails and tyres in railway service. *Wear.* **3**(1), 43–59 (1960). [https://doi.org/10.1016/0043-1648\(60\)90174-5](https://doi.org/10.1016/0043-1648(60)90174-5)
44. Z. Ławrynowicz, Plastic deformation and softening of the surface layer of railway wheel. *Adv. Mater. Sci.* **15**(4), 5–13 (2015). <https://doi.org/10.1515/adms-2015-0018>
45. B. Gao et al., Influence of non-uniform microstructure on rolling contact fatigue behavior of high-speed wheel steels. *Eng. Fail. Anal.* **100**, 485–491 (2019). <https://doi.org/10.1016/j.engfailanal.2019.03.002>
46. T. Vernersson, S. Caprioli, E. Kabo, H. Hansson, A. Ekberg, Wheel tread damage: a numerical study of railway wheel tread plasticity under thermomechanical loading. *Proc. Inst. Mech. Eng. Part F J. Rail Rapid Trans.* **224**(5), 435–443 (2010). <https://doi.org/10.1243/09544097JRR328>

47. A. Kumar et al., In situ study on fracture behaviour of white etching layers formed on rails. *Acta Mater.* **180**, 60–72 (2019). <https://doi.org/10.1016/j.actamat.2019.08.060>
48. M. Freisinger, L. Zauner, R. Hahn, H. Riedl, P.H. Mayrhofer, In-situ micro-cantilever bending studies of a white etching layer thermally induced on rail wheels. *Mater. Sci. Eng. A.* **869**, 144805 (2023). <https://doi.org/10.1016/j.msea.2023.144805>
49. Y. Zhou, J.F. Peng, W.J. Wang, X.S. Jin, M.H. Zhu, Slippage effect on rolling contact wear and damage behavior of pearlitic steels. *Wear.* **362–363**, 78–86 (2016). <https://doi.org/10.1016/j.wear.2016.05.001>
50. W.T. Zhu et al., Wear and damage transitions of two kinds of wheel materials in the rolling-sliding contact. *Wear.* **398–399**, 79–89 (2018). <https://doi.org/10.1016/j.wear.2017.11.023>
51. C.G. He et al., On the microstructure evolution and nanocrystalline formation of pearlitic wheel material in a rolling-sliding contact. *Mater. Charact.* **164**, 110333 (2020). <https://doi.org/10.1016/j.matchar.2020.110333>
52. Y. Hu et al., Microstructure evolution of railway pearlitic wheel steels under rolling-sliding contact loading. *Tribol. Int.* **154**, 106685 (2021). <https://doi.org/10.1016/j.triboint.2020.106685>
53. J. Hua, X. Zhao, P. Liu, J. Pan, C. Su, R. Ren, Study on the mechanism for polygonisation formation of D2 wheel steel and its effect on microstructure and properties under rolling wear conditions. *Wear.* **450–451**, 203261 (2020). <https://doi.org/10.1016/j.wear.2020.203261>
54. Y. Hu et al., Effect of rolling direction on microstructure evolution of CL60 wheel steel. *Wear.* **424–425**, 203–215 (2019). <https://doi.org/10.1016/j.wear.2019.02.022>
55. J. Hua et al., EBSD Study on proeutectoid ferrite and eutectoid ferrite refinement mechanism of D2 wheel steel under a rolling condition. *Tribol. Lett.* **69**(4), 148 (2021). <https://doi.org/10.1007/s11249-021-01527-6>
56. C. Liu, R. Ren, D. Liu, X. Zhao, C. Chen, An EBSD investigation on the evolution of the surface microstructure of D2 wheel steel during rolling contact fatigue. *Tribol. Lett.* **68**(1), 47 (2020). <https://doi.org/10.1007/s11249-020-1277-1>
57. L. Ma et al., Study on wear and rolling contact fatigue behaviors of wheel/rail materials under different slip ratio conditions. *Wear.* **366–367**, 13–26 (2016). <https://doi.org/10.1016/j.wear.2016.04.028>
58. G. Donzella, M. Faccoli, A. Mazzù, C. Petrogalli, R. Roberti, Progressive damage assessment in the near-surface layer of railway wheel–rail couple under cyclic contact. *Wear.* **271**(1–2), 408–416 (2011). <https://doi.org/10.1016/j.wear.2010.10.042>
59. C.G. He et al., Experimental investigation on the effect of tangential force on wear and rolling contact fatigue behaviors of wheel material. *Tribol. Int.* **92**, 307–316 (2015). <https://doi.org/10.1016/j.triboint.2015.07.012>
60. T. Kato, Effect of elevated temperature on shelling property of railway wheel steel. *Wear.* **266–267**, 359–367 (2016). <https://doi.org/10.1016/j.wear.2016.04.015>
61. D.F.C. Peixoto, P.M.S.T. de Castro, Fatigue crack growth of a railway wheel. *Eng. Fail. Anal.* **82**, 420–434 (2017). <https://doi.org/10.1016/j.engfailanal.2017.07.036>

Publisher's Note Springer Nature remains neutral with regard to jurisdictional claims in published maps and institutional affiliations.

Publication II



Influence of the evolution of near-surface rail wheel microstructure on
crack initiation by micro-bending investigations

M. Freisinger, A. Trausmuth, R. Hahn, E. Badisch
Journal of Rail and Rapid Transit, published online (2023)
DOI: 10.1177/09544097231191550

Influence of the evolution of near-surface rail wheel microstructure on crack initiation by micro-bending investigations

Proc IMechE Part F:
J Rail and Rapid Transit
2023, Vol. 0(0) 1–7
© IMechE 2023
Article reuse guidelines:
sagepub.com/journals-permissions
DOI: 10.1177/09544097231191550
journals.sagepub.com/home/pif


Matthias Freisinger^{1,2} , Andreas Trausmuth¹, Rainer Hahn³  and Ewald Badisch³

Abstract

Severe mechanical and thermal loadings, as well as the corrosive environment change the near-surface microstructure of rail wheels during service. Resulting severely plastically deformed (SPD) and corrosion affected microstructures are prone to influence crack initiation along the wheel tread. To evaluate the crack initiation and fracture behaviour, the *in-situ* micro-bending method is first applied on rail wheel samples from field within this work. Results reveal detailed insights in material behaviour of SPD microstructures, where the conducted micro-bending investigations point out predominant plastic behaviour without cracks initiated at the artificial notch of the micro-cantilevers during bending. In contrast, micro-bending investigations in microstructural regions with increased oxygen and silicon composition show crack initiation, fracture, and low maximum stress levels (approximately one seventh of the SPD microstructure). The presented study underlines the increased risk of crack initiation in corrosion affected regions by a novel testing method in this field with high spatial resolution and acknowledge the importance of periodic reprofiling of the rail wheels in service.

Keywords

Railway wheel, severe plastic deformation, corrosion, micro-bending

Date received: 7 March 2023; accepted: 15 July 2023

Introduction

The integrity of the wheel material is a major contributor to railway network safety and costs. Due to severe mechanical and thermal loadings in service, the near-surface wheel microstructure is changing to a severely plastically deformed (SPD) microstructure.^{1–6} Besides continuous wear leading to the degradation of the rail wheel material, crack initiation within the near-surface SPD microstructure can lead to fatigue crack growth at certain conditions.^{7–11} Furthermore, corrosion occurring due to the environmental influences on the rail wheels in service can also act as crack initiation sites.^{12–14} Initiated at non-metallic inclusions or pits creating spalling along the tread surface,¹⁵ the formation of oxides changes mechanical properties such as strength, plasticity, and wear resistance.¹⁶ In addition, corrosion pits act as a stress concentration factor.^{17,18} Although pitting and fatigue crack growth are independent processes, a certain degree of interaction is evident, making it difficult to describe the crack initiation in a holistic view.¹⁵

Due to the small scale of microstructural characteristics of near-surface evolution in rail-wheel contacts, standard mechanical testing methods are often inapplicable due to size limitation criteria.¹⁹ Investigations on crack propagation behavior of SPD pearlitic steel processed by high pressure torsion (HPT) have been conducted by Leitner et al.^{20,21} with compact tension specimens with a thickness of 1.3 mm. Specimen from field often reveal smaller

dimensions, therefore, the focus ion beam (FIB) technique enables testing with higher spatial resolution. Developments of micro-mechanical testing methods in the last decades focused on brittle materials such as hard coatings.^{22–24} However, in recent years efforts have been made to conduct micro-mechanical testing methods on materials with a certain degree of plasticity.^{25,26} Regarding the evaluation of fracture behaviour and toughness, the micro-bending method is a promising testing method for rail and wheel materials in recent years.^{27–29} Recently published work of the author demonstrates the applicability of the presented micro-bending testing method for the evaluation of evolved martensitic microstructures in wheel-rail contacts, imitated in laboratory.²⁹

Within this work, other characteristic local microstructures occurring in wheel-rail contacts are investigated, namely SPD and corrosion affected microstructures, by applying micro-bending tests to show the potential of this method in testing local evolved microstructures of field

¹AC2T research GmbH, Wiener Neustadt, Austria

²Institute of Materials Science and Technology, Wien, Austria

³Christian Doppler Laboratory for Surface Engineering of High-performance Components, Wien, Austria

Corresponding author:

Matthias Freisinger, AC2T research GmbH, Viktor Kaplan Straße 2/C, Wiener Neustadt 2700, Austria.

Email: matthias.freisinger@ac2t.at

samples. The aim is to point out differences of structural integrity within SPD microstructures with different intended crack directions and within corrosion affected microstructural regions to enhance the understanding of material behavior in near-surface microstructures of rail wheel samples from field.

Materials and methods

A rail wheel, nearly 200,000 km in service (steel grade ER7)³⁰, was provided by the Austrian Federal Railways (ÖBB). The wheel material has a Brinell hardness >235 HB and a fracture toughness between 40 and 80 MPa m^{1/2}. The upper yield strength R_{eH} is ≥ 520 MPa, the tensile strength R_m between 820 and 940 MPa, and the fracture tension $A_5 \geq 14\%$. The chemical composition is given in Table 1. A slice was cut out of the wheel with a bandsaw, followed by cutting samples out of the middle of the tread surface for microscopic and micro-bending investigations using a laboratory cutting device (Struers Disotom-50; Struers ApS, Denmark). Cross-sectional cuts were embedded in conductive compounds and prepared by coarse grinding, 1 μ m diamond fine polishing, and etching with ethanolic nitric acid (3% HNO₃, 97% ethanol).

The microstructure was studied by light optical microscopy (LOM) Axio Imager M2m, Carl Zeiss AG, Germany) and scanning electron microscopy ((SEM) Jeol JIB 4700F, Jeol Ltd., Japan). Chemical analysis was done by energy dispersive X-ray (EDX) analysis performed with an X-flash 6|30 detector (Bruker Corp., USA) to identify specific areas of interest.

For the *in-situ* micro-bending investigations (Figure 1(a)), cubic samples (5 × 5 × 5 mm) were cut out of the middle of the tread surface. FIB milling created 10 cantilevers with a rectangular cross-section on the sample edges with different notch directions: Cantilevers C1–C6 were prepared with notch direction in rolling direction

Table 1. Maximum percentages of elements for ER7 according to the standard EN13262.³⁰

C	Si	Mn	P	S	Cr	Cu	Mo	Ni	V
[wt%]									
0.52	0.40	0.80	0.020	0.015	0.30	0.30	0.08	0.30	0.06

(RD), in contrast to cantilevers C7–C10 with a notch orientation in normal direction (ND) (Figure 1(b)). A Quanta 200 3D dual beam system (ThermoScientific, USA), a FIB system combined with an SEM, was used to manufacture the micro-cantilevers. Two prepared cubic ER7 samples were mounted on a custom-made sample holder and arranged in two directions regarding the different notch directions. The two-pin sample holder allows rotating the samples by 90°C; consequently, material sputtering from two perpendicular directions is possible. A region near the horizontal cube edge was smoothed with the Ga⁺ ion beam under grazing ion incidence to remove damaged material from the preparation. The coarse milling steps were performed with 20 nA and 7 nA ion beam current on both sides near the cube edge, resulting in three about 70 μ m long microbeams for each cube. Each microbeam was divided into two cantilevers by removing material in the centre of the microbeam. A significantly large amount of material around the microbeams was removed at the coarse milling steps to avoid material redeposition to the cantilevers during the fine milling steps. All fine milling steps were carried out with 1 nA ion beam current. The tapering angle was corrected by overtilting the sample $\pm 2^\circ$ with regard to the ion beam incidence direction to obtain nearly square-shaped cantilever cross-sections. First, the surfaces normal to the loading direction were ion beam polished on each cantilever. In a second step, the notch was produced, defining a nominally 100 nm wide milling area, with 50 pA ion beam current, resulting in an approximately 200 nm wide and 1.5 μ m deep (a) wedge-shaped trench, extending over the whole width of the completed cantilever. Finally, the cantilever surfaces parallel to the loading direction were polished, whereas milling artefacts from notch milling were removed from the side walls as an ancillary effect. The geometrical dimensions of the cantilevers, their notch direction and the microstructural region are given in Table 2. Region I represents a corrosion unaffected microstructure, in contrast to region III. Further, cantilevers situated in region II show a mixture of corrosion unaffected microstructure and oxidized microstructure.

The micromechanical bending experiments were performed in a FEI Quanta 250 FEGSEM (FEI, USA) equipped with a FemtoTools FT-NMT04 (FemtoTools, Suisse) displacement-controlled *in-situ* indenter (Figure 1(c)). The system is equipped with a 20 mN force

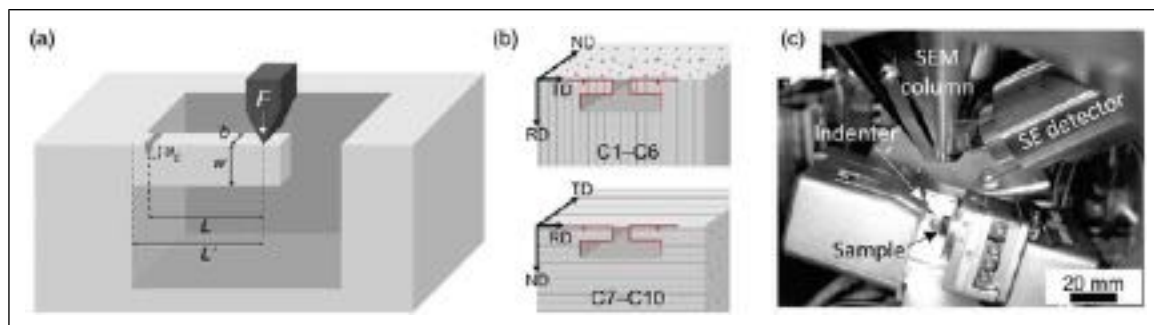


Figure 1. The schematic overview of the *in-situ* micro-bending method conducted on the wheel microstructures (a) shows the geometrical parameters and the point of loading. The arrangement of the cantilevers with different notch direction on two cubic samples extracted from the rail wheel is schematically shown in (b). The set-up in the SEM chamber is given in (c).

sensor having a noise floor $<0.05 \mu\text{N}$. The experiments were performed in CSM indentation mode (using an overlaid frequency of 20 Hz and displacement of 5 nm), enabling the constant measure of the stiffness of the cantilevers while performing the experiment. The overall displacement rate was set to $10 \text{ nm}\cdot\text{s}^{-1}$, and the maximum depth was limited by the 60°C diamond wedge used for indentation.

Results and discussion

The macroscopic appearance of the investigated ER7 wheel from service shows a worn and rough tread surface with corroded regions randomly distributed (Figure 2(a)). The microstructure in the cross-sectional cut (Figure 2(b)) shows the evolution of the near-surface microstructure due to the service conditions: Within around $200 \mu\text{m}$ from surface in depth, an SPD microstructure with very fine grains aligned under a certain angle to the surface can be seen, further, cracks propagating along the alignment

direction. With increasing distance from the surface, grain size increases gradually. In the “transition zone” ($200 - 400 \mu\text{m}$ from the surface in depth) the microstructure consists of lengthened ferrite and pearlite grains with a certain degree of alignment parallel to the surface. In a depth of $400 - 500 \mu\text{m}$, the microstructure passes over to the initial bulk microstructure of the rail wheel without significant mechanical or thermal influences from service.

Along the surface, numerous pits of various sizes and shapes can be detected in the cross-sectional cuts, presumably created by spalling and pitting corrosion (Figure 2(c)). Cracks are initiated outside and within some pits, propagating mainly along the alignment of the SPD microstructure.

The results of the micro-bending investigations to evaluate crack initiation and fracture behavior of distinctive microstructural regions, namely corrosion unaffected microstructure and corrosion affected regions are shown in Figure 3. The corrosion unaffected microstructure is called region I, a representative micro-cantilever before testing is

Table 2. Details for the conducted micro-bending experiments. Cantilevers C1–6 are prepared with notch directed in rolling direction (RD), C7–10 are built with notch direction in normal direction (ND). Cantilevers are situated in SPD microstructure without corroded areas (region I), in corrosion affected areas (region III) and in mixed microstructures (region II).

Cantilever	Notch direction	L'	L	b	w	a_0	Region
		μm					
C1	RD	30.4	20.1	5.63	5.76	0.97	I
C2	RD	31.7	20.5	5.73	5.76	0.89	II
C3	RD	29.7	19.8	5.63	5.76	1.48	II
C4	RD	32.3	19.9	5.73	5.77	1.23	III
C5	RD	30.3	19.9	5.85	5.76	1.45	I
C6	RD	31.5	20.2	6.12	5.76	0.96	III
C7	ND	29.1	22.0	5.25	6.30	1.26	I
C8	ND	32.5	19.8	5.47	6.31	1.33	I
C9	ND	30.2	19.7	5.85	5.96	1.37	I
C10	ND	29.7	20.1	6.02	5.96	1.36	I

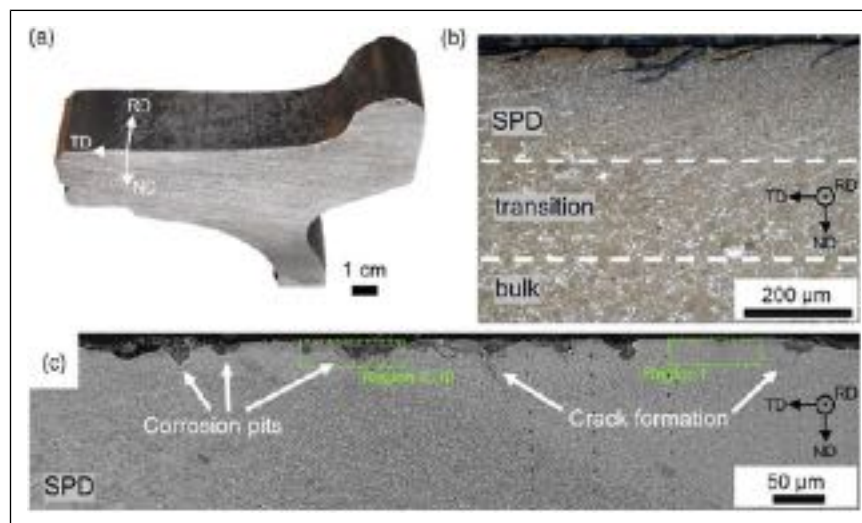


Figure 2. The cut slice of the ER7 wheel after $\sim 200,000 \text{ km}$ in service (a) shows a corrosion affected tread surface. The cross-sectional cut in rolling direction (RD) (b) reveals an SPD zone with numerous cracks, followed by a transition zone and a bulk microstructure. SEM investigations (c) show the corrosion pits along the surface of the wheel, with cracks initiated at some pits. The regions I, II and III where the cantilevers for the micro-bending were prepared are indicated. Within region I, cantilevers with notch orientation in rolling direction (RD) and cantilevers with notch orientation normal to the rolling direction (ND) are prepared.

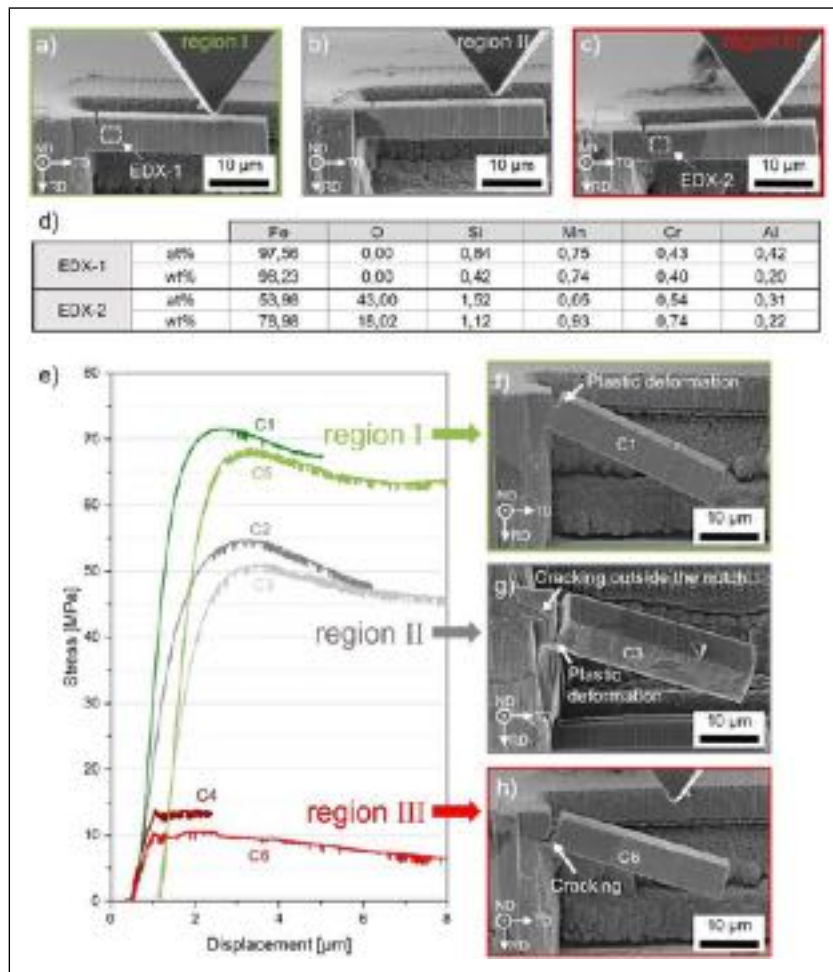


Figure 3. Representative micro-cantilevers before and after the micro-bending are shown: region I ((a), (f)) is the corrosion unaffected SPD microstructure, region II ((b), (g)) represents a mixture of corrosion influence and SPD microstructure, and region III ((c), (h)) represents cantilevers with the artificial notch located within corrosion affected microstructures. The chemical differences of “region I” and region III is given by EDX analysis in (d). Stress-displacement graphs of all cantilevers prepared with notch direction in rolling direction (C1–C6) are plotted in (e), where significant differences for each region can be seen.

shown in Figure 3(a). The results of the EDX analysis for region I (EDX-1) reveal iron, silicon, manganese, and chromium amounts according to the standard (Table 1) with no detected oxygen (Figure 3(d)). The corresponding stress-displacement curve (Figure 3(e)) shows an elastic behavior at the beginning going over to a plastic behavior at ~ 50 MPa, coming up with a maximum stress level between ~ 68 and ~ 71 MPa. The plastic behavior can be seen *in-situ* during the experiments by significant plastic flow at the sides of the cantilevers and no detectable crack initiation. A representative image of the micro-cantilever after testing is shown in Figure 3(f).

In contrast, micro-cantilevers prepared in corrosion-affected regions (region III) come up with different microstructural characteristics around the artificial notch (Figure 3(c)). The dark appearing, porous microstructure is indicated by EDX analysis (EDX-2) as oxidized microstructure, with a significant amount of oxygen and an increase in silicon. When executing the micro-bending, the stress-displacement curve shows a different behavior to the cantilever tested in region I (Figure 3(e)): No significant plastic behavior can be seen after the elastic contribution. An abrupt stop of the increase of the stress at a maximum

between 10 and 15 MPa indicates crack initiation and propagation. Post-testing SEM investigations nicely show crack initiation at the artificial notch and fracture of the cantilevers (Figure 3(h)).

Two cantilevers tested were situated with the notch surrounded by a mixture of bright and dark-appearing regions (region II), an exemplary SEM image is shown in Figure 3(c). The characteristics of the stress-displacement graphs show somewhat similarities to those from the corrosion unaffected cantilevers, but with lower maximum stress values between 50 and 55 MPa (Figure 3(e)). SEM observations reveal purely plastic deformation in the bright appearing (corrosion-unaffected) areas but crack initiation and propagation in the dark appearing (oxidized) area, even outside the artificial notch (Figure 3(g)).

To investigate the influence of the alignment of the SPD microstructure on crack initiation and propagation the results of the micro-bending investigation with different cantilever orientations are presented in Figure 4. Figure 4(a) shows the stress-displacement graphs of the tested cantilevers C1 and C5 in region I with notch direction in rolling direction (RD). In addition, Figure 4(b) gives an image of a cross-sectional FIB cut of the micro-cantilever C5 after

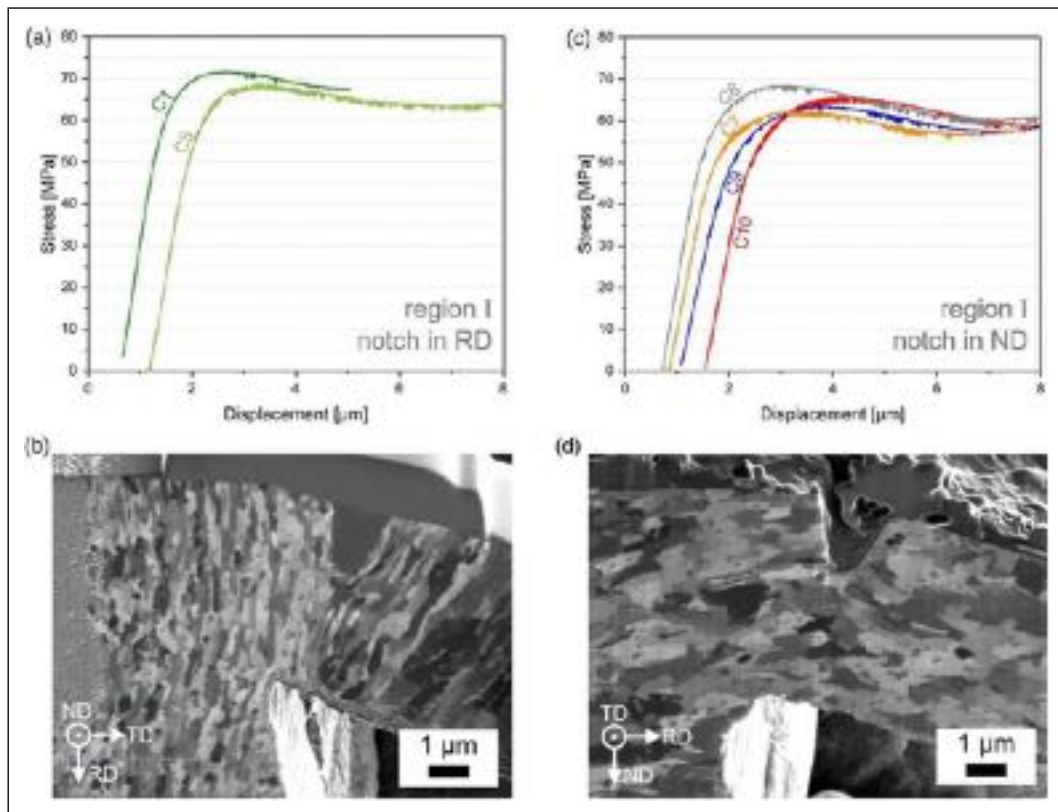


Figure 4. The stress-displacement graphs of the micro-bending investigations in the SPD microstructure with different directions of the artificial notch: Notch normal to the rolling direction is given in (a), a representative ICC image showing the alignment of the grains and the plastic material behavior can be seen in (c). Stress-displacement curves and ICC image of the cantilevers with the notch orientation in rolling direction are given in (b) and (d).

testing to identify grain orientation within the tested cantilever. The ion channelling contrast (ICC) image shows the fine-grained microstructure aligned in the rolling direction. The plasticity of the material is demonstrated by the blunting of the artificially created notch, no crack is initiated. Results of the micro-bending tests for the cantilevers prepared with notch direction normal to the rolling direction (ND) in corrosion-unaaffected microstructure (region I) are given in Figure 4(c). A corresponding ICC image of the cross-sectional cut of cantilever C8 is shown in Figure 4(d) with grains orientated normal to the artificial notch. Extensive plastic behaviour demonstrated by a predominant blunting of the notch can be detected, further, no crack is initiated during testing. Results show no significant differences for the cantilevers with notch orientation in RD and in ND, for all tested cantilevers in region I an elastic behavior at the beginning going over to a plastic behavior at ~ 50 MPa can be observed. The deviation of the tested cantilevers is low, coming up with a maximum stress level between ~ 72 and ~ 62 MPa.

Plastic flow at the sides of all tested cantilevers and the lack of crack initiation indicates predominant plastic behavior during bending. The results point out the predominant plastic behavior of SPD microstructures in a wheel-rail contact. However, the crack propagation rate and presumable differences for different directions with respect to the alignment of the grains cannot be identified in this work due to the lack of crack initiation at the notch.

Nevertheless, the *in-situ* micro-bending investigations presented show the potential of using micro-sized samples to evaluate mechanical behavior qualitatively or quantitatively. Because the experiment is conducted inside the SEM, an *in-situ* evaluation of the material behavior is possible improving the knowledge of material behavior in small scales. Advanced SEM possibilities can be used to characterize the tested microstructure, as instance post-testing FIB cross-sectional cuts and ICC images presented in this study. However, there are challenges in testing micro-scale structures, especially when it comes to plasticity.^{25,31,32} The micro-bending method executed on the corrosion-unaaffected SPD samples (with significant plastic material behavior) show no crack initiation at the artificial notch (Figure 3(f), 4). A possible reason can be the geometry of the notch,³³ where a sharper notch may lead to a crack formation, constituting potential for future investigations. When a crack is initiated, a faster crack propagation in rolling direction along the microstructural alignment would be expected, as presented in previous works on HPT samples.²⁰ In contrast to the lack of crack initiation for the SPD samples, cracks are initiated in region II and III, where corrosion has led to a more brittle material behavior (Figure 3(g) and (h)). The crack propagation and fracture at low stress maxima in comparison to cantilevers in region I clearly outpoints the increased risk of crack formation when corrosion occurs (Figure 3(e)). When analysing the bent cantilevers in region II in detail, cracks

commonly propagated within the boundary of corrosion unaffected SPD and the microstructural region with increased oxygen composition, in some cases the crack stopped when propagating in the corrosion-unaffected more ductile microstructure. EDX analysis of the corrosion affected microstructure within this study reveals beside iron oxide a significant increase in silicon. Its origin is assumed due to the use of SiO₂ sand to increase friction during braking.³⁴ Due to the high spatial resolution of the micro-bending method in combination of local variations of the microstructure on field samples, a reasonable comprise between the complex FIB preparation of the cantilevers and sufficient statistical representativeness must be taken into account. Based on experiments of existing literature^{27,28} and low scattering of the results within region I, II and III, the results within this work give an appropriate approach.

Conclusions

This work presents the first *in-situ* micro-bending investigations on near-surface microstructures of rail wheels from field. The micro-bending method is conducted in regions potentially prone to crack initiation: SPD and corrosion affected microstructures. These main conclusions can be stated:

- Micro-bending investigations on cantilevers in the corrosion unaffected SPD microstructure outpost predominant plastic material behavior with maximum stresses of 70 MPa and no crack initiation.
- Cantilevers in SPD microstructures with notch direction orientated normal to the aligned microstructure and parallel to the rolling direction show no differences in regard of plastic behavior, crack propagation cannot be evaluated to the miss of crack initiation.
- In contrast, micro-bending investigations in corrosion affected regions (with increased oxygen and silicon content) show more brittle material behavior. The maximum stress levels are one seventh of the SPD microstructure, cracks are initiated in the artificial notch and fracture of the micro-cantilever occurs.
- Results point out the increased risk of crack initiation and propagation in corrosion-affected microstructures, which underlines the corrosive destruction in service and the importance of anticorrosion measures at the storage and transportation of rail wheels.

Acknowledgements

This project has received funding from the Shift2Rail Joint Undertaking (JU) under grant agreement No. 826255 and No. 101012456. The JU receives support from the European Union's Horizon 2020 research and innovation programme and the Shift2Rail JU members other than the Union. In addition, this work was funded by the "Austrian COMET-Program" (project InTribology1, no. 872176) via the Austrian Research Promotion Agency (FFG) and the federal states of Niederösterreich and Vorarlberg and was carried out within the "Excellence Centre of Tribology" (AC2T research GmbH). The financial support by the Austrian Federal Ministry for Digital and Economic Affairs, the National Foundation for Research, Technology and Development,

and the Christian Doppler Research Association is gratefully acknowledged (Christian Doppler Laboratory "Surface Engineering of high-performance Components"). We would like to express our gratitude to Mr. Schachner (ÖBB TS Knittelfeld) for providing rail wheel from field. We are also thankful to Mr. Sarries (CAF, Construcciones y Auxiliar de Ferrocarriles) for useful discussion and the supply of rail wheel materials. The authors acknowledge the TU Wien Bibliothek for financial support through its Open Access Funding Program.



Declaration of conflicting interests

The authors declare that they have no known competing financial interests or personal relationships that could have appeared to influence the work reported in this paper.

Funding

The author(s) disclosed receipt of the following financial support for the research, authorship, and/or publication of this article: This work was supported by the Shift2Rail Joint Undertaking (101012456, 826255), Austrian COMET-Program (872176).

ORCID iDs

Matthias Freisinger  <https://orcid.org/0000-0001-9616-4613>
Rainer Hahn  <https://orcid.org/0000-0002-7322-8108>

References

1. Vernersson T and Lundén R. Temperatures at railway tread braking. Part 3: wheel and block temperatures and the influence of rail chill. *Proceedings of the Institution of Mechanical Engineers, Part F: Journal of Rail and Rapid Transit* 2007; 221(4): 443–454. DOI: [10.1243/09544097JRRT91](https://doi.org/10.1243/09544097JRRT91).
2. Ekberg A and Kabo E. Fatigue of railway wheels and rails under rolling contact and thermal loading—an overview. *Wear* 2005; 258(7–8): 1288–1300. DOI: [10.1016/j.wear.2004.03.039](https://doi.org/10.1016/j.wear.2004.03.039).
3. Tunna J, Sinclair J and Perez J. A Review of wheel wear and rolling contact fatigue. *Proceedings of the Institution of Mechanical Engineers, Part F: Journal of Rail and Rapid Transit* 2007; 221(2): 271–289. DOI: [10.1243/09544097JRRT72](https://doi.org/10.1243/09544097JRRT72).
4. Ahlstrom J and Karlsson B. Microstructural evaluation and interpretation of the mechanically and thermally affected zone under railway wheel flats. *Wear* 1999; 232(1): 1–14.
5. Sauvage X, Chbihi A and Quelebec X. Severe plastic deformation and phase transformations. *J. Phys.: Conf. Ser* 2010; 240: 012003. DOI: [10.1088/1742-6596/240/1/012003](https://doi.org/10.1088/1742-6596/240/1/012003).
6. Grassie SL. Squats and squat-type defects in rails: the understanding to date. *Proceedings of the Institution of Mechanical Engineers, Part F: Journal of Rail and Rapid Transit* 2012; 226(3): 235–242. DOI: [10.1177/0954409711422189](https://doi.org/10.1177/0954409711422189).
7. Donzella G, Mazzù A and Petrogalli C. Competition between wear and rolling contact fatigue at the wheel—rail interface: some experimental evidence on rail steel. *Proceedings of the Institution of Mechanical Engineers, Part F: Journal of Rail and Rapid Transit* 2009; 223(1): 31–44. DOI: [10.1243/09544097JRRT161](https://doi.org/10.1243/09544097JRRT161).

8. Lyu K. Analysis on the features and potential causes of wheel surface damage for heavy-haul locomotives. *Engineering Failure Analysis* 2020; 109: 104292. DOI: [10.1016/j.engfailanal.2019.104292](https://doi.org/10.1016/j.engfailanal.2019.104292).
9. Peixoto DFC and de Castro PMST. Fatigue crack growth of a railway wheel. *Engineering Failure Analysis* 2017; 82: 420–434. DOI: [10.1016/j.engfailanal.2017.07.036](https://doi.org/10.1016/j.engfailanal.2017.07.036).
10. Liu Y, Stratman B and Mahadevan S. Fatigue crack initiation life prediction of railroad wheels. *International Journal of Fatigue* 2006; 28(7): 747–756. DOI: [10.1016/j.ijfatigue.2005.09.007](https://doi.org/10.1016/j.ijfatigue.2005.09.007).
11. Zucarelli TA, Vieira MA, Moreira Filho LA, et al. Failure analysis in railway wheels. *Procedia Structural Integrity* 2016; 1: 212–217. DOI: [10.1016/j.prostr.2016.02.029](https://doi.org/10.1016/j.prostr.2016.02.029).
12. Fatoba O and Akid R. On the behaviour of small fatigue cracks emanating from corrosion pits: Part I – The influence of mechanical factors. *Theoretical and Applied Fracture Mechanics* 2022; 117: 103154. DOI: [10.1016/j.tafmec.2021.103154](https://doi.org/10.1016/j.tafmec.2021.103154).
13. Mansor NII, Abdullah S, Ariffin AK, et al. A review of the fatigue failure mechanism of metallic materials under a corroded environment. *Engineering Failure Analysis* 2014; 42: 353–365. DOI: [10.1016/j.engfailanal.2014.04.016](https://doi.org/10.1016/j.engfailanal.2014.04.016).
14. Ren X, Wu F, Xiao F, et al. Corrosion induced fatigue failure of railway wheels. *Engineering Failure Analysis* 2015; 55: 300–316. DOI: [10.1016/j.engfailanal.2015.06.009](https://doi.org/10.1016/j.engfailanal.2015.06.009).
15. Zerbst U, Madia M, Klinger C, et al. Defects as a root cause of fatigue failure of metallic components. III: Cavities, dents, corrosion pits, scratches. *Engineering Failure Analysis* 2019; 97: 759–776. DOI: [10.1016/j.engfailanal.2019.01.034](https://doi.org/10.1016/j.engfailanal.2019.01.034).
16. Moon AP. Corrosion behavior of newly developed high-strength bainitic railway wheel steels. *Journal of Materials Engineering and Performance* 2020; 29: 3443–3459.
17. Cerit M, Genel K and Eksi S. Numerical investigation on stress concentration of corrosion pit. *Engineering Failure Analysis* 2009; 16(7): 2467–2472. DOI: [10.1016/j.engfailanal.2009.04.004](https://doi.org/10.1016/j.engfailanal.2009.04.004).
18. Fantecelle Strey N, Bavaresco Rezende A, da Silva Miranda R, et al. Comparison of rolling contact fatigue damage between railway wheels and twin-disc test specimens. *Tribology International* 2021; 160: 107037. DOI: [10.1016/j.triboint.2021.107037](https://doi.org/10.1016/j.triboint.2021.107037).
19. Diener M and Ghidini A. Fracture toughness: a quality index for railway solid wheels. *Mats. Perf. Charact* 2014; 3(3): 20130047. DOI: [10.1520/MPC20130047](https://doi.org/10.1520/MPC20130047).
20. Leitner T, Trummer G, Pippin R, et al. Influence of severe plastic deformation and specimen orientation on the fatigue crack propagation behavior of a pearlitic steel. *Materials Science and Engineering: A* 2018; 710: 260–270. DOI: [10.1016/j.msea.2017.10.040](https://doi.org/10.1016/j.msea.2017.10.040).
21. Leitner T, Hohenwarter A, Ochensberger W, et al. Fatigue crack growth anisotropy in ultrafine-grained iron. *Acta Materialia* 2017; 126: 154–165. DOI: [10.1016/j.actamat.2016.12.059](https://doi.org/10.1016/j.actamat.2016.12.059).
22. Pippin R, Wurster S and Kiener D. Fracture mechanics of micro samples: Fundamental considerations. *Materials and Design* 2018; 159: 252–267. DOI: [10.1016/j.matdes.2018.09.004](https://doi.org/10.1016/j.matdes.2018.09.004).
23. Matoy K. A comparative micro-cantilever study of the mechanical behavior of silicon based passivation films. *Thin Solid Films* 2009; 518(1): 247–256. DOI: [10.1016/j.tsf.2009.07.143](https://doi.org/10.1016/j.tsf.2009.07.143).
24. Ast J, Przybilla T, Maier V, et al. Microcantilever bending experiments in NiAl – Evaluation, size effects, and crack tip plasticity. *J. Mater. Res* 2014; 29(18): 2129–2140. DOI: [10.1557/jmr.2014.240](https://doi.org/10.1557/jmr.2014.240).
25. Dehm G, Jaya BN, Raghavan R, et al. Overview on micro- and nanomechanical testing: New insights in interface plasticity and fracture at small length scales. *Acta Materialia* 2018; 142: 248–282. DOI: [10.1016/j.actamat.2017.06.019](https://doi.org/10.1016/j.actamat.2017.06.019).
26. Jaya BN and Jayaram V. Fracture testing at small-length scales: from plasticity in Si to Brittleness in Pt. *JOM* 2016; 68(1): 94–108. DOI: [10.1007/s11837-015-1489-2](https://doi.org/10.1007/s11837-015-1489-2).
27. Saxena AK, Kumar A, Herbig M, et al. Micro fracture investigations of white etching layers. *Materials and Design* 2019; 180: 107892. DOI: [10.1016/j.matdes.2019.107892](https://doi.org/10.1016/j.matdes.2019.107892).
28. Kumar A. In situ study on fracture behaviour of white etching layers formed on rails. *Acta Materialia* 2019; 180: 60–72. DOI: [10.1016/j.actamat.2019.08.060](https://doi.org/10.1016/j.actamat.2019.08.060).
29. Freisinger M, Zauner L, Hahn R, et al. In-situ micro-cantilever bending studies of a white etching layer thermally induced on rail wheels. *Materials Science and Engineering: A* 2023; 869: 144805. DOI: [10.1016/j.msea.2023.144805](https://doi.org/10.1016/j.msea.2023.144805).
30. *EN 13262:2004+A2:2011-Railway applications*: European Standard 2011.
31. Alfreider M, Kozic D, Kolednik O, et al. In-situ elastic-plastic fracture mechanics on the microscale by means of continuous dynamical testing. *Materials and Design* 2018; 148: 177–187. DOI: [10.1016/j.matdes.2018.03.051](https://doi.org/10.1016/j.matdes.2018.03.051).
32. Moser G. Sample Preparation by Metallography and Focused Ion Beam for Nanomechanical Testing. *PM* 2012; 49(6): 343–355. DOI: [10.3139/147.110171](https://doi.org/10.3139/147.110171).
33. Saxena AK, Brinckmann S, Völker B, et al. Experimental conditions affecting the measured fracture toughness at the microscale: Notch geometry and crack extension measurement. *Materials and Design* 2020; 191: 108582. DOI: [10.1016/j.matdes.2020.108582](https://doi.org/10.1016/j.matdes.2020.108582).
34. Lewis R and Dwyer-Joyce RS. Wear at the wheel/rail interface when sanding is used to increase adhesion. *Proceedings of the Institution of Mechanical Engineers, Part F: Journal of Rail and Rapid Transit* 2006; 220(1): 29–41. DOI: [10.1243/095440905X33260](https://doi.org/10.1243/095440905X33260).

Publication III



Research and Innovation

Open Research Europe

Microstructural characterization of near-surface microstructures on rail wheels in service – an insight into “stratified surface layers”

M. Freisinger, A. Trausmuth
Open Research Europe, vol. 3, no. 73 (2023)
DOI: 10.12688/openreseurope.15881.2



RESEARCH ARTICLE

REVISED **Microstructural characterization of near-surface microstructures on rail wheels in service – an insight into “stratified surface layers” [version 2; peer review: 2 approved]**

Matthias Freisinger , Andreas Trausmuth

AC2T research GmbH, Wiener Neustadt, Austria

V2 **First published:** 02 May 2023, 3:73
<https://doi.org/10.12688/openreseurope.15881.1>
Latest published: 03 Jul 2023, 3:73
<https://doi.org/10.12688/openreseurope.15881.2>

Abstract

Background: To decrease maintenance costs and improve safety in rail transportation, the understanding of rail and wheel defects is vital. Studies on “white etching layers” (WEL) on rails and wheels, prone to fatigue crack initiation, have been extensively studied. Recently, a relative named “brown etching layer” (BEL) and its combination, the so-called “stratified surface layer” (SSL), are observed in the field. This study presents an investigation on a rail wheel affected by mechanical and thermal loadings from service with focus on the different evolved layers in the near-surface region.

Methods: Optical microscopy is performed on etched cross-sectional cuts to identify different evolved microstructures (WEL, BEL, SSL), further, specific regions are investigated in detail by scanning electron microscopy to evaluate the microstructural characteristics. To analyze the change in mechanical properties, low-load Vickers hardness investigations are executed in distinctive zones.

Results: This study highlights the broad variety of evolved microstructures, however, a rough classification of WEL (fine mesh-like microstructure, 900 – 1200 HV0.01) and BEL (globular cementite particles, 400 – 600 HV0.01) is given. Further, results indicate that the BEL is commonly accompanied by a WEL, representing an SSL.


Conclusions: The complex loading situation in a wheel-rail contact can lead to the formation of WEL, BEL and SSL. The observation of numerous initiated fatigue cracks within these regions demonstrates the relevance of in-depth studies on evolved microstructures in wheel-rail contacts.


Keywords

Wheel-rail contact, White Etching Layer, Brown Etching Layer, Stratified Surface Layer

Open Peer Review

Approval Status  

	1	2
version 2 (revision) 03 Jul 2023		 view
version 1 02 May 2023	 view	 view

1. **Christoph Gammer** , Austrian Academy of Sciences, Leoben, Austria
2. **Roumen H. Petrov**, Universiteit Gent, Ghent, Belgium

Any reports and responses or comments on the article can be found at the end of the article.

Corresponding author: Matthias Freisinger (matthias.freisinger@ac2t.at)

Author roles: **Freisinger M:** Conceptualization, Data Curation, Investigation, Visualization, Writing – Original Draft Preparation;
Trausmuth A: Funding Acquisition, Project Administration, Resources

Competing interests: No competing interests were disclosed.

Grant information: This project has received funding from the [European Union's Horizon 2020 research and innovation programme under grant agreement No [826255](Research into enhanced track and switch and crossing system 2 [IN2TRACK2]) and No [101012456](Research into optimised and future railway infrastructure [IN2TRACK3]). In addition, this work was funded by the "Austrian COMET-Program" (project InTribology1, no. 872176) via the Austrian Research Promotion Agency (FFG) and the federal states of Niederösterreich and Vorarlberg and was carried out within the "Excellence Centre of Tribology" (AC2T research GmbH).

The funders had no role in study design, data collection and analysis, decision to publish, or preparation of the manuscript.

Copyright: © 2023 Freisinger M and Trausmuth A. This is an open access article distributed under the terms of the [Creative Commons Attribution License](#), which permits unrestricted use, distribution, and reproduction in any medium, provided the original work is properly cited.

How to cite this article: Freisinger M and Trausmuth A. **Microstructural characterization of near-surface microstructures on rail wheels in service – an insight into "stratified surface layers" [version 2; peer review: 2 approved]** Open Research Europe 2023, 3:73 <https://doi.org/10.12688/openreseurope.15881.2>

First published: 02 May 2023, 3:73 <https://doi.org/10.12688/openreseurope.15881.1>

REVISED Amendments from Version 1

The new version of the article includes improvements in the definition of the observed layers, based on the comments of the reviewers. After extensive further discussion of the authors and experts in the field, the wording is sharpened and the labelling within the presented images are revised. Especially the BEL-4 (former version: WEL-4) is renamed since the main message of the article is the categorization by optical appearance after etching with Nital, moreover, etching details are added. The higher hardness of BEL-4 points out the vast variety existing of WELs, BELs, and SSLs. Increased emphasis on this is highlighted in the discussion and results part, not least to underline the storyline of the published article. We hope that the reviewers can approve the article, and we are looking forward to further in-depth work on this highly relevant topic.

Any further responses from the reviewers can be found at the end of the article

Introduction

Material defects on rails and wheels are the main cause of maintenance costs in rail traffic¹. With increasing train frequency in recent years, increased wear and degradation of rails and wheels are expected, which emphasizes the importance of understanding rail and wheel defects to ensure safety and reliability of rail transportation. The terminology of rail and wheel defects is diverse and has been the subject of numerous studies in recent decades¹⁻⁴. However, it is evident that high mechanical and thermal loads affect the near-surface microstructure in a significant way, leading to a microstructure evolution over time in service, depending on the loading history experienced⁵⁻⁷. A well-known microstructure found on rail and wheel surfaces is the so-called “white etching layer” (WEL), named after its white appearance under optical microscopy when etching with an ethanol nitric acid. Its formation is described either mechanically by severe plastic deformation and/or thermally by increased temperature and rapid cooling⁸⁻¹¹. WELs are related to the stud defects on rails and presumed to affect the initiation of rolling contact fatigue clusters in wheels^{2,12-16}. In rolling-sliding contacts, WELs are commonly described as martensitic microstructure with thicknesses from several micrometers up to several hundreds of micrometers, high hardness values (700 – 1000 HV) and low fracture toughness^{9,17-21}. In recent studies a related near-surface microstructure evolved in wheel-rail contact is observed, the so-called “brown etching layer” (BEL)²²⁻²⁵, coming up with a brownish appearance under an optical microscope. The concurrent observation of WEL and BEL pictures a stratification of the near-surface microstructure, hence, the name “stratified surface layer” (SSL) is introduced²⁵. However, not many studies are done on BELs, especially on wheel samples. Due to the gradual wear of rails and wheels and the unknown local loading history of rail and wheel samples from the field, as well as the further influence of the degree of etching on the staining of the microstructure, a clear definition of WEL or BEL is rarely possible.

Within this work, we detected variations of WELs, BELs, and SSLs on an ER7 wheel from service with a mileage of ~200,000 km. The evolved near-surface microstructures are characterized to improve the understanding of specific evolved near-surface microstructures on rail wheels, with focus on the less studied BEL. The aim of this work is to point out the variety of mechanically and thermally affected microstructures on rail wheels to improve the knowledge which can contribute to the reduction of maintenance costs in rail transportation.

Methods

A rail wheel (0.95 m in diameter) after ~200,000 km in service is provided by the Austrian Federal Railways. The material is a wheel steel with a composition of Fe-0.52C-0.8Mn-0.4Si-0.3Cr-0.3Cu-0.3Ni (in wt%), which is widely used on European railway networks²⁶. The worn tread surface of this wheel is investigated by cutting out a slice (thickness of ~3 mm) of the wheel using a band saw (FMB Pegasus G; FMB s.r.l., Italy) (Figure 1a). Then, a laboratory cutting device (Struers Secotom-50; Struers ApS, Denmark) is used to cut the surface region of the slice in several cubic samples of ~1x1x1 mm. To create cross-sectional cuts in rolling direction, the cubic samples are embedded in conductive compounds (CitoPress-30, Resing: PolyFast; Struers ApS, Denmark). The embedded samples are then grinded and polished (Tegramin-30; Struers ApS, Denmark) in various steps (SiC Paper #220, MD-Largo 9µm, MD-Dac 3µm and MD-Nap 1µm; Struers ApS, Denmark). Finally, the cross-sectional cuts are etched with diluted nitric acid (3 vol% HNO₃, in 97 vol% ethanol for 3 s at room temperature).

Microstructural characterizations are primarily performed by optical microscopy (OM) (Axio Imager M2m, Carl Zeiss AG, Germany) in bright-field mode, images are captured and thicknesses of layers are measured by using IMS Client (Imagic Bildverarbeitung AG, Switzerland). Further, a scanning electron microscopy (SEM) (Jeol JIB 4700F, Jeol Ltd., Japan) is performed, where the secondary electron detector is used to investigate the characteristics of the observed microstructures, 15 kV acceleration voltage is applied. Low-load Vickers hardness measurements are executed using a Future-Tech FM-700 hardness tester (Future-Tech FM-700, Future Tech Corp., Japan) using a load of 0.01 kp (0.098 N). The diagonals of the indents are measured with an OM.

Results

Along the tread surface of the investigated wheel four specific regions of interest (ROIs) with mechanically and thermally affected microstructures are investigated, see Figure 1b. Discrepancies concerning the degree of etching can be excluded since all the regions are detected on the same cross-sectional sample in the middle of the tread. It can be seen how different the evolved microstructures are within several millimeters. Hence, the local contact situation and the environmental influences vary widely. Within ROI-1 – ROI-4 a brownish-appearing layer can be seen at the current magnification

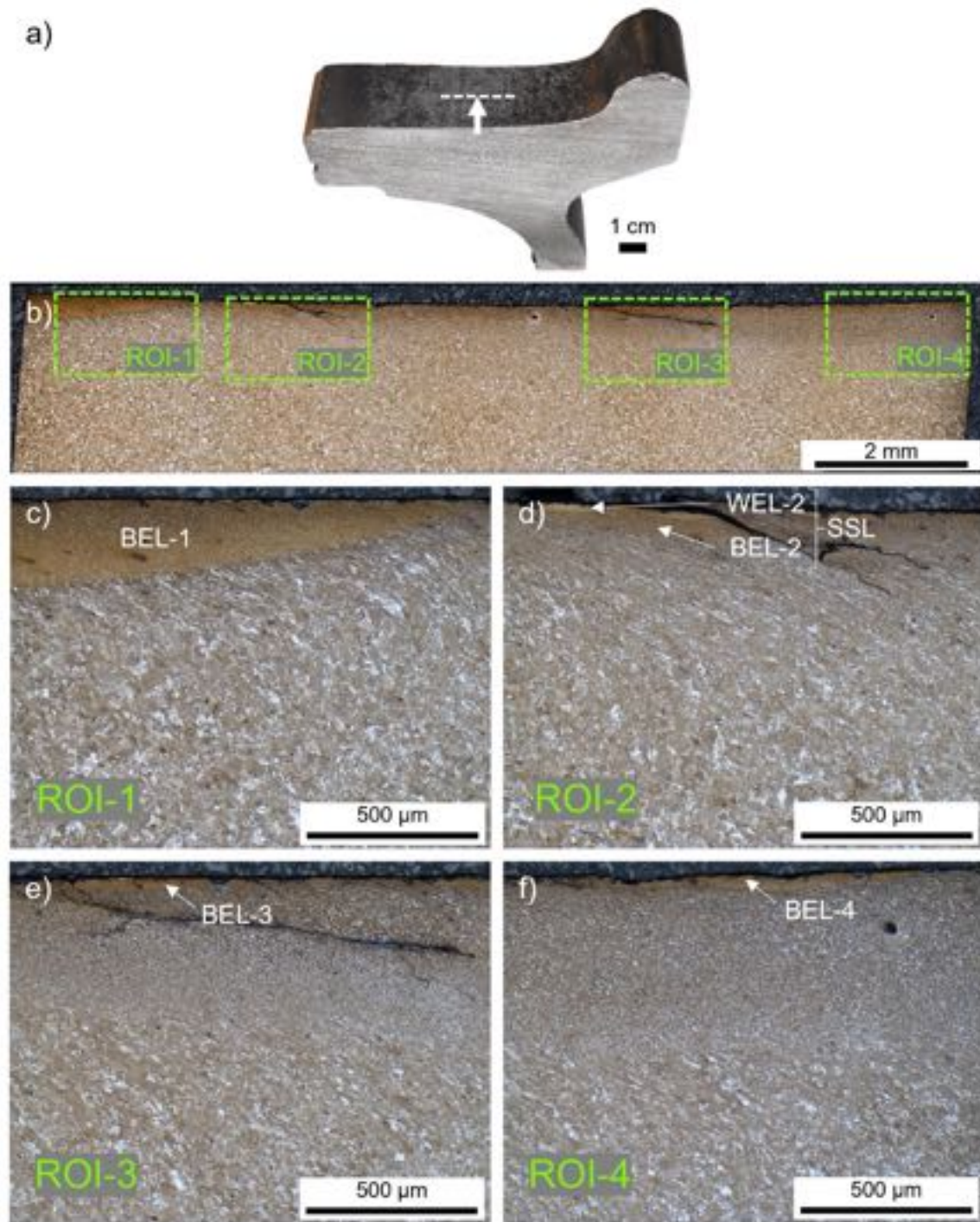


Figure 1. (a) The investigated ER7 wheel sample from the field and the related cross-sectional cut (b) in rolling direction. Four different regions of interest (ROI) with white etching layer (WEL)/brown etching layer (BEL) variations are investigated in more detail, optical microscope images are given for ROI-1 (c), ROI-2 (d), ROI-3 (e), and ROI-4 (f).

(Figures 1c, d, e and f), therefore these layers are indicated as BELs. In ROI-2 a stratification containing a white appearing layer (WEL-2) can be observed at the top of BEL-2. This combination is stated as an SSL where severe cracking is

evident (Figure 1d). To identify possible thinner WELs on top of the observed BELs, a more detailed microstructural analysis is presented in the following paragraphs for each ROI.

ROI-1 shows a massive brownish-appearing layer (named BEL-1) with an underlying deformed ferritic-pearlitic microstructure (Figure 1c). The thickness of the BEL-1 is up to 250 μm , with decreasing extent towards a transition to the deformed wheel material. With increased magnification (Figure 2a) a bright-appearing thin layer (WEL-1) can be observed on top of the BEL-1. Hence, this region can be stated as SSL, combining a WEL with an underlying BEL. Within the WEL-1 small breakouts can be seen, as well as crack initiation (Figure 2b), while the average layer thickness is $\sim 20 \mu\text{m}$. The morphology of the BEL-1 just underneath the WEL-1 is presented by the SEM image in Figure 2c, showing a severely plastically deformed (SPD) microstructure with an alignment under a certain angle to the surface. Further, globular particles can be identified as randomly distributed. Due to the high degree of deformation, the cementite lamellae of the pearlite of the ER7 microstructure break and thermal activation have led to the spheroidization of the cementite lamellae fragments. The low-load hardness measurements executed within the area of the BEL-1 region shown in Figure 2c come up with hardness values of $537 \pm 71 \text{ HV}0.01$.

Within ROI-2, an SSL can be seen in Figure 1d, accompanied by a crack initiation and propagation along an angle similar to the shear-deformed near-surface microstructure into depth. The SSL is shown by higher magnification OM in Figure 3a. The SSL consists of an almost featureless topmost layer with

a thickness of $\sim 30 \mu\text{m}$ (indicated as WEL-2) and an underlying brownish-appearing layer with a thickness of $\sim 50 \mu\text{m}$, designated as BEL-2. Micro-spalling can be seen in the WEL-2, a SE image of the SSL is given in Figure 3b. To analyze the different microstructural characteristics, high magnification SEM images are presented: Figure 3c shows the microstructure of WEL-2, coming up with a fine mesh-like structure without any preferred orientation detectable. The image indicates some nanometer-sized globular particles fine dispersed. Hardness values of $1184 \pm 28 \text{ HV}0.01$ are obtained within this region. In the region BEL-2 (Figure 3d), a coarser deformed microstructure aligned under an angle of $\sim 30^\circ$ to the surface can be identified, containing some globular particles with significantly larger proportions with respect to the WEL-2. The low load hardness measurements reveal results of $500 \pm 42 \text{ HV}0.01$. Comparable microstructure can be seen in the microstructure underneath the BEL-2 (Figure 3e), but with a slight change in the alignment angle of the deformed microstructure. Comparable hardness values are determined with $521 \pm 47 \text{ HV}0.01$. The globular particles are suggested to result from broken cementite lamellae (originating from the pearlite of the ER7 wheel microstructure), spheroidized due to thermal influences.

The brownish-appearing layer within ROI-3, where a severe crack network is visible (Figure 1e), is analyzed in more detail by higher magnification OM and SEM (Figure 4). The near-surface

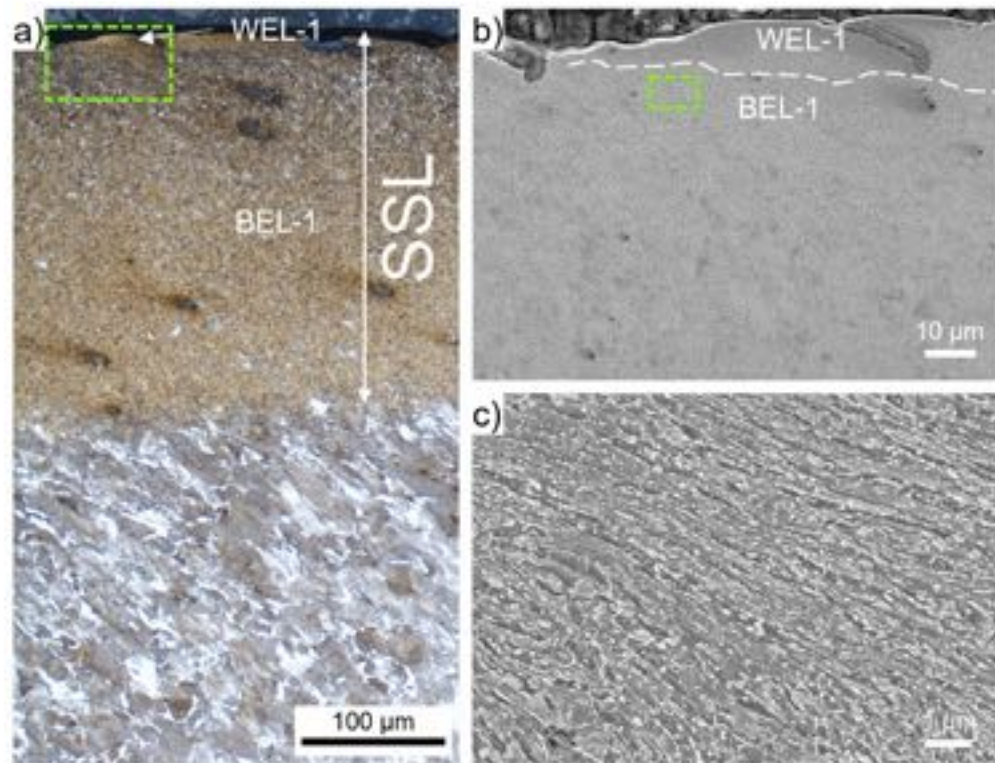


Figure 2. (a) shows the evolved microstructure within ROI-1 (see Figure 1b, c) consisting of a thin white etching layer (WEL) at the top, a $\sim 250 \mu\text{m}$ thick brown etching layer (BEL) underneath, segueing into a deformed ER7 microstructure. (b) presents a scanning electron microscope (SEM) image of the WEL and BEL area framed in (a). A higher magnification SEM image of the BEL-1 microstructure is given in (c).

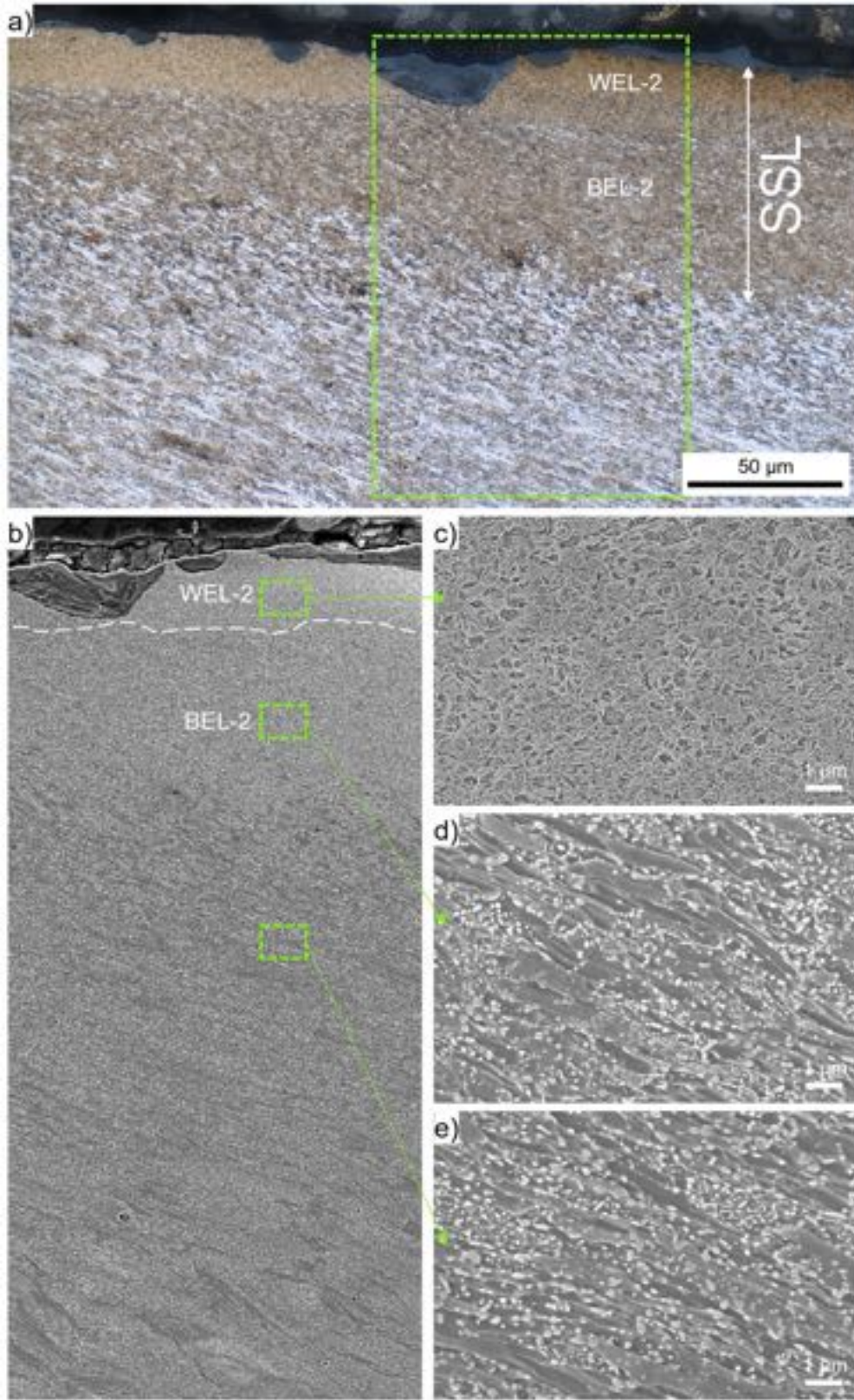


Figure 3. (a) shows the stratified surface layer (SSL) (white etching layer-2 (WEL-2) and brown etching layer-2 (BEL-2) within ROI-2 (see Figure 1b, d). (b) presents a scanning electron (SEM) image of the region framed in (a). For more details, higher magnification SEM images of certain locations are given: WEL-2 (c), BEL-2 (d), and the underlying deformed ER7 microstructure (e).

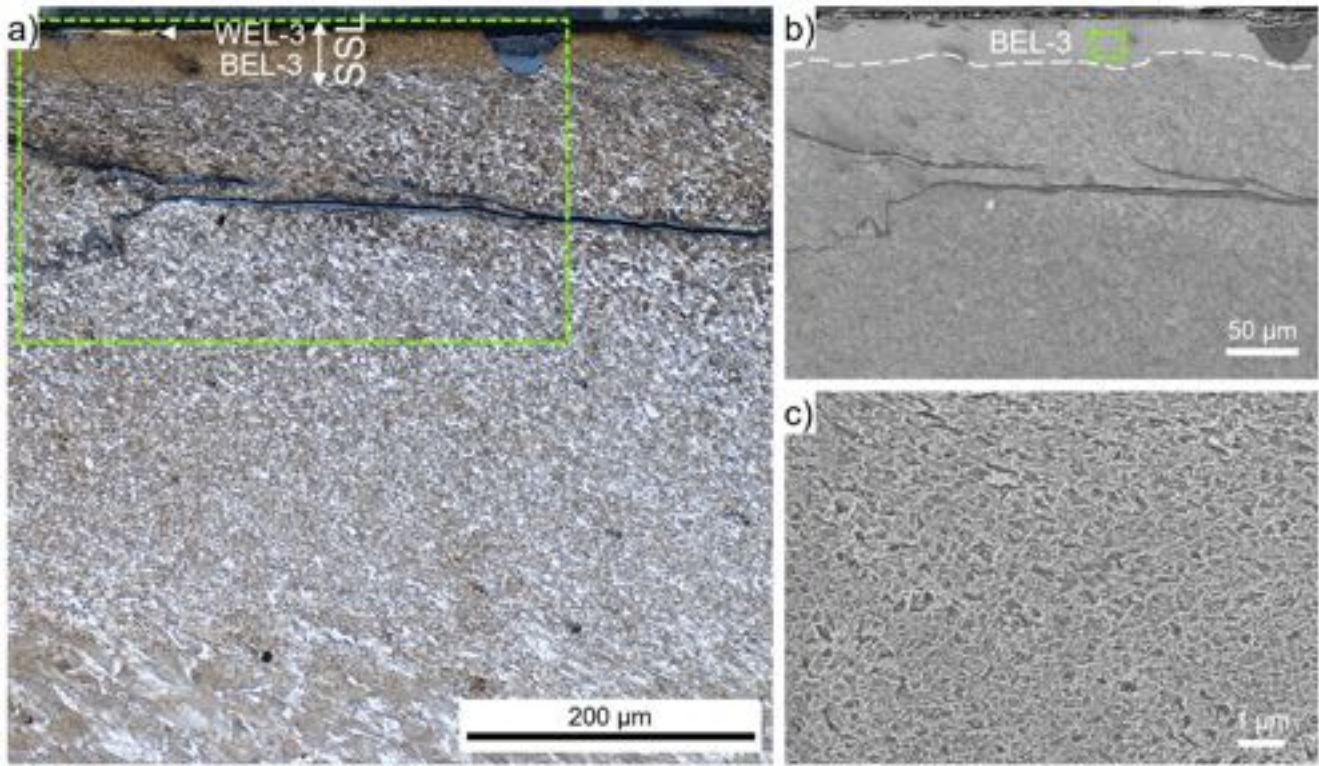


Figure 4. (a) shows the evolved microstructure within ROI-3 (see Figure 1b, e), where a very thin white etching layer (WEL) is on top of a brown etching layer (BEL) with a thickness of $\sim 50 \mu\text{m}$ (BEL-3). This layer is situated on a severely plastically deformed (SPD) microstructure accompanied by severe cracking. (b) presents a scanning electron microscope (SEM) image of the WEL and BEL area framed in (a). A higher magnification SEM image of the BEL-3 microstructure is given in (c).

microstructure shows parts of a white appearing thin layer on top of the BEL, named WEL-3 (Figure 4a). Crack initiation can be seen along the surface, propagating into a brownish appearing layer with a thickness of $\sim 50 \mu\text{m}$ (BEL-3). On the right side of the SE image (Figure 4b) a spalled BEL region can be detected. The cracks initiating at the surface seem to stop at the interface of the BEL-3 to the underlying SPD microstructure. However, severe horizontal cracks are observed at a depth of $\sim 100 - 200 \mu\text{m}$ from the surface. The SPD microstructure gradually changes to a deformed and aligned ER7 microstructure with increasing grain sizes. The focus of this study, the microstructure of the BEL, is further investigated by high magnification SE images presented in Figure 4c. A randomly orientated mesh-like microstructure can be seen, with a certain degree of spheroidization. The low load Vickers hardness measurements in this area show hardness values of $509 \pm 24 \text{HV}0.01$.

The layer observed at the wheel surface in ROI-4 is appearing brownish and therefore designated as BEL (Figure 1f). In contrast to the other BELs observed, no WEL can be identified on top of the BEL-4. Micro-spalling, crack initiation, and crack propagation through the WEL under almost 90° to the surface can be observed (Figure 5a), the layer is named WEL-4. The alignment of the underlying ER7 microstructure

is visible (Figures 5a and b). The microstructure within WEL-4 is shown by SE imaging in Figure 5c, indicating a fine-grained mesh-like structure. Further, a certain degree of spheroidization can be identified. The results of the hardness measurements come up with pronounced scattering, however, high hardness values are indicated with $979 \pm 141 \text{HV}0.01$.

Discussion

The characterization of different evolved near-surface microstructures on a well-established rail wheel from service outpoints the wide range of microstructural variations with respect to the location along the tread surface. The naming WEL and BEL is originally based on the appearance under the OM after etching with Nital, hence, based on the degree of etching and the image settings. Therefore, a common naming based on OM images is hardly possible and questionable. The information of the characterization by SEM and hardness measurements may enable a more consistent naming. The results within this work show the WEL as a fine-grained mesh-like microstructure without globular particles and high hardness ($\sim 1000 \text{HV}0.01$), see WEL-2. In some cases, even the brownish appearing regions can exhibit hardness values above $900 \text{HV}0.01$ (see BEL-4), but a more dissolved microstructure with spheroidization. The definition is in this case arguable, since no WEL can be detected on top of the

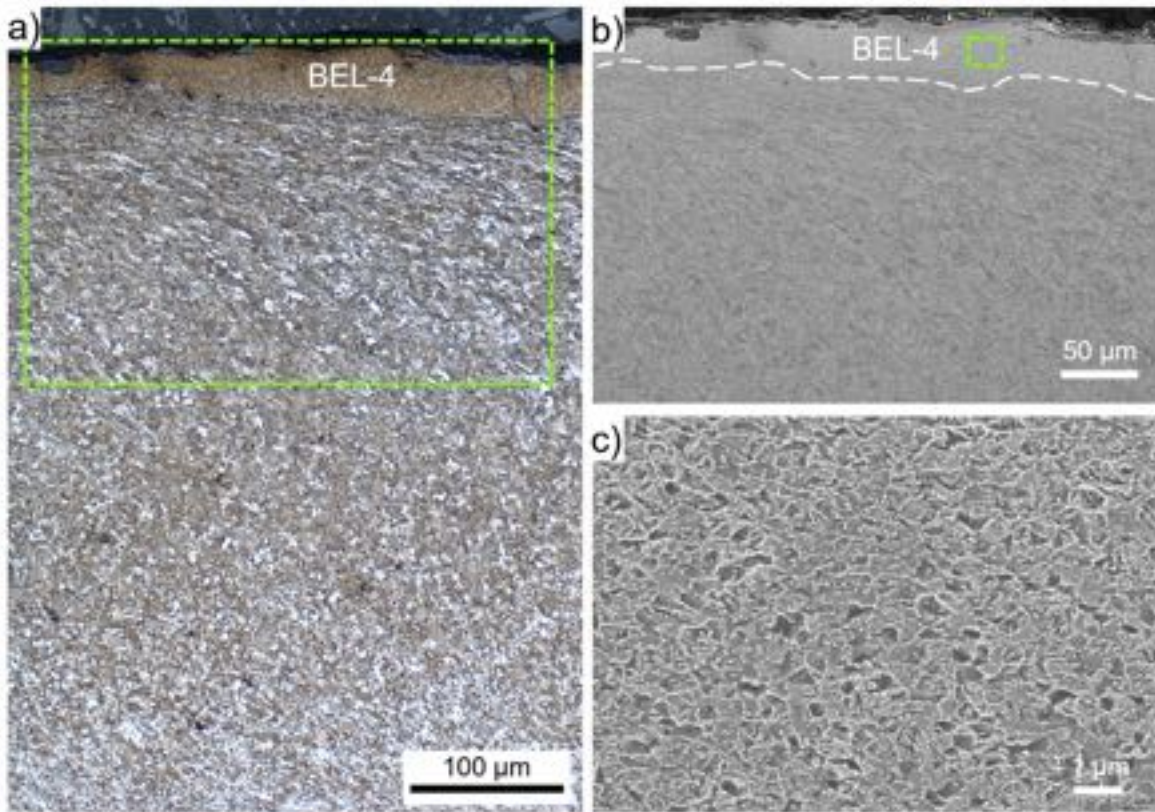


Figure 5. (a) shows the microstructure within ROI-4 (see Figure 1b, f), where a brown etching layer (BEL) with a thickness of $\sim 50 \mu\text{m}$ (BEL-4), is situated on an severely plastically deformed microstructure. (b) presents a scanning electron microscope (SEM) image of the WEL area framed in (a). A higher magnification SEM image of the WEL-4 microstructure is given in (c).

BEL, in contrast to the other regions investigated. But, the BEL-3 shows comparable microstructure in the SEM, with lower hardness ($\sim 500 \text{HV}0.01$). This demonstrates the demand of further in-depth analysis to understand the microstructural characteristics and therefore the formation process and naming. In general, evolved microstructures with hardness in the range of $400 - 600 \text{HV}0.01$, brownish appearance in the LOM, and pronounced spheroidized cementite lamellae leading to globular particles can be indicated as BEL. It is shown, that even within a BEL the microstructure can locally differ, see BEL-1. In most cases, when observing a BEL, a WEL can also be identified, representing an SSL. The thicknesses of the WEL and BEL is varying, hence, the SSL often is detectable only with higher magnification, see ROI-1 and ROI-3. Samples from field are worn and the analysis is always a short snapshot, which additionally complicates a common identification and classification.

Conclusions

The work shows the broad variety of evolved near-surface microstructures on rail wheels, which makes a common terminology hardly possible, however, with increasing numbers of published studies certain comparison is possible. A rough

classification can be made for the examined wheel steel (Fe-0.52C-0.8Mn-0.4Si-0.3Cr-0.3Cu-0.3Ni):

- A so-called WEL appears white in OM after etching with Nital, shows a fine mesh-like microstructure without globular particles in SEM, and hardness in the range of $900 - 1200 \text{HV}0.01$
- The BEL looks brownish in OM after etching with Nital, shows pronounced globular particles (spheroidized cementite lamellae) within SPD microstructure in SEM, and hardness in the range of $400 - 600 \text{HV}0.01$ (with variations up to 900HV)

In most cases, a BEL is always accompanied by a WEL, forming a so-called SSL. Crack initiation and crack networks are observed in the presence of SSLs on the ER7 wheel from service, indicating a relation to fatigue crack initiation and possible failure of the wheel.

Data and software availability

Zenodo, Microstructural characterization of near-surface microstructures on rail wheels in service – an insight into “stratified

surface layers”: Supplementary Data. <https://doi.org/10.5281/zenodo.7836670>²⁷.

This project contains the following underlying data:

- fig_ORE_Freisinger (1).JPG
- fig_ORE_Freisinger (1).tif
- fig_ORE_Freisinger (10).jpg
- fig_ORE_Freisinger (10).tif
- fig_ORE_Freisinger (2).jpg
- fig_ORE_Freisinger (2).tif
- fig_ORE_Freisinger (3).jpg
- fig_ORE_Freisinger (3).tif
- fig_ORE_Freisinger (4).jpg
- fig_ORE_Freisinger (4).tif
- fig_ORE_Freisinger (5).jpg
- fig_ORE_Freisinger (5).tif
- fig_ORE_Freisinger (6).jpg
- fig_ORE_Freisinger (6).tif
- fig_ORE_Freisinger (7).jpg
- fig_ORE_Freisinger (7).tif
- fig_ORE_Freisinger (8).jpg
- fig_ORE_Freisinger (8).tif
- fig_ORE_Freisinger (9).jpg
- fig_ORE_Freisinger (9).tif
- hardness_ORE_Freisinger.xlsx

Data are available under the terms of the [Creative Commons Attribution 4.0 International license \(CC-BY 4.0\)](https://creativecommons.org/licenses/by/4.0/).

Acknowledgments

We thank DI Roman Schmid and Andreas Schachner from the Austrian Federal Railways Holding Stock Company for providing ex-service material and their help in this work. We are also thankful to Iñigo Sarries (CAF, Construcciones y Auxiliars de Ferrocarriles) for useful discussion and the supply of rail wheel materials.

References

1. Ekberg A, Åkesson B, Kabo E: **Wheel/rail rolling contact fatigue - Probe, predict, prevent.** *Wear.* 2014; **314**(1–2): 2–12. [Publisher Full Text](#)
2. Grassie SL: **Studs and squats: The evolving story.** *Wear.* 2016; **366–367**: 194–199. [Publisher Full Text](#)
3. Ahlstrom J, Karlsson B: **Microstructural evaluation and interpretation of the mechanically and thermally affected zone under railway wheel flats.** *Wear.* 1999; **232**(1): 1–14. [Publisher Full Text](#)
4. Steenbergen M: **On the genesis of squat-type defects on rails - Toward a unified explanation.** *Wear.* 2021; **478–479**: 203906. [Publisher Full Text](#)
5. Eden HC, Garnham JE, Davis CL: **Influential microstructural changes on rolling contact fatigue crack initiation in pearlitic rail steels.** *Mater Sci Technol.* 2005; **21**(6): 623–629. [Publisher Full Text](#)
6. Cvetkovski K, Ahlström J: **Characterisation of plastic deformation and thermal softening of the surface layer of railway passenger wheel treads.** *Wear.* 2013; **300**(1–2): 200–204. [Publisher Full Text](#)
7. Molyneux-Berry P, Davis C, Bevan A: **The Influence of Wheel/Rail Contact Conditions on the Microstructure and Hardness of Railway Wheels.** *ScientificWorldJournal.* 2014; **2014**: 209752. [PubMed Abstract](#) | [Publisher Full Text](#) | [Free Full Text](#)
8. Nguyen BH, Al-Juboori A, Zhu H, et al.: **Formation Mechanism and Evolution of White Etching Layers on Different Rail Grades.** *Int J Fatigue.* 2022; **163**: 107100. [Publisher Full Text](#)
9. Al-Juboori A, Zhu H, Wexler D, et al.: **Characterisation of White Etching Layers formed on rails subjected to different traffic conditions.** *Wear.* 2019; **436–437**: 202998. [Publisher Full Text](#)
10. Freisinger M, Rojacz H, Pichelbauer K, et al.: **Comparative study on the influence of initial deformation and temperature of thermally induced white etching layers on rail wheels.** *Tribol Int.* 2023; **177**: 107990. [Publisher Full Text](#)
11. Pan R, Chen Y, Lan H, et al.: **Investigation into the evolution of tribological white etching layers.** *Materials Characterization.* 2022; **190**: 112076. [Publisher Full Text](#)
12. Steenbergen M: **Squat formation and rolling contact fatigue in curved rail track.** *Eng Fract Mech.* 2015; **143**: 80–96. [Publisher Full Text](#)
13. Ekberg A, Kabo E: **Fatigue of railway wheels and rails under rolling contact and thermal loading—an overview.** *Wear.* 2005; **258**(7–8): 1288–1300. [Publisher Full Text](#)
14. Liu C, Zhang G, Chen C, et al.: **Formation mechanism for the white etching microstructure in the subsurface of the failure pearlite wheel steel.** *Wear.* 2022; **494–495**: 204243. [Publisher Full Text](#)
15. Zhang YM, Xiao ZM, Fan M: **Fatigue Investigation on Railway Wheel Steel with White Etching Layer.** *Int J Steel Struct.* 2020; **20**(1): 80–88. [Publisher Full Text](#)
16. Kato T, Kato H, Makino T: **Effect of elevated temperature on shelling property of railway wheel steel.** *Wear.* 2016; **366–367**: 359–367. [Publisher Full Text](#)
17. Carroll RI, Beynon JH: **Rolling contact fatigue of white etching layer: Part 1: Crack morphology.** *Wear.* 2007; **262**(9–10): 1253–1266. [Publisher Full Text](#)
18. Bernsteiner C, Meierhofer A, Trummer G, et al.: **Simulation and experiment based investigations of squat formation mechanisms.** *Wear.* 2019; **440–441**: 203093. [Publisher Full Text](#)
19. Pan R, Ren R, Chen C, et al.: **The microstructure analysis of white etching layer on treads of rails.** *Eng Fail Anal.* 2017; **82**: 39–46. [Publisher Full Text](#)
20. Freisinger M, Zauner L, Hahn R, et al.: **In-situ micro-cantilever bending studies of a white etching layer thermally induced on rail wheels.** *Mater Sci Eng A.* 2023; **869**: 144805. [Publisher Full Text](#)
21. Kumar A, Saxena AK, Kirchlechner C, et al.: **In situ study on fracture behaviour of white etching layers formed on rails.** *Acta Materialia.* 2019; **180**: 60–72. [Publisher Full Text](#)
22. Li S, Wu J, Petrov RH, et al.: **“Brown etching layer”: A possible new insight into the crack initiation of rolling contact fatigue in rail steels?** *Eng Fail Anal.* 2016; **66**: 8–18. [Publisher Full Text](#)
23. Kumar A, Agarwal G, Petrov R, et al.: **Microstructural evolution of white and brown etching layers in pearlitic rail steels.** *Acta Materialia.* 2019; **171**: 48–64. [Publisher Full Text](#)
24. Tung PY, Zhou X, Morsdorf L, et al.: **Formation mechanism of brown etching**

layers in pearlitic rail steel. *Materialia*. 2022; **26**: 101625.

[Publisher Full Text](#)

25. Messaadi M, Steenbergen M: **Stratified surface layers on rails**. *Wear*. 2018; **414-415**: 151-162.
[Publisher Full Text](#)
26. Lewis R, Olofsson U: **Wheel-rail interface handbook**. Woodhead Publishing

Limited, 2009.

[Publisher Full Text](#)

27. Freisinger M: **Microstructural characterization of near-surface microstructures on rail wheels in service - an insight into "stratified surface layers": Supplementary Data**. [Dataset] *Zenodo*. 2023.
<http://www.doi.org/10.5281/zenodo.7836670>

Open Peer Review

Current Peer Review Status:  

Version 2

Reviewer Report 10 July 2023

<https://doi.org/10.21956/openreseurope.17524.r33449>

© 2023 Petrov R. This is an open access peer review report distributed under the terms of the [Creative Commons Attribution License](#), which permits unrestricted use, distribution, and reproduction in any medium, provided the original work is properly cited.



Roumen H. Petrov

Department of Electromechanical, Systems and Metal Engineering, Universiteit Gent, Ghent, Flanders, Belgium

The authors did their best to implement the requested changes. Now the submission is enough good to be indexed. It provides interesting results and can be a good base for further in-depth studies of the phenomena WEL/BEL on wheels.

One minor comment:

- In the description of the etching technique please replace "HNO3" with "HNO₃"; The symbol in the subscript are used to show atomic percents which is the correct description of the nitric acid.

Competing Interests: No competing interests were disclosed.

Reviewer Expertise: Micro structural characterization of damage and fracture. Optical microscopy, Scanning and transmission Electron Microscopy, XRD, texture, EBSD, TKD, ACOM-TEM, 3D-EBSD. Damage on rails and bearings. Metals technology-thermal and thermo-chemical treatment;

I confirm that I have read this submission and believe that I have an appropriate level of expertise to confirm that it is of an acceptable scientific standard.

Version 1

Reviewer Report 30 May 2023

<https://doi.org/10.21956/openreseurope.17155.r31402>

© 2023 Petrov R. This is an open access peer review report distributed under the terms of the [Creative Commons Attribution License](#), which permits unrestricted use, distribution, and reproduction in any medium, provided the original work is properly cited.



Roumen H. Petrov

Department of Electromechanical, Systems and Metal Engineering, Universiteit Gent, Ghent, Flanders, Belgium

The paper is interesting and shows nice metallographic microstructures on the rail wheel. The number of papers that characterize the WEL on wheels is not very large and this work could be an interesting contribution, provided that it corrects several important elements. I am afraid that I cannot recommend the paper for indexing as it is. The authors must re-work it and show very clear their message. Additional characterizations and the use of high-resolution characterization techniques are required in order to understand better the WEL and BEL microstructures on these steels.

A few more detailed comments follow:

1. I advise the authors not to use directly the abbreviation ER7 without explanation. ER7 Material 650mm Railway Wagon Wheels AAR Standard is known only by specialists in the field but not by general metallurgists.
2. The sentence: "Finally, the cross-sectional cuts are etched with diluted nitric acid (3% HNO₃, 97% ethanol)." Should be: "Finally, the cross-sectional cuts are etched with diluted nitric acid (3vol% HNO₃, in 97vol% ethanol for XXX s at room temperature)." It is of critical importance to mention the exact etching conditions, because all the discussions in this work are based on the differences in the appearance of the microstructure. This appearance is critically dependent on the way of sample preparation and especially the etching technique.
3. What is "...load of 0.01 kp"? kp is not mentioned in any standards. It should be 10gf (gram force) which is much more understandable.

Comments on the results:

1. The observed results are critically dependent on the loading conditions which were not given. It is written: "...with a milage of ~200,000 km." It is not enough to mention only the mileage. The load should be mentioned as well because it is an important part of the damage formation. Additionally, the friction conditions determine the temperature changes in the contact zones. They should be known in order to have a meaningful observation of the formation of these structures in the wheel.
2. The characterization of the microstructures is based mainly on SEM and OM but does it represents all possible microstructures that can form in the damaged wheel? It is well known that WEL in rails is a mixture of ultrafine-grained martensitic structures and retained austenite (RA). Here the authors did not mention any RA. Finally, is there are differences between the WEL on the rail and the steel?
3. In Fig. 5a the authors show WEL which is actually brown? Why do they call it white? Its microstructure is exactly the same as the microstructure of the BEL shown in Fig. 4.

(compare Fig.4c and Fig.5c). In the cited works [22] and [23] and [25] the differences between the BEL and WEL are very clear and they appear indeed in the white and brown colors, not in the shades of brown. To understand better the nature of the formed microstructures additional X-ray diffraction should be carried out and if possible EBSD.

Is the work clearly and accurately presented and does it cite the current literature?

Yes

Is the study design appropriate and does the work have academic merit?

Partly

Are sufficient details of methods and analysis provided to allow replication by others?

Partly

If applicable, is the statistical analysis and its interpretation appropriate?

Not applicable

Are all the source data underlying the results available to ensure full reproducibility?

No

Are the conclusions drawn adequately supported by the results?

No

Competing Interests: No competing interests were disclosed.

Reviewer Expertise: Micro structural characterization of damage and fracture. Optical microscopy, Scanning and transmission Electron Microscopy, XRD, texture , EBSD, TKD, ACOM -TEM, 3D-EBSD. Damage on rails and bearings. Metals technology-thermal and thermo-chemical treatment;

I confirm that I have read this submission and believe that I have an appropriate level of expertise to state that I do not consider it to be of an acceptable scientific standard, for reasons outlined above.

Author Response 19 Jun 2023

Matthias Freisinger

We highly appreciate your review based on your excellent scientific background in this topic and hope that we meet your comments in the revised article. We try to sharpen our message of the article – as it presents an overview of evolved layers formed on rail wheels in service (with unknown loading history). Further, we are pleased you recognize the modest number of papers on WELs on wheels and the contribution of our article. Additional in-depth characterisations of evolved WELs and BELs are of high interest, however, due to the numerous variations of the evolved microstructures this would go beyond the scope of the current article. In the following section, we want to give answers to your valuable comments of the review:

1. Thank you for this comment, we see this issue and changed the wording without

using the “ER7” abbreviation.

2. We highly appreciate your comment regarding etching procedure. In fact, this is crucial since the current analysis is solely based on optical microscopy appearance. Further, in-depth analysis is of great interest, but not aim of this overview article.
3. Based on our knowledge, Vickers hardness measurements are defined by the applied Kilopond (kp), however, since this is a non-standard gravitational metric unit of force, we specified the testing parameters in Newtons (N) in the revised manuscript.
4. In fact, the loading conditions are critical on the formation of evolved microstructures on rail wheels. Unfortunately, it is practically impossible to know the detailed mechanical and thermal loading history of samples from the field. This is the case in the analysed sample in this article as well. Hence, we cannot give better loading parameters. However, the article should show a rough overview about the evolved microstructural layers. To study these layers systematically, a lab approach with defined loading parameters is vital, hence, the authors are presenting such a lab approach at the ECOTRIB conference in Bari (IT) in June 2023. Further, a manuscript is in progress on the fatigue behaviour of defined WELs and BELs formed by reproducible thermal and mechanical loadings in the lab on wheel steels.
5. Thanks for this comment. The current article is indeed restricted on SEM and OM. Due to the vast variety of WELs and BELs more detailed analysis would be preferable for more detailed results. However, the aim of this article is a rough overview, and the etching analysis shows the desired microstructural changes. The current work does not claim a detailed description of formation (detection of RA,...). Differences between WEL on rails and wheels are not studied, which would require a comparison of numerous variations detected on rails and wheels and would go beyond the scope of the submitted article.
6. When revising the article, we decided to name this BEL, based on the comparable microstructure. Moreover, we sharpened the discussion, and we hope we address your comment. Advanced analysis would be needed, but, beyond the scope of this overview work.

Competing Interests: No competing interests were disclosed.

Reviewer Report 25 May 2023

<https://doi.org/10.21956/openreseurope.17155.r31786>

© 2023 Gammer C. This is an open access peer review report distributed under the terms of the [Creative Commons Attribution License](#), which permits unrestricted use, distribution, and reproduction in any medium, provided the original work is properly cited.

**Christoph Gammer** 

Erich Schmid Institute of Materials Science, Austrian Academy of Sciences, Leoben, Austria

This article analyzes the near-surface microstructure of a rail wheel after service. The white etching layer (WEL) and brown etching layer (BEL) forming the stratified surface layer (SSL) are identified. In addition to detailed optical microscopy after Nital etching, microhardness measurements and scanning electron microscopy are performed from the WEL and BEL. Finally, cracks are shown in the SSL.

The manuscript is motivated, well written and the microstructure is clearly described. In addition, the results are discussed with respect to general problems of accurately describing microstructures in rail wheels.

A small typos should be fixed (HV0.0.1) and care should be taken that all abbreviations are introduced (SE). In addition, it would help readers that are not clearly familiar with railway wheels to include some schematic in Figure 1 showing how the piece was extracted from an actual wheel.

Is the work clearly and accurately presented and does it cite the current literature?

Yes

Is the study design appropriate and does the work have academic merit?

Yes

Are sufficient details of methods and analysis provided to allow replication by others?

Yes

If applicable, is the statistical analysis and its interpretation appropriate?

Yes

Are all the source data underlying the results available to ensure full reproducibility?

Yes

Are the conclusions drawn adequately supported by the results?

Yes

Competing Interests: No competing interests were disclosed.**Reviewer Expertise:** Transmission electron microscopy, Metallic Glasses, Nanostructured Materials**I confirm that I have read this submission and believe that I have an appropriate level of expertise to confirm that it is of an acceptable scientific standard.**

Author Response 19 Jun 2023

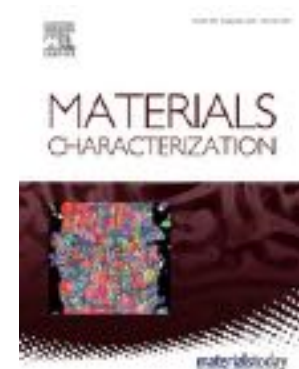
Matthias Freisinger

We want to thank you for your thorough review and the approval of our article to show

relevant results on the analysis of evolved microstructural regions on rail wheels during service. Revision on typos and minor changes based on your comments are done.

Competing Interests: No competing interests were disclosed.

Publication IV



Microstructural characteristics of stratified surface layers affecting crack propagation in rail wheel near-surface regions
M. Freisinger, S. Fellner, C. Gammer, H. Riedl, R. Hahn
submitted to *Materials Characterization* (19.09.2023)

Materials Characterization

Microstructural characteristics of stratified surface layers affecting crack propagation in rail wheel near-surface regions --Manuscript Draft--

Manuscript Number:	MATERIALSCHAR-D-23-03438
Article Type:	Research Paper
Keywords:	wheel-rail contact; White etching layer; brown etching layer; stratified surface layer; Rolling contact fatigue
Corresponding Author:	Matthias Freisinger AC2T research GmbH Wiener Neustadt, AUSTRIA
First Author:	Matthias Freisinger
Order of Authors:	Matthias Freisinger Simon Fellner Christoph Gammer Helmut Riedl-Tragenreif Rainer Hahn
Abstract:	<p>To withstand increasing mechanical and thermal loads affecting rails and wheels due to intensified rail transportation, comprehensive knowledge of evolving near-surface microstructures is vital to manage rolling contact fatigue (RCF) damage. Recently, stratified surface layers (SSLs) observed on samples from the field indicate their contribution to RCF crack behavior. Therefore, this study investigates an SSL detected on a rail wheel in service in terms of microstructural characteristic and related micro-mechanical properties. Results show crack initiation in the white etching layer (WEL) with propagation into the underlying brown etching layer (BEL), whereby the crack growth direction is changing just underneath the WEL-BEL transition zone. Within the BEL, a microstructural gradient is observed with decreasing grain size and increasing hardness with increasing distance from the surface. The region underneath the WEL-BEL transition zone reveals a distorted bcc lattice, high dislocation density and globular particles, proposing the presence of tempered martensite. Moreover, in situ micro-bending experiments in this region show a predominant plastic material behaviour. This work provides new insights in the microstructural and micro-mechanical characteristics of SSLs and point out the relevance to crack initiation at rail wheel treads during service.</p>
Suggested Reviewers:	Johan Ahlström johan.ahlstrom@chalmers.se Roger Lewis roger.lewis@sheffield.ac.uk Michael Steenbergen M.J.M.M.Steenbergen@tudelft.nl Andreas Ekberg anders.ekberg@chalmers.se

Highlights

- Microstructure of a Stratified Surface Layer (SSL) on ex-service rail wheel is studied
- Microstructural gradient observed in brown etching layer (BEL) shown by EBSD analysis
- Micromechanical properties linked within the BEL by hardness measurements
- TEM analysis & micro-bending focused on upper BEL region (crack growth through SSL)

Microstructural characteristics of stratified surface layers affecting crack propagation in rail wheel near-surface regions

M. Freisinger ^{a,b*}, S. Fellner ^b, C. Gammer ^b, H. Riedl ^{c,d}, R. Hahn ^c

^a AC2T research GmbH, A-2700 Wiener Neustadt, Austria

^b Erich Schmid Institute of Materials Science, Austrian Academy of Sciences, A-8700 Leoben, Austria

^c Christian Doppler Laboratory for Surface Engineering of high-performance Components, TU Wien, Austria

^d Institute of Materials Science and Technology, TU Wien, Austria

Abstract

To withstand increasing mechanical and thermal loads affecting rails and wheels due to intensified rail transportation, comprehensive knowledge of evolving near-surface microstructures is vital to manage rolling contact fatigue (RCF) damage. Recently, stratified surface layers (SSLs) observed on samples from the field indicate their contribution to RCF crack behavior. Therefore, this study investigates an SSL detected on a rail wheel in service in terms of microstructural characteristic and related micro-mechanical properties. Results show crack initiation in the white etching layer (WEL) with propagation into the underlying brown etching layer (BEL), whereby the crack growth direction is changing just underneath the WEL-BEL transition zone. Within the BEL, a microstructural gradient is observed with decreasing grain size and increasing hardness with increasing distance from the surface. The region underneath the WEL-BEL transition zone reveals a distorted *bcc* lattice, high dislocation density and globular particles, proposing the presence of tempered martensite. Moreover, *in situ* micro-bending experiments in this region show a predominant plastic material behaviour. This work provides new insights in the microstructural and micro-mechanical characteristics of SSLs and point out the relevance to crack initiation at rail wheel treads during service.

Keywords: wheel-rail contact; white etching layer; brown etching layer; stratified surface layer; rolling contact fatigue;

* Corresponding author

E-Mail address: matthias.freisinger@ac2t.at

1. Introduction

The rail network faces increasing train speeds, reduced train intervals, and higher axle loads to reduce carbon emissions, increasing wear and rolling contact fatigue (RCF) damage on rails and wheels. Hence, improving the knowledge about material defects is vital to ensure the reliability of rail transportation.

Extensively studied on rails, the formation of a white etching layer (WEL) is suspected of affecting RCF damage on rails and wheels [1]–[7]. The naming is based on its white and featureless appearance in optical microscopy after etching with diluted nitric acid. More recently, the brown etching layer (BEL) has been gaining interest in research since this layer is often observed underneath the WEL on samples from the field [8]–[14]. The combination of WEL and BEL is named stratified surface layer (SSL), and its formation mechanism is controversially discussed in recent literature [9], [14]. However, the complex loading situation in wheel-rail contacts accompanied by environmental influences leads to a vast variation of observed WELs, BELs, and SSLs. SSLs seem crucial regarding RCF crack initiation and propagation, potentially linked to undesired damage patterns such as squats and studs [15]–[19].

Regarding fatigue crack propagation, the transition region WEL-BEL is considered highly relevant. The brittle nature of WELs is prone to crack initiation; however, the crack propagation at the WEL-BEL transition region is supposed to be a deciding factor as to whether the crack arrests and causes negligible damage, or, propagates further potentially results in a critical macroscopic crack. For rail wheels, visible cracks may lead to significant wheel damage or, in the worst case, to catastrophic failure of the wheel [6], [7], [20]–[22].

It is crucial to study the microstructural characteristics of the different layers and evaluate their mechanical properties to improve the understanding of SSLs on rail wheels influencing RCF damage. The current study analyzes an SSL detected on a wheel from service with a macroscopic RCF crack, addressing this issue. Detailed investigations are presented in the microstructural region underneath the WEL-BEL transition region to improve the understanding of crack propagation within the BEL of the SSLs formed under service conditions.

2. Experimental

The microstructural regions investigated within this work originate from an ex-service rail wheel (hypoeutectoid steel grade ER7, chemical composition given in [Figure 1 a](#)) with a mileage

of ~200,000 km. The wheel with a diameter of 0.95 m is provided by the Austrian Federal Railways. A section of the wheel (Figure 1b) is cut out using a conventional band saw. Further, a cubic sample (~5x5x5 mm³) out of the middle of the wheel tread zone (red rectangle in Figure 1b) is cut by using a laboratory cutting device (Struers Secotom-50; Struers ApS, Denmark), subsequently embedded in a conductive compound followed by metallographic sample preparation in various steps to a mirror-polished surface quality (1 µm diamond fine polishing). Prior to light optical microscopy (LOM) (Axio Imager M2m, Carl Zeiss AG, Germany) and field emission scanning electron microscopy (SEM) (Jeol JIB 4700F, Jeol Ltd., Japan), the sample is etched with diluted nitric acid (3% HNO₃, 97% ethanol; etching duration 3s). SEM investigations in secondary electron (SE) and backscattered electron (BE) modes are performed at 15 kV acceleration voltage and 10 pA probe current. The surface quality of the embedded sample is further improved by additional finish polishing (colloidal Silica <0.25 µm) to ensure high-quality electron backscatter diffraction (EBSD) measurements. The EBSD investigations (Bruker e-Flash HR, USA) are performed at 30 kV acceleration voltage, 3.6 nA probe current, 15 mm working distance, and 18 mm detector distance. The Kikuchi patterns, acquired at 160×120 px with an exposure time of 40 ms, are analyzed with the Bruker Esprit 2.2 software package using the AMCSD database for phase identification. Samples for transmission electron microscopy (TEM) are prepared by focused ion beam (FIB) (Jeol JIB 4700F Multi Beam System, Jeol Ltd., Japan) just underneath the transition from the WEL to the BEL. Microstructure is analyzed using a TEM (Jeol JEM 2200FS, Jeol Ltd., Japan) operated at 200kV.

Micro-mechanical properties of distinctive zones within the SSL are evaluated by executing low-load Vickers hardness measurements (Future-Tech FM-700, Future Tech Corp., Japan) with a load of 0.05 kp (0.49 N), diagonals of the indents are measured with a LOM. Further, nanoindentation measurements are performed with a Bruker Hysitron Triboindenter TI980 – Performech II (equipped with a Berkovich diamond tip), executing an array of 5x5 indents for each zone. The load-displacement curves (with a peak load of 5 mN) are evaluated, and hardness was deduced via the load/area ratio, whereby the reduced Young's modulus was assessed via the Oliver and Pharr method [23].

In-situ V-notched micro-cantilever bending is executed to evaluate material behavior in the microstructure just underneath the transition of the WEL to the BEL. Cantilevers with a rectangular cross-section and lengths of ~25 µm are prepared by FIB milling, whereby the ratio of cantilever length (L'):height (w):breadth (b) is about 5:1:1 according to [24]. FIB milling is conducted with 30 keV Ga⁺ ions in various steps, starting with coarse milling at 10 nA and a

dose of $100 \text{ nC}/\mu\text{m}^2$, followed by fine milling at $1 \text{ nA}/8 \text{ nC}/\mu\text{m}^2$. Straight through-thickness notches with a final notch depth of $\sim 1.2 \mu\text{m}$ are made at $30 \text{ pA}/8 \text{ nC}/\mu\text{m}^2$. In the last step, the cantilevers are polished at the side surfaces at $300 \text{ pA}/5 \text{ nC}/\mu\text{m}^2$ to avoid side-notch effects.

A FemtoTools FT-NMT04 *in-situ* nanoindentation system built in a Zeiss Sigma 500 VP SEM is used to perform the micro-bending experiments. The nanoindenter is equipped with a diamond wedge (tip length $\sim 10 \mu\text{m}$), and after careful alignment of the samples, they are loaded in a displacement-controlled mode at a speed of $20 \text{ nm}\cdot\text{s}^{-1}$ and a distance L from the notch in the normal direction (ND) of the wheel tread surface. A sinusoidal signal is superimposed (at an amplitude of 5 nm and a frequency of 200 Hz), for continuous stiffness measurement (CSM), thus allowing to record the force F , displacement u , and stiffness k of the cantilever during the measurement.

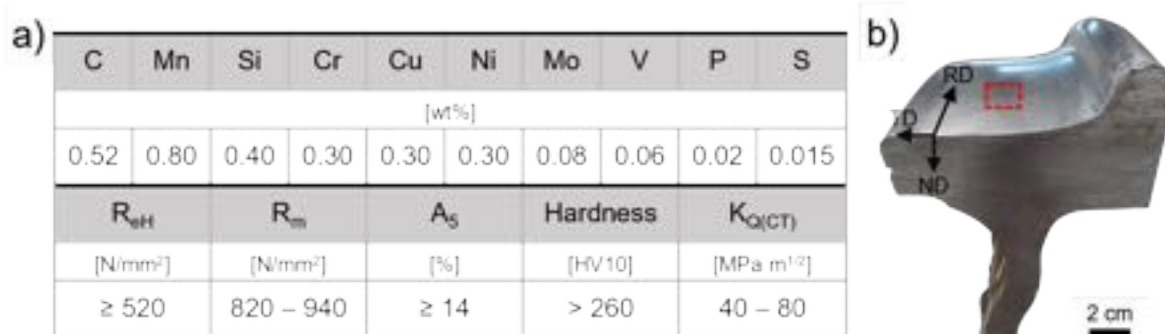


Figure 1: The chemical composition of the investigated rail wheel sample (grade ER7) is given in (a), while the extracted section from the wheel is shown in (b). The rectangle marked demonstrates the region for the conducted microstructural and micro-mechanical analysis.

3. Results

The investigation of the near-surface microstructure in the middle of the tread surface of the railway wheel from service shows dominant stratification under LOM (Figure 2a). An SSL is observed with fatigue crack initiation within the WEL and propagation through the BEL. The detected crack with a length of more than 1 mm propagates with changing angles from the surface, reaching a plastically deformed and aligned underlying ferritic-pearlitic microstructure of the rail wheel. Further initiated cracks are detected within the WEL; some stop at the WEL-BEL interface. Besides the varying stress states in dependence on the distance from the surface, the microstructural characteristics are likely to influence crack growth; therefore, SEM investigations are presented in different depths (Figure 2b). Within the WEL (Figure 2c), a fine-grained martensitic microstructure is observed in BE mode (Figure 2c). The SE mode images taken at higher magnification (Figure 2d) show a mesh-like microstructure with a certain degree of deterioration. Within the BEL, just underneath the WEL-BEL transition, the BE mode image shows a coarser microstructure (Figure 2e), whereat the SE mode image reveals decomposed martensite with spheroidized carbides at deformed laths boundaries (Figure 2f). The microstructural gradient detectable by LOM imaging (Figure 2a) is underlined by BE and SE mode images in the lower part of the BEL, see Figure 2g and h, respectively. This BEL microstructure shows smaller grain sizes and a mixture of mesh-like microstructure with additional spherical carbides. The region underneath the SSL represents a plastically deformed ferritic-pearlitic microstructure (Figure 2i) with aligned and broken cementite lamellae (Figure 2j). A closer look at the microstructural gradient within the BEL (Figure 3a) is taken by performing an EBSD analysis (Figure 3b). Inverse pole figure (IPFX) plots show a pronounced grain size gradient with decreasing grain size with increasing distance from the surface. In direction of the underlying deformed ferritic-pearlitic microstructure, the decreasing grain size in the BEL leads to an insufficient pattern detection with an increased fraction of zero-solutions, which is also the case within the fine-grained WEL.

Figure 3c shows the related results of the hardness measurements (low-load Vickers analysis as well as nanoindentation) within different microstructural regions plotted on the EBSD quality image: The WEL shows hardness values of 831 ± 54 HV_{0.05} and 7.2 ± 0.3 GPa, respectively. The microstructural variation within the BEL is also shown by the hardness measurements within this layer, where just underneath the WEL-BEL transition, a hardness of 483 ± 8 HV_{0.05} and 5.3 ± 0.5 GPa is measured. With decreasing grain size, the hardness increases, reaching 635 ± 50 HV_{0.05} and 6.5 ± 0.3 GPa in the lower part of the BEL. Under the SSL, within the

plastically deformed ferritic-pearlitic microstructure, a hardness of 332 ± 17 HV0.05 and 4.1 ± 0.3 GPa is measured.

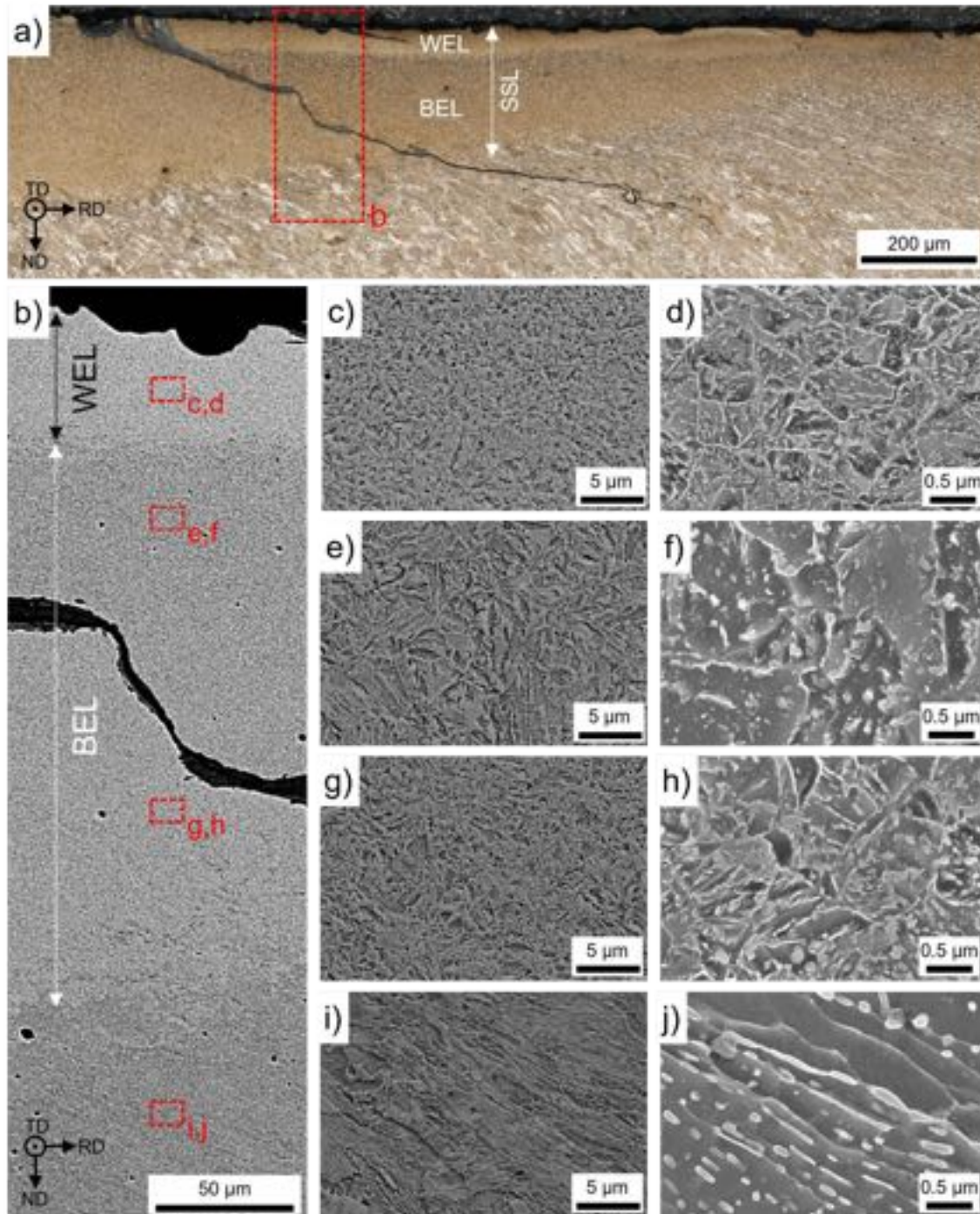


Figure 2: (a) LOM image of the investigated SSL in the middle of the tread surface of the rail wheel from service, where a microstructural gradient within the BEL is observed in the region of the fatigue crack. (b) SEM image (BE mode) of the area indicated in (a). Detailed SEM analysis is done at different distances from the surface: (c) and (d) represents the WEL microstructure, (e) and (f) the BEL just underneath the WEL-BEL transition, (g) and (h) the lower part of the BEL, and (i) and (j) the underlying plastically deformed ferritic-pearlitic rail

wheel microstructure. For each location images are taken in BE mode and higher magnification SE mode.

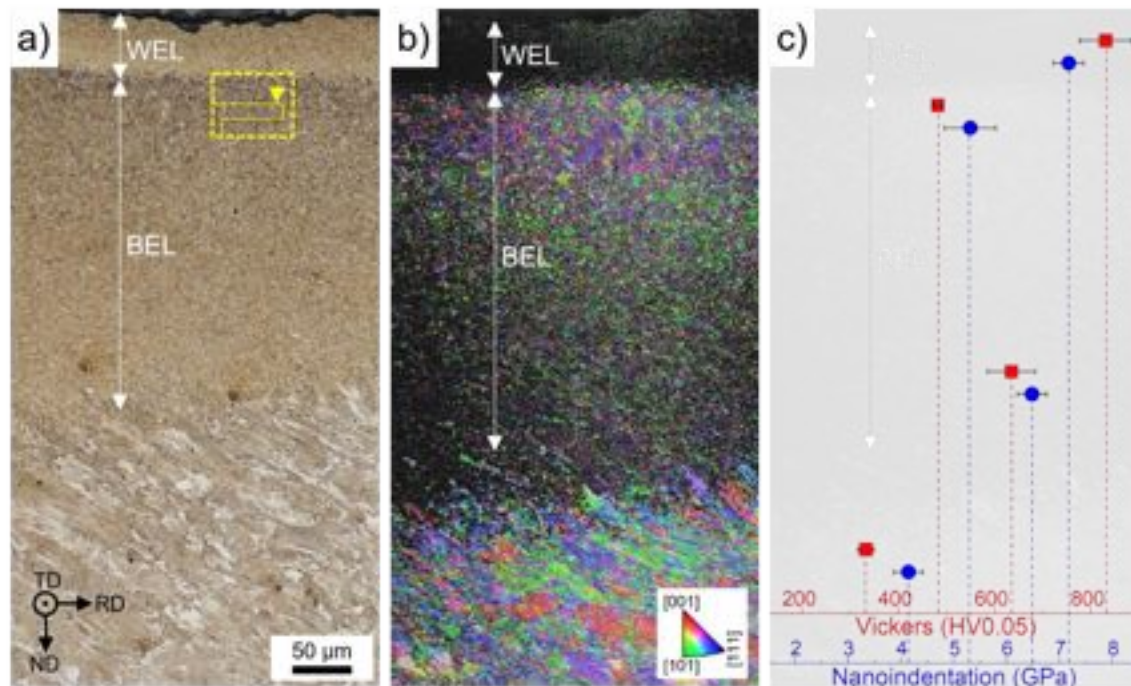


Figure 3: (a) shows the SSL consisting of WEL and BEL, whereat the microstructural gradient within the BEL can be seen. The dashed yellow line rectangular gives the region for further TEM and micro-bending studies. (b) IPFX image shows low quality due to fine grain size within the WEL and the lower part of the BEL. The grain size gradient within the BEL is clearly demonstrated. (c) gives the Vickers hardness and nanoindentation results of distinctive regions within the SSL and the underlying microstructure.

To further investigate the BEL region obtaining decreased hardness (marked in [Figure 3a](#)), microstructural characteristics and related micro-mechanical properties are analyzed by TEM investigations and micro-bending experiments. The high magnification bright field (BF) and dark field (DF) TEM images with corresponding diffraction patterns are given in [Figure 4a – c](#). The microstructure appears as a fine polycrystalline structure, whereas the very fine fragmented particles are believed to be cementite. There is no evidence of austenite, as the selected area diffraction (SAED) pattern covering the whole TEM image solely represents a *bcc* lattice in $[\bar{1}11]$ direction with a certain degree of lattice distortion. Moreover, the BF TEM image in [Figure 4d](#) shows lamella structure residue associated with high dislocation density. The referring SAED pattern ([Figure 4e](#)) represents a distorted *bcc* structure in the $[012]$ direction. In some regions ([Figure 4f](#)), globular particles are detected adjacent to areas with high dislocation density.

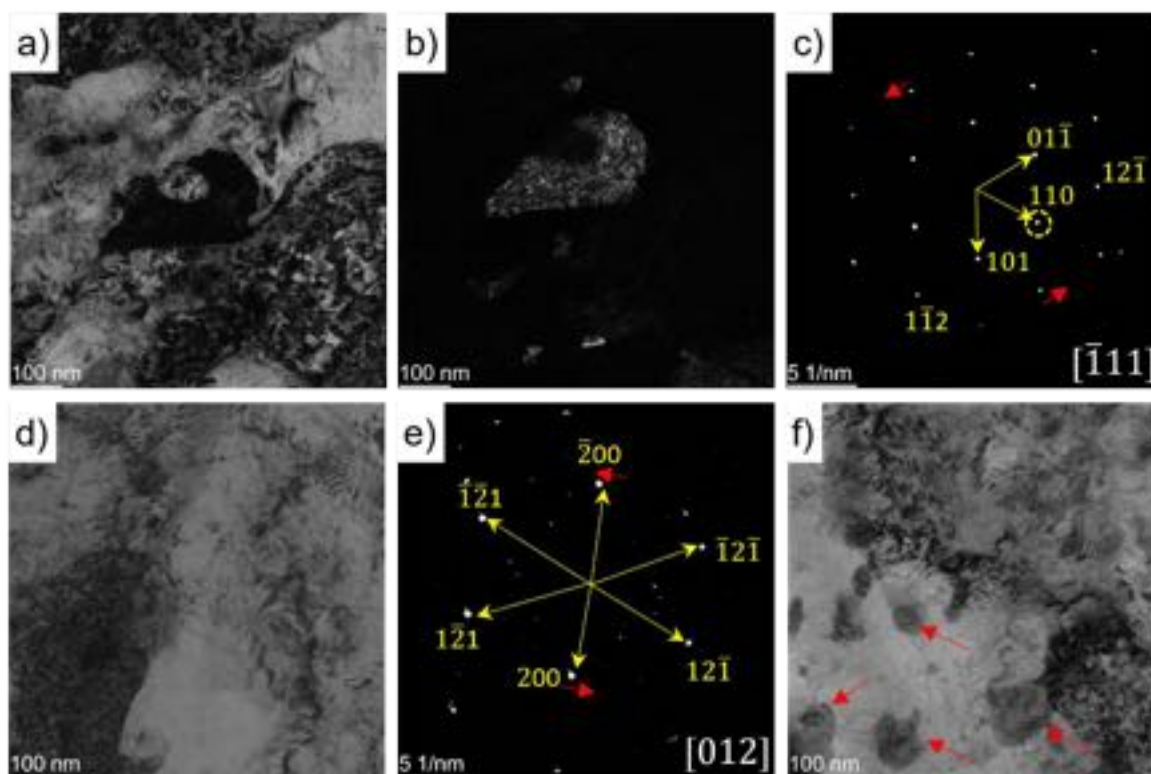


Figure 4: TEM imaging within the BEL region just underneath the WEL-BEL transition: (a) BF and (b) DF image with corresponding SAED pattern (c) show the fine-grained, polycrystalline, distorted bcc microstructure. Further, the BF image presented in (d) shows regions with high dislocation density, while the corresponding SAED pattern (e) represents a distorted bcc lattice in the $[012]$ direction. In addition, in some areas, globular particles are detected (f).

In-situ bending experiments of V-notched micro-cantilevers are executed in addition to hardness evaluation to link the microstructure to its micro-mechanical behaviors. The recorded stress-displacement curves are plotted in Figure 5a. Seven valid micro-bending tests are performed out of eight cantilevers (C-1 to -7). The curves show an initial linear increase, representing the initial elastic behavior of the cantilevers, segueing into a plastic material behavior up to the maximum stress in the range of 65 – 90 N/mm². No crack initiation is detected in the graphs. Beyond the maximum stress reached at a displacement of ~ 3 μm , a decrease in stress can be observed for all cantilevers except cantilevers C4 and C6. Figures 5b and c show a representative cantilever prior- and post-testing. During the loading of the cantilevers, the notch region of the cantilevers is observed, exemplarily shown in Figure 5d. Predominant plastic material is seen by blunting of the FIB prepared notch without crack initiation and material flow at the side of the cantilevers. Besides the continuous stiffness

measurement performed for all conducted micro-bending tests, the lack of crack initiation in the notch makes a fracture toughness calculation unreasonable since calculating the J -integral based on the stiffness change of the cantilevers requires crack propagation.

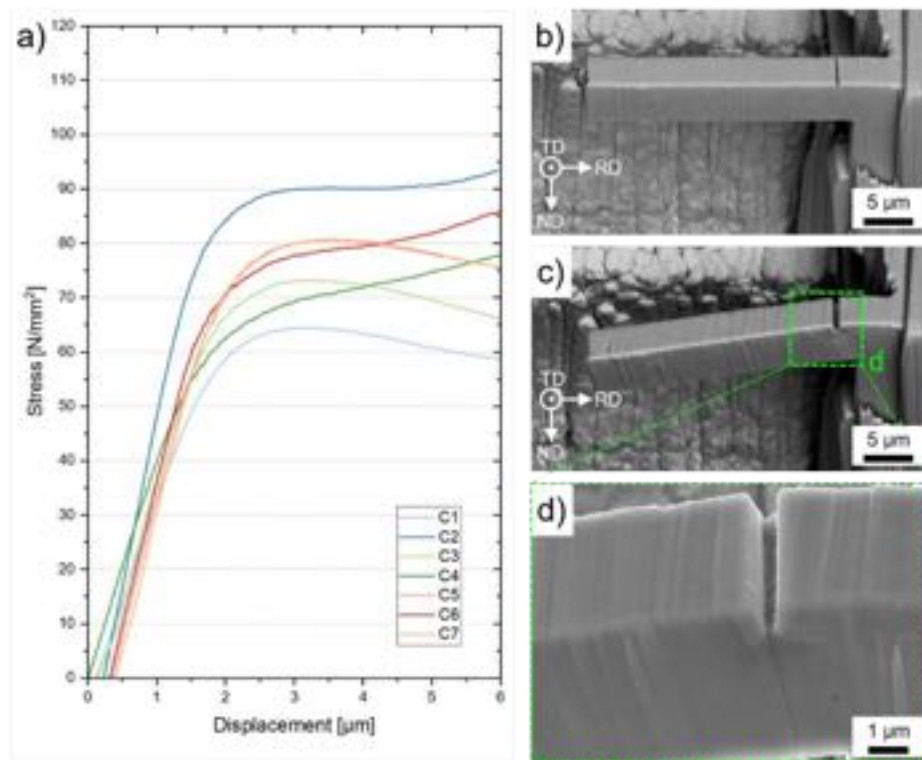


Figure 5: (a) Stress-displacement graphs of the conducted *in-situ* V-notched micro-cantilever bending experiments show a predominant plastic material behavior with maximum stress reaching 65 – 90 N/mm². SEM images of a representative cantilever prior- (b) and post-testing (c) point out the material behavior under bending, with no crack initiation at the notch (d).

4. Discussion

The results of this work demonstrate the vast variety of evolving near-surface layers in rolling-sliding contacts, often related to RCF cracking [9], [12]–[14], [16], [25], and points out the importance of in-depth microstructural and micro-mechanical studies. The analysis of the WEL within this work (Figure 2 and Figure 3) shows comparable characteristics to further studies revealing a destructed martensitic microstructure and hardness in the range of 7 – 10 GPa. This indicates extensive mechanical loading after the formation of the WEL, which is concluded due to lab-imitated WELs induced by laser surface treatments. In contrast, a virgin WEL not affected by subsequent mechanical loading after its formation shows differences in martensite morphology and higher hardness [26]–[28]. However, the time of WEL formation and the following amount of mechanical loading on the studied rail wheel is unclear, which is the main

drawback when analyzing samples from the field. In the course of the analysis of the SSL, a significant microstructural difference within the BEL is observed (Figure 2 and Figure 3). In addition, the crack growth direction changes at a certain depth within this BEL region. Research activities on BELs are less established, however, most studies propose tempering of a prior existing WEL as the formation mechanism [9], [10], [29]. This follows the current results, where the microstructural characteristics reveal tempered martensite with hardness in the 500 – 700 HV range. The pronounced gradient within a BEL is suggested to originate from a minor thermal loading with advanced loading time, leading to a recrystallization process and grain growth within the BEL. However, the formation of the observed SSL can be suggested in several sequences. Either the BEL microstructure was affected by the formation of the current WEL on top, or the current WEL was formed on the BEL with pre-existing grain size gradient. In the authors' opinion, a reasonable statement of the SSL formation mechanism cannot be made by investigating samples from the field. A systematic study with defined SSLs (formed by reproducible thermal and mechanical loadings) is needed.

On the other hand, investigations of microstructural and micro-mechanical properties are crucial to evaluate the influence on fatigue crack initiation and propagation and further the resulting degree of RCF damage. Therefore, this study focusses with further analysis methods on the BEL region underneath the WEL-BEL transition, where a changing crack direction is observed. TEM analyses show a distorted *bcc* lattice with high dislocation density indicated. In contrast to TEM analysis on WELs [1] no retained austenite or distinctive plate-like crystals of martensite are identified in this region of the BEL. More detailed analyses in different depths will be conducted in future works. However, results indicate deformed tempered martensite in the examined region. The globular particles observed (Figure 4f) can not be fully described. Either these are spheroidized cementite lamellae, which are detected by SEM analyses (e.g. Figure 2f) or – as investigated in BEL in bainitic rail steels [8] – oxide rich particles primarily formed through local oxidation. However, the latter is not suggested for the investigated region of this sample. Plastic behavior is seen when conducting micro-bending experiments, hindering crack initiation at the artificial notch. Even so, the loading of the cantilevers is executed under continuous stiffness measurement, and the calculation of fracture toughness is not possible without crack initiation since the calculation by the elastoplastic fracture mechanics – used in previous studies of the authors [27] – is based on stiffness decrease and crack extension, respectively. Adequate sharpness of the FIB-prepared notch is critical [30]–[32] but guaranteed for the presented cantilevers and comparable to previous work [27] where cracks are initiated. Saxena et al. [33] presented micro-bending results of BELs on a rail from service, where cracks

were formed, and fracture toughness of $\sim 20 \text{ MPam}^{1/2}$ was calculated. Besides a different testing procedure and chemical composition of the steel, the hardness within the BEL was 600 – 700 HV, significantly higher compared to the current BEL microstructure ($483 \pm 8 \text{ HV}_{0.05}$, [Figure 3](#)). For ductile materials, the dominant plastic behavior is a limiting factor of the applicability of the V-notched micro-cantilever bending method [32], [34], [35]. The qualitative analysis of the conducted experiments points out the plastic material behavior. Therefore, the recrystallization observed within the BEL just underneath the WEL-BEL transition is supposed to lower the tendency of critical crack growth on the rail wheel. Hence, the microstructural characteristics may explain the crack growth direction, where the angle of the propagating crack tends to get smaller in the upper part of the BEL but increases in the lower part (smaller grain size, higher hardness). Finally, the crack propagates along the alignment of the deformed ferritic-pearlitic microstructure.

5. Conclusions

Within this study, an SSL formed on a rail wheel after $\sim 200.000 \text{ km}$ in service is studied by microstructural and micro-mechanical analysis methods with respect to the influence on RCF crack propagation:

- The WEL within the SSL represents a destructed martensitic microstructure with a hardness of $>800 \text{ HV}$ and $>7.0 \text{ GPa}$, respectively, indicating experienced mechanical loading after formation. An RCF crack is initiated in the WEL and propagates the underlying BEL downwards.
- The tempered martensitic microstructure of the BEL shows a significant grain size gradient with decreasing grain size in depth. Recrystallization leads to lower hardness at the upper part of the BEL ($<500 \text{ HV}$, $<5.5 \text{ GPa}$) and significant plastic material behavior, provoking the crack to grow under a shallower angle to the surface.
- The lower part of the BEL comes up with increasing hardness ($>600 \text{ HV}$, $>6 \text{ GPa}$), smaller grain size, and less tempering effect, causing the change in crack growth direction downwards into the underlying deformed wheel microstructure.

The observed inconsistent microstructural characteristic of the BEL underlines the influence on RCF crack behavior in rail wheels and emphasizes the importance of linking microstructure to its micro-mechanical properties.

Acknowledgments

The authors acknowledge the TU Wien Bibliothek for financial support through its Open Access Funding Program. This project has received funding from the Shift2Rail Joint Undertaking (JU) under grant agreement No 826255 and No 101012456. The JU receives support from the European Union's Horizon 2020 research and innovation program and the Shift2Rail JU members other than the Union. In addition, this work was funded by the "Austrian COMET-Program" (project InTribology1, no. 872176) via the Austrian Research Promotion Agency (FFG) and the federal states of Niederösterreich and Vorarlberg and was carried out within the "Excellence Centre of Tribology" (AC2T research GmbH). The financial support by the Austrian Federal Ministry for Digital and Economic Affairs, the National Foundation for Research, Technology and Development, and the Christian Doppler Research Association is gratefully acknowledged (Christian Doppler Laboratory "Surface Engineering of high-performance Components"). We would further like to express our gratitude to Mr. Schachner (ÖBB TS Knittelfeld) for providing the railway wheel from the field.

Data Availability

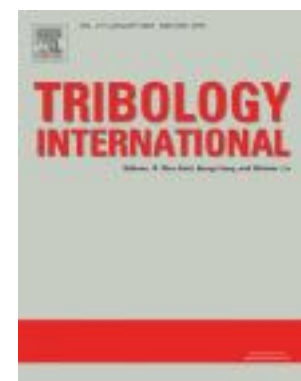
The raw/processed data required to reproduce these findings cannot be shared at this time as the data also forms part of an ongoing study.

References

- [1] A. Al-Juboori *et al.*, ‘Characterisation of White Etching Layers formed on rails subjected to different traffic conditions’, *Wear*, vol. 436–437, p. 202998, Oct. 2019, doi: 10.1016/j.wear.2019.202998.
- [2] C. Bernsteiner, G. Müller, A. Meierhofer, K. Six, D. Künstner, and P. Dietmaier, ‘Development of white etching layers on rails: simulations and experiments’, *Wear*, vol. 366–367, pp. 116–122, 2016, doi: 10.1016/j.wear.2016.03.028.
- [3] B. Hieu Nguyen, A. Al-Juboori, H. Zhu, Q. Zhu, H. Li, and K. Tieu, ‘Formation Mechanism and Evolution of White Etching Layers on Different Rail Grades’, *International Journal of Fatigue*, p. 107100, Jun. 2022, doi: 10.1016/j.ijfatigue.2022.107100.
- [4] R. Pan, R. Ren, C. Chen, and X. Zhao, ‘The microstructure analysis of white etching layer on treads of rails’, *Engineering Failure Analysis*, vol. 82, pp. 39–46, Dec. 2017, doi: 10.1016/j.engfailanal.2017.06.018.
- [5] A. Kumar *et al.*, ‘In situ study on fracture behaviour of white etching layers formed on rails’, *Acta Materialia*, vol. 180, pp. 60–72, Nov. 2019, doi: 10.1016/j.actamat.2019.08.060.
- [6] Y. Z. Chen, C. G. He, X. J. Zhao, L. B. Shi, Q. Y. Liu, and W. J. Wang, ‘The influence of wheel flats formed from different braking conditions on rolling contact fatigue of railway wheel’, *Engineering Failure Analysis*, vol. 93, pp. 183–199, Nov. 2018, doi: 10.1016/j.engfailanal.2018.07.006.
- [7] C. Liu *et al.*, ‘Formation mechanism for the white etching microstructure in the subsurface of the failure pearlite wheel steel’, *Wear*, vol. 494–495, p. 204243, Apr. 2022, doi: 10.1016/j.wear.2022.204243.
- [8] G. Gao *et al.*, ‘Heterogenous structure and formation mechanism of white and brown etching layers in bainitic rail steel’, *Acta Materialia*, vol. 250, p. 118887, May 2023, doi: 10.1016/j.actamat.2023.118887.
- [9] A. Kumar, G. Agarwal, R. Petrov, S. Goto, J. Sietsma, and M. Herbig, ‘Microstructural evolution of white and brown etching layers in pearlitic rail steels’, *Acta Materialia*, vol. 171, pp. 48–64, Jun. 2019, doi: 10.1016/j.actamat.2019.04.012.
- [10] S. Li, J. Wu, R. H. Petrov, Z. Li, R. Dollevoet, and J. Sietsma, ‘“Brown etching layer”: A possible new insight into the crack initiation of rolling contact fatigue in rail steels?’, *Engineering Failure Analysis*, vol. 66, pp. 8–18, Aug. 2016, doi: 10.1016/j.engfailanal.2016.03.019.
- [11] P.-Y. Tung, X. Zhou, L. Morsdorf, and M. Herbig, ‘Formation mechanism of brown etching layers in pearlitic rail steel’, *Materialia*, vol. 26, p. 101625, Dec. 2022, doi: 10.1016/j.mtla.2022.101625.
- [12] M. Freisinger, H. Rojacz, A. Trausmuth, and P. H. Mayrhofer, ‘Severe Plastic Deformed Zones and White Etching Layers Formed During Service of Railway Wheels’, *Metallogr. Microstruct. Anal.*, vol. 12, no. 3, pp. 515–527, Jun. 2023, doi: 10.1007/s13632-023-00967-x.
- [13] M. Freisinger and A. Trausmuth, ‘Microstructural characterization of near-surface microstructures on rail wheels in service – an insight into “stratified surface layers”’, *Open Res Europe*, vol. 3, p. 73, May 2023, doi: 10.12688/openreseurope.15881.2.
- [14] M. Messaadi and M. Steenbergen, ‘Stratified surface layers on rails’, *Wear*, vol. 414–415, pp. 151–162, Nov. 2018, doi: 10.1016/j.wear.2018.07.019.
- [15] S. L. Grassie, ‘Studs and squats: The evolving story’, *Wear*, vol. 366–367, pp. 194–199, Nov. 2016, doi: 10.1016/j.wear.2016.03.021.
- [16] S. Pal, W. J. T. Daniel, and M. Farjoo, ‘Early stages of rail squat formation and the role of a white etching layer’, *International Journal of Fatigue*, vol. 52, pp. 144–156, Jul. 2013, doi: 10.1016/j.ijfatigue.2013.02.016.
- [17] M. Kerr, A. Wilson, and S. Marich, ‘The epidemiology of squats and related rail defects’, *Conference On Railway Engineering*, p. 14, 2008.
- [18] M. Steenbergen, ‘On the genesis of squat-type defects on rails – Toward a unified explanation’, *Wear*, vol. 478–479, p. 203906, Aug. 2021, doi: 10.1016/j.wear.2021.203906.
- [19] M. Steenbergen and R. Dollevoet, ‘On the mechanism of squat formation on train rails – Part I: Origination’, *International Journal of Fatigue*, vol. 47, pp. 361–372, Feb. 2013, doi: 10.1016/j.ijfatigue.2012.04.023.
- [20] T. Kato, A. Sugeta, and E. Nakayama, ‘Investigation of influence of white layer geometry on spalling property in railway wheel steel’, *Wear*, vol. 271, no. 1–2, pp. 400–407, May 2011, doi: 10.1016/j.wear.2010.10.024.
- [21] T. Kato, Y. Yamamoto, H. Kato, S. Dedmon, and J. Pilch, ‘Effect of fracture toughness on vertical split rim failure in railway wheels’, *Engineering Fracture Mechanics*, vol. 186, pp. 255–267, Dec. 2017, doi: 10.1016/j.engfracmech.2017.09.025.
- [22] S. J. Kwon, D. H. Lee, S. T. Kwon, and B. C. Goo, ‘Failure Analysis of Railway Wheel Tread’, *KEM*, vol. 321–323, pp. 649–653, Oct. 2006, doi: 10.4028/www.scientific.net/KEM.321-323.649.
- [23] W. C. Oliver and G. M. Pharr, ‘An improved technique for determining hardness and elastic modulus using load and displacement sensing indentation experiments’, *J. Mater. Res.*, vol. 7, no. 6, pp. 1564–1583, Jun. 1992, doi: 10.1557/JMR.1992.1564.
- [24] K. Matoy *et al.*, ‘A comparative micro-cantilever study of the mechanical behavior of silicon based passivation films’, *Thin Solid Films*, vol. 518, no. 1, pp. 247–256, Nov. 2009, doi: 10.1016/j.tsf.2009.07.143.
- [25] W. Lojkowski, M. Djahanbakhsh, G. Bürkle, S. Gierlotka, W. Zielinski, and H.-J. Fecht, ‘Nanostructure formation on the surface of railway tracks’, *Materials Science and Engineering: A*, vol. 303, no. 1–2, pp. 197–208, May 2001, doi: 10.1016/S0921-5093(00)01947-X.

- [26] M. Freisinger *et al.*, ‘Comparative study on the influence of initial deformation and temperature of thermally induced white etching layers on rail wheels’, *Tribology International*, vol. 177, p. 107990, Jan. 2023, doi: 10.1016/j.triboint.2022.107990.
- [27] M. Freisinger, L. Zauner, R. Hahn, H. Riedl, and P. H. Mayrhofer, ‘In-situ micro-cantilever bending studies of a white etching layer thermally induced on rail wheels’, *Materials Science and Engineering: A*, vol. 869, p. 144805, Mar. 2023, doi: 10.1016/j.msea.2023.144805.
- [28] Y. Chen, X. Zhao, P. Liu, R. Pan, and R. Ren, ‘Influences of local laser quenching on wear performance of D1 wheel steel’, *Wear*, vol. 414–415, pp. 243–250, Nov. 2018, doi: 10.1016/j.wear.2018.07.016.
- [29] J. Ahlström and B. Karlsson, ‘Microstructural evaluation and interpretation of the mechanically and thermally affected zone under railway wheel flats’, *Wear*, vol. 232, no. 1, pp. 1–14, Sep. 1999, doi: 10.1016/S0043-1648(99)00166-0.
- [30] S. Brinckmann, K. Matoy, C. Kirchlechner, and G. Dehm, ‘On the influence of microcantilever pre-crack geometries on the apparent fracture toughness of brittle materials’, *Acta Materialia*, vol. 136, pp. 281–287, Sep. 2017, doi: 10.1016/j.actamat.2017.07.014.
- [31] G. Dehm, B. N. Jaya, R. Raghavan, and C. Kirchlechner, ‘Overview on micro- and nanomechanical testing: New insights in interface plasticity and fracture at small length scales’, *Acta Materialia*, vol. 142, pp. 248–282, Jan. 2018, doi: 10.1016/j.actamat.2017.06.019.
- [32] R. Pippin, S. Wurster, and D. Kiener, ‘Fracture mechanics of micro samples: Fundamental considerations’, *Materials & Design*, vol. 159, pp. 252–267, Dec. 2018, doi: 10.1016/j.matdes.2018.09.004.
- [33] A. K. Saxena, A. Kumar, M. Herbig, S. Brinckmann, G. Dehm, and C. Kirchlechner, ‘Micro fracture investigations of white etching layers’, *Materials & Design*, vol. 180, p. 107892, Oct. 2019, doi: 10.1016/j.matdes.2019.107892.
- [34] B. N. Jaya and V. Jayaram, ‘Fracture Testing at Small-Length Scales: From Plasticity in Si to Brittleness in Pt’, *JOM*, vol. 68, no. 1, pp. 94–108, Jan. 2016, doi: 10.1007/s11837-015-1489-2.
- [35] M. Freisinger, A. Trausmuth, R. Hahn, and E. Badisch, ‘Influence of the evolution of near-surface rail wheel microstructure on crack initiation by micro-bending investigations’, *Proceedings of the Institution of Mechanical Engineers, Part F: Journal of Rail and Rapid Transit*, p. 09544097231191550, Jul. 2023, doi: 10.1177/09544097231191550.

Publication V



Comparative study on the influence of initial deformation and temperature
of thermally induced white etching layers on rail wheels

M. Freisinger, H. Rojacz, K. Pichelbauer, A. Trausmuth, G. Trummer, K. Six, P.H. Mayrhofer
Tribology International, vol. 177 (2023)
DOI: 10.1016/j.triboint.2022.107990



Comparative study on the influence of initial deformation and temperature of thermally induced white etching layers on rail wheels

M. Freisinger^{a,*}, H. Rojacz^a, K. Pichelbauer^a, A. Trausmuth^a, G. Trummer^b, K. Six^b, P.H. Mayrhofer^c

^a AC2T research GmbH, 2700 Wiener Neustadt, Austria

^b Virtual Vehicle Research GmbH, 8010 Graz, Austria

^c Institute of Materials Science and Technology, TU Wien, 1060 Wien, Austria

ARTICLE INFO

Keywords:

Rail-wheel tribology
Steel
Laser processing
Electron microscopy

ABSTRACT

Detailed investigations of white etching layers (WELs) formed on rails and wheels are of utmost importance to improve railway safety. This calls for lab-generated WELs with well-comparable characteristics to conduct further testing such as in twin-disc experiments. In this work, laser surface treatments were applied on wheel steels to induce thermally induced WELs. To evaluate the influence of the initial deformation state of the sample, undeformed and severely plastically deformed ER7 wheel steels were selected. In this study, it is shown that surface temperatures of > 640 °C lead to thermally induced WELs, with differences based on the initial deformation state. The thermally induced WELs are compared to a field-WEL present on an ex-service railway wheel. Results indicate that the WEL induced by laser treatment on an initially deformed wheel material provides the best match with the field-WEL. The most distinct difference is a grain size gradient within the outermost 30 μm of the field-WEL caused by deformation after the formation in service. This study clearly shows that the variation in initial microstructures and laser process parameters leads to differences in microstructural characteristics of thermally induced WELs and must be considered when imitating and testing WELs in laboratories.

1. Introduction

White Etching Layers (WELs) are frequently observed on both wheel and rail surfaces acting as a critical initiator for rolling contact fatigue cracks and stud defects [1,2]. The name originates from the fact that such layers appear white after etching with ethanol nitric acid. A wide range of variability is reported with regard to the microstructural properties of WELs. In the literature, however, WELs are often associated with martensite-like structures with a hardness of up to 600–750 HV10 and thicknesses of up to several hundred microns, manifesting as brittle surface layers [3–7].

Such WELs, with considerably different material properties compared to the surrounding undeformed or plastically deformed bulk material, indicate some kind of damage on wheel and rail surfaces [8]. That does not mean that every WEL automatically leads to a damage pattern that requires maintenance actions. Cracks initiating in narrow WELs mostly result in the WEL spalling of and therefore an increased wear rate [5]. With increasing depth of the WEL and in combination of

other influencing factors like the residual stresses and the strain history of the underlying microstructure [5,9,10] cracks propagating through the WEL can be the initiation point for serious damage patterns, which must be removed by maintenance activities (wheel turning intervals) or, in the worst case, can negatively affect the safety of railway service. For example, WELs are often associated with the formation of squats on rail surfaces [3–7,11–22]. On the wheel side, WELs can contribute to the formation of spallation in the tread region of wheels, for example [23, 24].

The formation mechanisms of WEL have been extensively studied for several decades, hence two main hypotheses have been proposed [25–29]. The first one assumes that severe plastic deformation (SPD) at temperatures below the austenitization temperature causes the formation of WELs, the second one that WELs develop due to heating above austenitization temperature followed by rapid cooling [30–33]. Under normal conditions, the austenitization temperature for steel with 0.45 wt% carbon is around 750 °C, but it can be lowered by multiaxial compression [7,34]. Thermally induced WELs can be formed in a

* Corresponding author.

E-mail address: matthias.freisinger@ac2t.at (M. Freisinger).

<https://doi.org/10.1016/j.triboint.2022.107990>

Received 8 August 2022; Received in revised form 4 October 2022; Accepted 8 October 2022

Available online 10 October 2022

0301-679X/© 2022 Elsevier Ltd. All rights reserved.

rail-wheel contact due to a pronounced heat source such as wheel slip, braking and acceleration events, or electrical leakage in electrified railway networks [3,34–37]. Regarding rails, the formation of thermally induced WELs is a major issue in rail grinding [38–40]. Flash temperatures up to 800 – 1000 °C are predicted in rail-wheel contact during operation [3,37,41]. An approach to create thermally induced WELs in the laboratory is via laser technologies. Various methods have been studied on materials such as rail-, wheel-, or bearing steels [34,42–44]. Detailed microstructural analysis of laser-induced WELs on rail wheel steel and the possible influence of the initial deformation state of the microstructure before laser surface treatment is currently not studied in detail. However, this can be highly important when using lab-induced WELs for experiments such as twin-disc experiments or other wear test setups.

In this study, the influence of the initial deformation state of thermally induced WELs created in laboratories is examined. Variations of laser surface treatments are conducted on a range of rail wheel materials with both initially undeformed and severely plastically deformed microstructures. The laser-induced WEL specimens are analyzed using Vickers hardness measurements, light optical microscopy, and scanning electron microscopy. Electron backscatter diffraction (EBSD) [45] is used as an additional technique to describe the materials' microstructural features in greater detail. The aim of this study is to gain a better understanding of the microstructural characteristics of WELs that were thermally induced in the laboratory, influenced by the initial deformation state and the process parameters. To evaluate the various laser-induced WELs we conduct a comparison to a WEL formed on a rail wheel during service in this work.

2. Material and methods

2.1. Material

The samples for the laser surface treatments and further investigations are obtained from an ex-service rail wheel (0.95 m in diameter), provided by the Austrian Federal Railways, with an estimated mileage of ~200,000 km. The base material of this wheel is an ER7 wheel steel (Table 1), which is a widely used steel grade for rail wheels on European railway networks. Laser surface treatments were applied on various extracted samples: The undeformed ER7 and the deformed ER7, named ER-u and ER7-d, respectively. The ER7-u sample was a cross-sectional cut of the wheel, where the investigated microstructure was at least 1 cm below the surface to represent the unaffected microstructure without prior deformation. For the ER7-d, the laser treatment was directly applied to the tread surface, where the initial microstructure comes up with severe plastic deformation. To remove rust and other surface products, the tread surface was gently hand-ground with SiC #1000 (18 µm grain size) paper. To ensure that no field-generated WEL is present on these samples, they were carefully selected based on a metallographical inspection after a Fe(III)Cl etching procedure. Additionally, various cross-sectional cuts from different zones along the worn tread surface of the wheel were analyzed, and a representative section serves as the reference for this work, simply named "field-WEL". All samples were cut out from the same ex-service rail wheel using a conventional band saw, followed by finer processing with a laboratory

cutting device (Struers Secotom-50; Struers ApS, Denmark).

2.2. Methods

2.2.1. Laser treatments

Laser treatments were carried out using a Direct Diode Laser System (HighLight 8000D, Coherent, U.S.). The targeted surface temperatures induced by the laser were increased in steps of 100 °C around the average austenitization temperature for ER7 from 540 °C to 840 °C, based on the range of the maximum temperatures in a rail-wheel contact. The dimensions of the rectangular laser spot are 3 mm in the moving direction and 24 mm in the lateral direction. The nominal continuous power output of the system is 8 kW at a wavelength of 975 nm. The laser power output is feedback-controlled with the sample surface temperature measured by an externally mounted pyrometer (LPC03, Mergenthaler, Germany), which is configured as a single-color pyrometer with an emission coefficient $\epsilon = 0.7$. In order to determine the correct emission coefficient, the measurement of the pyrometer and a calibrated thermocouple are compared on an already laser-oxidized ER7 steel surface at 700 °C.

The laser system is mounted on a 6-axis robot arm (IRB 4600–60/2.05, ABB, Austria) controlled via the teach pendant of the controller system of the IRC5 (ABB, Austria) for careful positioning and movement. The starting temperature of the surface for each laser-treated track or spot was room temperature. Individual tracks, see Fig. 1a, are generated by moving the laser spot at a constant speed of 12 mm/s and various selected surface temperatures (via different energy-density inputs). These tracks are referred to as "feed-mode". In the regions between these tracks, the surfaces are laser-treated without moving the laser (Fig. 1b), which is operated in pulse-mode. The pulse parameters are a repetition rate of 1 Hz, a pulse width of 0.5 s, and a total laser treatment duration of 15 s. The thus generated spots are referred to as "pulse-mode". These two different laser treatments (feed-mode, "fm", and pulse-mode, "pm") were applied to the undeformed and deformed ER7 samples (ER7-u and ER7-d).

2.2.2. Analysis methods

Microstructural characterizations of cross-sectional cuts were performed by light optical microscopy (LOM) (Axio Imager M2m, Carl Zeiss AG, Germany) as well as by scanning electron microscopy (SEM) (Jeol JIB 4700F, Jeol Ltd., Japan). The latter is equipped with a Schottky field emission gun, secondary and backscattered electron detectors, and an electron backscatter diffraction (EBSD) detector (Bruker e-Flash HR, USA). The corresponding samples were prepared by embedding small pieces in conductive compounds. After the metallographic sample-preparation to a mirror-polished surface quality (1 µm diamond fine polishing), the cross-sectional cuts were etched with diluted nitric acid (3% HNO₃, 97% ethanol). SEM investigations were performed at 15 kV acceleration voltage. For the EBSD measurements, the surface quality was further improved by additional finish polishing (colloidal Silica <0.25 µm) according to Ref. [48]. The parameters used for the EBSD investigations were 15 kV acceleration voltage, 3.6 nA probe current, 16 mm working distance, and 18 mm of detector distance. The Kikuchi patterns, acquired at 240 × 160 px with an exposure time of 25 ms, were analyzed with the Bruker Esprit 2.2 software package using the

Table 1

Chemical composition and mechanical properties of the steel grade ER7 according to the standard EN13262 [46], fracture toughness K_{Ic} by compact tension specimens [47].

C	Si	Mn	P	S	Cr	Cu	Mo	Ni	V
(wt%)									
0.52	0.40	0.80	0.020	0.015	0.30	0.30	0.08	0.30	0.06
Tensile strength R_m (N/mm ²)				Elongation A_5 (%)		Minimum Hardness (HV10)		Fracture toughness K_{Ic} (MPa m ^{1/2})	
820–940				≥ 14		260		40–80	

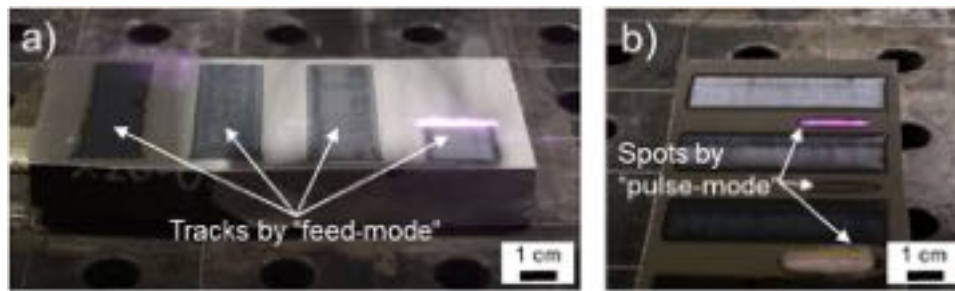


Fig. 1. The images show the sample with the undeformed initial microstructure on a welding table: (a) Tracks created by “feed-mode” (constant laser spot travel speed of 12 mm/s), (b) Spots created by the “pulse-mode” (no movement of the laser spot) treatments.

AMCSD database for phase identification.

Vickers hardness depth profiles were obtained by indenting the cross-sections at increasing distances from the surface with a Future-Tech FM-700 hardness tester using a load of 0.05 kp (0.49 N). The diagonals of the indents are measured with a LOM.

Finite element simulation (Comsol Multiphysics 5.2a) was used to calculate the temperature over time for the various laser methods and surface target temperatures. The surface temperatures measured using the pyrometer during the laser treatments function as input data, while temperature-dependent material properties were used for the calculations.

3. Results

Finite element simulations model the thermal loading over time during our laser surface treatments (Fig. 2). Fig. 2a shows that the heating curves (presented here for selected surface temperatures of 540 and 840 °C) for the feed-mode setup are very similar at different locations because of the high laser spot speed of 12 mm/s, which prevents significant pre-heating in laser travelling direction. However, the cooling rates for regions close to each other are much smaller, see the wider tail of the curves for $x = 20, 30,$ and 40 mm, compared to those at $x = 0$ and 60 mm.

Fig. 2b clearly shows – for selected surface temperatures of 540 and 840 °C – that the surface temperature in the off-time of the laser pulses continuously increases with the treatment time. Due to this effect, the pulse-mode setup requires a lower energy-input to achieve the same surface temperature during the treatment time (Table 2 and Table 3).

The experimental parameters of the laser adjustments for the feed-mode setup, measured mean surface temperatures, and thicknesses of the feed-mode-prepared laser-WELs are shown in Table 2. No WEL can be detected by LOM if the pre-set surface temperature is only 540 °C, whereas higher temperatures clearly lead to the formation of WELs. The thicknesses of the laser-WELs are almost identical on the undeformed and deformed ER7 steel, with a small tendency towards thicker laser-WELs for the latter. With increasing surface temperature – obtained through increasing the laser energy density – the WELs become thicker. The individual target surface temperatures are obtained with smaller laser energy density for the deformed ER7 steels.

For the pulse-mode setup – see Table 3 for the experimental details of the corresponding laser parameters as well as measured mean surface temperature and thicknesses of the pulse-mode prepared laser-WELs – no WEL can be detected by LOM for surface temperatures of ~540 and 640 °C. The data further show that the two samples (undeformed and deformed ER7) respond similarly to this laser treatment, in terms of power-temperature relation and generated WEL thicknesses for temperatures of ~735 and 835 °C. Compared with the feed-mode setup, smaller laser powers are required to obtain the same surface temperature. Nevertheless, for both setups and samples, the WEL thickness is $300 \pm 20 \mu\text{m}$ for a surface temperature of ~835 °C, compare Tables 2 and 3. Thus, these four samples were selected for further detailed microstructural investigations.

The undeformed ER7 steel (Fig. 3a) reveals a coarse ferritic-pearlitic microstructure with ~21% proeutectoid ferrite along the former austenite grain boundaries and an interlamellar spacing of ~80 nm. EBSD measurements indicate equiaxed Pearlite grains with no specific

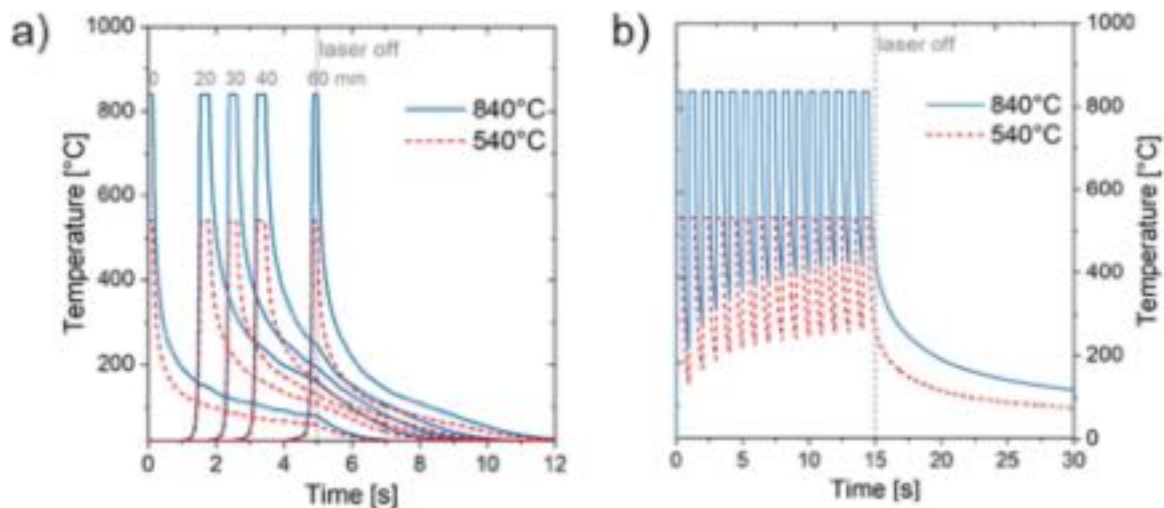


Fig. 2. Finite element simulations of heating and cooling curves for the feed-mode setup (a) and the pulse-mode setup (b). For the feed-mode setup a continuous moving of the laser spot with 12 mm/s is used. The graphs show therefore the temperature over time for different locations along the path of the laser spot (starting point, 20 mm, 30 mm, 40 mm, and the ending point). For the pulse-mode setup the laser treatment is on the same location during the laser treatment. For both modes, representative graphs for pre-set surface temperatures of 540 and 840 °C are shown.

Table 2

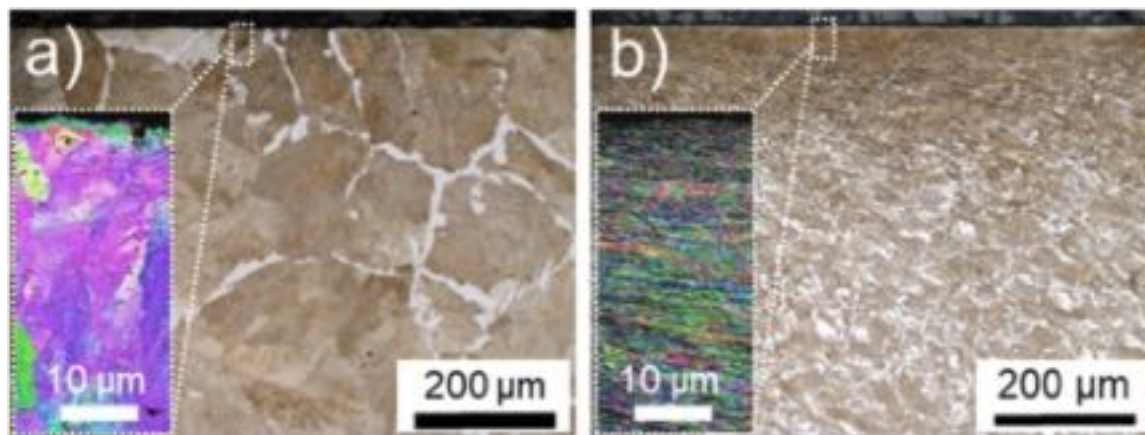
WEL thicknesses and laser parameters of the feed-mode laser treatments. Values in italic font are measured during or after the experiment.

Lens		Beam speed (mm/s)	Laser power (kW)	Power density (W/mm ²)	Energy density (Ws/mm ²)	Pre-set surface temperature (°C)	Measured mean surface temperature	WEL thickness (µm)
pos.	neg.							
(mm)	(mm)							
undeformed material								
24	3	12	2.89	15.23	3.81	540	541	–
			3.06	16.23	4.06	640	638	25
			3.20	16.88	4.22	740	736	165
			3.30	17.51	4.38	840	833	280
deformed material								
24	3	12	2.60	13.74	3.44	540	542	–
			2.83	14.94	3.74	640	638	27
			2.95	15.56	3.89	740	736	170
			3.15	16.61	4.15	840	833	310

Table 3

WEL thicknesses and laser parameters of the pulse-mode laser treatments. Values written in italic font are measured during or after the experiment.

Lens		Pulse duration (mm/s)	Total treatment duration (kW)	Laser power (W/mm ²)	Pulse energy density (Ws/mm ²)	Pre-set surface temperature (°C)	Measured mean surface temperature	WEL thickness
pos.	neg.							
(mm)	(mm)							
undeformed material								
24	3	0.5	15	1.87	1.87	4.95	540	541
				2.00	2.00	5.29	640	643
				2.13	2.13	5.62	740	736
				2.28	2.28	6.01	840	834
deformed material								
24	3	0.5	15	1.87	1.87	4.95	540	542
				1.99	1.99	5.25	640	638
				2.14	2.14	5.66	740	737
				2.26	2.26	5.97	840	833

**Fig. 3.** Initial microstructure of the ER7 material of an ex-service wheel before the laser treatment experiments: (a) undeformed ER7 (ER7-u) from regions at least 1 cm below the tread surface, (b) deformed ER7 (ER7-d) from regions directly below the tread surface.

orientation. The near-surface region (down to 3–5 µm from the surface) exhibits grain orientation variations and grain refinement due to the grinding process, see the inset of Fig. 3a, which shows the inverse pole figure (IPF) plot. The initial Vickers hardness of this sample prior to the laser treatment is 254 ± 22 HV0.05.

The deformed ER7 sample has a fine microstructure (Fig. 3b), which changes with the distance from the surface. The average interlamellar spacing could not be obtained due to massive breaking and dissolving of the cementite lamellae. EBSD analysis reveals a highly deformed microstructure with elongated grains. Especially within 50–100 µm from the surface, the microstructure is severely deformed, leading to a high number of pixels that are not indexed during EBSD measurements

(inset of Fig. 3b). A gradual change in the degree of deformation can be seen with increasing distance from the surface.

The average core hardness of this deformed sample is 340 ± 17 HV0.05, thus about 100 HV0.05 higher than that in undeformed condition (see Fig. 4). Towards the surface, the hardness increases further due to a growing degree of deformation and subsequent microstructural changes, reaching a maximum of 460 HV0.05.

The hardness depth profiles of the laser-treated undeformed samples exhibit slightly higher mean values (793 ± 44 HV0.05) when prepared in feed-mode than those prepared in pulse-mode (699 ± 61 HV0.05), compare the curves fm-ER7-u and pm-ER7-u in Fig. 4. Note that the

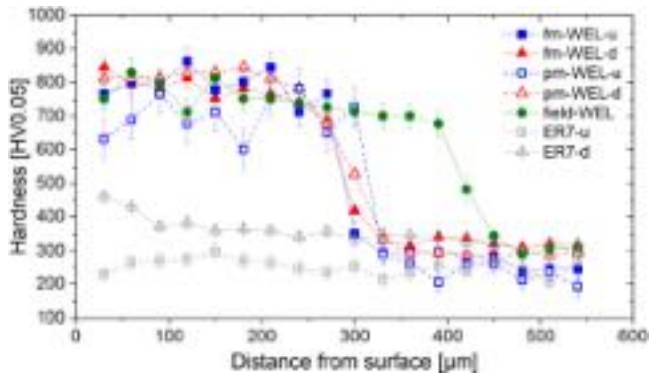


Fig. 4. Vickers hardness depth profiles across the WELs prepared with the laser in feed-mode and pulse-mode on an undeformed and deformed ER7 steel (fm-WEL-u, fm-WEL-d, pm-WEL-u, pm-WEL-d). For comparison, the hardness depth profiles of the undeformed and deformed ER7 steel without laser treatment (ER7-u, ER7-d) as well as of a sample taken from the tread surface of an ex-service ER7 rail wheel with a WEL (field-WEL) are shown.

scattering of hardness data is more pronounced for the sample prepared in pulse-mode.

The hardness depth profiles of the thermally induced WELs on deformed samples are quite similar regardless of the used laser method,

see the curves fm-ER7-d and pm-ER7-d in Fig. 4. Essentially, the hardness is ~ 800 HV0.05 in the outermost ~ 250 μm , after which it sharply declines to meet the hardness of the deformed sample of ~ 340 HV0.05 at a distance of ~ 330 μm from the surface. The pronounced decline in hardness for the laser-treated samples is at ~ 300 μm from the surface, which is essentially at the end of the WEL, see Tables 2 and 3.

Contrary to these laser-treated samples, the field-sample shows the pronounced hardness decline in the range from 400 to 480 μm from the surface. The core hardness of this sample (~ 300 HV0.05) is essentially the same as that of the deformed material at this distance from the surface (Fig. 4). The near-surface regions, within the WEL zone, show a hardness of ~ 800 HV0.05, which is comparable to the hardness within the WEL zone of the laser-treated samples.

LOM images of the laser-WELs for the pre-set surface temperature of 840 $^{\circ}\text{C}$ are shown in Fig. 5 for the undeformed and deformed initial microstructures. The microstructural characteristics described in the following section are similar for all laser energy densities at which the WEL was generated, only the thicknesses of the WELs decreased with decreasing surface temperatures. For comparison, Fig. 5g shows the field-WEL.

Laser surface treatments of the initially undeformed samples (Fig. 5a) lead to WELs with a sharp transition to the underlying ferritic-pearlitic matrix for both feed-mode (Fig. 5b) and pulse-mode (Fig. 5c). Treatments of the initially deformed microstructure (Fig. 5d) result in a

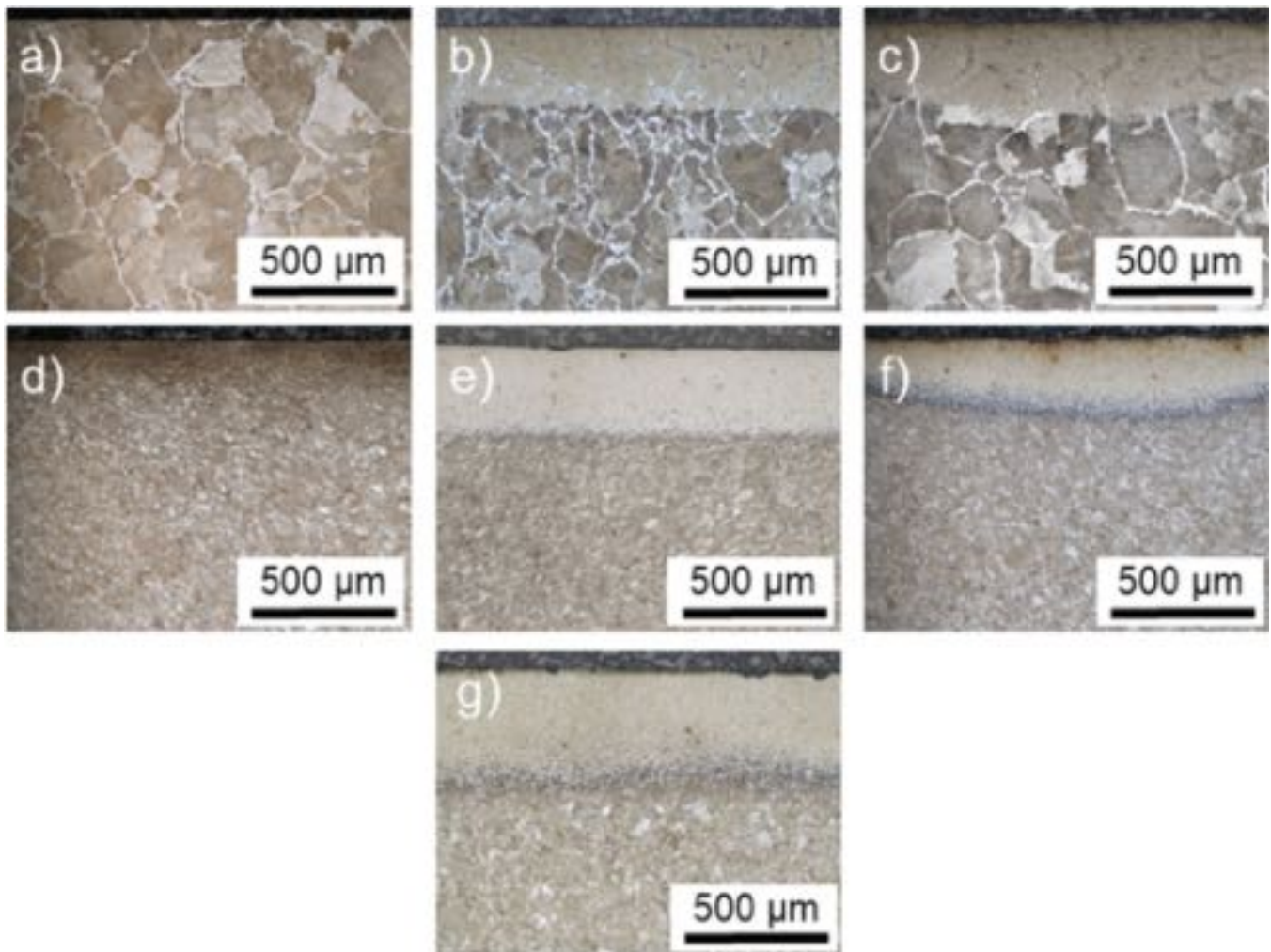


Fig. 5. LOM images: Microstructure of (a) the undeformed sample and its change (b) after the feed-mode laser treatment ($T_{\text{pre-set}}=840$ $^{\circ}\text{C}$) and (c) after the pulse-mode laser treatment ($T_{\text{pre-set}}=840$ $^{\circ}\text{C}$); Microstructure of (d) the deformed sample and its change (e) after feed-mode laser treatment ($T_{\text{pre-set}}=840$ $^{\circ}\text{C}$) and (f) after pulse-mode laser treatment ($T_{\text{pre-set}}=840$ $^{\circ}\text{C}$). The field-WEL is shown in (g).

distinct formation of WELs as well, being slightly thicker for feed-mode (Fig. 5e) than for pulse-mode (Fig. 5f). The WEL created in feed-mode (fm-WEL) is more homogenous than that created in pulse-mode (pm-WEL), compare Fig. 5b and c. This is due to the laser process characteristic and even more pronounced when performing the laser treatment on the deformed material, see Fig. 5f.

Generally, the WELs formed on the deformed material, which has a much finer overall microstructure, are more homogeneous, compare for example fm-WEL-u and fm-WEL-d in Fig. 5b and e, respectively.

For the undeformed material, proeutectoid ferrite along the original austenitic grain boundaries is present up to the surface (throughout the formed WEL), see the SEM cross section Fig. 6a. This is not the case for the deformed material, as also in the initial state (before the laser treatment) such a feature is not present, Fig. 6b.

EBSD measurements show a homogenous martensitic microstructure with martensite plates and laths (average martensite lath size of $\sim 2 \mu\text{m}$) for the feed-mode generated WEL on the undeformed ER7 (fm-WEL-u), Fig. 7a. At the transition region from the WEL to the undeformed base material (Fig. 7b), at a distance of 280–300 μm from the surface, the similar martensitic structure (within the WEL) abruptly changes to the unaffected ferritic-pearlitic microstructure. The martensitic structure within the WEL formed on the deformed material (fm-WEL-d), Fig. 7c, is similar in orientation difference and lath size. The WEL extends slightly deeper into the base material, and the transition is not as prompt, Fig. 7c. However, as already mentioned, finer grains are present in the base material of the deformed sample.

By contrast, EBSD measurements of the field-WEL (Fig. 7e) reveal much shorter martensite laths, especially within the outermost 10–15 μm . With increasing distance from the surface, the martensitic microstructure slightly coarsens, but up to a depth of $\sim 30 \mu\text{m}$, a much finer-grained structure is present, compared with the laser-generated WELs. Below that, the martensitic microstructure is comparable with that of the laser-WELs. The misorientation between the individual laths is similar (between 1° and 2°), whether the WEL is generated by laser treatment of the undeformed or deformed material, or during service of the wheel (field-WEL), see the corresponding kernel average misorientation (KAM) images shown in Fig. 7f, g, h, i, and j. The KAM is defined as the average misorientation angle between a given point and its

nearest neighbors (in this study a 3×3 kernel is defined). KAM maps are useful for evaluating the strain distribution and local lattice distortions from which even dislocation densities can be estimated. However, this is outside the focus of this work. Here, we use these maps to qualitatively compare the individual microstructure within the WELs formed by the laser treatments on undeformed and deformed ER7 material (fm-WEL-u and fm-WEL-d) with those from field samples.

Pronounced changes within the martensitic microstructure of the WELs are only present for the outermost 50 μm (from the surface) and only for the field sample, Fig. 7e and j. In the region 50–250 μm from the surface (the area not shown in Fig. 7), the microstructure is essentially the same as at $\sim 50 \mu\text{m}$ from the surface.

Detailed EBSD analyses of this region (at $\sim 100 \mu\text{m}$ from the surface) are conducted by also evaluating the grain average misorientation (GAM) factor along with the already mentioned kernel average misorientation (KAM) factor presented in Fig. 7. The GAM provides information concerning the orientation changes inside grains. The average misorientation value is then determined and assigned to each point within the grain.

The IPF maps of the laser-WELs (Fig. 8a and b) and the field-WEL (Fig. 8c) do not indicate any preferred orientation of the individual martensitic grains, but suggest that the fm-WEL-d (Fig. 8b) is more similar (in morphology) to the field-WEL (Fig. 8c). The fm-WEL-d and the field-WEL exhibit a higher fraction of smaller grains than the fm-WEL-u.

The corresponding GAM maps (Fig. 8d–f) show a similar misorientation within the grains of all three samples, with the highest misorientation angles along the outer regions of the grains. The evaluated GAM angle distribution plot (Fig. 8g) yields identical curves for the three samples (fm-WEL-u, fm-WEL-d, and field-WEL), with a maximum angle of $\sim 1.1^\circ$.

In addition, the KAM maps qualitatively reveal a similar result for the laser-WELs and the field-WEL, see Fig. 8h–j. The corresponding KAM angle distribution curves (Fig. 8k) exhibit a peak-angle of $\sim 1.05^\circ$ for the field-WEL, a slightly lower value of $\sim 0.95^\circ$ for the fm-WEL-u sample, but a slightly higher value of $\sim 1.10^\circ$ for the fm-WEL-d sample. The latter also exhibits a higher fraction of KAM angles above 1.1° than the other samples.

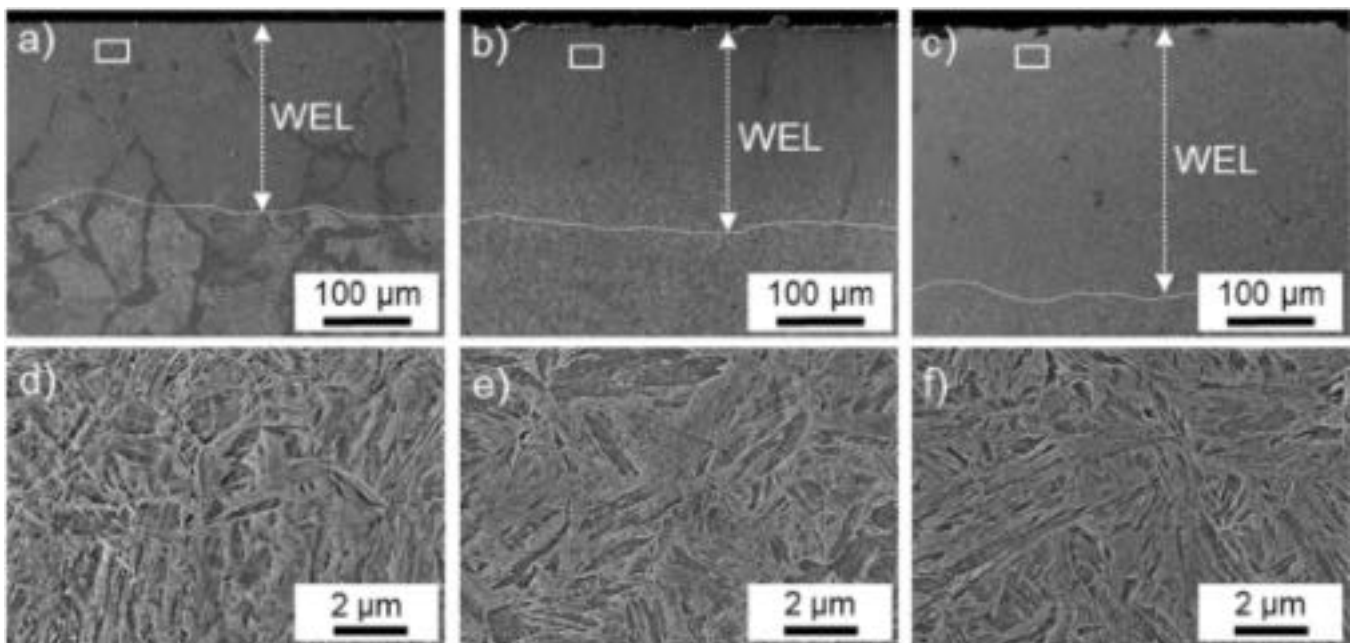


Fig. 6. SEM images with different magnifications of the microstructure of the (a),(d) fm-WEL-u and (b),(e) fm-WEL-d. The WEL on both samples was created by a feed-mode laser treatment ($T_{\text{pre-set}}=840^\circ\text{C}$). The field-WEL is shown in (c),(f). The WEL regions are indicated, although there is no distinctive boundary but more of a gradual transition to the underlying material for the fm-WEL-d and the field-WEL.

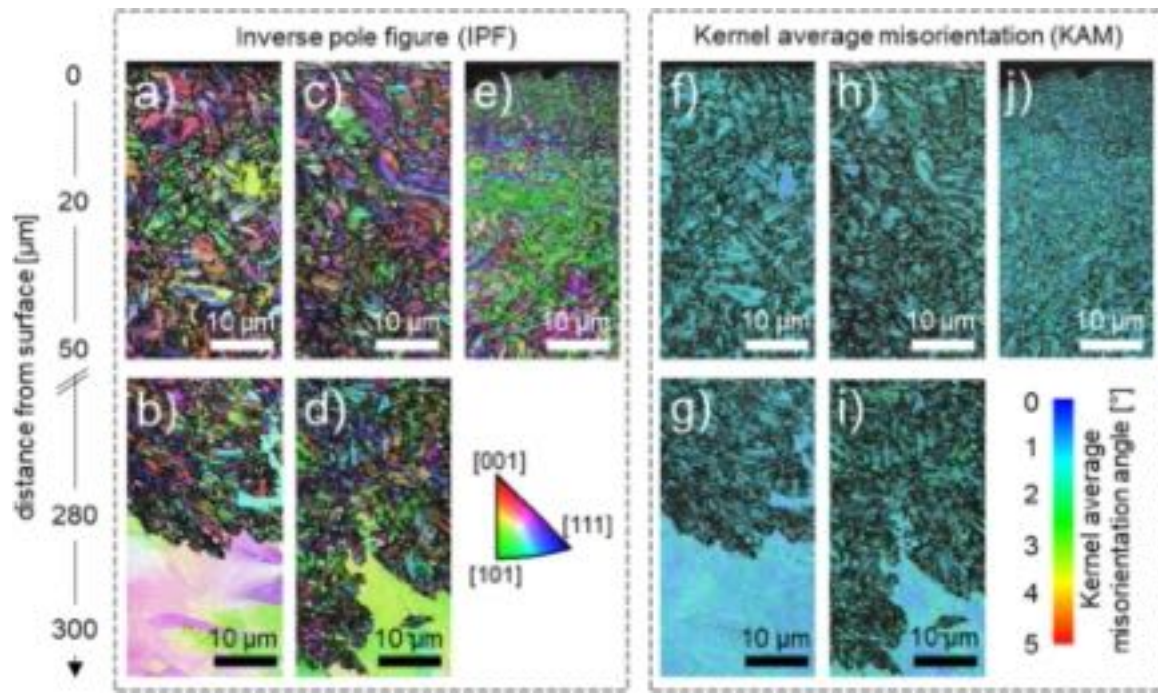


Fig. 7. EBSD analysis at different locations of the various laser-WELs created in feed-mode. Inverse pole figure (IPF) maps are shown for fm-WEL-u (a and b), fm-WEL-d (c and d), and the field-WEL (e). The corresponding For comparison, the kernel average misorientation (KAM) within these investigated microstructures is given for fm-WEL-u (f and g), fm-WEL-d (h and i), and the field-WEL (j).

4. Discussion

Reproducible formation of thermally induced WELs in the laboratory is vital when it comes to testing WELs in twin disc test setups or creating samples for full-scale test rigs. Therefore, lab-generated WELs, which can be realized by laser surface treatments [32,33,43,44], are required that are in good agreement regarding their characteristics with those generated during service (“field-WEL”). However, the influence of the initial deformation state of the samples has to be taken into account, since the characteristics of the induced WELs may vary, as in the case of different base materials [49]. Due to the vast variety of WELs and the terminology “WEL” itself, we discuss some aspects in the following that have received less attention in previous works.

The term “WEL” is used quite broadly. In fact, there are countless varieties of such microstructural features since this is a history-dependent microstructure, especially with respect to WELs on rails and wheels [28,29,50,51]. Field samples experience unknown combinations and sequences of thermal and mechanical loadings; hence, the loading history of any field sample is unknown. Esmaeili et al. [52] presented a modeling framework for phase transformations in rolling contact loadings, but creating variations of WELs in lab comparable to the field remains a challenge. The field-WEL analyzed in this work has characteristics of what is described in literature as a rather undeformed WEL. Field-WELs that are deformed within the near-surface regions exhibit distinctive zones, as shown by Wu et al. [53] for example, which are not present in our case. Furthermore, the bright white appearance of our field-WEL (Fig. 6g) suggests no intensive tempering, since annealed WELs tend to be more brownish [54]. However, some amount of deformation seems to be indicated at the outermost $\sim 30 \mu\text{m}$ from the surface (Fig. 7).

The two different laser methods used in this work (feed / pulse-mode) are based on Ref. [44], where numerous laser surface treatments have been performed on 100CrMn6 steel. Due to the focus on microstructure analysis in this work, the applied laser methods have a practical reason as well. Pulse-mode is more closely related to spots on the surface, e.g., caused by electric leakage [36]. This method may be

used to imitate a local WEL zone [43]. The WEL thicknesses resulting from the applied laser powers are plotted in Fig. 9a and b for feed and pulse-mode, respectively. This comparison clearly shows that for the same WEL thickness, the feed-mode requires a higher laser power input. This can be explained considering the thermodynamic modeling results, which give no evidence of cooling to room temperature between two pulses of the pulse-mode laser treatment (Fig. 9). By contrast, in feed-mode, the laser always moves into non-heated material areas, relatively fast at 12 mm/s. Therefore, a high amount of power is needed to reach the target surface temperature in feed mode. The heating of the surrounding microstructure in pulse mode possibly also affects the hardness of the thermally induced WEL. However, the influence of impurities (inclusions of oxides or sulphides) or inhomogeneities within the ferritic-pearlitic microstructure produced by the pulse-mode method probably led to higher scattering of hardness and WEL thicknesses, since the laser spot remained at the same position over time.

With increasing surface temperature and laser power, the thickness of the WELs increases. The results further show that especially in feed-mode, less power is needed to reach the same surface temperature with the deformed material. The latter is significantly finer grained than the undeformed one, which exhibits a coarse grained ferritic-pearlitic microstructure with proeutectoid ferrite along the original austenite grain boundaries. Such an undeformed coarse-grained microstructure is unlikely to still be present before a WEL forms in service. As reported in literature, severe plastic deformation promotes the solution of cementite, hence, ferrite supersaturated with carbon is present, which has a lower α -to- γ transformation temperature [55] and might therefore be the reason why a WEL ($\sim 24 \mu\text{m}$ thick) is already formed at a surface temperature of $\sim 640 \text{ }^\circ\text{C}$ in feed-mode. By contrast, this effect cannot be seen for pulse-mode, compare Fig. 9a and b.

Detailed investigations by cross-sectional scanning electron microscopy, inverse pole figure (IPF), grain average misorientation (GAM), and kernel average misorientation (KAM) maps highlight that the laser-generated WELs present a relatively homogenous martensitic microstructure (in grain size and orientation) across their entire thickness ($\sim 300 \mu\text{m}$ for a surface temperature of $840 \text{ }^\circ\text{C}$). The field-WEL, on the

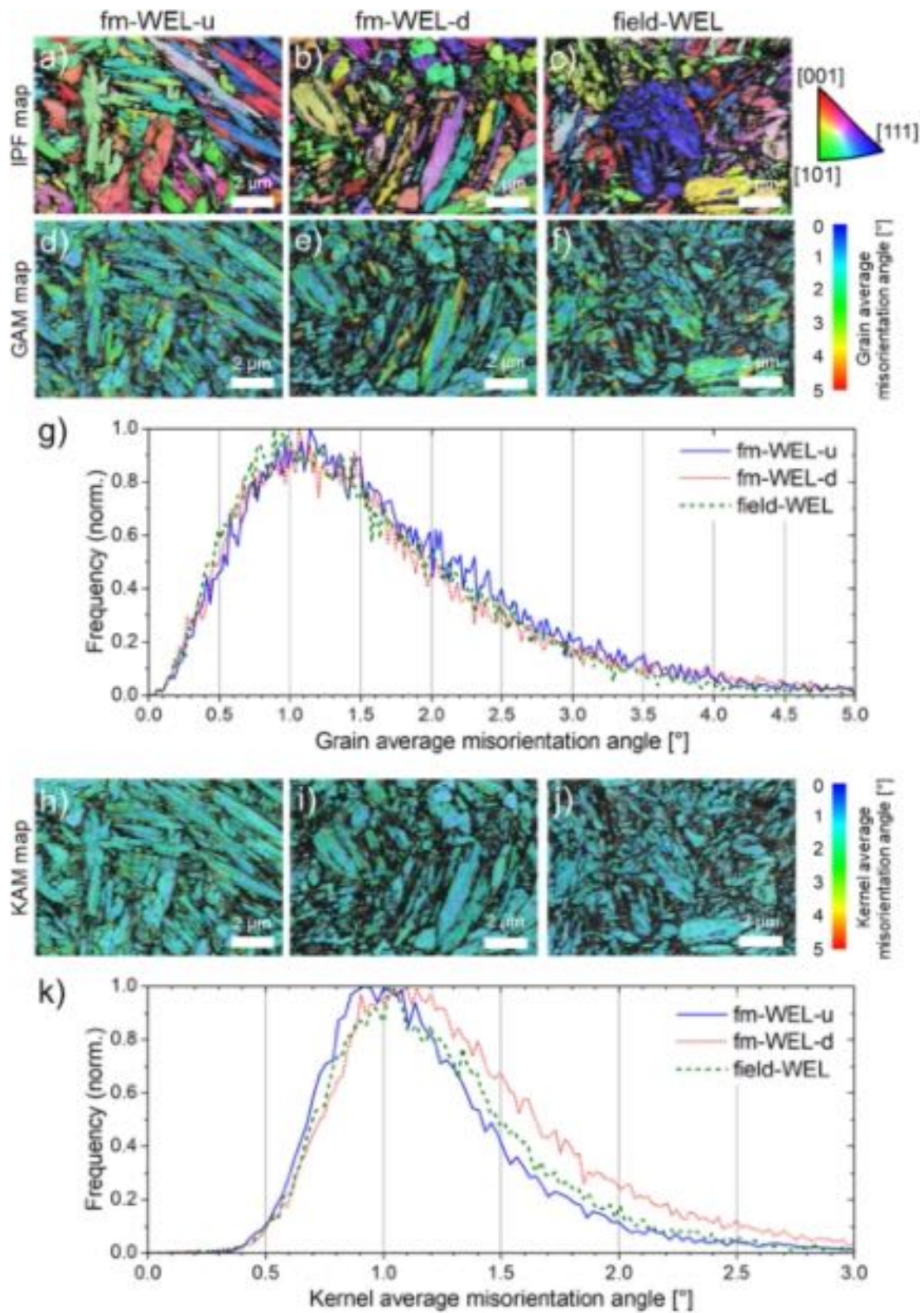


Fig. 8. EBSD measurements at a depth of 100 μm from the surface. The first row shows the inverse pole figure (IPF) maps for (a) fm-WEL-u, (b) fm-WEL-d, and (c) field-WEL. In the second row, panels (d), (e), and (f) show the related grain average misorientation (GAM) maps. The plot of the GAM angle distribution is shown in (g). Corresponding kernel average misorientation (KAM) maps for fm-WEL-u, fm-WEL-d, and field-WEL are presented in (h), (i), and (j). The KAM angle distribution is shown in (k).

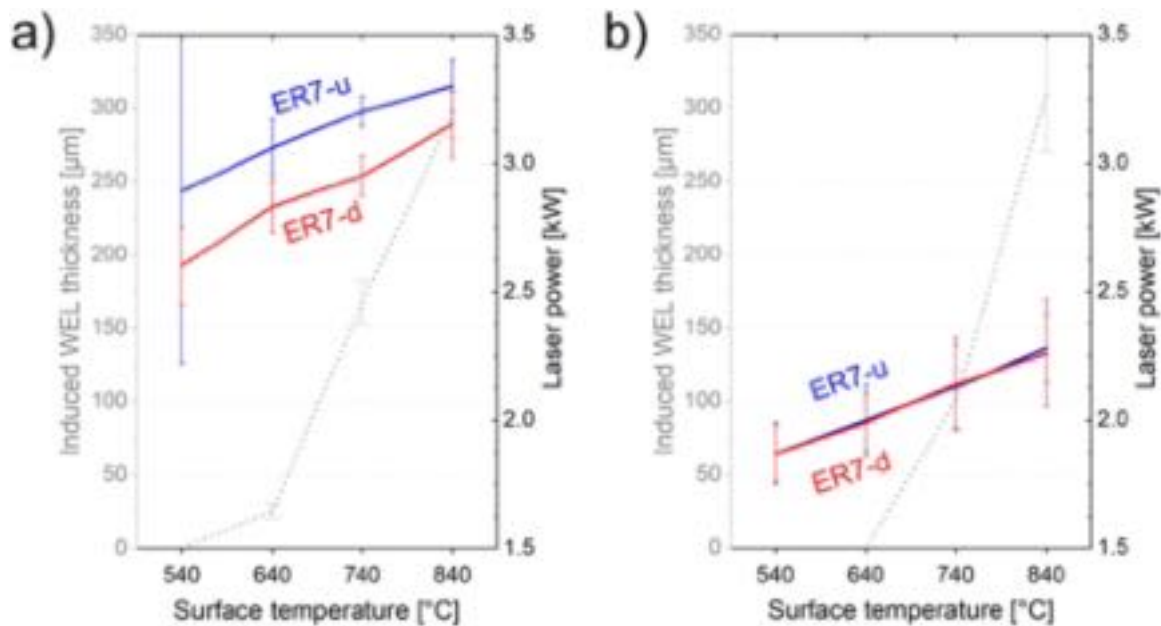


Fig. 9. Dotted lines show the average thicknesses of the laser-WELs on ER7-u and ER7-d produced in (a) feed-mode, and (b) pulse-mode for defined pre-set surface temperatures. The colored lines represent the necessary laser power to reach the defined surface temperatures (blue lines refer to the initial undeformed microstructure (ER7-u), red lines to the initial deformed microstructure (ER7-d)).

other side, shows a more pronounced increase in grain size of the martensitic microstructure within the outermost $\sim 50 \mu\text{m}$, after which it also presents a more homogenous region. At this depth, the misorientations within the individual martensitic grains (obtained from GAM maps) and across them (obtained from KAM maps) are similar, which suggests a similar defect structure. This is supported by their comparable Vickers hardness depth profiles, exhibiting $\sim 800 \text{HV}0.05$ within the WEL regions, with a small hardness reduction towards the transition to the WEL-free microstructure. In particular, the martensitic lath sizes and shapes differ between the WELs formed using laser treatment (feed-mode) on an undeformed or deformed ER7 material, and the field-WEL. Larger laths, also with a larger aspect ratio, are present within the WEL formed on the undeformed ER7, and the finest-grained martensitic microstructure is present in the field-WEL. The WEL formed on the deformed ER7 material exhibits a martensitic microstructure between these two. The obtained hardness values of the thermally induced WELs on the ER7 wheel steel of $\sim 800 \text{HV}0.05$ is in the range of the analyzed field-WEL on an ex-service ER7 wheel. By contrast, typical WELs on rail materials from the field often exhibit hardness values of $900\text{--}1100 \text{HV}$ [29,31,38,51,56–58]. However, differences in material composition – rail materials usually have $> 0.6 \text{ wt}\% \text{ C}$ – and the variation of the load for the micro hardness measurements lead to differences in the results. Comparable hardness values ($\sim 800 \text{HV}0.05$) with the same applied load during Vickers hardness measurement were obtained by Zhou et al. [40] investigating rail grinding processes, and by Chen et al. [59] generating wheel flats in a wheel/rail test rig. The martensitic microstructure of the thermally induced WEL by laser surface treatments in this work shows similarities to investigations of WELs from the field [30,31,56,57]. The presented SEM images (Fig. 6) are further comparable to a laser treated wheel steel presented by Chen et al. [43]. EBSD measurements on WEL-like structures are rare in literature [60,61], since it is difficult to measure very fine-grained and distorted microstructures, hence, the presented results are primarily in comparison to the different WELs within this study. Based on our detailed investigations, especially the WEL formed using laser treatment (feed-mode) on a deformed ER7 material with a target surface temperature of $840 \text{ }^{\circ}\text{C}$ (abbreviated fm-WEL-d), can be seen as an appropriate imitation of WELs formed thermally during service. This is especially the

case because the material underneath the WELs also has a comparable fine-grained and deformed microstructure.

5. Conclusions

In this work, laser surface treatment methods were presented to reproducibly thermally induce WELs on rail wheel materials (ER7). The lowest surface temperature, generated in continuous feed-mode, at which a WEL was induced is $640 \text{ }^{\circ}\text{C}$, compared to $740 \text{ }^{\circ}\text{C}$ in case of pulse-mode. In general, the necessary laser power to reach a defined surface temperature was lower in pulse-mode, where the laser spot remains at a certain position, in contrast to feed-mode, where the laser spot moves into non-heated material areas during the process. The laser powers required to generate WELs ranged from 2.1 to 2.3 kW for pulse-mode and $2.8\text{--}3.3 \text{ kW}$ for feed-mode.

The influence of the initial deformation state of the sample on WEL formation was studied by using an undeformed (ER7-u) and deformed (ER7-d) material. On the latter, a thicker induced laser-WEL was generated for the same surface temperature, and the necessary laser energies for reaching this temperature were lower (especially when operating the laser in feed-mode). Besides a similar Vickers hardness of $750\text{--}850 \text{HV}0.05$ for the laser-WELs, their microstructure was different with a pronounced proeutectoid ferrite present in the WEL formed on the undeformed ER7 material.

The field-WEL from a rail wheel tread surface yielded a hardness and martensitic microstructure similar to those of WELs formed on deformed ER7 material. But contrary to the latter, which showed a homogeneous microstructure throughout the WEL and a rather distinctive transition to the base material, the field-WEL exhibited significant deformation and a grain size gradient. Detailed EBSD measurements and inverse pole figure, grain average misorientation, and kernel average misorientation map analyses revealed that the microstructural characteristics of the laser-induced WEL formed in feed-mode on a deformed ER7 material was most comparable to the presented field-WEL except for the outermost $\sim 30 \mu\text{m}$ where a pronounced gradient in the microstructure due to deformation in service was detected.

Author agreement

The authors declare that this manuscript is original, has not been published before and is not currently being considered for publication elsewhere.

We confirm that the manuscript has been read and approved by all named authors and that there are no other persons who satisfied the criteria for authorship but are not listed. We further confirm that the order of authors listed in the manuscript has been approved by all of us.

We understand that the Corresponding Author is the sole contact for the Editorial process. He/she is responsible for communicating with the other authors about progress, submissions of revisions and final approval of proofs.

Declaration of Competing Interest

The authors declare that they have no known competing financial interests or personal relationships that could have appeared to influence the work reported in this paper.

Data availability

Data will be made available on request.

Acknowledgements

This project has received funding from the Shift2Rail Joint Undertaking (JU) under grant agreement No 826255 and No 101012456. The JU receives support from the European Union's Horizon 2020 research and innovation programme and the Shift2Rail JU members other than the Union. In addition, this work was funded by the "Austrian COMET-Program" (project InTribology1, no. 872176) via the Austrian Research Promotion Agency (FFG) and the federal states of Niederösterreich and Vorarlberg and was carried out within the "Excellence Centre of Tribology" (AC2T research GmbH). This study was done in cooperation with Virtual Vehicle Research GmbH in Graz, Austria. The authors would like to acknowledge the financial support within the COMET K2 Competence Centers for Excellent Technologies from the Austrian Federal Ministry for Climate Action (BMK), the Austrian Federal Ministry for Digital and Economic Affairs (BMDW), the Province of Styria (Dept. 12) and the Styrian Business Promotion Agency (SFG). The Austrian Research Promotion Agency (FFG) has been authorized for the programme management.

References

- Andersson R, Ahlström J, Kabo E, Larsson F, Ekberg A. Numerical investigation of crack initiation in rails and wheels affected by martensite spots. *Int J Fatigue* 2018; vol. 114:238–51. <https://doi.org/10.1016/j.ijfatigue.2018.05.023>.
- Zhang SY, et al. Rail rolling contact fatigue formation and evolution with surface defects. *Int J Fatigue* 2022;vol. 158:106762. <https://doi.org/10.1016/j.ijfatigue.2022.106762>.
- Bernsteiner C, Müller G, Meierhofer A, Six K, Künstner D, Dietmaier P. 'Development of white etching layers on rails: simulations and experiments'. *Wear* 2016;vol. 366–367:116–22. <https://doi.org/10.1016/j.wear.2016.03.028>.
- Bernsteiner C, et al. Simulation and experiment based investigations of squat formation mechanisms. *Wear* 2019;vol. 440–441:203093. <https://doi.org/10.1016/j.wear.2019.203093>.
- R.I. Carroll and J.H. Beynon, 'Rolling contact fatigue of white etching layer: Part 1 Crack morphology', p. 14, 2007.
- M. Kerr, A. Wilson, and S. Marich, 'The epidemiology of squats and related rail defects', Conference On Railway Engineering, p. 14, 2008.
- Steenbergen M, Dollevoet R. On the mechanism of squat formation on train rails – Part I: origination. *Int J Fatigue* 2013;vol. 47:361–72. <https://doi.org/10.1016/j.ijfatigue.2012.04.023>.
- Mahdavi H, Poullos K, Kadin Y, Niordson CF. 'On the effect of microplasticity on crack initiation from subsurface defects in rolling contact fatigue'. *Int J Fatigue* 2022;vol. 161:106870. <https://doi.org/10.1016/j.ijfatigue.2022.106870>.
- Masoudi Nejad R, Farhangdoost K, Shariati M. 'Numerical study on fatigue crack growth in railway wheels under the influence of residual stresses'. *Eng Fail Anal* 2015;vol. 52:75–89. <https://doi.org/10.1016/j.engfailanal.2015.03.002>.
- Caprioli S, Vernersson T, Handa K, Ikeuchi K. 'Thermal cracking of railway wheels: towards experimental validation'. *Tribol Int* 2016;vol. 94:409–20. <https://doi.org/10.1016/j.triboint.2015.09.042>.
- Clayton P, Allery MBP. Metallurgical aspects of surface damage problems in rails. *Can Metall Q* 1982:16.
- S.L. Grassie, 'Squats and squat-type defects in rails: the understanding to date', Proceedings of the Institution of Mechanical Engineers, Part F: Journal of Rail and Rapid Transit, vol. 226, no. 3, pp. 235–242, May 2012, doi: 10.1177/0954409711422189.
- S.L. Grassie, D.I. Fletcher, E.A. Gallardo Hernandez, and P. Summers, 'Studs: a squat-type defect in rails', Proceedings of the Institution of Mechanical Engineers, Part F: Journal of Rail and Rapid Transit, vol. 226, no. 3, pp. 243–256, May 2012, doi: 10.1177/0954409711422189.
- S. Marich, 'The development of squat defects under high axle load operations', Conference On Railway Engineering, p. 10, 2002.
- Pal S, Daniel WJT, Farjoo M. Early stages of rail squat formation and the role of a white etching layer. *Int J Fatigue* 2013;vol. 52:144–56. <https://doi.org/10.1016/j.ijfatigue.2013.02.016>.
- Carroll RI, Beynon JH. Rolling contact fatigue of white etching layer Part 2. Numerical results' 2007:7.
- Simon S, Saulot A, Dayot C, Quost X, Berthier Y. Tribological characterization of rail squat defects. *Wear* 2013;vol. 297(1–2):926–42. <https://doi.org/10.1016/j.wear.2012.11.011>.
- Li Z, Dollevoet R, Molodova M, Zhao X. Squat growth—some observations and the validation of numerical predictions. *Wear* 2011;vol. 271(1–2):148–57. <https://doi.org/10.1016/j.wear.2010.10.051>.
- Li Z, Zhao X, Esveld C, Dollevoet R, Molodova M. An investigation into the causes of squats—correlation analysis and numerical modeling. *Wear* 2008;vol. 265(9–10):1349–55. <https://doi.org/10.1016/j.wear.2008.02.037>.
- M. Ishida, 'Rolling contact fatigue (RCF) defects of rails in Japanese railways and its mitigation strategies', p. 8, 2013.
- Stock R, Kubin W, Daves W, Six K. Advanced maintenance strategies for improved squat mitigation. *Wear* 2019;vol. 436–437:203034. <https://doi.org/10.1016/j.wear.2019.203034>.
- Muhamedsalih Y, Hawksbee S, Tucker G, Stow J, Burstow M. Squats on the Great Britain rail network: Possible root causes and research recommendations. *Int J Fatigue* 2021;vol. 149:106267. <https://doi.org/10.1016/j.ijfatigue.2021.106267>.
- Zhang YM, Xiao ZM, Fan M. Fatigue investigation on railway wheel steel with white etching layer. *Int J Steel Struct* 2020;vol. 20(1):80–8. <https://doi.org/10.1007/s13296-019-00271-x>.
- Kato T, Sugeta A, Nakayama E. Investigation of influence of white layer geometry on spalling property in railway wheel steel. *Wear* 2011;vol. 271(1–2):400–7. <https://doi.org/10.1016/j.wear.2010.10.024>.
- Fletcher DJ, Sanusi SH. 'The potential for suppressing rail defect growth through tailoring rail thermo-mechanical properties'. *Wear* 2016;vol. 366–367:401–6. <https://doi.org/10.1016/j.wear.2016.06.022>.
- Ivanisenko J, MacLaren I, Sauvage X, Valiev R, Fecht HJ. Phase transformations in pearlitic steels induced by severe plastic deformation. *SSP* 2006;vol. 114:133–44. <https://doi.org/10.4028/www.scientific.net/SSP.114.133>.
- Baumann G, Fecht HJ, Liebelt S. Formation of white-etching layers on rail treads. *Wear* 1996;vol. 191(1–2):133–40. [https://doi.org/10.1016/0043-1648\(95\)06733-7](https://doi.org/10.1016/0043-1648(95)06733-7).
- Zhou Y, Peng JF, Luo ZP, Cao BB, Jin XS, Zhu MH. Phase and microstructural evolution in white etching layer of a pearlitic steel during rolling-sliding friction. *Wear* 2016;vol. 362–363:8–17. <https://doi.org/10.1016/j.wear.2016.05.007>.
- Kumar A, Agarwal G, Petrov R, Goto S, Sietsma J, Herbig M. Microstructural evolution of white and brown etching layers in pearlitic rail steels. *Acta Mater* 2019;vol. 171:48–64. <https://doi.org/10.1016/j.actamat.2019.04.012>.
- Al-Juboori A, et al. Squat formation and the occurrence of two distinct classes of white etching layer on the surface of rail steel. *Int J Fatigue* 2017;vol. 104:52–60. <https://doi.org/10.1016/j.ijfatigue.2017.07.005>.
- Al-Juboori A, et al. Characterisation of White Etching Layers formed on rails subjected to different traffic conditions. *Wear* 2019;vol. 436–437:202998. <https://doi.org/10.1016/j.wear.2019.202998>.
- Buling A, Sändker H, Stollenwerk J, Krupp U, Hamann-Steinmeier A. Laser surface pretreatment of 100Cr6 bearing steel – Hardening effects and white etching zones. *Appl Surf Sci* 2016;vol. 378:564–71. <https://doi.org/10.1016/j.apsusc.2016.03.088>.
- Xiong Y, et al. Microstructure and microhardness of pearlitic steel after laser shock processing and annealing. *Mater Sci Technol* 2015;vol. 31(15):1825–31. <https://doi.org/10.1179/1743284715X.0000000020>.
- Wu J, Petrov RH, Naeimi M, Li Z, Dollevoet R, Sietsma J. Laboratory simulation of martensite formation of white etching layer in rail steel. *Int J Fatigue* 2016;vol. 91:11–20. <https://doi.org/10.1016/j.ijfatigue.2016.05.016>.
- Newcomb SB, Stobbs WM. A transmission electron microscopy study of the white-etching layer on a rail head. *Mater Sci Eng* 1984;vol. 66(2):195–204. [https://doi.org/10.1016/0025-5416\(84\)90180-0](https://doi.org/10.1016/0025-5416(84)90180-0).
- Al-Juboori A, et al. Microstructural changes on railway track surfaces caused by electrical leakage between wheel and rail. *Tribol Int* 2019;vol. 140:105875. <https://doi.org/10.1016/j.triboint.2019.105875>.
- Ahlstrom J, Karlsson B. Microstructural evaluation and interpretation of the mechanically and thermally affected zone under railway wheel flats. *Wear* 1999; vol. 14.
- Lin B, Zhou K, Guo J, Liu QY, Wang WJ. Influence of grinding parameters on surface temperature and burn behaviors of grinding rail. *Tribol Int* 2018;vol. 122:151–62. <https://doi.org/10.1016/j.triboint.2018.02.017>.

- [39] Mesaritis M, et al. A laboratory demonstration of rail grinding and analysis of running roughness and wear. *Wear* 2020;vol. 456–457:203379. <https://doi.org/10.1016/j.wear.2020.203379>.
- [40] Zhou K, et al. Experimental investigation on material removal mechanism during rail grinding at different forward speeds. *Tribol Int* 2020;vol. 143:106040. <https://doi.org/10.1016/j.triboint.2019.106040>.
- [41] Lian Q, et al. Evolution of thermally induced white etching layer at rail surface during multiple wheel/train passages. *Int J Fatigue* 2022;vol. 159:106799. <https://doi.org/10.1016/j.ijfatigue.2022.106799>.
- [42] Ding HH, et al. Investigation on the rolling wear and damage properties of laser discrete quenched rail material with different quenching shapes and patterns. *Surf Coat Technol* 2019;vol. 378:124991. <https://doi.org/10.1016/j.surfcoat.2019.124991>.
- [43] Chen Y, Zhao X, Liu P, Pan R, Ren R. Influences of local laser quenching on wear performance of D1 wheel steel. *Wear* 2018;vol. 414–415:243–50. <https://doi.org/10.1016/j.wear.2018.07.016>.
- [44] Gutiérrez Guzmán F, Sous C, van Lier H, Jacobs G. An energetic approach for the prognosis of thermally induced white etching layers in bearing steel 100CrMn6. *Tribol Int* 2020;vol. 143:106096. <https://doi.org/10.1016/j.triboint.2019.106096>.
- [45] Electron Backscatter Diffraction in Materials Science. In: Schwartz AJ, Kumar M, Adams BL, Field DP, editors. Boston, MA: Springer US; 2009. <https://doi.org/10.1007/978-0-387-88136-2>.
- [46] 'EN 13262:2004+A2:2011: Railway applications - Wheelsets and bogies - Wheels - Product requirements'.
- [47] Diener M, Ghidini A. Fracture toughness: a quality index for railway solid wheels. *Mats Perf Charact* . 2014;vol. 3(3):20130047. <https://doi.org/10.1520/MPC20130047>.
- [48] Rojacz H, Premauer M, Nevosad A. Conductive and edge retaining embedding compounds: influence of graphite content in compounds on Specimen's SEM and EBSD performance. *Pract Metallogr* 2021;vol. 58(5):236–63. <https://doi.org/10.1515/pm-2021-0018>.
- [49] Hieu Nguyen B, Al-Juboori A, Zhu H, Zhu Q, Li H, Tieu K. Formation mechanism and evolution of white etching layers on different rail grades. *Int J Fatigue* 2022: 107100. <https://doi.org/10.1016/j.ijfatigue.2022.107100>.
- [50] Österle W, Rooch H, Pyzalla A, Wang L. Investigation of white etching layers on rails by optical microscopy, electron microscopy, X-ray and synchrotron X-ray diffraction. *Mater Sci Eng: A* 2001;vol. 303(1–2):150–7. [https://doi.org/10.1016/S0921-5093\(00\)01842-6](https://doi.org/10.1016/S0921-5093(00)01842-6).
- [51] Zhang HW, Ohsaki S, Mitao S, Ohnuma M, Hono K. Microstructural investigation of white etching layer on pearlite steel rail. *Mater Sci Eng: A* 2006;vol. 421(1–2): 191–9. <https://doi.org/10.1016/j.msea.2006.01.033>.
- [52] Esmaeili A, Ahlström J, Andersson B, Ekh M. Modelling of cyclic plasticity and phase transformations during repeated local heating events in rail and wheel steels. *Int J Fatigue* 2021;vol. 151:106361. <https://doi.org/10.1016/j.ijfatigue.2021.106361>.
- [53] Wu J, et al. Micro and nanoscale characterization of complex multilayer-structured white etching layer in rails. *Metals* 2018;vol. 8(10):749. <https://doi.org/10.3390/met8100749>.
- [54] Li S, Wu J, Petrov RH, Li Z, Dollevoet R, Sietsma J. "Brown etching layer": a possible new insight into the crack initiation of rolling contact fatigue in rail steels?. *Eng Fail Anal* 2016;vol. 66:8–18. <https://doi.org/10.1016/j.engfailanal.2016.03.019>.
- [55] Min N, Li W, Jin X. α to γ transformation in the nanostructured surface layer of pearlitic steels near room temperature. *Scr Mater* 2008;vol. 59(8):806–9. <https://doi.org/10.1016/j.scriptamat.2008.05.038>.
- [56] Pan R, Ren R, Chen C, Zhao X. The microstructure analysis of white etching layer on treads of rails. *Eng Fail Anal* 2017;vol. 82:39–46. <https://doi.org/10.1016/j.engfailanal.2017.06.018>.
- [57] Pan R, Chen Y, Lan H, E S, Ren R. Investigation into the microstructure evolution and damage on rail at curved tracks. *Wear* 2022;vol. 504–505:204420. <https://doi.org/10.1016/j.wear.2022.204420>.
- [58] Seo J, Kwon S, Jun H, Lee D. Numerical stress analysis and rolling contact fatigue of White Etching Layer on rail steel. *Int J Fatigue* 2011;vol. 33(2):203–11. <https://doi.org/10.1016/j.ijfatigue.2010.08.007>.
- [59] Chen YZ, He CG, Zhao XJ, Shi LB, Liu QY, Wang WJ. The influence of wheel flats formed from different braking conditions on rolling contact fatigue of railway wheel. *Eng Fail Anal* 2018;vol. 93:183–99. <https://doi.org/10.1016/j.engfailanal.2018.07.006>.
- [60] Merino P, et al. An attempt to generate mechanical white etching layer on rail surface on a new rolling contact test bench. *Wear* 2021;vol. 482–483:203945. <https://doi.org/10.1016/j.wear.2021.203945>.
- [61] Liu C, Ren R, Liu D, Zhao X, Chen C. An EBSD investigation on the evolution of the surface microstructure of D2 wheel steel during rolling contact fatigue. *Tribol Lett* 2020;vol. 68(1):47. <https://doi.org/10.1007/s11249-020-1277-1>.

Publication VI



In-situ micro-cantilever bending studies of a white etching layer thermally induced on rail wheels

M. Freisinger, L. Zauner, R. Hahn, H. Riedl, P.H. Mayrhofer
Materials Science & Engineering A, 869 (2023)
DOI: 10.1016/j.msea.2023.144805



Contents lists available at ScienceDirect

Materials Science & Engineering A

journal homepage: www.elsevier.com/locate/msea

In-situ micro-cantilever bending studies of a white etching layer thermally induced on rail wheels

M. Freisinger^{a,c,*}, L. Zauner^b, R. Hahn^b, H. Riedl^{b,c}, P.H. Mayrhofer^c^a AC2T Research GmbH, A-2700, Wiener Neustadt, Austria^b Christian Doppler Laboratory for Surface Engineering of High-performance Components, TU Wien, Austria^c Institute of Materials Science and Technology, TU Wien, Austria

ARTICLE INFO

Keywords:

Rail-wheel contact
White etching layer
Micromechanical properties
J-integral

ABSTRACT

A complex and untraceable mechanical and thermal loading situation in rolling-sliding contacts can lead to the formation of white etching layers (WELs), depicting critical crack initiation sites. For our detailed studies, to obtain a holistic view of the microstructural characteristics and micro-mechanical properties, we prepared a WEL on a decommissioned (after 200,000 km service life) rail wheel by laser surface treatments with a defined energy input. This WEL is predominantly martensitic down to a depth of 30–40 μm , after which a transition to the deformed ferritic-pearlitic microstructure of the hypoeutectoid rail wheel steel is present. The martensitic region is with 6.98 ± 0.68 GPa significantly harder than the transition zone (5.17 ± 0.39 GPa) and the deformed ferritic-pearlitic base material (3.30 ± 0.33 GPa). *In-situ* V-notched micro-cantilever bending experiments of the martensitic (and thus most brittle) region show crack initiation and propagation – mostly along the boundaries of the martensitic grains – besides a plastic behavior. Applying the elastoplastic fracture mechanics allows to derive the local fracture toughness K_{I0} , which is 16.4 ± 1.2 MPa $\text{m}^{1/2}$ for this martensitic region of the WEL. The results outpoint the application of micro-cantilever bending tests in addition to hardness testing as a promising tool to discuss the relationship of microstructural characteristics with its micro-mechanical properties.

1. Introduction

As one of the most common structural materials over several decades, understanding the damage patterns and failure of steels in engineering applications is still a significant issue for material science. Contact fatigue failure represents an important economic and safety issue, for instance, in bearings, rails, and wheels [1–4], and is strongly affected by near-surface microstructural changes. Hypoeutectoid steels are prone to form a so-called white etching layer (WEL), a nano-crystalline layer appearing white under light optical microscopy after etching with a nitric acid. The formation process is still in discussion, predominantly described due to severe mechanical and/or thermal loads [5–11]. Especially in rolling-sliding contacts, there are numerous variations of so-called WELs occurring [8,12–15] due to a complex time- and location-dependent loading situation. WEL-like microstructures are prominent crack initiation sites where cracks usually propagate perpendicular to the surface through the WEL or at the interface between the WEL and the underlying material [16–21]. This is associated with the commonly assumed brittle behavior of white etching layers.

However, studies on the mechanical properties of WEL-like microstructures going beyond hardness evaluation are scarce due to the non-applicability of conventional testing of such small-scale features. Recent studies from A. Kumar et al. [8] and A.K. Saxena et al. [22] presented the first correlation between microstructural evolution and fracture characteristics of white etching layers formed on pearlitic rail steel during service. Based on spatially resolved sample preparation by focused ion beam (FIB) technology, micro-mechanical testing of distinct microstructural features is an interesting approach to gain a more detailed understanding on elasto-plastic material response [23,24]. *In-situ* micromechanical testing is well established for brittle materials such as single crystals and hard coatings [25–28], where linear elastic fracture mechanics (LEFM) can be applied. For materials exhibiting a significant plastic zone at the crack tip (semi-brittle/ductile materials), the elastoplastic fracture mechanics (EPFM) must be applied, which is less established for micro-scale mechanical testing [29,30].

Damage and failure of rail wheels – typically affected by near-surface microstructural changes and referred to the formation of WEL domains – demands detailed knowledge about the microstructure's fracture

* Corresponding author. AC2T Research GmbH, A-2700, Wiener Neustadt, Austria.

E-mail address: matthias.freisinger@ac2t.at (M. Freisinger).

<https://doi.org/10.1016/j.msea.2023.144805>

Received 13 January 2023; Received in revised form 14 February 2023; Accepted 15 February 2023

Available online 16 February 2023

0921-5093/© 2023 The Authors. Published by Elsevier B.V. This is an open access article under the CC BY license (<http://creativecommons.org/licenses/by/4.0/>).

behavior and toughness [2,31–35]. To improve the understanding on WEL-affected failure mechanisms, qualitative and quantitative analysis of their fracture behavior is essential. Detailed data sets are also of utmost importance for modelling approaches. Currently, no data on fracture behavior and local fracture toughness of WEL on rail wheels are available.

This study applies a holistic approach to characterize the microstructure of a WEL thermally induced by laser surface treatment with defined and reproducible energy input of a decommissioned hypoeutectoid rail wheel steel as well as their mechanical properties, particularly hardness and fracture toughness. The latter is also quantitatively evaluated with *in-situ* micro-mechanical bending experiments and applying EPFM.

2. Materials and methods

2.1. Materials

The hypoeutectoid steel chosen within this work is the rail wheel steel grade ER7 (Table 1). To picture the degree of deformation of a near-surface microstructure in service, the Austrian Federal Railways provides an ex-service rail wheel with a mileage of $\sim 200,000$ km. The wheel (diameter of 0.95 m) is cut by a conventional band saw. The preparation of the wheel tread surface includes the removal of rust by gentle hand-grinding with a SiC #1000 paper (18 μm grain size) and additionally a careful Fe(III)Cl etching to identify possible WEL induced during service. A laser surface treatment is conducted on regions obtaining no WEL from service to thermally induce a WEL with a distinct thermal loading on the deformed microstructure. A Direct Diode Laser System (HighLight 8000D, Coherent, U.S.) with a rectangular laser spot (3×24 mm) is used at a constant travel speed of 12 mm/s. To induce a WEL with a thickness of ~ 30 μm , the laser parameters used within this work are based on a previous work [36]. The average energy density is 3.74 J/mm² with a pre-set surface temperature of 640 °C, measured by an externally mounted pyrometer (LPC03, Mergenthaler, Germany). Out of this laser-treated region, samples in size of $\sim 5 \times 5 \times 5$ mm³ are cut out using a laboratory cutting device (Struers Secotom-50; Struers ApS, Denmark) and subsequently mechanically polished.

2.2. Microstructural characterization

Characterization of the microstructure is executed by light optical microscopy (LOM) (Axio Imager M2m, Carl Zeiss AG, Germany) as well as by scanning electron microscopy (SEM) (Jeol JIB 4700F, Jeol Ltd., Japan). The latter is equipped with a Schottky field emission gun, secondary and backscattered electron detectors, and an electron backscatter diffraction (EBSD) detector (Bruker e-Flash HR, USA). The corresponding samples are prepared by embedding small pieces in conductive compounds. After the metallographic sample preparation to a mirror-polished surface quality (1 μm diamond fine polishing), the cross-sectional cuts are etched with diluted nitric acid (3% HNO₃, 97% ethanol). SEM investigations are performed at 15 kV acceleration voltage and 10 pA probe current. For the EBSD measurements, the samples are embedded in an advanced embedding compound [39], and the surface quality was further improved by additional finish polishing

(colloidal Silica <0.25 μm). The parameters used for the EBSD investigations are 15 kV acceleration voltage, 3.6 nA probe current, 16 mm working distance, and 18 mm detector distance. The Kikuchi patterns, acquired at 240×160 px with an exposure time of 40 ms, are analyzed with the Bruker Esprit 2.2 software package using the AMCSO database for phase identification.

2.3. Micro-mechanical investigations

Vickers hardness depth profiles are executed with a load of 0.05 kp (0.49 N), indenting the cross-sections at increasing distances from the surface with a Future-Tech FM-700 hardness tester. The diagonals of the indents are measured with a LOM. Further, nanoindentation measurements are performed with a Bruker Hysitron Triboindenter TI980 – Performech II (equipped with a Berkovich diamond tip) to address hardness and Young's modulus, an array of 5×5 indents was performed for each zone. The load-displacement curves (with a peak load of 5 mN) were evaluated, and hardness was deduced via the load/area ratio, whereby the reduced Young's modulus was evaluated via the Oliver and Pharr method [40].

To evaluate fracture toughness, *in-situ* micro-cantilever bending experiments are carried out using the geometrical relations depicted in Fig. 1. Cantilevers are milled by a focused ion beam (FIB) on the edge of the $\sim 5 \times 5 \times 5$ mm³ samples. A scanning electron microscopy (SEM) equipped with FIB (Jeol JIB 4700F Multi Beam System, Jeol Ltd., Japan) is used with 30 keV Ga⁺ ions to create eight cantilevers on the sample. FIB milling starts with coarse milling at 10 nA and a dose of 100 nC/ μm^2 , followed by fine milling at 1 nA||8 nC/ μm^2 . Straight through-thickness notches with a final notch depth of ~ 1.2 μm are made at 10 nA||8 nC/ μm^2 . The last cantilever preparation step is polishing the side surfaces at 300 pA||5 nC/ μm^2 to avoid side-notch effects. The cantilevers have a rectangular cross-section with lengths of ~ 25 μm , whereby the ratio of cantilever length (L'):height (w):breadth (b) is about 5:1:1 [41].

The micromechanical experiments are performed using a Femto-Tools FT-NMT04 *in-situ* nanoindentation system built in a Zeiss Sigma 500 VP SEM. A detailed depiction of the indenter tip above the laser-treated steel surface is depicted in Fig. 2a. The nanoindenter is

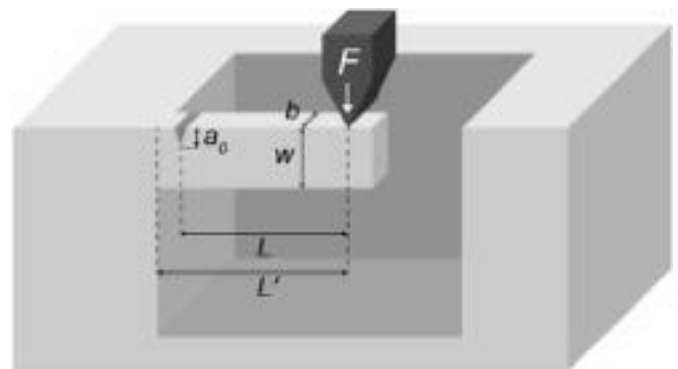


Fig. 1. Schematic overview of the micro-cantilever prepared by FIB milling with the diamond wedge applying the load at a distance L from the notch.

Table 1

Material properties of the steel grade ER7 according to the standard EN13262 [37].

C	Si	Mn	P	S	Cr	Cu	Mo	Ni	V	Cr + Mo + Ni
[wt%]										
0.52	0.40	0.80	0.020	0.015	0.30	0.30	0.08	0.30	0.06	0.50
R_{eH}		R_m		A_5		Minimum Hardness			K_Q (CT specimens [38])	
[N/mm ²]		[N/mm ²]		[%]		[HV10]			[MPa m ^{1/2}]	
≥ 520		820–940		≥ 14		260			40–80	

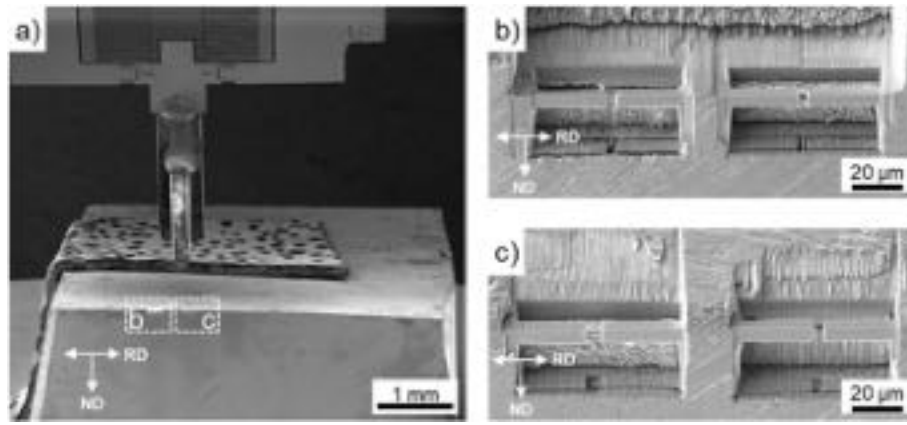


Fig. 2. (a) Cube cut-out of the laser-treated steel surface as placed inside the SEM chamber, with the diamond wedge of the nanoindentation system approaching from the top. Details of the FIB milled cantilevers – marked in (a) with rectangles – are shown in (b) and (c) before testing.

equipped with a diamond wedge (tip length $\sim 10 \mu\text{m}$), and after careful alignment of the samples, they are loaded in a displacement-controlled mode at a speed of 20 nm s^{-1} and a distance L from the notch (Fig. 1). The intended crack plane is normal to the rolling direction (RD) of the wheel (Fig. 2b and c). A sinusoidal signal is superimposed (at an amplitude of 5 nm and a frequency of 200 Hz , continuous stiffness measurement CSM) to record the force F , displacement u , and stiffness k of the cantilever during the measurement.

Since the materials experienced extensive plastic deformation during the bending tests, the evaluation was performed according to the elastic-plastic fracture behavior in the context of the J -integral. A detailed explanation of the conducted analytical procedure and an alternative data evaluation can be found in works by Alfreider et al. [42–45].

The J -integral as proposed by Rice was used for our analysis [46]:

$$J_n = \frac{2A_{tot,n}}{b(w - a_n)} \quad (1)$$

where J_n is the J -integral corresponding to data point n , $A_{tot,n}$ is the area under the force-displacement curve (F - u) up to point n , a_n denotes the crack length at point n , and b as well as w are geometric parameters as described above. $A_{tot,n}$ is calculated after:

$$A_{tot,n} = \int_0^{u_n} F du \quad (2)$$

The calculation of the current crack length is conducted using the recorded cantilever stiffness k following:

$$\int_0^{a_n} \frac{a}{w} Y\left(\frac{a}{w}\right)^2 da = \frac{\left(\frac{k_0}{k_n} - 1\right) L^3}{18\pi(1 - \nu^2)L'^2} \quad (3)$$

where $Y\left(\frac{a}{w}\right)$ is a dimensionless shape factor proposed by Riedl et al. [47], ν denotes Poisson's ratio (chosen as 0.3 for all calculations), k_0 is the stiffness of the unnotched cantilever, whereas k is the stiffness of the notched cantilever at point n . Furthermore, k_0 can be calculated from the steady state stiffness value $k(a_0)$ where proper contact between cantilever and indenter tip is established, yet without any crack propagation:

$$k_0 = k(a_0) \left(1 + \frac{18\pi(1 - \nu^2)L'^2}{L^3} \int_0^{a_0} \frac{a}{w} Y\left(\frac{a}{w}\right)^2 da \right) \quad (4)$$

By plotting the J -integral vs. the crack propagation Δa (crack resistance curve) the J_Q can be obtained by the criteria of Wurster et al. [48]. This approach states that the blunting of the artificial FIB milled notch starts to initiate a natural crack with stable crack growth at a crack propagation Δa of $0.5 \mu\text{m}$. Finally, the fracture toughness K_{IQ} can be

calculated:

$$K_{IQ} = \sqrt{J_Q \frac{E}{(1 - \nu^2)}} \quad (5)$$

All calculations were conducted using a self-written MATLAB script (The MathWorks Inc., version R2019b, Natick, Massachusetts).

3. Results

Due to the laser surface treatment, the surface is blue-greyish with darker regions marking the border of the laser track (Fig. 3a). Cross-sectional cuts in transversal direction (CS-TD) and rolling direction (CS-RD) are given in Fig. 3b and c, respectively. At the very top of the laser track, a thin oxide layer is present, which is responsible for the colored surface. A WEL formed down to a depth of $30\text{--}40 \mu\text{m}$ from the surface, which already in these lower magnification SEM images looks martensitic-based. Further more, detailed cross-sectional SEM investigations in transversal direction (Fig. 4a, b, c, d, e) and rolling direction (Fig. 4f, g, h, i, j) confirm the martensitic structure at the top region, followed by a gradual transition towards the base material with increasing distance from the surface. The martensitic-based top region of the WEL is fine-grained and randomly orientated (with acicular-like martensite gains) both in the transversal as well as in the rolling direction, Fig. 4b and c, respectively. Further down from the surface ($30\text{--}40 \mu\text{m}$) also randomly distributed ferrite grains are present. After this, at a distance of $40\text{--}50 \mu\text{m}$ from the surface, the microstructure contains a mixture of martensite, deformed ferrite, and pearlite grains, again very similar for the transversal as well as rolling direction, Fig. 4c and h, respectively. Underneath this gradual transition zone, the microstructure is deformed ferritic-pearlitic with slightly more alignment in transversal direction (Fig. 4d) than in rolling direction (Fig. 4i). The almost undeformed virgin ferritic-pearlitic microstructure in both directions is given in Fig. 4e and j. These cross-sections taken at a distance of $\sim 1 \text{ cm}$ from the surface exhibit a globular ferritic-pearlitic microstructure without deformation signs and without a specific alignment.

Inverse pole figure (IPF) maps of the EBSD analysis from the cross-section in transversal direction highlight the massive grains-size difference between the outer-most martensitic structure of the WEL, the transition zone, and the deformed ferritic-pearlitic microstructure underneath, see Fig. 5a. The individual misorientations of the grains is evaluated by applying a 3×3 kernel (Fig. 4b), resulting in an average kernel average misorientation (KAM) angle of $1\text{--}2^\circ$ for the ferritic-pearlitic microstructure. The KAM angle within the WEL seems to be larger. However, no quantitative analysis was possible due to small grain size within this region.

Representative low-load Vickers hardness measurements for these

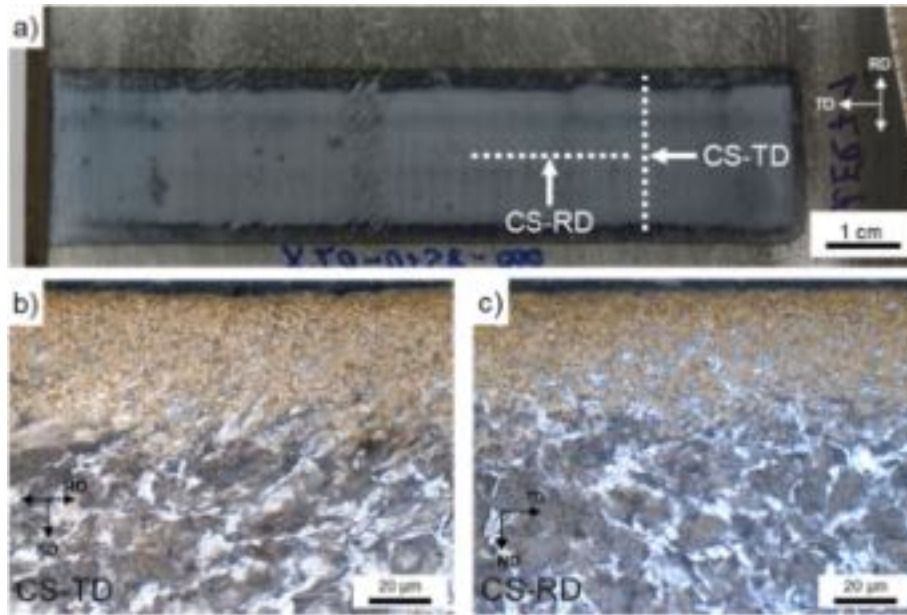


Fig. 3. (a) Top-view of the rail wheel tread surface with the track of the laser surface treatment. LOM images of the cross-sectional cut in transversal direction (CS-TD, (b)) and in rolling direction (CS-RD, (c)) picture the martensitic WEL, the transition zone, and the ferritic-pearlitic underlying microstructure. CS-TD shows a weak alignment of the deformed microstructure.

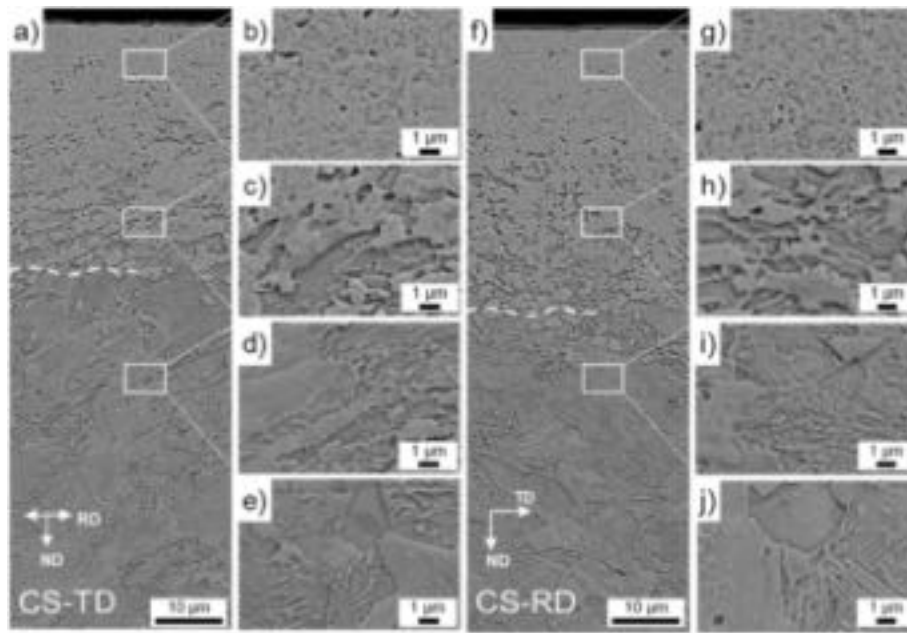


Fig. 4. Electron backscattered images representing the cross-sectional cut in transversal direction (CS-TD, (a)) and rolling direction (CS-RD, (f)). Insets with higher magnification images show the WEL (b, g), the transition zone (c, h), the underlying deformed microstructure (d, i), and the undeformed bulk microstructure (e, j).

regions yield 739 ± 34 HV0.05 within the martensitic dominated top-most region and 516 ± 11 HV0.05 for the transition zone of the WEL, while the deformed ferritic-pearlitic microstructure underneath exhibits 308 ± 16 HV0.05. Nanoindentations from these zones yield 6.98 ± 0.68 and 5.17 ± 0.39 GPa for the martensitic dominated and the transition zone of the WEL, respectively, whereas the deformed ferritic-pearlitic microstructure yields 3.30 ± 0.33 GPa. Thus, confirming the observed trend of the low-load Vickers hardness measurements. Fig. 5c shows the areas within these regions where these measurements were conducted, in addition to the obtained hardness values.

In-situ bending experiments of V-notched micro-cantilevers taken out from the martensitic-dominated top region of the WEL are conducted to

evaluate its fracture behavior qualitatively and to determine its fracture toughness value. Out of eight cantilevers tested, six (C-2, -3, -4, -6, -7, -8) provided valid fracture experiments. Their stress-displacement curves calculated from the recorded force-displacement signals are given in Fig. 6a. These clearly show, after an initial linear behavior, a plastic behavior, followed by a region with features characteristic for crack initiation and propagation. Although the maximum stress scatters between ~ 70 and 100 mN/mm², which could also originate from errors of the cross-section measurements, their fracture behavior shows nearly no differences during the *in-situ* studies, which are exemplarily shown in Fig. 6b, c, and d for the cantilevers C-2, C-4, and C-8, respectively.

Crack initiation and propagation lead to a decrease in stiffness of the

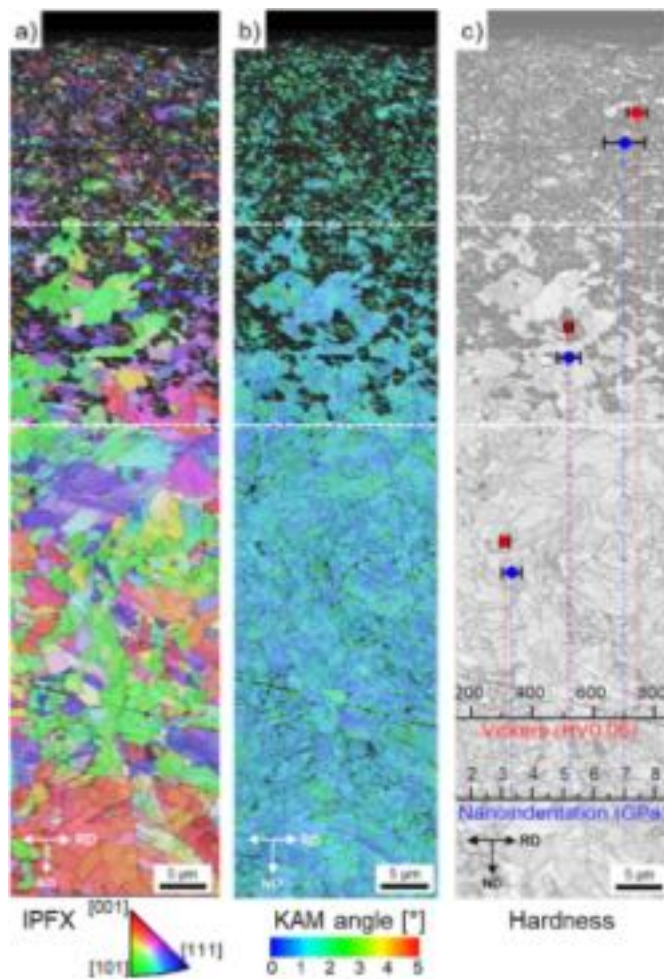


Fig. 5. The EBSD measurements are performed on the cross-sectional cut in transversal direction (CS-TD) and include the WEL with low pattern quality and a high fraction of zero-solutions, the transition zone, and the underlying deformed hypoeutectoid steel. The inverse pole figure (IPFX) map (a) and the Kernel average misorientation (KAM) angle map (b) is shown. In (c), the hardness values within the three zones evaluated by the low-load Vickers technique and nanoindentation are presented.

cantilever (Fig. 7a) from which the crack propagation can be calculated (Fig. 7b) using a constant elastic modulus. This is used to obtain the evolution of the J -integral during the crack propagation (Fig. 7c), which shows similar curves for the individual cantilevers. Their evaluation yields fracture toughness values K_{IQ} of $16.4 \pm 1.2 \text{ MPam}^{1/2}$.

Exemplarily, Fig. 8 shows detailed SEM studies of the two cantilevers C-2 (Fig. 8a, b and c) and C-6 (Fig. 8d, e and f) after the bending experiment. These clearly show the propagating crack from the FIB milled pre-notch of the sample. Because at the sidewalls of the cantilevers only a plain-stress situation is active (contraction is allowed), the plastic deformation zone at these surfaces is typically 9-times (when using a Poisson's ratio of 1/3) of that within the center of the sample where essentially a plain-strain situation is active (contraction is hindered). The contraction of the side walls of the cantilevers can nicely be seen in the SEM images for the samples C-2 (Fig. 8a) and C-6 (Fig. 8d). FIB milling the cantilever at the region of the crack propagation down to its center allows to observe the area of a plain-strain situation. For this, the opened crack was filled with tungsten to protect the surface during FIB milling, Fig. 8b shows the sample C-2 and Fig. 8e sample C-6. Especially the latter shows a clear crack deflection, which can be related to the microstructural features of this sample, which are better seen during ion channeling contrast imaging Fig. 8f. These investigations

suggest that the crack is deflected at the individual grain and phase boundaries of the acicular martensite. In this region, at the crack tip, the sample C-2 shows fewer zig-zag arrangements of martensite grains (Fig. 8c), thus the crack propagation is little deflected. These differences in crack propagation can account for the higher (even highest) J values of sample C-6, see Fig. 7c.

4. Discussion

Laser surface treatments are commonly used to create WELs to improve wear resistance of steel surfaces or to imitate the near-surface microstructures present due to rail-wheel contacts [12–16]. Such WELs are often termed “thermal WELs” to indicate their origin, since under certain parameters WEL-like microstructures can also be formed mechanically [49]. In both cases, the WEL is frequently the origin of many crack initiations, and its brittle nature only provides a limited resistance against crack growth. Recently we showed that the microstructural characteristics of laser-induced thermal WELs on deformed wheel steel surfaces are comparable to WELs formed on a rail wheel tread surfaces during railway operation [36]. Essential is, that a deformed wheel steel is used, as the same laser treatment of an undeformed wheel steel base material leads to a “thermal WEL” with significantly different microstructural features as compared to the “field WEL” [36]. This motivated us to prepare “thermal WELs” with significant thickness and areal expansion on a deformed decommissioned rail wheel, to allow for detailed microstructural characterizations and FIB machining of eight microcantilevers used for *in-situ* micromechanical investigations. In contrast to investigations on WELs from field with estimated loading history, the artificial formation by laser surface treatments serves as a defined and reproducible approach to imitate WELs in terms of their energy and temperature input, respectively. These allowed for a holistic view of the microstructural characteristics and the mechanical properties (here especially strength and fracture toughness) of the WEL, which is needed to understand the fracture behavior of this most sensitive region.

The thermal WEL, which is induced on a deformed rail wheel by laser surface treatments, is characterized by a 30–40 μm thick outer-most martensitic-based region and a 20–30 μm wide transition zone to the deformed ferritic-pearlitic microstructure of the hypoeutectoid steel. The $739 \pm 34 \text{ HV0.05}$ respectively $6.98 \pm 0.68 \text{ GPa}$ hardness of the martensitic region of the WEL compares well to those of WELs on rails, with hardness values of $\sim 700\text{--}800 \text{ HV0.05}$ respectively $\sim 7 \text{ GPa}$ [15, 50–52]. When it comes to fracture toughness – which strongly depends on microstructural characteristics and often shows an inverse correlation with hardness [53] – in-depth studies are quite rare [22,54–56]. Often, only semi-empirical descriptors are used to estimate the fracture toughness based on hardness values. But besides uncertain estimations, which make such fracture toughness evaluations demanding [24], toughness and hardness often go separate ways, as mentioned above. Thus, qualitative and quantitative evaluations of the fracture behavior of such WELs are needed. Kumar et al. [56] pioneered the experimental study, by *in-situ* micromechanical investigations, of the fracture toughness of a WEL formed during service on a R350HT rail steel (Fe-0.72C-1.1Mn-0.56Si-0.11Cr (wt.%)). They report about fracture toughness values of 21.5 ± 3.0 to $25.4 \pm 2.3 \text{ MPam}^{1/2}$ and a hardness of 1000–700 HV0.025. While the hardness values are comparable, the fracture toughness values are much higher than the $16.4 \pm 1.2 \text{ MPam}^{1/2}$ obtained in this work. This might originate from the different chemical composition of the steel grade and the deformation state, but also the different approach for evaluating the stiffness and J -integral. Kumar et al. used unloading cycles to evaluate the stiffness change and estimated the J -integral by intersection of the blunting line and the stable crack growth, whereas we used a superimposed sinusoidal signal with an amplitude of 5 nm and a frequency of 200 Hz and obtained the J -integral at a crack propagation Δa of 0.5 μm according to Wurster et al. [48]. Our results are in good agreement with the results of Saxena et al. [22],

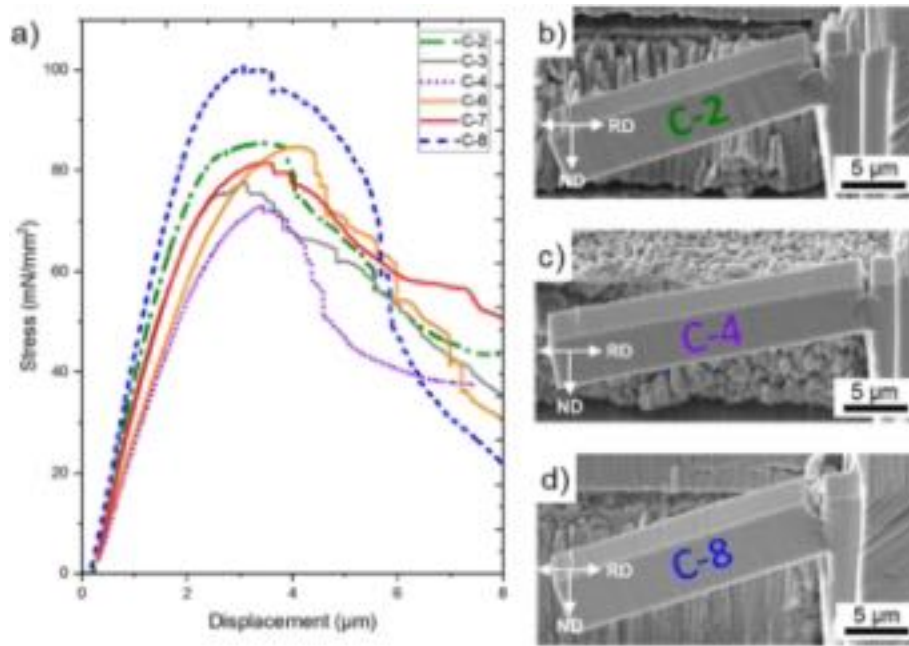


Fig. 6. (a) Stress-displacement curves for all seven valid tested micro-cantilevers show elastic deformation at the beginning, followed by plastic deformation, crack initiation, and propagation. SEM images of representative cantilevers prove this after testing, where cantilever C-2 (b) shows maximum stress of $\sim 85 \text{ N/mm}^2$, cantilever C-4 (c) with the lowest ($\sim 72 \text{ N/mm}^2$), and cantilever C-8 (d) reveals the highest maximum stress of $\sim 100 \text{ N/mm}^2$.

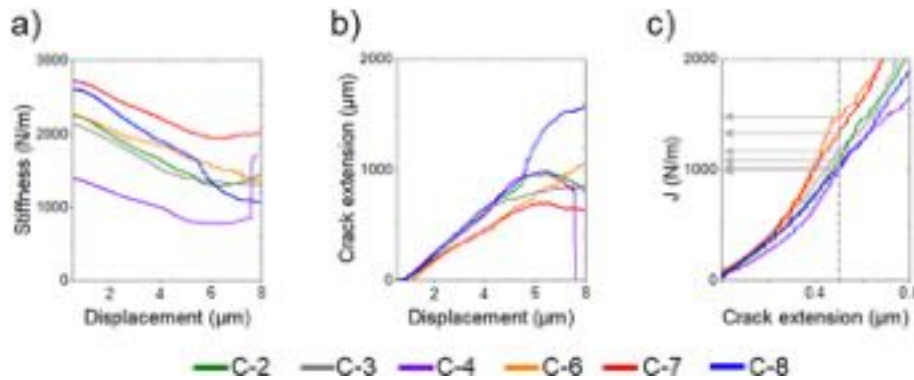


Fig. 7. Based on each cantilever's stiffness change (a), the crack extension is calculated (b). To determine the J -integral, the crack resistance curve (c) is plotted where J_Q is determined at a crack extension of $0.5 \mu\text{m}$.

where a WEL from a R350HT rail and a lab-simulated martensite reveal $14.4 \pm 1.1 \text{ MPam}^{1/2}$ and $16.9 \pm 1.2 \text{ MPam}^{1/2}$ by using the same toughness criteria to estimate the J -integral.

Detailed microstructural investigations – especially after the fracture experiments, Fig. 8 – allowed to explain the deviating J -integral values using the samples C-2 and C-6 (Fig. 7). Thereby, the rather high J -integral values of C-6 could be related to the more pronounced crack deflection at the boundaries of the more acicular-like martensite grains, resulting in calculated fracture toughness values of $\sim 18 \text{ MPam}^{1/2}$. In contrast, the fracture toughness calculated for C-2 is $\sim 16 \text{ MPam}^{1/2}$. As these results suggest, comparing localized micro-mechanical testing needs to be done with caution, as differences in local morphology and stress state easily influence the results, especially if the grain size of certain structures is in the range of the specimen geometry. Despite the experimental challenges [24], the quantitative as well as qualitative results from the micro-mechanical testing of the martensitic-based region of the WEL thermally induced by surface laser treatment of a hypoeutectoid steel are in good agreement with the rare literature about micro-mechanical testing of WELs on rail steels from the field [22,56]. Besides well-established microstructural characterization methods and

micro-hardness testing methods, this work underlines the need for micro-cantilever bending experiments to characterize the fracture behavior and evaluate the fracture toughness. A holistic view of the various mechanical properties is required, since toughness cannot be estimated without error from hardness and microstructure, but is essential to understand small-scale microstructural phenomena prone to crack initiation, growth, and failure [57–59].

5. Conclusions

Within this work, the microstructure of a thermal WEL induced by laser surface treatment with defined thermal loading parameters and a pre-deformation state from the rail-wheel contact is investigated in terms of microstructural and micro-mechanical characteristics.

This thermal WEL contains a fine-grained, randomly orientated acicular martensitic microstructure with an increasing fraction of ferrite islands from the surface towards the transition to the underlying deformed ferritic-pearlitic microstructure. The $30\text{--}40 \mu\text{m}$ thick outermost martensitic-based region exhibits a hardness of $739 \pm 34 \text{ HV0.05}$ respectively $6.98 \pm 0.68 \text{ GPa}$ while the $20\text{--}30 \mu\text{m}$ wide transition zone

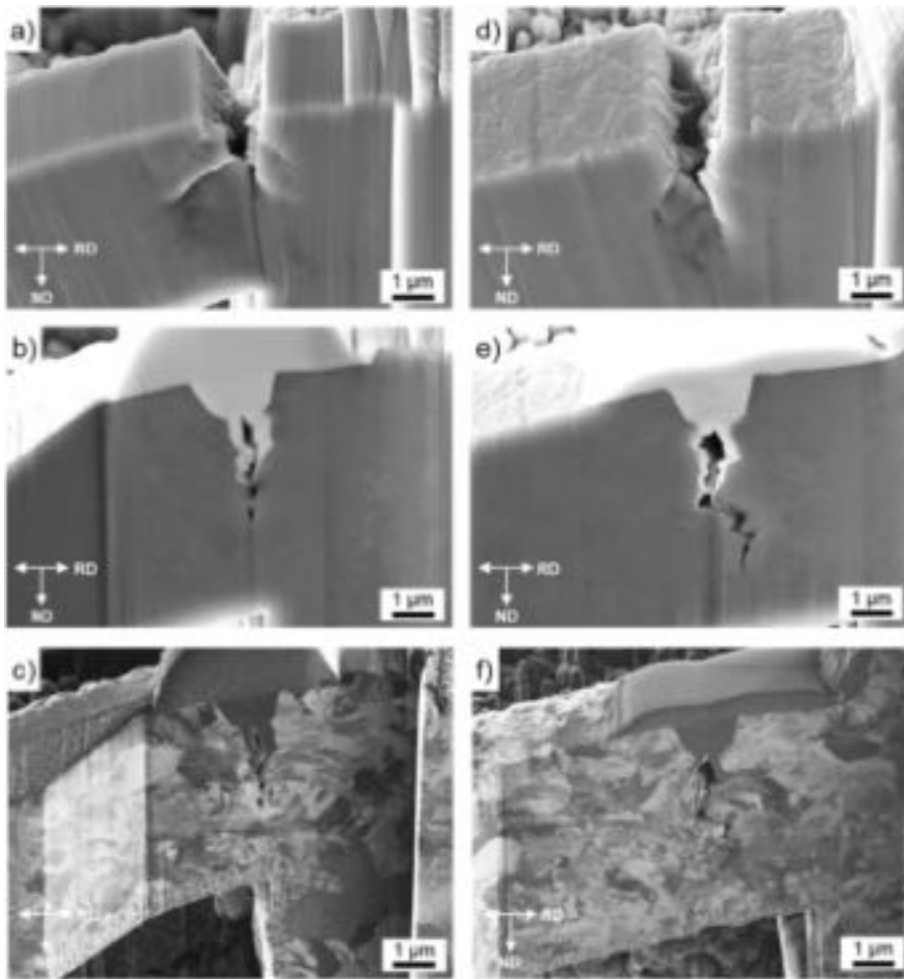


Fig. 8. In the first row, secondary electron (SE) images of the fractured cantilever C-2 (a) and C-6 (d) are presented. The cantilevers reveal the same stress level during bending but different J_Q values. After depositing tungsten onto the notch region to protect the cantilever, FIB milling is done to prepare a cross-section in the middle of the cantilever, displayed in the second row (b, e). Ion channeling contrast images are shown additionally (c, f) to highlight the crack evolution within the microstructure.

shows 516 ± 11 HV0.05 respectively 5.17 ± 0.39 GPa, and the deformed ferritic-pearlitic microstructure yields 308 ± 16 HV0.05 respectively 3.30 ± 0.33 GPa. Detailed microstructural investigations in combination with *in-situ* V-notched micro-cantilever bending experiments show that crack propagation is preferred at the boundaries of the acicular martensite grains. The generally elastic-plastic fracture behavior required the evaluation with the J -integral, obtained by continuous stiffness measurement, yielding $K_{I,Q}$ of 16.4 ± 1.2 MPam^{1/2}. It is shown that the application of micro-cantilever bending tests is a promising tool to describe the micro-mechanical properties in addition to common nanoindentation, instead of unprecise estimations of the fracture toughness based on obtained hardness values. The improvements in the field of micro-testing enables a holistic view of micro-mechanical properties, especially hardness and toughness, in relation to its microstructural characteristics.

CRedit authorship contribution statement

M. Freisinger: Conceptualization, Methodology, Validation, Writing – original draft. **L. Zauner:** Software, Data curation, Writing – review & editing. **R. Hahn:** Methodology, Data curation, Writing – review & editing. **H. Riedl:** Supervision, Writing – review & editing. **P.H. Mayrhofer:** Supervision, Writing – review & editing.

Declaration of competing interest

The authors declare that they have no known competing financial interests or personal relationships that could have appeared to influence

the work reported in this paper.

Data availability

Data will be made available on request.

Acknowledgments

This project has received funding from the Shift2Rail Joint Undertaking (JU) under grant agreement No 826255 and No 101012456. The JU receives support from the European Union's Horizon 2020 research and innovation program and the Shift2Rail JU members other than the Union. In addition, this work was funded by the "Austrian COMET-Program" (project InTribology1, no. 872176) via the Austrian Research Promotion Agency (FFG) and the federal states of Niederösterreich and Vorarlberg and was carried out within the "Excellence Center of Tribology" (AC2T research GmbH). The financial support by the Austrian Federal Ministry for Digital and Economic Affairs, the National Foundation for Research, Technology and Development, and the Christian Doppler Research Association is gratefully acknowledged (Christian Doppler Laboratory "Surface Engineering of high-performance Components").

References

- [1] X. Jin, Y. Chen, L. Wang, H. Han, P. Chen, Failure prediction, monitoring and diagnosis methods for slewing bearings of large-scale wind turbine: a review, *Measurement* 172 (Feb. 2021), 108855, <https://doi.org/10.1016/j.measurement.2020.108855>.

- [2] C. Suetrong, Investigations of fatigue crack propagation in ER8 railway wheel steel with varying microstructures, *Mater. Sci.* 17 (2022).
- [3] Y. Liu, B. Stratman, S. Mahadevan, Fatigue crack initiation life prediction of railroad wheels, *Int. J. Fatig.* 28 (7) (Jul. 2006) 747–756, <https://doi.org/10.1016/j.ijfatigue.2005.09.007>.
- [4] H.C. Eden, J.E. Garnham, C.L. Davis, Influential microstructural changes on rolling contact fatigue crack initiation in pearlitic rail steels, *Mater. Sci. Technol.* 21 (6) (Jun. 2005) 623–629, <https://doi.org/10.1179/174328405X43207>.
- [5] C. Liu, et al., Formation mechanism for the white etching microstructure in the subsurface of the failure pearlite wheel steel, *Wear* 494 (495) (Apr. 2022), 204243, <https://doi.org/10.1016/j.wear.2022.204243>.
- [6] C. Bernsteiner, et al., Simulation and experiment based investigations of squat formation mechanisms, *Wear* 440–441 (2019), 203093, <https://doi.org/10.1016/j.wear.2019.203093>.
- [7] A. Al-Juboori, et al., Characterisation of White Etching Layers formed on rails subjected to different traffic conditions, *Wear* 436 (437) (Oct. 2019), 202998, <https://doi.org/10.1016/j.wear.2019.202998>.
- [8] A. Kumar, G. Agarwal, R. Petrov, S. Goto, J. Sietsma, M. Herbig, Microstructure evolution of white and brown etching layers in pearlitic rail steels, *Acta Mater.* 171 (Jun. 2019) 48–64, <https://doi.org/10.1016/j.actamat.2019.04.012>.
- [9] M. Shamsujjoha, Evolution of microstructures, dislocation density and arrangement during deformation of low carbon lath martensitic steels, *Mater. Sci. Eng., A* 776 (Mar. 2020), 139039, <https://doi.org/10.1016/j.msea.2020.139039>.
- [10] J.I. Pereira, G. Tressia, E.J. Kina, A. Sinatora, R.M. Souza, Analysis of subsurface layer formation on a pearlitic rail under heavy haul conditions: spalling characterization, *Eng. Fail. Anal.* 130 (Dec. 2021), 105549, <https://doi.org/10.1016/j.engfailanal.2021.105549>.
- [11] G. Baumann, H.J. Fecht, S. Liebelt, Formation of white-etching layers on rail trends, *Wear* 191 (1–2) (Jan. 1996) 133–140, [https://doi.org/10.1016/0043-1648\(95\)06733-7](https://doi.org/10.1016/0043-1648(95)06733-7).
- [12] S. Li, J. Wu, R.H. Petrov, Z. Li, R. Dollevoet, J. Sietsma, Brown etching layer: a possible new insight into the crack initiation of rolling contact fatigue in rail steels? *Eng. Fail. Anal.* 66 (Aug. 2016) 8–18, <https://doi.org/10.1016/j.engfailanal.2016.03.019>.
- [13] M. Messaadi, M. Steenbergen, Stratified surface layers on rails, *Wear* 414–415 (Nov. 2018) 151–162, <https://doi.org/10.1016/j.wear.2018.07.019>.
- [14] Q. Lian, et al., Evolution of thermally induced white etching layer at rail surface during multiple wheel/train passages, *Int. J. Fatig.* 159 (Jun. 2022), 106799, <https://doi.org/10.1016/j.ijfatigue.2022.106799>.
- [15] Y.Z. Chen, C.G. He, X.J. Zhao, L.B. Shi, Q.Y. Liu, W.J. Wang, The influence of wheel flats formed from different braking conditions on rolling contact fatigue of railway wheel, *Eng. Fail. Anal.* 93 (Nov. 2018) 183–199, <https://doi.org/10.1016/j.engfailanal.2018.07.006>.
- [16] B. Hieu Nguyen, A. Al-Juboori, H. Zhu, A.A. Gazder, H. Li, K. Tieu, Fracture mechanisms in rails with mechanically and thermomechanically-induced white etching layers under three-point bending, *Eng. Fail. Anal.* 131 (Jan. 2022), 105813, <https://doi.org/10.1016/j.engfailanal.2021.105813>.
- [17] Q. Lian, et al., Crack propagation behavior in white etching layer on rail steel surface, *Eng. Fail. Anal.* 104 (Oct. 2019) 816–829, <https://doi.org/10.1016/j.engfailanal.2019.06.067>.
- [18] A. Al-Juboori, et al., Squat formation and the occurrence of two distinct classes of white etching layer on the surface of rail steel, *Int. J. Fatig.* 104 (Nov. 2017) 52–60, <https://doi.org/10.1016/j.ijfatigue.2017.07.005>.
- [19] S. Pal, W.J.T. Daniel, M. Farjoo, Early stages of rail squat formation and the role of a white etching layer, *Int. J. Fatig.* 52 (Jul. 2013) 144–156, <https://doi.org/10.1016/j.ijfatigue.2013.02.016>.
- [20] R.I. Carroll, J.H. Beynon, Rolling contact fatigue of white etching layer: Part 1 Crack morphology, *Wear* 262 (2007) 1253–1266, <https://doi.org/10.1016/j.wear.2007.01.003>.
- [21] C.J. Rasmussen, S. Fæster, S. Dhar, J.V. Quaade, M. Bini, H.K. Danielsen, Surface crack formation on rails at grinding induced martensite white etching layers, *Wear* 384–385 (Aug. 2017) 8–14, <https://doi.org/10.1016/j.wear.2017.04.014>.
- [22] A.K. Saxena, A. Kumar, M. Herbig, S. Brinckmann, G. Dehm, C. Kirchlechner, Micro fracture investigations of white etching layers, *Mater. Des.* 180 (Oct. 2019), 107892, <https://doi.org/10.1016/j.matdes.2019.107892>.
- [23] G. Dehm, B.N. Jaya, R. Raghavan, C. Kirchlechner, Overview on micro- and nanomechanical testing: new insights in interface plasticity and fracture at small length scales, *Acta Mater.* 142 (Jan. 2018) 248–282, <https://doi.org/10.1016/j.actamat.2017.06.019>.
- [24] R. Pippin, S. Wurster, D. Kiener, Fracture mechanics of micro samples: fundamental considerations, *Mater. Des.* 159 (Dec. 2018) 252–267, <https://doi.org/10.1016/j.matdes.2018.09.004>.
- [25] B.N. Jaya, C. Kirchlechner, G. Dehm, Can microscale fracture tests provide reliable fracture toughness values? A case study in silicon, *J. Mater. Res.* 30 (5) (Mar. 2015) 686–698, <https://doi.org/10.1557/jmr.2015.2>.
- [26] J.P. Best, et al., A comparison of three different notching ions for small-scale fracture toughness measurement, *Scripta Mater.* 112 (Feb. 2016) 71–74, <https://doi.org/10.1016/j.scriptamat.2015.09.014>.
- [27] R. Hahn, M. Bartosik, R. Soler, C. Kirchlechner, G. Dehm, P.H. Mayrhofer, Superlattice effect for enhanced fracture toughness of hard coatings, *Scripta Mater.* 124 (Nov. 2016) 67–70, <https://doi.org/10.1016/j.scriptamat.2016.06.030>.
- [28] R. Daniel, et al., Grain boundary design of thin films: using tilted brittle interfaces for multiple crack deflection toughening, *Acta Mater.* 122 (Jan. 2017) 130–137, <https://doi.org/10.1016/j.actamat.2016.09.027>.
- [29] M. Alfreider, D. Kozic, O. Kolednik, D. Kiener, In-situ elastic-plastic fracture mechanics on the microscale by means of continuous dynamical testing, *Mater. Des.* 148 (Jun. 2018) 177–187, <https://doi.org/10.1016/j.matdes.2018.03.051>.
- [30] B.N. Jaya, V. Jayaram, Fracture testing at small-length scales: from plasticity in Si to brittleness in Pt, *J. Occup. Med.* 68 (1) (Jan. 2016) 94–108, <https://doi.org/10.1007/s11837-015-1489-2>.
- [31] O.P. Ostash, V.V. Kulyk, T.M. Lenkovskiy, Z.A. Duriagina, V.V. Vira, T.L. Tepla, Relationships between the fatigue crack growth resistance characteristics of a steel and the tread surface damage of railway wheel, *Archives of Materials Science and Engineering* 2 (90) (Apr. 2018) 49–55, <https://doi.org/10.5604/01.3001.0012.0662>.
- [32] T. Kato, Y. Yamamoto, H. Kato, S. Dedmon, J. Pilch, Effect of fracture toughness on vertical split rim failure in railway wheels, *Eng. Fract. Mech.* 186 (Dec. 2017) 255–267, <https://doi.org/10.1016/j.engfracmech.2017.09.025>.
- [33] H.P. Rossmannith, F. Loibnegger, R. Huber, Thermomechanical fatigue fracture due to repeated braking of railway wheels, *Mater. Sci.* 42 (4) (Jul. 2006) 466–475, <https://doi.org/10.1007/s11003-006-0102-9>.
- [34] D. Peng, R. Jones, T. Constable, A study into crack growth in a railway wheel under thermal stop brake loading spectrum, *Eng. Fail. Anal.* 25 (Oct. 2012) 280–290, <https://doi.org/10.1016/j.engfailanal.2012.05.018>.
- [35] A. Ekberg, E. Kabo, Fatigue of railway wheels and rails under rolling contact and thermal loading—an overview, *Wear* 258 (7–8) (2005) 1288–1300, Mar, <https://doi.org/10.1016/j.wear.2004.03.039>.
- [36] M. Freisinger, et al., Comparative study on the influence of initial deformation and temperature of thermally induced white etching layers on rail wheels, *Tribol. Int.* 177 (Jan. 2023), 107990, <https://doi.org/10.1016/j.triboint.2022.107990>.
- [37] EN 13262:2004+A2:2011: Railway Applications - Wheelsets and Bogies - Wheels - Product Requirements.
- [38] M. Diener, A. Ghidini, Fracture toughness: a quality index for railway solid wheels, *Mats. Perf. Charact.* 3 (3) (Jun. 2014), 20130047, <https://doi.org/10.1520/MPC20130047>.
- [39] H. Rojacz, M. Premauer, A. Nevasod, Conductive and edge retaining embedding compounds: influence of graphite content in compounds on specimen's SEM and EBSD performance, *Pract. Metallogr.* 58 (5) (May 2021) 236–263, <https://doi.org/10.1515/pm-2021-0018>.
- [40] W.C. Oliver, G.M. Pharr, An improved technique for determining hardness and elastic modulus using load and displacement sensing indentation experiments, *J. Mater. Res.* 7 (6) (Jun. 1992) 1564–1583, <https://doi.org/10.1557/JMR.1992.1564>.
- [41] K. Matoy, et al., A comparative micro-cantilever study of the mechanical behavior of silicon based passivation films, *Thin Solid Films* 518 (1) (Nov. 2009) 247–256, <https://doi.org/10.1016/j.tsf.2009.07.143>.
- [42] M. Alfreider, S. Kolitsch, S. Wurster, D. Kiener, An analytical solution for the correct determination of crack lengths via cantilever stiffness - SUPP, *Mater. Des.* 194 (Sep. 2020), 108914, <https://doi.org/10.1016/j.matdes.2020.108914>.
- [43] M. Alfreider, R. Bodlos, L. Romaner, D. Kiener, The influence of chemistry on the interface toughness in a WTi-Cu system, *Acta Mater.* 230 (May 2022), 117813, <https://doi.org/10.1016/j.actamat.2022.117813>.
- [44] M. Alfreider, J. Zechner, D. Kiener, Addressing fracture properties of individual constituents within a Cu-WTi-SiOx-Si multilayer, *J. Occup. Med.* 72 (12) (Dec. 2020) 4551–4558, <https://doi.org/10.1007/s11837-020-04444-6>.
- [45] M. Alfreider, D. Kozic, O. Kolednik, D. Kiener, In-situ elastic-plastic fracture mechanics on the microscale by means of continuous dynamical testing, *Mater. Des.* 148 (Jun. 2018) 177–187, <https://doi.org/10.1016/j.matdes.2018.03.051>.
- [46] X.-K. Zhu, J.A. Joyce, Review of fracture toughness (G, K, J, CTOD, CTOA) testing and standardization, *Eng. Fract. Mech.* 85 (May 2012) 1–46, <https://doi.org/10.1016/j.engfracmech.2012.02.001>.
- [47] A. Riedl, et al., A novel approach for determining fracture toughness of hard coatings on the micrometer scale, *Scripta Mater.* 67 (7–8) (Oct. 2012) 708–711, <https://doi.org/10.1016/j.scriptamat.2012.06.034>.
- [48] S. Wurster, C. Motz, R. Pippin, Characterization of the fracture toughness of micro-sized tungsten single crystal notched specimens, *Phil. Mag.* 92 (14) (May 2012) 1803–1825, <https://doi.org/10.1080/14786435.2012.658449>.
- [49] R. Pan, Y. Chen, H. Lan, S. E. R. Ren, Investigation into the microstructure evolution and damage on rail at curved tracks, *Wear* 504 (505) (Sep. 2022), 204420, <https://doi.org/10.1016/j.wear.2022.204420>.
- [50] Y. Zhou, J.F. Peng, Z.P. Luo, B.B. Cao, X.S. Jin, M.H. Zhu, Phase and microstructural evolution in white etching layer of a pearlitic steel during rolling-sliding friction, *Wear* 362 (363) (Sep. 2016) 8–17, <https://doi.org/10.1016/j.wear.2016.05.007>.
- [51] W. Österle, H. Rooch, A. Pyzalla, L. Wang, Investigation of white etching layers on rails by optical microscopy, electron microscopy, X-ray and synchrotron X-ray diffraction, *Mater. Sci. Eng., A* 303 (1–2) (May 2001) 150–157, [https://doi.org/10.1016/S0921-5093\(00\)01842-6](https://doi.org/10.1016/S0921-5093(00)01842-6).
- [52] W. Lojkowski, M. Džahanbakhsh, G. Bürkle, S. Gierlotka, W. Zielinski, H.-J. Fecht, Nanostructure formation on the surface of railway tracks, *Mater. Sci. Eng., A* 303 (1–2) (May 2001) 197–208, [https://doi.org/10.1016/S0921-5093\(00\)01947-X](https://doi.org/10.1016/S0921-5093(00)01947-X).
- [53] Robert O. Ritchie, The conflicts between strength and toughness, *Nat. Mater.* 10 (2011) 817–822.
- [54] A. Chabok, E. Van der Aa, J.T.M. De Hosson, Y. Pei, Characterization of Fracture Toughness for Different Zones of Resistance Spot Welded Dual Phase Steel Using Micro-cantilever Testing: International Conference on PROCESSING & MANUFACTURING OF ADVANCED MATERIALS, International Conference on PROCESSING & MANUFACTURING OF ADVANCED MATERIALS, Jul. 2018.
- [55] B.N. Jaya, Fracture behavior of nanostructured heavily cold drawn pearlitic steel wires before and after annealing, *Mater. Sci.* 8 (2017).

- [56] A. Kumar, et al., In situ study on fracture behaviour of white etching layers formed on rails, *Acta Mater.* 180 (Nov. 2019) 60–72, <https://doi.org/10.1016/j.actamat.2019.08.060>.
- [57] B. Li, P. Li, R. Zhou, X.-Q. Feng, K. Zhou, Contact mechanics in tribological and contact damage-related problems: a review, *Tribol. Int.* 171 (Jul. 2022), 107534, <https://doi.org/10.1016/j.triboint.2022.107534>.
- [58] Q. Lian, G. Deng, H. Zhu, H. Li, X. Wang, Z. Liu, Influence of white etching layer on rolling contact behavior at wheel-rail interface, *Friction* 8 (6) (Dec. 2020) 1178–1196, <https://doi.org/10.1007/s40544-020-0388-x>.
- [59] J. Pan, L. Chen, C. Liu, G. Zhang, R. Ren, Relationship between the microstructural evolution and wear behavior of U71Mn rail steel, *J. Mater. Eng. Perform.* 30 (2) (Feb. 2021) 1090–1098, <https://doi.org/10.1007/s11665-021-05452-6>.

Publication VII



Influence of thermal loading parameters and microstructure on the formation of stratified surface layers on railway wheels

M. Freisinger, K. Pichelbauer, G. Trummer, K. Six
under review at *Journal of Rail and Rapid Transit* (17.07.2023)



Influence of thermal loading parameters and microstructure on the formation of stratified surface layers on railway wheels

Journal:	<i>Part F: Journal of Rail and Rapid Transit</i>
Manuscript ID	JRRT-23-0166
Manuscript Type:	Article
Date Submitted by the Author:	17-Jul-2023
Complete List of Authors:	Freisinger, Matthias; Vienna Technical University Institute of Materials Science and Technology, ; AC2T research GmbH, Pichelbauer, Kurt; AC2T research GmbH, Trummer, Gerald; Virtual Vehicle Research Center, Vehicle Dynamics - Rail Applications Six, Klaus; Virtual Vehicle Research Center, Vehicle Dynamics - Rail Systems
Keywords:	Wheel-rail contact, white etching layer, brown etching layer, stratified surface layer, laser surface treatment
Abstract:	Due to an increasing trend towards environmentally friendly public transport, rail networks face higher speeds and wheel loads affecting the material degradation of the railway components. Within this study, influencing parameters on the formation of stratified surface layers, forming on railway wheels during service due to thermal loadings in the wheel-rail contact, are studied. These layers consist of white etching layer and underlying brown etching layer and are susceptible to fatigue crack initiation. By using laser surface treatments, its formation based on two consecutive thermal loadings is systematically demonstrated on ER7 wheel steel. Further, a decrease in layer thickness with decreasing laser power, and an increase in brown etching layer thickness with increasing laser power difference is shown. Moreover, the effect of grain size leading to an increased layer thickness, and the influence of the chemical composition by comparing the standard ER7 wheel steel to a micro-alloyed ER7 steel are demonstrated.

Influence of thermal loading parameters and microstructure on the formation of stratified surface layers on railway wheels

M. Freisinger^{a,c*}, K. Pichelbauer^a, G. Trummer^b, K. Six^b

^a AC2T research GmbH, A-2700 Wiener Neustadt, Austria

^b Virtual Vehicle Research GmbH, A-8010 Graz, Austria

^c Institute of Materials Science and Technology, TU Wien, A-1060 Wien, Austria

*corresponding author: matthias.freisinger@ac2t.at; ORCID: 0000-0001-9616-4613

1
2
3
4
5
6
7
8
9
10
11
12
13
14
15
16
17
18
19
20
21
22
23
24
25
26
27
28
29
30
31
32
33
34
35
36
37
38
39
40
41
42
43
44
45
46
47
48
49
50
51
52

For Peer Review



Influence of thermal loading parameters and microstructure on the formation of stratified surface layers on railway wheels

Abstract

Due to an increasing trend towards environmentally friendly public transport, rail networks face higher speeds and wheel loads affecting the material degradation of the railway components. Within this study, influencing parameters on the formation of stratified surface layers, forming on railway wheels during service due to thermal loadings in the wheel-rail contact, are studied. These layers consist of white etching layer and underlying brown etching layer and are susceptible to fatigue crack initiation. By using laser surface treatments, its formation based on two consecutive thermal loadings is systematically demonstrated on ER7 wheel steel. Further, a decrease in layer thickness with decreasing laser power, and an increase in brown etching layer thickness with increasing laser power difference is shown. Moreover, the effect of grain size leading to an increased layer thickness, and the influence of the chemical composition by comparing the standard ER7 wheel steel to a micro-alloyed ER7 steel are demonstrated.

Keywords: wheel-rail contact; stratified surface layer; white etching layer; brown etching layer; laser surface treatment; near-surface microstructure

Statements and Declarations

The authors declare that they have no known competing financial interests or personal relationships that could have appeared to influence the work reported in this paper.

Introduction

To meet the world climate targets it is crucial to enhance rail transportation, hence, the rail infrastructure is currently faced with increasing train intervals and loads. To ensure reliability and safety of rails and wheels in service an improved understanding of material defects is vital. This will help to make maintenance of railway components more efficient in the future.

Recently, so-called “Stratified Surface Layers” (SSLs) – observed on wheels in service – devote growing research interest due to its predicted relation to fatigue crack initiation [1]–[6]. Such near-surface microstructures are a combination of a white etching layer (WEL) and an underlying brown etching layer (BEL). WEL and BEL are named based on their appearance under a light optical microscope (LOM), where the layer appears white and brown after etching with a nitric acid, respectively. The vast variety of SSLs observed on rails and wheels seems to be an insurmountable obstacle for a systematic study of the formation mechanism and its influencing parameters, since the loading history of samples from field is never fully clear. This demands a reproducible approach to create defined SSLs.

Besides mechanical loads in the wheel-rail contact, thermal loads are predicted to be the major reason for the formation of extensive WELs, hence, studies applying laser surface treatments to imitate thermal loads in rolling-sliding contacts and following WEL formation have been resented in the last years [7]–[9]. In addition to the complex thermal loading situation in wheel-rail contacts, the chemical composition of rail and wheel steels are another influencing parameter on the formation of SSLs. Besides micro-alloyed steels are discussed as wheel materials with improved wear resistance [10]–[14], the influence on the formation of thermally induced layers, such as WELs or SSLs, is not studied yet.

1
2
3 Within this work, laser surface treatments are conducted on railway wheel steels – with
4 different prior laboratory heat treatments – to study the formation mechanism of SSLs.
5
6 By varying the parameters of the laser surface treatments, influences of different thermal
7 load sequences and parameters are investigated. Moreover, influences of the initial
8 microstructure with respect to grain size and chemical composition are evaluated. This
9 works presents a systematic study on SSLs and contribute to an increased knowledge of
10 crack-related near-surface microstructures formed on railway wheels in service.
11
12
13
14
15
16
17
18
19
20

21 **Materials and methods**

22 The materials used in this study are obtained from wheels provided by the Austrian
23 Federal Railways (OEBB, Austria) and CAF AG (Construcciones y Auxiliar de
24 Ferrocarriles, Spain). For evaluating the influences of the thermal loading parameters and
25 the influence of the grain size, the wheel steel grade ER7 – commonly used in European
26 rail traffic – is used. Further, a micro-alloyed ER7 steel (ER7-MA) is investigated to
27 determine the influence of changes in the chemical composition of the wheel steel on the
28 formation of SSLs (chemical compositions are given in [Table 1](#)). For the conducted laser
29 surface treatments rectangular plates (~70x70x2 cm) are cut out from the wheels
30 approximately 1 cm below the tread surface to exclude microstructural changes
31 originating from service ([Figure 1a](#)) using a conventional band saw (FMB Pegasus G,
32 FMB s.r.l., Italy) followed by finer processing with a laboratory cutting device (Struers
33 Secotom-50; Struers ApS, Denmark). To ensure a reasonable comparison of the different
34 influencing parameters, comparable sample surfaces are guaranteed. For comparing the
35 railway wheel steels with different chemical composition two different wheel steels (ER7,
36 ER7-MA) the samples extracted from the wheel are heat treated to ensures a consistent
37 microstructure with comparable grain size distribution. Using a chamber furnace
38
39
40
41
42
43
44
45
46
47
48
49
50
51
52

(Carbolite GmbH, CWF 12/23, Germany) austenitization is achieved by holding a temperature of 900°C for 1h with subsequent quenching in oil. Afterwards, tempering at 510°C for 1h is done. The heat-treated plates are further plane-parallel grinded to a surface roughness of $R_a \approx 0.2$. Finally, uniform cleaning of the samples before the laser surface treatments is executed in three steps by using soapy water, ethanol, and acetone.

Table 1: Chemical compositions of the wheel materials.

	C	Si	Mn	Cr	Cu	Ni	P	S	Mo	V	Nb
	wt%										
ER7	0.54	0.30	0.60	0.25	0.15	0.10	0.001	0.02	0.04	0.001	0.002
ER7-MA	0.43	0.30	0.60	0.25	0.15	0.10	0.001	0.02	0.04	0.015	0.015



Figure 1: (a) The samples for the laser treatment are cut out from wheels ~1 cm below the tread surface followed by uniform heat treatment. (b) shows the laser system which is used for applying thermal loads. (c) gives an exemplary wheel plate sample after three laser surface treatments are conducted. Red dotted lines and arrows show the cross-sectional cuts which are analysed by light optical microscopy.

Laser surface treatments are conducted by using a Direct Diode Laser System (HighLight 8000D, Coherent, U.S.). To ensure a careful positioning and movement, the laser system is mounted on a 6-axis robot arm (IRB 4600-60/2.05, ABB, Austria) controlled via the teach-pedant of the controller system of the IRC5 (ABB, Austria), see [Figure 1b](#). A rectangular laser spot with 3 mm in the moving direction (x) and 24 mm in the lateral

direction (y) is used with a constant travel speed (v) of 12 mm/s, laser surface treatments of 30 mm are executed (Figure 1c). Different sequences of laser surface treatments with varying laser powers (P_{laser}) are applied to mimic different energy and thermal inputs, respectively.

Since the surface quality significantly influences the energy input, a thermal camera (FLIR SC7600, Teledyne FLIR LLC, U.S.) is used to determine the surface temperature of the steel samples during the laser treatments. The emission coefficient for calculating the temperature is set to 0.8.

Cross-sectional cuts in laser spot moving direction (Figure 1c) are embedded in conductive compounds (CitoPress-30, Resing: PolyFast; Struers ApS, Denmark), further grinded and polished (Tegramin-30; Struers ApS, Denmark) in various steps to a mirror-polished surface quality (1 μm diamond fine polishing). To evaluate microstructural features the sample is etched with diluted nitric acid (3% HNO_3 , 97% ethanol) and then analysed by LOM (Axio Imager M2m, Carl Zeiss AG, Germany). Images are captured and thicknesses of layers are measured by using IMS Client (Imagic Bildverarbeitung AG, Switzerland). The hardness of the evolved microstructures is determined by low-load Vickers hardness measurements (Future-Tech FM-700, Future Tech Corp., Japan) using a load of 0.05 kp (0.49 N). The diagonals of the indents are measured with the LOM.

Results

Influence of thermal load sequences on SSL formation

In the first section, the effect of different laser surface treatment sequences on the

formation of SSLs on ER7 railway wheel steel are presented: First, two consecutive thermal loads with same laser powers ($P_{\text{Laser},1} = P_{\text{Laser},2} = 4.3 \text{ kW}$) are applied. The results show a martensitic WEL of $\sim 500 \mu\text{m}$ layer thickness without underlying BEL (Figure 2a). Comparable results are achieved when the second thermal load has a higher laser power compared to the first one ($P_{\text{Laser},1} = 4.0 \text{ kW}$, $P_{\text{Laser},2} = 4.3 \text{ kW}$), (Figure 2b). If the laser power of the first laser treatment is higher than the laser power of the second laser treatment ($P_{\text{Laser},1} > P_{\text{Laser},2}$) the formation of an SSL (Figure 2c) is observed. In Figure 2c the laser powers were $P_{\text{Laser},1} = 4.5 \text{ kW}$ and $P_{\text{Laser},2} = 3.8 \text{ kW}$. A sharp transition can be detected from the BEL to the underlying bulk material, whereas the transition region WEL-BEL seems to be more diffuse.

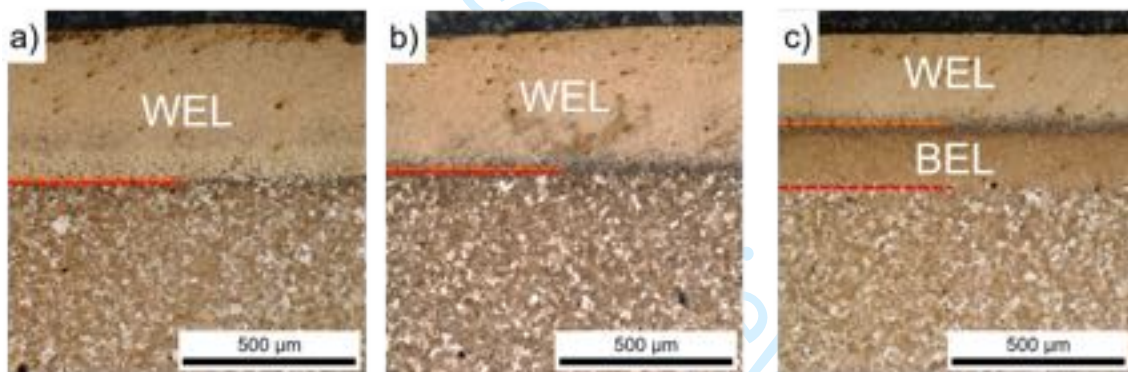


Figure 2: Two consecutive thermal loads are applied by laser surface treatment on ER7 railway wheel steel with varying laser powers: (a) $P_{\text{Laser},1} = P_{\text{Laser},2} = 4.3 \text{ kW}$, (b) $P_{\text{Laser},1} = 4.0 \text{ kW}$, $P_{\text{Laser},2} = 4.3 \text{ kW}$, and (c) $P_{\text{Laser},1} = 4.5 \text{ kW}$, $P_{\text{Laser},2} = 3.8 \text{ kW}$. Only the latter sequence ($P_{\text{Laser},1} > P_{\text{Laser},2}$) induces an SSL, showing a WEL with an underlying BEL.

Influence of thermal load parameters on SSL formation

In this section, the influence of the laser power on the formation of SSLs on ER7 railway wheel steel is shown. Figure 3a reveals an SSL with a thickness of $\sim 180 \mu\text{m}$ formed by consecutive thermal loadings with laser powers of $P_{\text{Laser},1} = 2.3 \text{ kW}$ and $P_{\text{Laser},2} = 1.7 \text{ kW}$.

By increasing the laser powers to 2.4 kW and 1.8 kW (with the same ΔP_{Laser}) the SSL thickness increases by almost 17% up to $\sim 210 \mu\text{m}$ (Figure 3b), while the ratio of WEL and BEL remains the same.

When changing the laser power difference between the first and second thermal loading (change of ΔP_{Laser}) while keeping the laser power for the first loading constant, the ratio of WEL and BEL is changing with consistent SSL thickness: Figure 3c shows an SSLs formed with $\Delta P_{\text{Laser}} = 0.6 \text{ kW}$ ($P_{\text{Laser},1} = 2.4 \text{ kW}$, $P_{\text{Laser},2} = 1.8 \text{ kW}$), that results in SSL layer thickness of $\sim 210 \mu\text{m}$ (WEL: $120 \mu\text{m}$, BEL: $90 \mu\text{m}$). A laser power difference of $\Delta P_{\text{Laser}} = 0.8 \text{ kW}$ ($P_{\text{Laser},1} = 2.4 \text{ kW}$, $P_{\text{Laser},2} = 1.6 \text{ kW}$) also results in an SSL thickness of $\sim 210 \mu\text{m}$ but different thicknesses of the WEL and the BEL (WEL: $30 \mu\text{m}$, BEL: $180 \mu\text{m}$). Within the BEL of this SSL, a significant gradient in the morphology of the microstructure can be seen with decreasing amount of ferrite grains in direction to the WEL (Figure 3d).

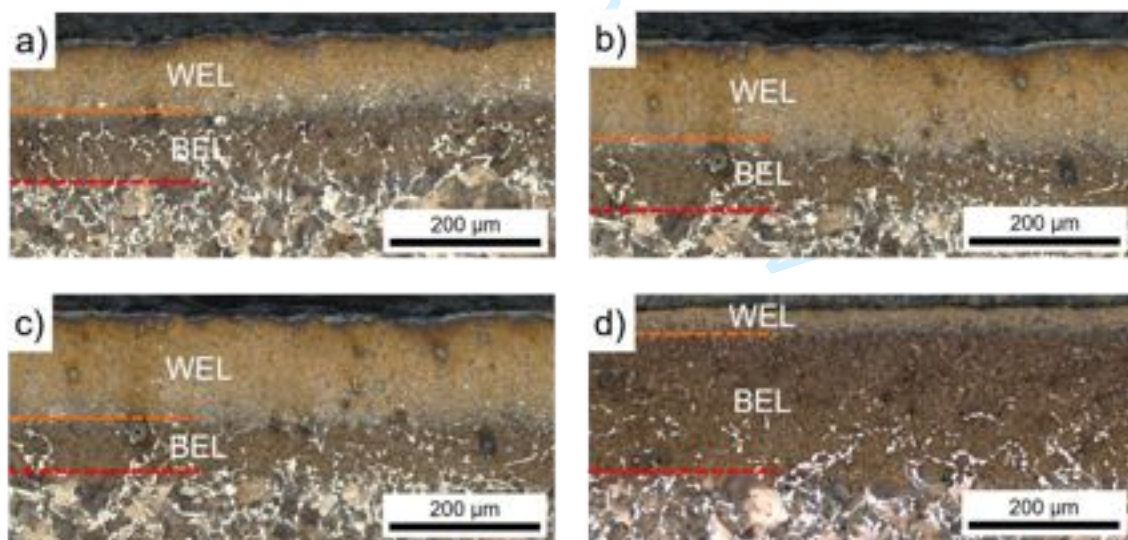


Figure 3: Influence of thermal loading parameters on SSL formation (ER7 railway wheel steel): An increase of laser power leads to increased SSL thickness: (a) $P_{\text{Laser},1} = 2.3 \text{ kW}$ and $P_{\text{Laser},2} = 1.7 \text{ kW}$, (b) $P_{\text{Laser},1} = 2.4 \text{ kW}$ and $P_{\text{Laser},2} = 1.8 \text{ kW}$. By varying the laser power difference between the first and second thermal loading (ΔP_{Laser}) the ratio of WEL and BEL is changing: (c) $\Delta P_{\text{Laser}} = 0.6 \text{ kW}$, (d) $\Delta P_{\text{Laser}} = 0.8 \text{ kW}$.

Microstructural influences on SSL formation

In the following section, influences of the initial microstructure prior laser surface treatment are shown (Figure 4 and Figure 5). Two consecutive thermal loadings with same laser parameters are applied ($P_{\text{Laser},1} = 2.3 \text{ kW}$, $P_{\text{Laser},2} = 1.7 \text{ kW}$) to two samples of ER7 with different grain size. The initial microstructure with coarser grain size (Figure 4a) shows an SSL thickness of $\sim 150 \mu\text{m}$ (WEL: $60 \mu\text{m}$, BEL: $90 \mu\text{m}$). In contrast, the SSL formed on an initially finer grained microstructure (Figure 4b) results a larger layer thickness of $\sim 180 \mu\text{m}$ (WEL: $90 \mu\text{m}$, BEL: $90 \mu\text{m}$). The BEL thickness is constant, as well as the laser power difference between the first and second thermal loading ($\Delta P_{\text{Laser}} = 0.6 \text{ kW}$). The grain size also affects the residual ferrite grains not transformed during thermal loading. The initial coarse grain sized sample show coarse ferrite grains within the BEL and WEL (Figure 4a), in contrast to smaller and more homogeneously distributed ferrite grains for the initially fine-grained microstructure (Figure 4b).

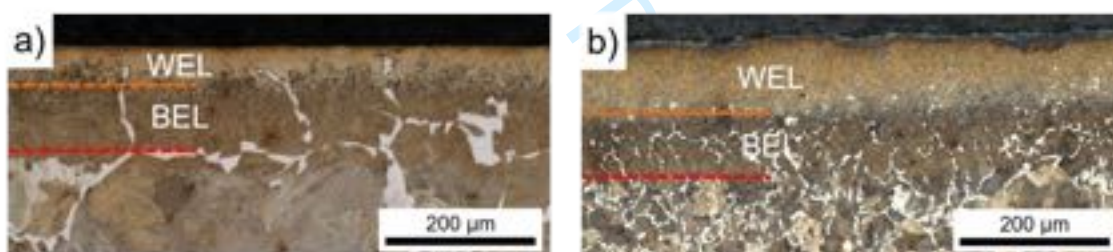


Figure 4: Influence of the initial microstructure of ER7 railway wheel steel on SSL formation: (a) Coarse grain size leads to smaller SSL compared to (b) a fine-grained initial microstructure, with same thermal loadings ($P_{\text{Laser},1} = 2.3 \text{ kW}$, $P_{\text{Laser},2} = 1.7 \text{ kW}$).

The influence of the chemical composition of the wheel steel on SSL formation is shown by two consecutive thermal treatments with laser powers of $P_{\text{Laser},1} = 2.0 \text{ kW}$ and $P_{\text{Laser},2} = 1.6 \text{ kW}$ on heat-treated samples of ER7 and ER7-MA with comparable grain sizes (Figure 5). The SSL formed on the wheel steel grade ER7 shows a SSL with a layer thickness of $91 \pm 1 \mu\text{m}$ (Figure 5a), while for the ER7-MA steel a SSL of $76 \pm 3 \mu\text{m}$ is detected (Figure 5b). A comparable ratio of WEL and BEL within the SSLs is observed

(Figure 5c). Hardness measurements within the SSL on ER7 show hardness values within the WEL of ~ 900 HV0.01 with a gradual decrease in the BEL towards the bulk hardness of ~ 370 HV0.01 (Figure 5d). The hardness measured within the SSL of the ER7-MA wheel steel reveals a decrease from ~ 700 to 500 HV0.01 within the WEL, followed by a further decrease towards the bulk hardness of ~ 360 HV0.01.

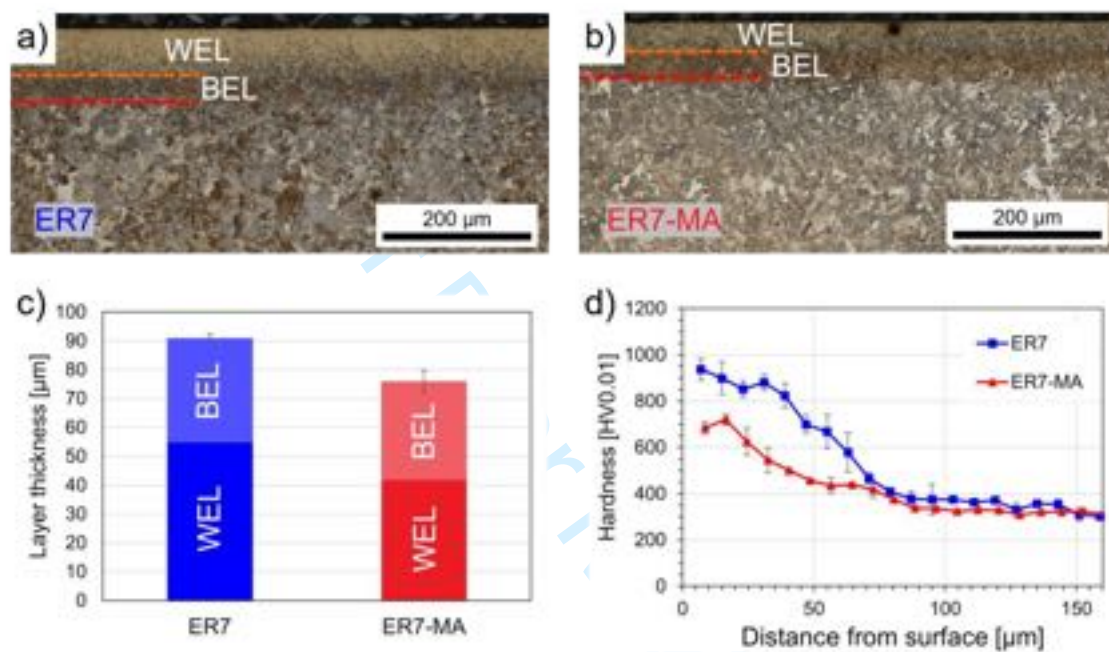


Figure 5: Influence of the chemical composition is shown by SSL formed (PLaser,1 = 2.0 kW and PLaser,2 = 1.6 kW) on (c) ER7 compared to (d) ER7-MA with decreased SSL thickness. (e) Layer thickness plot and (f) hardness measurement graphs of the different wheel steel grades.

Discussion

Based on the results of different conducted sequences of thermal loads applied by laser surface treatments ($P_{\text{Laser},1} = P_{\text{Laser},2}$, $P_{\text{Laser},1} < P_{\text{Laser},2}$, and $P_{\text{Laser},1} > P_{\text{Laser},2}$; Figure 2) a formation of SSL is only possible if the laser power of the second laser treatment is lower than the first one ($P_{\text{Laser},1} < P_{\text{Laser},2}$; Figure 2c). The formation process of SSLs is schematically shown in Figure 6. Applying a laser surface treatment with a certain laser power $P_{\text{Laser},1}$ represent a thermal load on the railway wheel surface, that causes a maximum temperature $T_{1,\text{max}}$ within the sample that changes with depth below the surface (Figure 6a). Depending on the energy and power applied to the surface a near-surface layer austenitizes, followed by WEL formation due rapid cooling (Figure 6b). For the conducted laser surface treatments the thermal loading is defined by the laser power, as well as the size, shape and moving speed of the laser spot. The layer is formed down to a depth of the samples where the austenitization temperature is reached and the cooling rate v_l equals the critical cooling rate v_{crit} for martensitic transformation [15]–[17]. To create an underlying BEL, a second thermal load is needed, represented by a second laser surface treatment with lower laser power $P_{\text{Laser},2} < P_{\text{Laser},1}$ (Figure 6c). The second thermal load recreates a WEL on the top part of the WEL resulting from the first thermal load and causes a tempering of the bottom part of the existing WEL that appears as a BEL in the metallographic sections. (Figure 6d). Based on this systematic study the formation process of comparable microstructures observed on wheels and rails from the field [1]–[4], [6], [18] can be better understood, even though the thermal loading history of samples from the field is always unclear. However, the presented study is focussing on the thermal formation process, mechanical loadings leading to a massive change of the near-surface microstructure [19]–[23] are not considered. Deformation of the near-surface wheel microstructure before / during the thermal induced transformation process is affecting the

morphology of the formed WEL and BEL, which is shown in previous work by the authors [8].

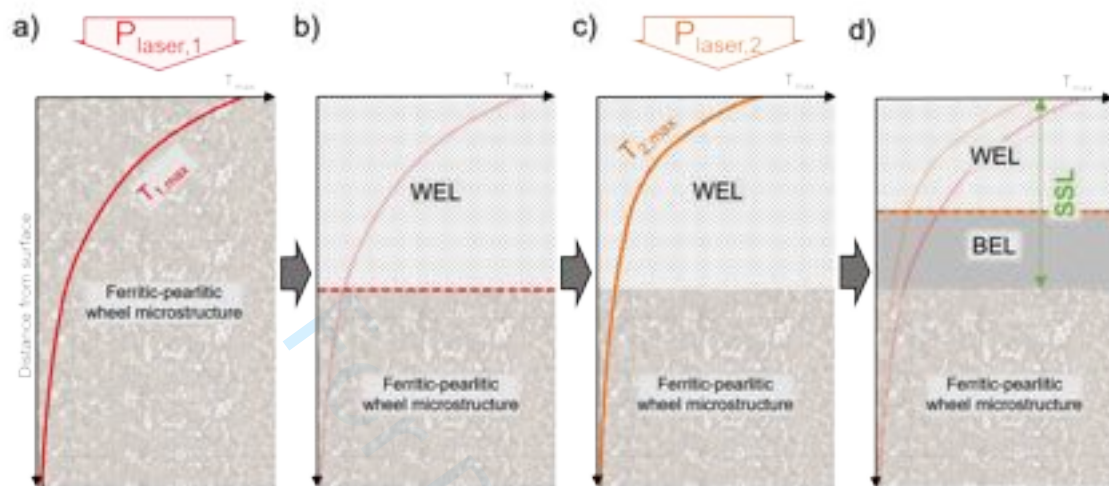


Figure 6: Formation mechanism of SSL on ferritic-pearlitic railway wheels imitated by laser surface treatment: (a) The first thermal load applied with laser power $P_{Laser,1}$ leads to (b) a martensitic WEL layer near the surface. (c) The second thermal load with lower laser power $P_{Laser,2}$ (resulting in a lower surface temperature) leads to (d) the tempering of the lower part of the existing WEL, resulting in a BEL. The combination of WEL and BEL is called SSL.

The presented influence of the thermal loading parameters clearly shows increased SSL thickness with higher laser power and temperature at the surface, respectively (Figure 3a and b). This is based on higher temperature reached in increased distance from the surface. Hence, the loading parameters of slip events occurring for railway wheels or the degree of thermal influence when grinding rails are significantly affecting the thickness of a possible induced WEL [18], [24]–[29].

With respect to the underlying BEL of the SSL formed, the energy / temperature difference of the first and second thermal treatment is crucial (Figure 3c and d). Based on the literature, thermal induced WELs are formed at temperatures in the range of the austenitization temperature of the wheel or rail steel [4], [28]. In this study, thermal

1
2
3 camera measurements revealed maximum surface temperatures for the formation of WEL
4 of 850 – 950 °C (first laser treatment), and 700 – 850 °C for the formation of BEL (second
5 laser treatment). The latter is in the tempering regime of the WEL, leading to the
6 formation of BEL in between the WEL and the ferritic-pearlitic bulk microstructure
7 (Figure 3, Figure 4 and Figure 5). This formation mechanism of BEL is in accordance to
8 recently published work of Kumar et al. [4].
9

10
11
12
13
14
15
16
17 The studied influence of the initial grain size on the formation of SSL reveals a trend
18 towards increasing layer thickness for initial microstructures with fine grain size, which
19 is in accordance to previous work from the authors [8]. This is based on an increased
20 transformation rate due to higher nuclei density of fine grained microstructures [30]. A
21 comparable effect is suggested for plastic deformation on the wheel treads in service,
22 which leads to grain refinement of the near-surface microstructure [19], [31]–[34].
23
24
25
26
27
28
29
30

31
32
33
34
35
36
37
38
39
40
41
42
43
44
45
46
47
48
49
50
51
52
The chemical composition of the steel is expected to affect phase transformations [35]–
[37] as it occurs when thermally inducing an SSL. Within this study the sample with the
chemical composition of standard wheel steel grade ER7 shows an increased SSL
thickness compared to the sample with the chemical composition of wheel steel ER7-
MA. Both samples have been subjected to the same laboratory heat treatment prior laser
surface treatment. (Figure 5a – d). It must be mentioned, that due to the conducted heat
treatment within this work the results are not directly transferable to ER7 and ER7-MA
railway wheels used in service, since they are processed by individual heat treatment
procedures by the manufacturers. The decreased thickness of the SSLs at laser powers of
2.3 kW and 1.7 kW are in consequence of a different sample surface preparation after the
conducted heat treatment of these samples. However, thermal camera measurements
prove an induced maximum surface temperature of ~900 °C for the first thermal load and
~750 °C for the second thermal load. In addition to the smaller SSL thickness (Figure 5c)

1
2
3 a lower hardness is measured in the SSL for the ER7-MA (Figure 5d). However, further
4 studies are necessary to evaluate the relation of distinctive alloying elements to the
5 characteristics of the formed SSLs.
6
7
8
9
10
11
12
13

14 Conclusions

15 The presented study uses a laboratory approach by laser surface treatment to imitate
16 reproducible SSLs on rail wheel materials with a defined thermal loading history, which
17 enables a systematic study on influencing parameters. By executing different thermal load
18 sequences, it is shown that SSLs are formed by two consecutive thermal loadings if the
19 second laser treatment is executed with lower laser powers than the first treatment ($P_{\text{Laser},1}$
20 $> P_{\text{Laser},2}$). The first thermal loading results in a WEL, while the second thermal loading
21 leads to a tempering of the lower part of the WEL, hence, forming a BEL.
22
23
24
25
26
27
28
29
30

31 Further variations of thermal loading parameters and initial microstructures reveal:

- 32 ▪ An increase in the laser power P_{Laser} leads to an increase in SSL thickness.
- 33 ▪ The difference of the first and the second thermal treatment ΔP_{Laser} defines the ratio of
34 the WEL and the BEL within the SSL, with a more pronounced BEL with increasing
35 ΔP_{Laser} .
- 36 ▪ A finer grain size of the initial wheel microstructure results in an increased SSL
37 thickness.
- 38 ▪ Comparing laboratory heat treated ER-7 railway wheel steel samples to ER7-MA steel
39 samples with lower carbon content and micro-alloyed with Vanadium and Niobium,
40 the SSL formed on the ER7-MA show a smaller SSL thickness and lower hardness.
41
42
43
44
45
46
47
48
49
50
51
52

References

- [1] M. Messaadi and M. Steenbergen, "Stratified surface layers on rails," *Wear*, vol. 414–415, pp. 151–162, Nov. 2018, doi: 10.1016/j.wear.2018.07.019.
- [2] M. Freisinger and A. Trausmuth, "Microstructural characterization of near-surface microstructures on rail wheels in service – an insight into 'stratified surface layers,'" *Open Res Europe*, vol. 3, p. 73, May 2023, doi: 10.12688/openreseurope.15881.2.
- [3] G. Gao *et al.*, "Heterogenous structure and formation mechanism of white and brown etching layers in bainitic rail steel," *Acta Materialia*, vol. 250, p. 118887, May 2023, doi: 10.1016/j.actamat.2023.118887.
- [4] A. Kumar, G. Agarwal, R. Petrov, S. Goto, J. Sietsma, and M. Herbig, "Microstructural evolution of white and brown etching layers in pearlitic rail steels," *Acta Materialia*, vol. 171, pp. 48–64, Jun. 2019, doi: 10.1016/j.actamat.2019.04.012.
- [5] P.-Y. Tung, X. Zhou, L. Morsdorf, and M. Herbig, "Formation mechanism of brown etching layers in pearlitic rail steel," *Materialia*, vol. 26, p. 101625, Dec. 2022, doi: 10.1016/j.mtla.2022.101625.
- [6] S. Li, J. Wu, R. H. Petrov, Z. Li, R. Dollevoet, and J. Sietsma, "'Brown etching layer': A possible new insight into the crack initiation of rolling contact fatigue in rail steels?," *Engineering Failure Analysis*, vol. 66, pp. 8–18, Aug. 2016, doi: 10.1016/j.engfailanal.2016.03.019.
- [7] Y. Chen, X. Zhao, P. Liu, R. Pan, and R. Ren, "Influences of local laser quenching on wear performance of D1 wheel steel," *Wear*, vol. 414–415, pp. 243–250, Nov. 2018, doi: 10.1016/j.wear.2018.07.016.
- [8] M. Freisinger *et al.*, "Comparative study on the influence of initial deformation and temperature of thermally induced white etching layers on rail wheels," *Tribology International*, vol. 177, p. 107990, Jan. 2023, doi: 10.1016/j.triboint.2022.107990.
- [9] H. H. Ding *et al.*, "Investigation on the rolling wear and damage properties of laser discrete quenched rail material with different quenching shapes and patterns," *Surface and Coatings Technology*, vol. 378, p. 124991, Nov. 2019, doi: 10.1016/j.surfcoat.2019.124991.
- [10] D. J. Minicucci, S. T. Fonseca, R. L. V. Boas, H. Goldenstein, and P. R. Mei, "Development of Niobium Microalloyed Steel for Railway Wheel with Pearlitic Bainitic Microstructure," *Mat. Res.*, vol. 22, no. 6, p. e20190324, 2019, doi: 10.1590/1980-5373-mr-2019-0324.
- [11] A. B. Rezende *et al.*, "Wear behavior of bainitic and pearlitic microstructures from microalloyed railway wheel steel," *Wear*, vol. 456–457, p. 203377, Sep. 2020, doi: 10.1016/j.wear.2020.203377.
- [12] S. M. Shariff, T. K. Pal, G. Padmanabham, and S. V. Joshi, "Influence of chemical composition and prior microstructure on diode laser hardening of railroad steels," *Surface and Coatings Technology*, vol. 228, pp. 14–26, Aug. 2013, doi: 10.1016/j.surfcoat.2013.03.046.
- [13] U. P. Singh, A. M. Popli, D. K. Jain, B. Roy, and S. Jha, "Influence of Microalloying on Mechanical and Metallurgical Properties of Wear Resistant Coach and Wagon Wheel Steel," *Journal of Materials Engineering and Performance*, vol. 12, no. 5, pp. 573–580, Oct. 2003, doi: 10.1361/105994903100277085.
- [14] C. Qiu, J. Cookson, and P. Mutton, "The role of microstructure and its stability in performance of wheels in heavy haul service," *J. Mod. Transport.*, vol. 25, no. 4, pp. 261–267, Dec. 2017, doi: 10.1007/s40534-017-0143-9.
- [15] A. R. Entwisle, "The kinetics of martensite formation in steel," *Metall Trans*, vol. 2, no. 9, pp. 2395–2407, Sep. 1971, doi: 10.1007/BF02814877.
- [16] J. H. Liu, N. Binot, D. Delagnes, and M. Jahazi, "Influence of the cooling rate below Ms on the martensitic transformation in a low alloy medium-carbon steel," *Journal of Materials Research and Technology*, vol. 12, pp. 234–242, May 2021, doi: 10.1016/j.jmrt.2021.02.075.
- [17] A. Stormvinter, A. Borgenstam, and J. Ågren, "Thermodynamically Based Prediction of the Martensite Start Temperature for Commercial Steels," *Metall Mater Trans A*, vol. 43, no. 10, pp. 3870–3879, Oct. 2012, doi: 10.1007/s11661-012-1171-z.
- [18] Y. Z. Chen, C. G. He, X. J. Zhao, L. B. Shi, Q. Y. Liu, and W. J. Wang, "The influence of wheel flats formed from different braking conditions on rolling contact fatigue of railway wheel," *Engineering Failure Analysis*, vol. 93, pp. 183–199, Nov. 2018, doi: 10.1016/j.engfailanal.2018.07.006.
- [19] M. Freisinger, H. Rojacz, A. Trausmuth, and P. H. Mayrhofer, "Severe Plastic Deformed Zones and White Etching Layers Formed During Service of Railway Wheels," *Metallogr. Microstruct. Anal.*, vol. 12, no. 3, pp. 515–527, Jun. 2023, doi: 10.1007/s13632-023-00967-x.
- [20] J. Ahlström and B. Karlsson, "Microstructural evaluation and interpretation of the mechanically and thermally affected zone under railway wheel flats," *Wear*, vol. 232, no. 1, pp. 1–14, Sep. 1999, doi: 10.1016/S0043-1648(99)00166-0.

- 1
2
3 [21] D. Nikas, J. Ahlström, and A. Malakizadi, "Mechanical properties and fatigue behaviour of railway
4 wheel steels as influenced by mechanical and thermal loadings," *Wear*, vol. 366–367, pp. 407–415,
5 Nov. 2016, doi: 10.1016/j.wear.2016.04.009.
- 6 [22] Y. Hu *et al.*, "Microstructure evolution of railway pearlitic wheel steels under rolling-sliding
7 contact loading," *Tribology International*, vol. 154, p. 106685, Feb. 2021, doi:
8 10.1016/j.triboint.2020.106685.
- 9 [23] T. Vernersson, S. Caprioli, E. Kabo, H. Hansson, and A. Ekberg, "Wheel Tread Damage: A
10 Numerical Study of Railway Wheel Tread Plasticity under Thermomechanical Loading,"
11 *Proceedings of the Institution of Mechanical Engineers, Part F: Journal of Rail and Rapid Transit*,
12 vol. 224, no. 5, pp. 435–443, Sep. 2010, doi: 10.1243/09544097JRRT358.
- 13 [24] A. Al-Juboori *et al.*, "Characterisation of White Etching Layers formed on rails subjected to
14 different traffic conditions," *Wear*, vol. 436–437, p. 202998, Oct. 2019, doi:
15 10.1016/j.wear.2019.202998.
- 16 [25] A. D. Bedoya-Zapata *et al.*, "White Etching Layer (WEL) formation in different rail grades after
17 grinding operations in the field," *Wear*, vol. 502–503, p. 204371, Aug. 2022, doi:
18 10.1016/j.wear.2022.204371.
- 19 [26] C. J. Rasmussen, S. Fæster, S. Dhar, J. V. Quaade, M. Bini, and H. K. Danielsen, "Surface crack
20 formation on rails at grinding induced martensite white etching layers," *Wear*, vol. 384–385, pp. 8–
21 14, Aug. 2017, doi: 10.1016/j.wear.2017.04.014.
- 22 [27] E. Uhlmann, P. Lypovka, L. Hochschild, and N. Schröer, "Influence of rail grinding process
23 parameters on rail surface roughness and surface layer hardness," *Wear*, vol. 366–367, pp. 287–
24 293, Nov. 2016, doi: 10.1016/j.wear.2016.03.023.
- 25 [28] C. Bernsteiner, G. Müller, A. Meierhofer, K. Six, D. Künstner, and P. Dietmaier, "Development of
26 white etching layers on rails: simulations and experiments," *Wear*, vol. 366–367, pp. 116–122,
27 2016, doi: 10.1016/j.wear.2016.03.028.
- 28 [29] K. Zhou, H. Ding, M. Steenbergen, W. Wang, J. Guo, and Q. Liu, "Temperature field and material
29 response as a function of rail grinding parameters," *International Journal of Heat and Mass
30 Transfer*, vol. 175, p. 121366, Aug. 2021, doi: 10.1016/j.ijheatmasstransfer.2021.121366.
- 31 [30] C. Celada-Casero, J. Sietsma, and M. J. Santofimia, "The role of the austenite grain size in the
32 martensitic transformation in low carbon steels," *Materials & Design*, vol. 167, p. 107625, Apr.
33 2019, doi: 10.1016/j.matdes.2019.107625.
- 34 [31] H. C. Eden, J. E. Garnham, and C. L. Davis, "Influential microstructural changes on rolling contact
35 fatigue crack initiation in pearlitic rail steels," *Materials Science and Technology*, vol. 21, no. 6,
36 pp. 623–629, Jun. 2005, doi: 10.1179/174328405X43207.
- 37 [32] J. Ahlstrom and B. Karlsson, "Microstructural evaluation and interpretation of the mechanically
38 and thermally affected zone under railway wheel flats," *Wear*, p. 14, 1999.
- 39 [33] A. Ekberg and E. Kabo, "Fatigue of railway wheels and rails under rolling contact and thermal
40 loading—an overview," *Wear*, vol. 258, no. 7–8, pp. 1288–1300, Mar. 2005, doi:
41 10.1016/j.wear.2004.03.039.
- 42 [34] G. Y. Zhou, J. H. Liu, W. J. Wang, G. Wen, and Q. Y. Liu, "Study on the fatigue and wear
43 characteristics of four wheel materials," *J. Mod. Transport.*, vol. 21, no. 3, pp. 182–193, Sep. 2013,
44 doi: 10.1007/s40534-013-0021-z.
- 45 [35] J.-B. Seol, J. E. Jung, Y. W. Jang, and C. G. Park, "Influence of carbon content on the
46 microstructure, martensitic transformation and mechanical properties in austenite/ ϵ -martensite
47 dual-phase Fe–Mn–C steels," *Acta Materialia*, vol. 61, no. 2, pp. 558–578, Jan. 2013, doi:
48 10.1016/j.actamat.2012.09.078.
- 49 [36] C. Capdevila, F. G. Caballero, and C. García De Andrés, "Analysis of effect of alloying elements
50 on martensite start temperature of steels," *Materials Science and Technology*, vol. 19, no. 5, pp.
51 581–586, May 2003, doi: 10.1179/026708303225001902.
- 52 [37] Y. Li, D. S. Martín, J. Wang, C. Wang, and W. Xu, "A review of the thermal stability of metastable
austenite in steels: Martensite formation," *Journal of Materials Science & Technology*, vol. 91, pp.
200–214, Nov. 2021, doi: 10.1016/j.jmst.2021.03.020.

Publication VIII



Fatigue crack initiation in the presence of stratified surface layers on rail wheels

M. Freisinger, B. Jakab, K. Pichelbauer, G. Trummer, K. Six, P.H. Mayrhofer
International Journal of Fatigue, accepted (19.09.2023)

Fatigue crack initiation in the presence of stratified surface layers on rail wheels

M. Freisinger ^{a,c}, B. Jakab^a, K. Pichelbauer^a, G. Trummer^b, K. Six^b, P.H. Mayrhofer^c

^aAC2T research GmbH, A-2700 Wiener Neustadt, Austria

^bVirtual Vehicle Research Center, A-8010 Graz, Austria

^cInstitute of Materials Science and Technology, TU Wien, A-1060 Wien, Austria

Abstract

This work presents a study on the fatigue crack initiation in the presence of stratified surface layers (SSL) – a combination of white and brown etching layer – on rail wheels. Reproducible SSLs comparable to field samples are created by a defined mechanical load and two consecutive laser surface treatments on discs made from two wheel materials (ER7, ER9). Fatigue testing is done by a twin disc tribometer, where the wheel discs with SSLs are driven against discs made from R260 rail material. The results show significant fatigue crack initiation and propagation in the presence of the SSLs, exclusively on the leading edge of the SSL, more pronounced for the wheel grade ER9. Based on topographical, light optical and scanning electron microscopy analysis an explanatory model is presented, describing fatigue crack morphologies and outpointing the relevance of SSLs on rail wheels to fatigue crack initiation.

1. Introduction

In order to meet the worldwide climate targets, public transportation gains in significance in recent years, especially rail traffic. Higher train frequency increases load on rail and wheel materials. Thus, for further guaranteed safety and reliability in railway transportations, understanding the most dominating damaging mechanisms of rail and wheel materials is crucial. Additionally, maintenance costs can be

reduced by clarifying the interaction of certain mechanical and thermal loads, materials, and their failure mechanisms. Therefore, the number of published investigations of rail and wheel defects increased and also a more sophisticated terminology developed [1]–[6]. Regarding rails, two types of apparently similar looking defects are discussed in recent literature, namely the squat defect and the stud defect [1], [7]–[9]. Squat defects – a result of rolling contact fatigue (RCF) –

originate from plastic deformation [10], while stud defects are stated to originate from brittle white etching layers (WEL) [11]. The latter is named after its white appearance during light optical microscopy (LOM) when etching with an ethanol nitric acid. This layer forms either mechanically by severe plastic deformation (SPD) or thermally by increased temperature and rapid cooling [12]–[15]. In rolling-sliding contacts, the WEL frequently contains a martensitic microstructure with hardness values of 700 – 1000 HV and fracture toughness values of approximately 15 MPa m^{1/2}, which lead to a brittle behavior [13], [16]–[18]. In terms of RCF damage related to WELs, studies have been predominantly presented on rails from service [19]–[22]. We envision that squat and stud related defects also play important roles for wheels. Especially the RCF clusters in the center of wheel treads show similarities to squat and stud defects [23]. The WELs formed on wheel surfaces – due to extensive slipping and braking [3], [24]–[26] – have their impact on the formation of RCF clusters. For rails, Farjoo et al. [19] suggest the relation of WEL to squat formation and give results of finite element modeling to point out that a short crack in the WEL increases the bending stress and peak effective stress intensity factors. This consequently leads to a higher crack growth rate. Seo et al. [22] investigated the fatigue life of rail samples

with WELs simulated by wheel flats. The authors show that the highest risk of RCF occurs at the leading edge of the WEL. Lian et al. [20] applied a finite element modeling with elastic plastic as well as linear elastic fracture mechanics theory and present similar results. Under the same loading conditions, the cracks initiating at the leading edge of the WEL show the most likely growing tendency. However, various influences such as material properties, sample geometry or axle loads are mentioned. By now, no studies on wheel materials are known by the authors, moreover, most studies are limited due to the uncertain loading history of the samples from the field.

In addition to the WEL, increasing attention is paid to another important, modified surface-near region – the so-called brown etching layer (BEL) [27]–[30]. Earlier studies by Ahlström et al. [31] mentioned this as tempered martensite. Later, Li et al. [27] named the frequently formed sublayers of WELs due to their brownish appearance during metallographic studies as BEL, which is significantly softer than the WEL. They also proposed that BELs are formed by repeated martensite-austenite-martensite transformations, leading to tempered martensite (in agreement with Ahlström et al. [31]). A clear formation mechanism could not be given, as the loading profiles of field samples are unknown. But they additionally

stated that the BEL reveals an increased risk to RCF, because cracks propagate deeper into the material than observed for WELs. Messaadi and Steenbergen [30] named the combination of WEL and underlying BEL as stratified surface layer (SSL) and concluded that the BEL – being a globular bainitic microstructure and formed by a thermomechanical loading cycle – contributes to the development of RCF. The wheel–rail contact situation during operation leads to temperatures and loading profiles sufficient for austenitization of their near-surface regions. The different cooling rates in different surface-regions causes the formation of various microstructures.

Kumar et al. [28] extended the formation mechanisms for BELs based on investigating a curved rail track (with unknown loading history, as typical for field samples) and came to the conclusions that the multiple cycles of severe plastic deformation and loading combined with the increased temperature (upon loading) cause a modification of the pearlitic microstructure in near-surface regions where the temperature was too low for austenitization. The cementite laths of pearlite are fragmented and partially dissolved, as a finer microstructure allows for a higher C content in the alpha regions [32]. Regions experiencing a temperature sufficient for austenitization contain a high

fraction of martensite, which under certain wheel–rail contact conditions or for certain temperature-profiles (due to specific regions in the wheel or rail) are tempered to precipitate secondary carbides, forming the BEL. The gaining interest on BELs underneath WELs and extensive studies on their microstructural characteristics suggest a possible influence on RCF damage. Besides analysis of samples from the field, systematic studies are needed to clarify the effect of underlying BELs to RCF crack initiation and growth of rail and wheel materials.

Hence, this paper presents a novel experimental procedure to investigate fatigue crack initiation in the presence of SSLs (WELs + BELs) in wheel materials. A laboratory approach to create SSLs with defined loading history (mechanical and thermal loadings) is introduced to eliminate the uncertainty due to unknown loading histories of samples from field. Mechanical loads are applied by using a twin disc tribometer, followed by defined thermal loads via laser surface treatments. This approach shows good comparability to field samples and paving the way to study fatigue crack initiation of SSLs under defined and reproducible conditions. Based on tribometer tests with following topographical and microscopical analysis an explanatory model for the fatigue crack initiation in the presence of SSL on rail

wheels is presented. This improves the understanding of RCF failures caused by SSL, leading to unplanned maintenance and therefore decreased capacity and delays of rail transportation systems.

2. Materials and Methods

Two wheel materials with different carbon content (grades ER7 and ER9), and one rail material (grade R260) – Table 1 summarizes chemical and mechanical details of these commonly used materials on European rail networks – are used as base material for further treatments and investigations. From the heads and the crown of the rail and wheel, provided by the Austrian Federal Railways (ÖBB), specimens (original 60x60x15 mm³) were cut out. The end faces of the discs are

parallel to the running track of the wheel or rail. Still in their cut-out cuboid shape, the samples were heat treated (homogeneous austenitization in a chamber furnace for 30 min at 900 °C followed by quenching in oil and tempering for 60 min at 510 °C followed by cooling in ambient air) to achieve a microstructure comparable to the original near-surface microstructure of an as-manufactured wheel and rail. For the wheel materials, a pearlitic microstructure with pro-eutectoid ferrite is achieved with a bulk hardness of ~300 HV (ER7) and ~330 HV (ER9). The rail discs show a pearlitic microstructure and a hardness of ~260 HV. After heat treatment, the specimens were machined to their final disc dimensions (Figure 1).

Table 1: Chemical composition and mechanical properties of the steel grades ER7, ER9 and R260 according to the standard EN13262 [33] and [34], fracture toughness K_Q value obtained by compact tension specimens [35].

	C	Si	Mn	P	S	Cr	Cu	Mo	Ni	V	Cr + Mo + Ni
	[wt%]										
ER7	0.52	0.40	0.80	0.020	0.015	0.30	0.30	0.08	0.30	0.06	0.50
ER9	0.60	0.40	0.80	0.020	0.015	0.30	0.30	0.08	0.30	0.06	0.50
R260	0.74	0.31	1.08	0.013	0.018	0.040	-	-	-	-	-
	R_{eH}		R_m		A_5		Minimum Hardness			K_Q	
	[N/mm ²]		[N/mm ²]		[%]		[HB]			[MPa m ^{1/2}]	
ER7	≥ 520		820-940		≥ 14		235			40-80	
ER9	≥ 580		900-1050		≥ 12		255			-	
R260	528		923		11.4		260			-	

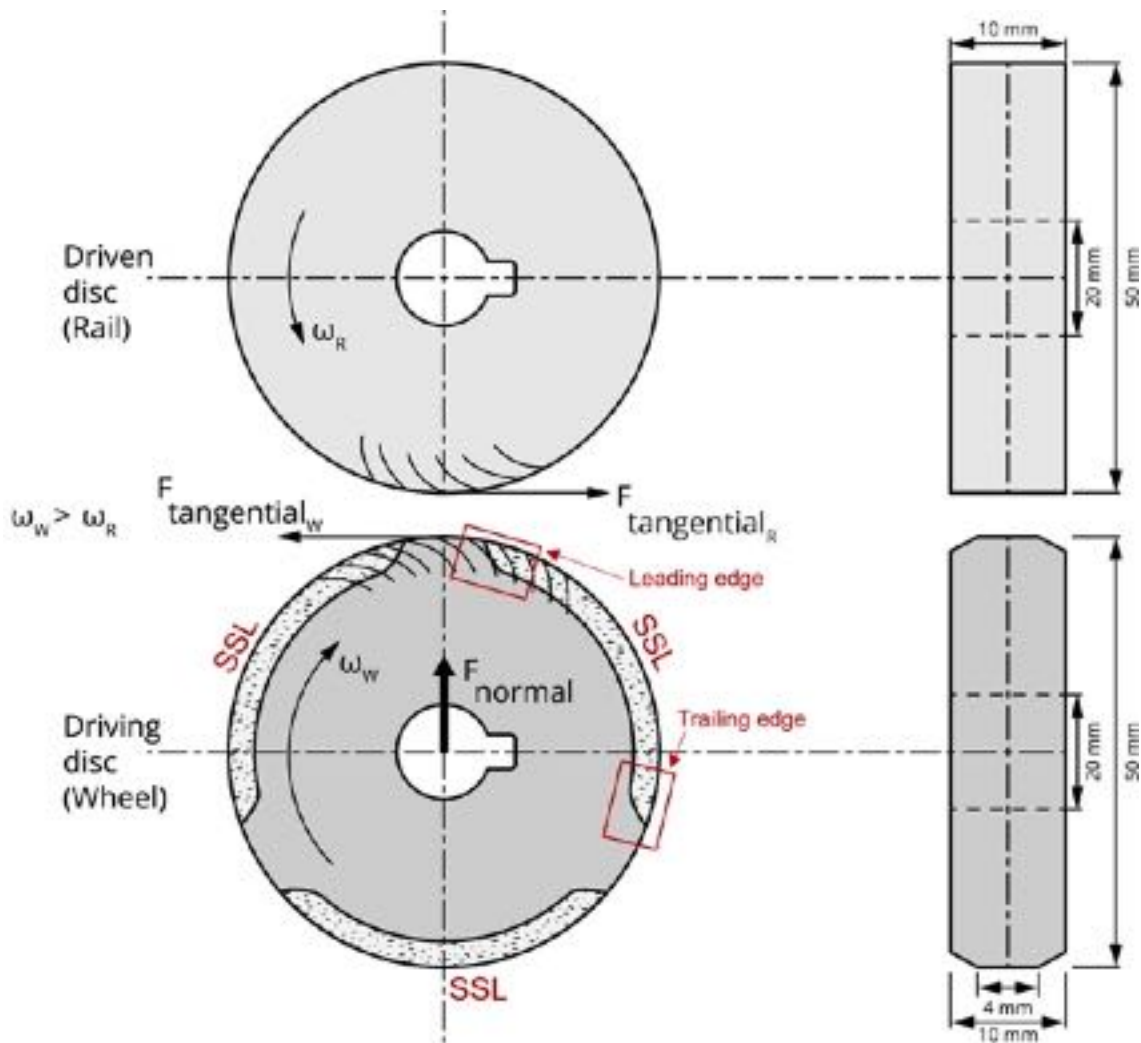


Figure 1: The configuration of the twin disc tribometer used for the initial mechanical loading before the thermal loadings, and for the fatigue testing of the created SSLs. The driving disc (wheel material, grade ER7/ER9) is pressed with a normal load F_{normal} towards the driven disc (rail material, grade R260). The wheel samples for the fatigue testing feature three SSL sections, whereby the leading edge of the SSL is named side A and the trailing edge side B.

In a previous study [14], we showed that for a representative lab-produced WEL (via laser treatments) on wheel materials a pre-deformed state is crucial. Otherwise, the lab-produced WEL significantly deviates in its microcharacteristics from the field-generated WEL on rails or wheels. While in the previous study we used a pre-deformed material from field (naturally without a deep knowledge of the loading history),

here we introduce a combination of a twin disc tribometer and a diode laser system to allow for a well-defined mechanical and thermal loading profile. After the mechanical loading (mechanical load M1) under controlled conditions (Figure 1) followed the laser treatment (thermal load T1 and T2) via a Direct Diode Laser System (HighLight 8000D, Coherent, U.S.). This novel laboratory approach is schematically

shown in Figure 2. Within the customized twin disc tribometer, two discs (diameter: 50 ± 2 mm, thickness: 10 mm) roll against each other while being pressed together with a defined normal load of 800 N (Hertzian pressure of 766 MPa). The driving disc is made of the wheel material, and the driven disc is made of the rail material. Both speeds (ω_W for wheel and ω_R for rail) can be controlled individually and continuously, allowing to control the resulting slip, s , according to:

$$s = \frac{2 * (\omega_W - \omega_R)}{\omega_W + \omega_R} \quad (1)$$

The tests were conducted at room temperature, without intermediate medium (dry), with $\omega_W = 500$ rpm and a slip of $s = +1\%$, for 100,000 cycles.

The following laser treatments are conducted with a rectangular laser spot (3

mm in moving direction and 36 mm perpendicular to it), a nominal continuous power output of 8 kW at a wavelength of 975 nm. The laser system (mounted on a 6-axis robot arm (IRB 4600-60/2.05, ABB, Austria) and controlled via the teach-pendant of the controller system of the IRC5 (ABB, Austria)) can precisely be positioning and moved. The starting temperature of the surface for each laser-treated track was room temperature, and along the circumference of the discs three sections were treated by moving the laser spot with a constant speed of 12 mm/s, Figure 1 and Figure 2. Pre-studies showed that for a field-near development of the SSL a double-laser treatment is needed, with an initial laser power (T1) of 4.0 kW followed by 3.2 kW (T2). Between the laser treatments a cooling to room temperature of the samples was guaranteed.

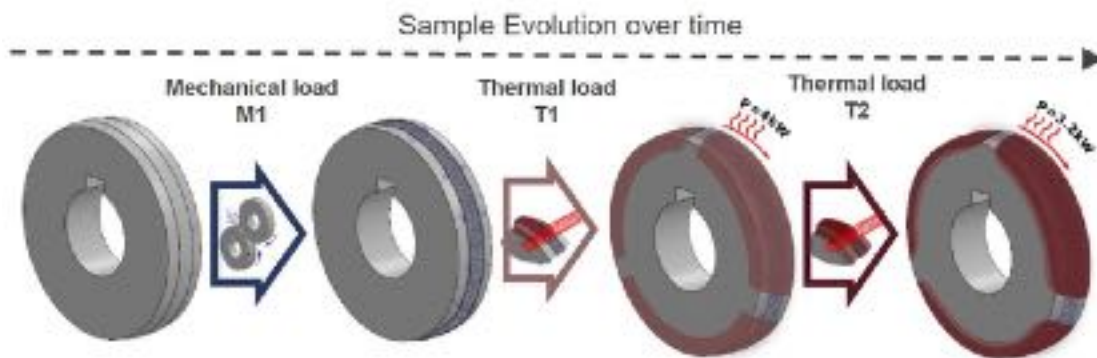


Figure 2: Approach to imitate reproducible SSLs with defined loading history: In the first step, the material is mechanically deformed by a twin disc tribometer run (M1), followed by two thermal loads with different laser energy powers in three distinctive regions of the sample (T1: $P = 4.0$ kW, T2: $P = 3.2$ kW).

To introduce RCF cracks, the prepared wheel disc samples (ER7, ER9) with three SSL sections along the tread surface were run against rail material discs (R260). Same loading parameters are applied as used initially ($F_N = 800$ N, 500 rpm, $s = +1\%$, 100,000 cycles).

The tested samples were characterized with a focus-variation microscope (Alicona InfiniteFocus G5, Alicona Imaging GmbH, Austria) for their surface topography. After metallographic sample preparation of cross-sections to a mirror-polished surface quality (1 μm diamond fine polishing), their

surfaces were etched with diluted nitric acid (3% HNO_3 , 97% ethanol) and analyzed via light optical microscopy (LOM, Axio Imager M2m, Carl Zeiss AG, Germany) and field emission gun scanning electron microscopy (SEM, Jeol JIB 4700F, Jeol Ltd., Japan) operated at 15 kV acceleration voltage using secondary electron (SE) and backscattered electron (BE) mode. Certain regions of the samples were characterized for their low load Vickers hardness using a Future-Tech FM-700 hardness tester (Future Tech Corp., Japan) with a load of 0.01 kp (0.098 N).

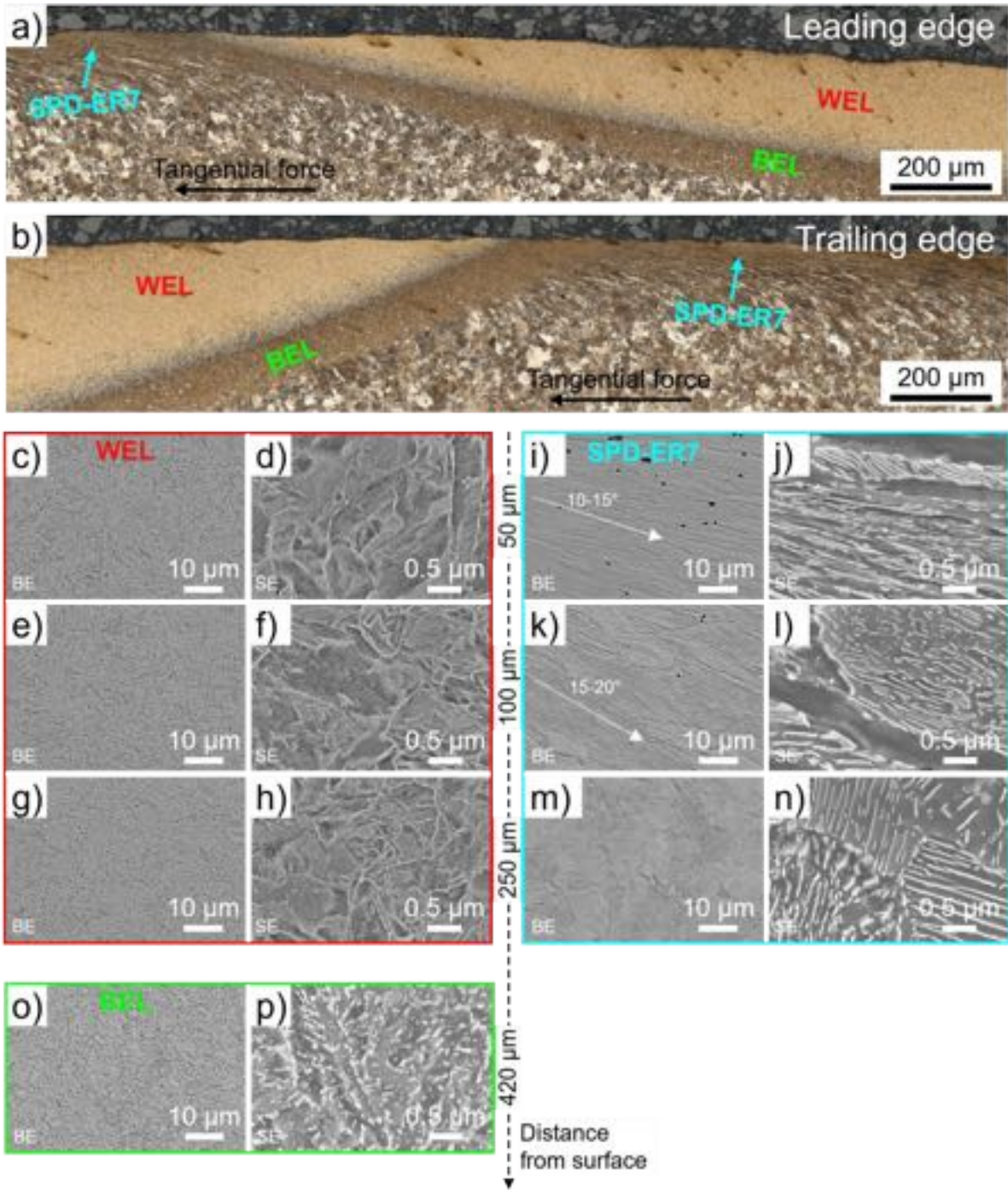


Figure 3: (a), (b): LOM images of the transition regions showing the initial ER7 microstructure deformed by mechanical loading (M1) (SPD-ER7) and the thermally induced SSL consisting of the WEL and BEL. Detailed BE and SE images in various depths from surface are presented for the WEL ((c)–(h)), the SPD-ER7 ((i)–(n)) and the BEL ((o),(p)).

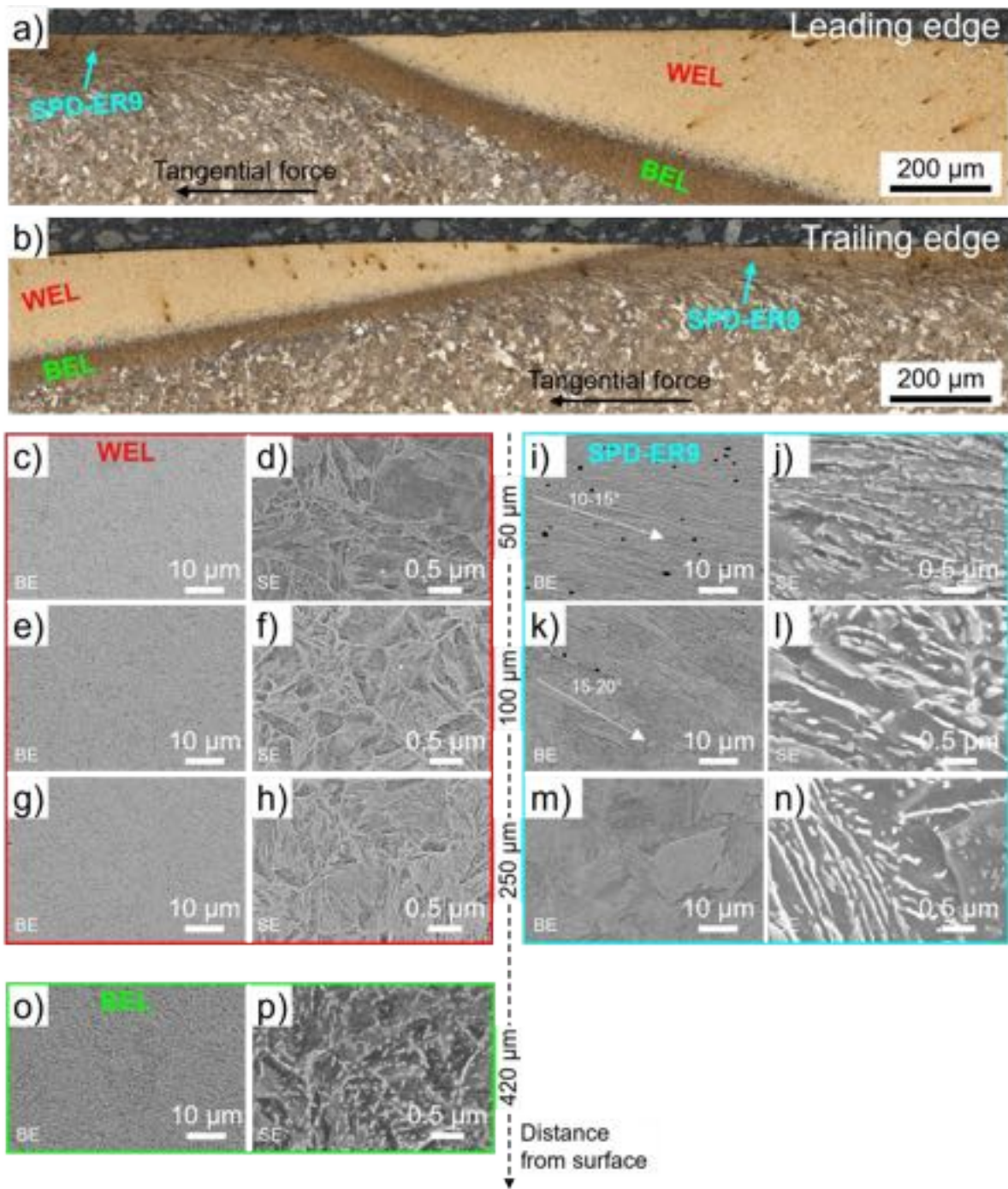


Figure 4: (a), (b): LOM images of the transition regions showing the initial ER9 microstructure deformed by mechanical loading (M1) (SPD-ER9) and the thermally induced SSL consisting of the WEL and BEL. Detailed BE and SE images in various depths from surface are presented for the WEL ((c)–(h)), the SPD-ER9 ((i)–(n)) and the BEL ((o),(p)).

4. Results

4.1. Formation of SSL with defined mechanical and thermal loads

Combining a twin disc tribometer with a diode laser system allows the imitation of a SSL with distinctive regions of WEL and BEL, see [Figure 3](#) and [Figure 4](#), respectively. The initial mechanical load (M1) by the twin disc tribometer leads to an SPD near-surface microstructure (SPD-ER7) within a distance of $\sim 200 \mu\text{m}$ from surface, see the cross-sectional cuts of a representative SSL on ER7 wheel material given in [Figure 3a](#) and [b](#). The following laser treatments cause thermal loads (T1, T2) leading to the formation of an SSL with an average thickness of $\sim 500 \mu\text{m}$. The transition zones along the surface (SPD-ER7 – BEL – WEL) shows no severe cracking due to residual stresses within the treated regions.

Within the SSL, a WEL and BEL region can be identified, where the WEL comes up with an average thickness of $\sim 350 \mu\text{m}$. The martensitic microstructure in various depths from surface can be seen through BE and SE images, [Figure 3c](#) and [d](#) ($50 \mu\text{m}$), [Figure 3e](#) and [f](#) ($100 \mu\text{m}$), and [Figure 3g](#) and [h](#) ($250 \mu\text{m}$), respectively. Even though the initial degree of deformation of the ER7 wheel material before the thermal loads ([Figure 3i–n](#)) is different, no significant difference

in the martensitic microstructure can be identified. The BE image of the SPD-ER7 microstructure in a depth of $50 \mu\text{m}$ from surface ([Figure 3i](#)) shows an SPD microstructure with an alignment of $10\text{--}15^\circ$ to the surface. The higher magnification SE image ([Figure 3j](#)) indicates deformation, fracture, and alignment of the cementite lamellae. In a depth of $100 \mu\text{m}$ from the surface ([Figure 3k](#) and [l](#)) the degree of deformation is decreasing, and the alignment angle is increasing ($15\text{--}20^\circ$). An undeformed ferritic-pearlitic microstructure can be identified in a depth of $250 \mu\text{m}$ from the surface ([Figure 3m](#) and [n](#)). The BEL region of the SSL can be clearly seen due to its brownish appearing microstructure in the LOM images ([Figure 3a](#) and [b](#)) and reveals a thickness of $\sim 150 \mu\text{m}$. Analysis of the microstructure in the middle of the BEL region ($420 \mu\text{m}$ from surface) indicates a trend for an increased grain size ([Figure 3o](#)) in comparison with the WEL microstructure, and the SE image ([Figure 3p](#)) shows a proceeded cementite spheroidization ([Figure 3o](#)).

Images of the cross-sectional cuts after the initial mechanical loading (M1) and followed thermal loads (T1, T2) for the wheel grade ER9 are given in [Figure 4](#). Comparable SSLs (WEL+BEL) with thicknesses of $\sim 510 \mu\text{m}$ on an initially deformed microstructure (SPD-ER9) and crack-free transitions are present ([Figure 4a](#)

and b). The BE and SE images of the WEL region (Figure 4c–h) show a martensitic microstructure without significant differences for the presented depths from the surface (50, 100, and 250 μm). Figure 4i–n show the related initial ER9 microstructure before the thermal loads. Deformed and fractured cementite lamellae can be identified, with an alignment angle of 10–15° in a depth of 50 μm and 15–20° to the surface in a depth of 100 μm . In a depth of 250 μm from surface the ER9 microstructure is mechanically unaffected. The brownish appearing BEL region within the LOM images comes up with an average thickness of 140 μm and a tempered martensite microstructure (Figure 4o and p) with globular cementite particles due to spheroidization during the second thermal load (T2).

4.2. Fatigue testing of SSLs on rail wheel materials

The defined SSLs created by mechanical and thermal loads (M1, T1 and T2) are further treated by another mechanical load (M2) applied by the twin disc tribometer, which mimics the wheel–rail contact in service. Being most critical in terms of crack initiation, the transition regions are the focus when analyzing the specimens.

Figure 5 shows LOM images of cross-sectional cuts in the transition zones of the SSLs to the deformed ER7 base material

after 100,000 cycles under defined twin disc tribometer parameters (M2). Six thermal loaded zones are analyzed, significant differences in material behavior for the leading edge and the trailing edge of the SSL can be seen: 3 out of 6 transition zones at the leading edge showed no crack initiation (Figure 5a, g and i). Within the BEL and WEL transition regions, plastic deformations are present with shallow cracks and small spallation events along the WEL surface. The other transition zones at the leading edge of the SSL show different stages of crack propagation and failure. Figure 5e captures a crack within the BEL/WEL interface at the disc surface along the plastically deformed microstructure, but no significant crack propagation into the depth is present. More severe cracking is presented in the region captured by Figure 5k, which shows multiple cracks propagating under $\sim 90^\circ$ to the surface within the WEL region (Figure 5k: 1). At the interface to the BEL, the cracks branch (Figure 5k: 2). One crack-branch propagates in the direction of the tangential force along the WEL/BEL interface. Another crack-branch propagates in the other direction under a certain angle into the BEL. Joining of these cracks seems to result in WEL fragments, which are pushed against the underlying BEL due to the tangential and normal forces, leading to an SPD of the BEL (Figure 5k: 3). A similar

failure mechanism seems to be present in the region given in [Figure 5c](#), but the WEL fragments for this region are already spalled. The crack tip of the visible crack propagating under $\sim 90^\circ$ into the WEL is just in front of the WEL/BEL interface, hence, no branching can be seen in this case ([Figure 5c: 1](#)). At the edge of the spalled WEL region a branched crack, propagating under a certain angle into the BEL region, is present ([Figure 5c: 2](#)). This indicates a higher crack growth rate for cracks propagating along the WEL/BEL interface in the direction of the tangential force. At the region of the spalled WEL fragments, the BEL shows severe deformation ([Figure 5c: 3](#)).

Regarding the trailing edges of the SSLs, where the tangential force points from the base material to the SSL, no cracking is observed ([Figure 5b, d, f, h, j, l](#)). In contrast, there is major plastic deformation, and the ER7 material respectively the BEL seems to be pulled over the WEL to a certain degree. This is impressively present in the region captured by [Figure 5d](#), where the tangential

forces plastically deform the ER7 material over the WEL region.

A focus-variation microscope allows to extract additional information from these transition regions, [Figure 6](#). A smaller wear track is present in the grey blue appearing region, where the thermal loads have formed an SSL. The leading edges of the SSLs ([Figure 6a, c, e, g, i, k](#)) show some areas, where small regions spalled within the SSL, clearly visible in [Figure 6a](#). At the transition zone of the deformed ER7 material and the SSL, cracks ([Figure 6c: 1](#)), but also spallation ([Figure 6c: 2](#)) within the SSL next to the transition region are present. Within the transition region pictured in [Figure 6k](#) (referring to cross-section [Figure 5k](#)) massive crack patterns formed ([Figure 6k: 1](#)) and also spallation of some parts at the transition zone occurred ([Figure 6k: 2](#)). The trailing edges of the SSLs ([Figure 6b, d, f, h, j, l](#)) do not show significant damage patterns. Within the ER7 wear track, oxide lamella, adhered debris and ploughing features are present.

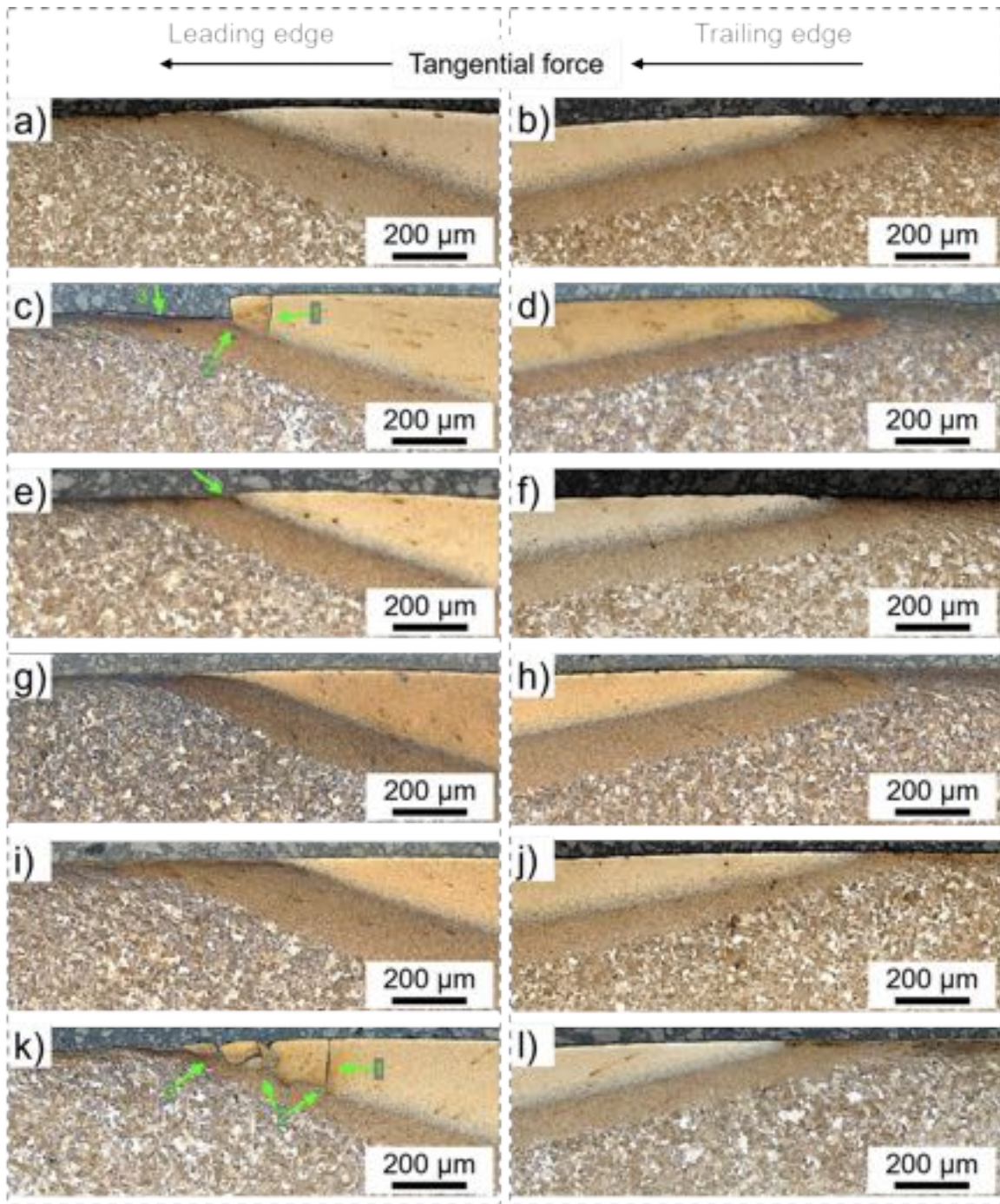


Figure 5: LOM images of the transition zones from base material to SSLs in cross-sectional cuts for wheel material ER7. The leading edges of the SSLs show failure patterns for 3/6 transition zones: Crack initiation and propagation under 90° to surface within the WEL (1), branching at the WEL/BEL interface (2), and deformation of the BEL due to WEL fragments (3). For the trailing edges of the SSLs, no cracking patterns are detected, but plastic material flow of the base material over the WEL region.

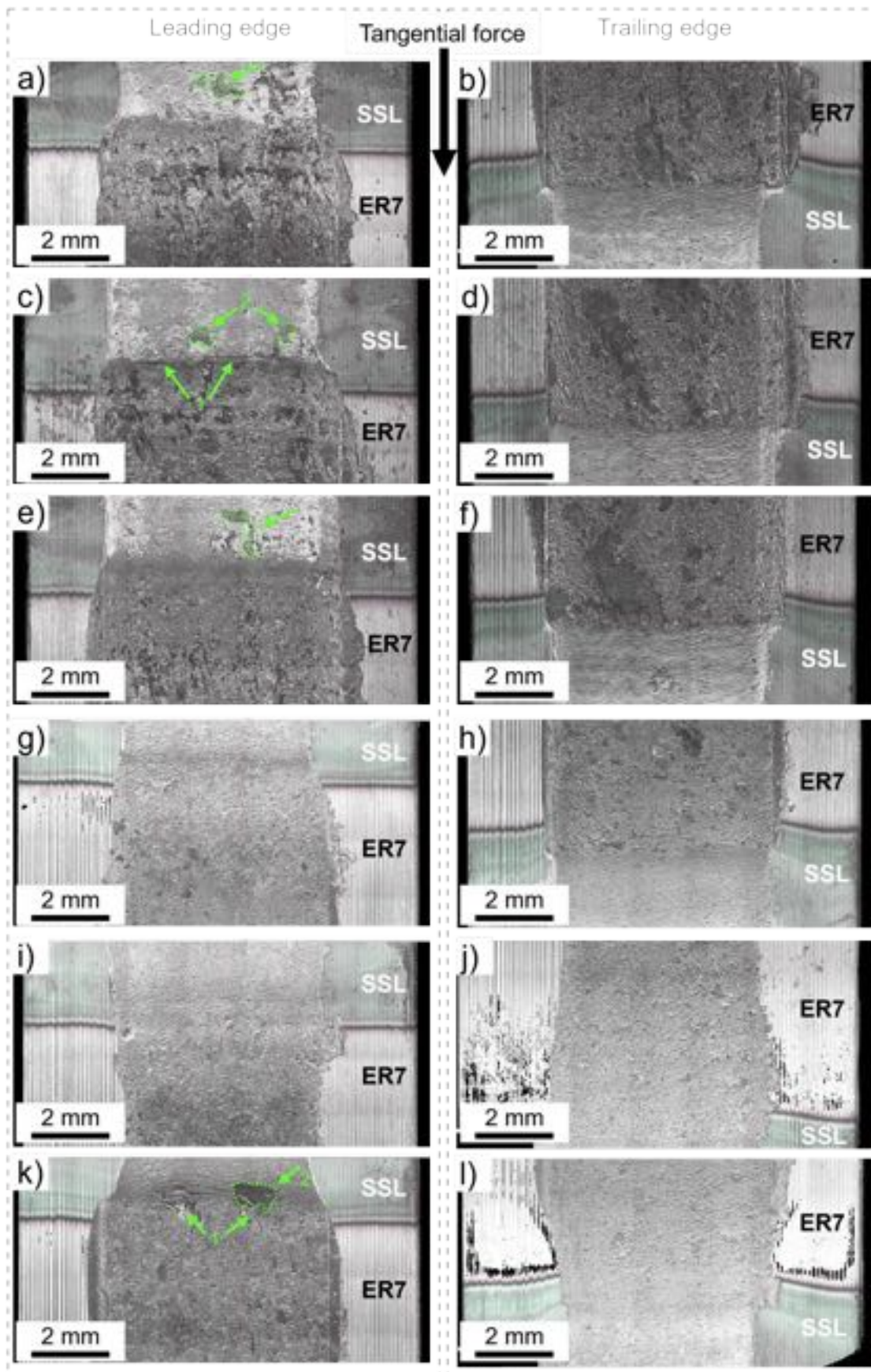


Figure 6: Surface images (focus-variation microscope) at the transition regions of the run ER7 wheels. Leading edges of the SSLs show crack initiation at the interface (1) for some samples and breakouts of SSL fragments (2). The trailing edges do not show significant damage patterns at the interfaces.

In the transition zones of the SSLs to the base material ER9 after twin disc tribometer testing, fatigue cracks are present in 4 out of 5 transition zones at the leading edge of the SSLs, see the LOM images of the cross-sectional cuts given in [Figure 7a, c, e, g, i](#). The damage patterns exhibit similar characteristics to those of the ER7 discs ([Figure 5](#)) but more severe. The crack propagating $\sim 90^\circ$ to the surface within the WEL region, [Figure 7e](#), is a sign of the first stage of fatigue damage of the SSLs. The tip of the crack (which seems to have no branching) is just before the WEL/BEL interface. Within the transition zone multiple cracks perpendicular to the surface formed ([Figure 7c: 1](#)), which branch at the WEL/BEL interface ([Figure 7c: 2](#)). As described for the ER7 wheel material, one crack branch propagates along the WEL/BEL interface in the direction of the tangential force, while the other propagates under a certain angle into the BEL in opposite direction. In addition, there is severe deformation of the BEL and an almost loose WEL fragment ([Figure 7c: 3](#)). The features present in the transition zone indicate an already proceeded stage where the initial cracks within the WEL ([Figure 7g: 1](#)) branched at the WEL/BEL interface ([Figure 7g:2](#)). Subsequent joining of the cracks leads to the formation of WEL fragments, followed by a deformation of the underlying BEL ([Figure 7g: 3](#)). Similar

characteristics are present in the regions shown in [Figure 7i](#). There, the WEL fragments already spalled, and a massive pit is formed. The LOM images for the trailing edge of the SSLs ([Figure 7b, d, f, h, j](#)) show no crack initiation at the transition zone, but plastic deformation and material flow in direction of the tangential force with some amount of material plastically deformed over the SSL.

As for the ER7 discs, the wear track along the grey-blue appearing region (SSL) is significantly smaller, see the surface images of the tested ER9 discs, [Figure 8](#). Radial cracks origin from the transition from the ER9 base material to the SSL extend throughout the SSL at the leading edge ([Figure 8a, c, e, g, i](#)). This is impressively shown in [Figure 8c: 1](#) (the corresponding cross section is given in [Figure 7c](#)), which regularly cause the spallation of large areas (labelled with 2 in [Figure 8c](#)). Corresponding characteristics are present in the region captured by [Figure 8g](#) (the corresponding cross-section is [Figure 7g](#)) and in a more severe stage in the region shown by [Figure 8i](#) (the corresponding cross-section is [Figure 7i](#)). Radial cracks but no spallation is present in the region presented in [Figure 8e](#) (the corresponding cross-section is [Figure 7e](#)). As for the ER7 discs, there is no severe damage in the transition regions of the trailing edge ([Figure 8b, d, f, h, j](#)). Within the wear track,

oxide lamella and adhered debris are present, with some amount of ploughing.

This is more significant within the wear track of the ER9 base material.

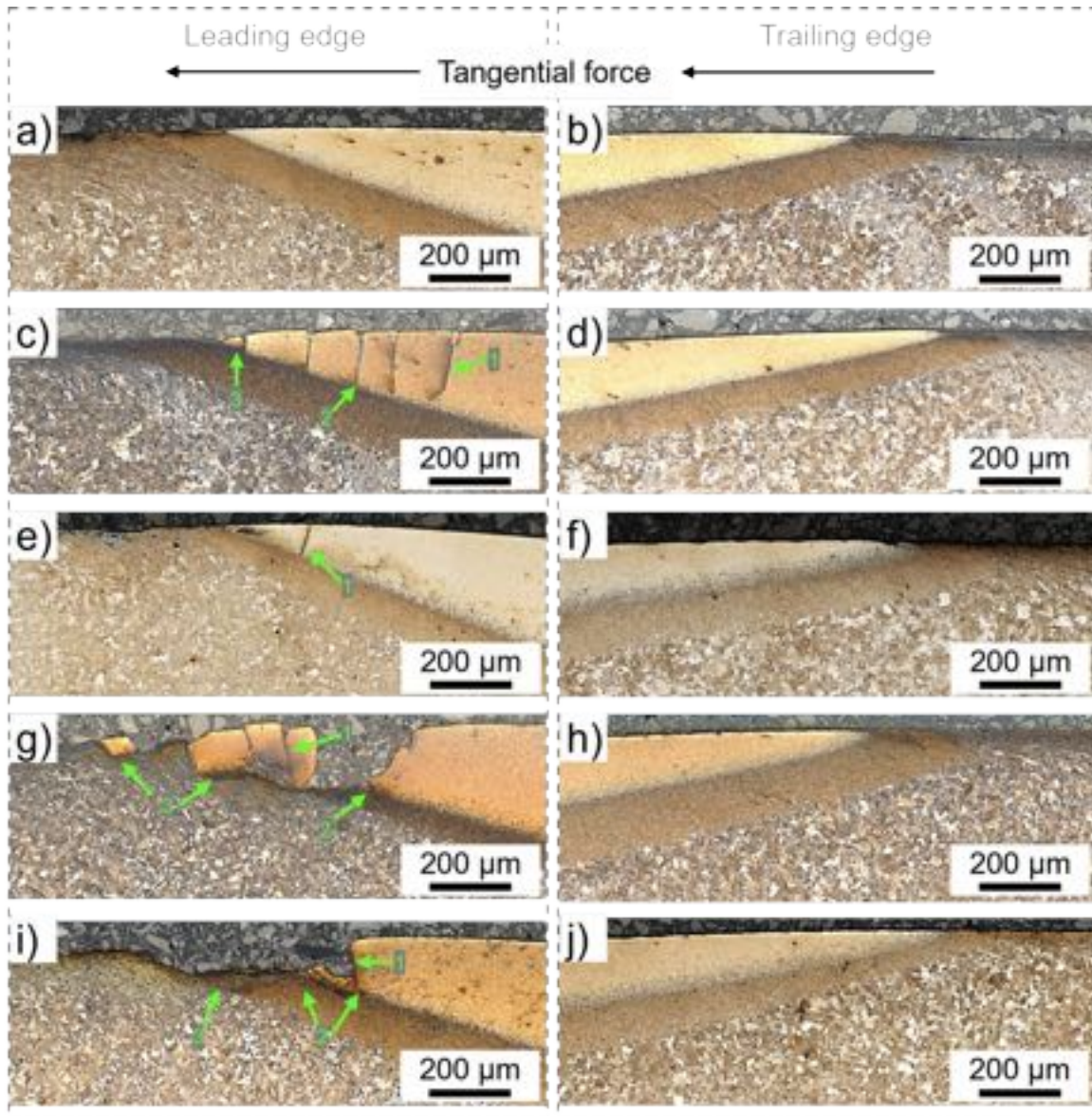


Figure 7: LOM images of the transition zones from base material to SSLs in cross-sectional cuts for wheel material ER9. The leading edges of the SSLs show failure patterns for 4/5 transition zones: Crack initiation and propagation under 90° to surface within the WEL (1), branching at the WEL/BEL interface (2), and deformation of the BEL due to WEL fragments (3). For the trailing edge, no cracking patterns are detected, but plastic material flow of the base material over the WEL region.

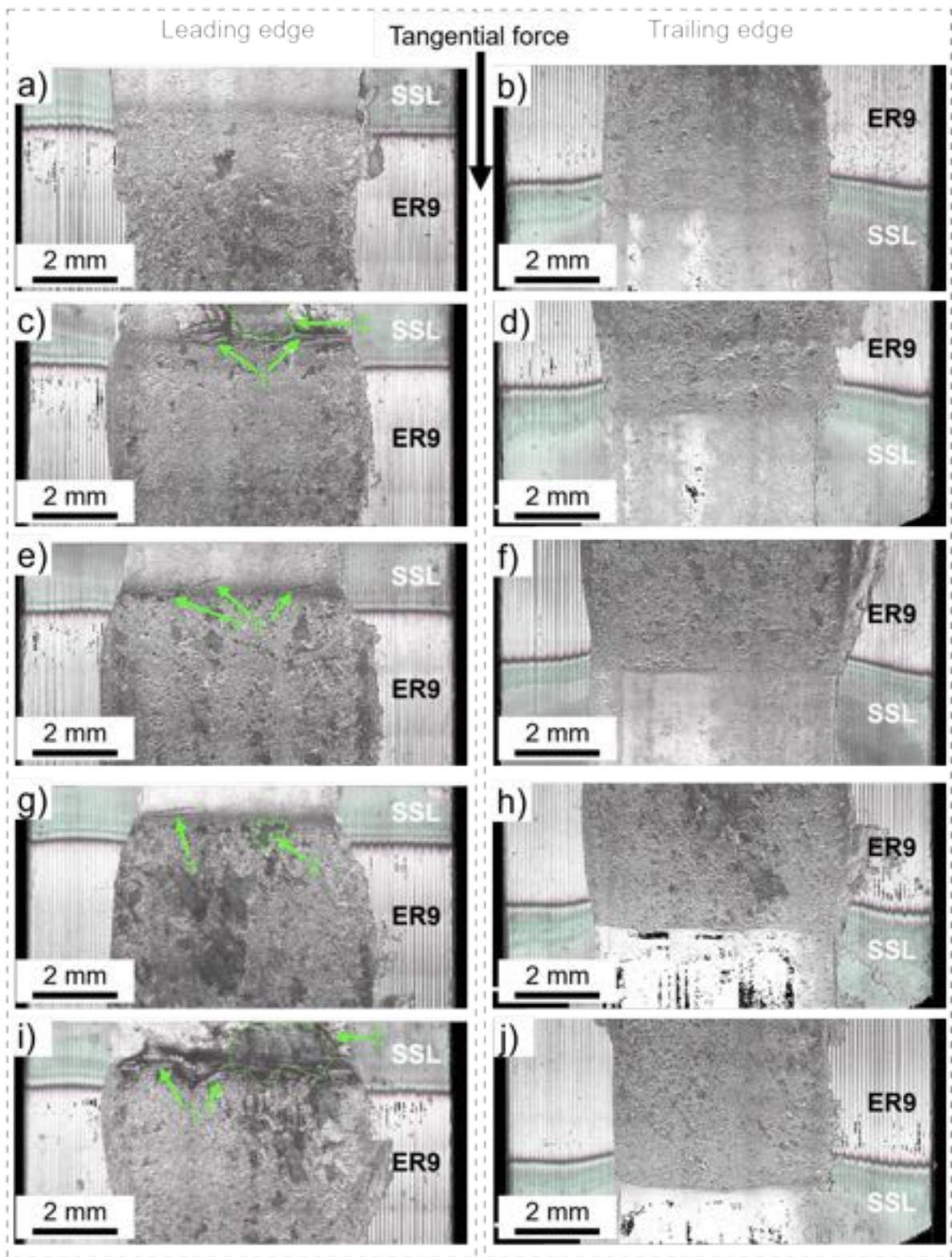


Figure 8: Surface images (focus-variation microscope) at the transition regions of the run ER9 wheels. The leading edges of the SSLs show crack initiation at the interface (1) for 5 out of 6, in some cases massive breakouts of SSL fragments (2) can be detected. In contrast, the trailing edges do not show significant damage patterns at the interfaces.

4.3. Explanatory model of fatigue crack initiation of SSLs on rail wheel materials

Based on the results of the twin disc tribometer tests, presented in the previous section, the fatigue crack initiation and propagation within SSLs on wheel materials can be divided into different stages. With the help of in-depth SEM investigations of representative ER7 and ER9 samples, an explanatory model was derived, featuring various stages:

The first stage (*Stage I*) is characterized by a dominating gradual wear without crack formation in the transition zone of the SSL to the deformed wheel base material (Figure 9a). At this stage, the mechanical load of the twin disc tribometer caused plastic deformation and detachments of wear debris. For the wheel material, the deformation is obvious down to $\sim 200\ \mu\text{m}$ from the surface, as described above (Figure 3 and Figure 4). Besides its hard and brittle nature, the WEL of the SSL shows plastic deformation down to $\sim 10\ \mu\text{m}$ from the surface with aligned martensite grains (increasing angle to the surface with increasing depth (Figure 9b)). The WEL region exhibits micro-cracks, which shallowly propagate at an angle of $10 - 15^\circ$ to the surface. At a certain point, the cracks tend to grow towards the surface leading to the formation of small, detached particles

(Figure 9c and d). This cracking mechanism is present along the WEL surface of the whole disc and is not related to the transition zones. It is the result of wear-related micro-crack formations, which are also present in regions without SSLs. However, no macroscopic cracks are formed and hence, no critical fatigue crack initiation takes place at this stage.

In the next stage, named *Stage II*, significant macroscopic crack initiation is evident within the WEL at the leading edge of the SSL (Figure 10a). Out of several micro-cracks initiated in *Stage I*, certain conditions lead to a crack propagating along the alignment of the deformed martensite microstructure. Further, crack propagation under $\sim 90^\circ$ to the surface into the material with a slight diversion towards the direction of the tangential force is detected. The cracks show some branches and arrest at the WEL/BEL interface (Figure 10b, c). Within the WEL the crack exhibits branches (Figure 10c), but the crack tip itself is almost blunted. This indicates that the region around the crack tip (being within the BEL) is prone for an increased fracture toughness (Figure 10d).

Multiple macroscopic cracks initiated within the first $\sim 500\ \mu\text{m}$ of the WEL at the leading edge of the SSL (Figure 11a) enters the next stage, named *Stage III*. Investigations show that some cracks propagated to the WEL/BEL interface,

where they branch. Two major crack-branches are identified: One crack-branch propagates along the WEL/BEL interface along the tangential force, the other in the opposite direction into the BEL (Figure 11b). Taking a closer look at the crack tips of these two branches shows a sharp crack tip in the WEL/BEL interface (Figure 11c), contrary to the blunted crack tip present in the BEL (Figure 11d). This, in combination with the increased length of the crack-branches within the WEL/BEL interface, indicates a faster crack growth there.

The final stage, *Stage IV*, represents fatigue damage of an SSL where significant spallation at the leading edge occurs. This results in a significant geometrical deviation on the wheel surface which can cause a considerable dynamic impact promoting further degradation (Figure 12a). In *Stage IV*, the crack-branches generated in *Stage III* grow together which leads to the fragmentation of the WEL. Due to the contact situation, the fragments are pushed towards the direction of the tangential and normal forces onto the underlying BEL. This results in a severe deformation of the BEL region (Figure 12b). Although some WEL fragments already spalled (Figure 12c), the results and discussions presented above suggest that the cracks branched at

the WEL/BEL interface, propagated into the BEL, and arrests there.

Regarding the trailing edges of the SSLs no different stages of fatigue mechanisms are observed (Figure 5 and Figure 7). Based on the tangential force pointing towards the SSL edge the material flow seems to strengthen the trailing edge of the SSL. In contrast to the leading edge, the supporting effect of the deformed material hinders macroscopic crack growth. Hence, only wear-related micro-cracks along the WEL surface are present (Figure 13a). The results further suggest that these cracks are not crucial for the fatigue damage. In some cases, the crack growth direction bends towards the surface leading to the formation of small debris (Figure 13b). The plastic flow of the BEL and the deformed ferritic-pearlitic microstructure in direction of the tangential force leads to cavities in the near-surface microstructure (Figure 13a, c, d). In one case, the more ductile BEL microstructure is sheared over the WEL microstructure and a crack, initiated within the WEL, propagates up to 150 μm along the interface of the WEL and the sheared material (Figure 13d). Since the crack arrests in the BEL, there is no critical crack propagation leading to significant formation of fragments that would spall.

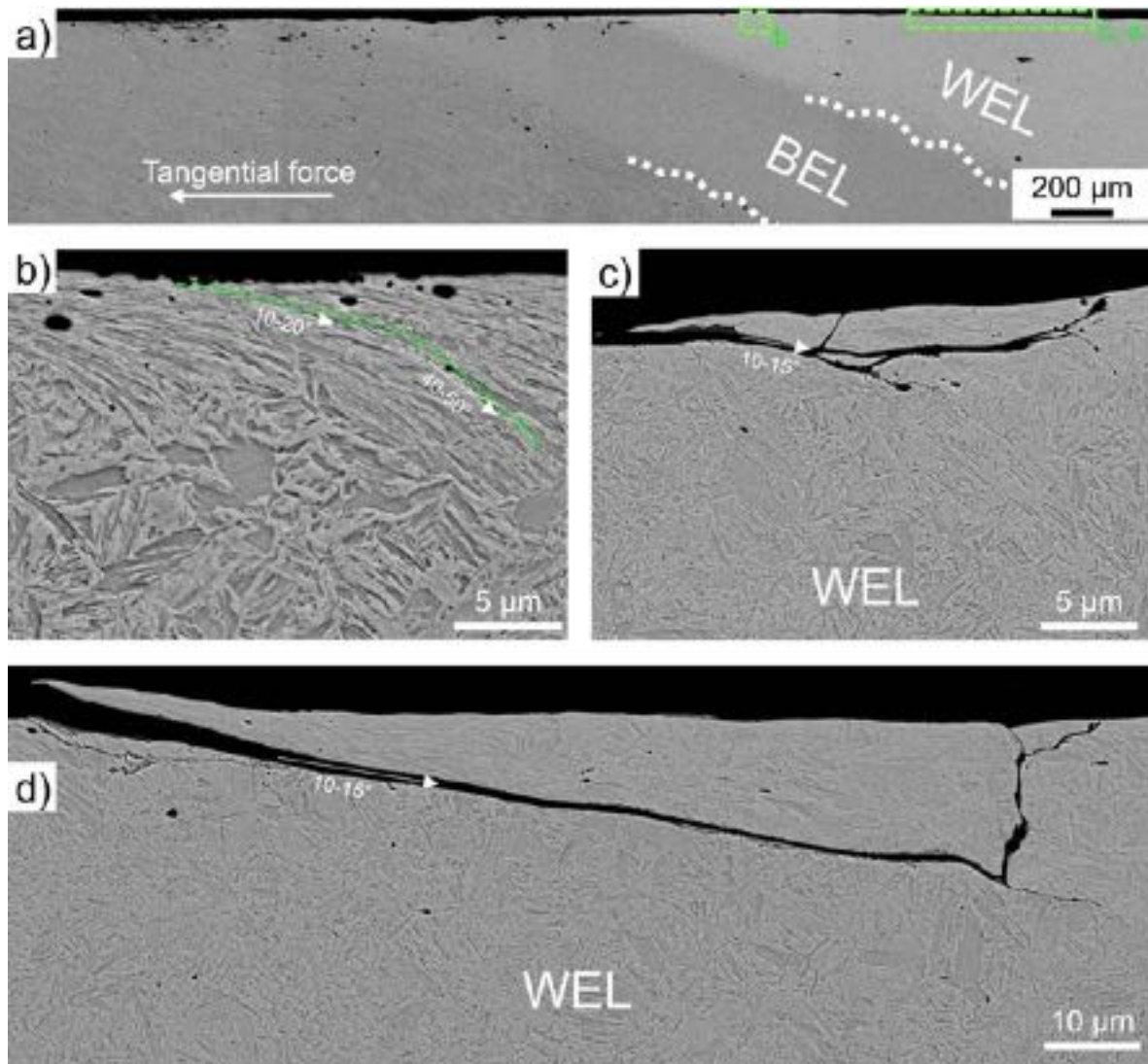


Figure 9: BE images of the leading edge of the SSL at *Stage I*: (a) No crack initiation within the transition zone of the SSL and the deformed wheel base material. (b) shows the plastic deformation of the WEL within $\sim 20 \mu\text{m}$ from surface and the alignment of the martensite microstructure. Micro-crack initiation occurs along the WEL surface, cracks under shallow angles ($10 - 15^\circ$ to the surface) either changing their direction towards the surface (c) or branch and propagate towards the surface (d). In both cases, detachment of wear debris is the result.

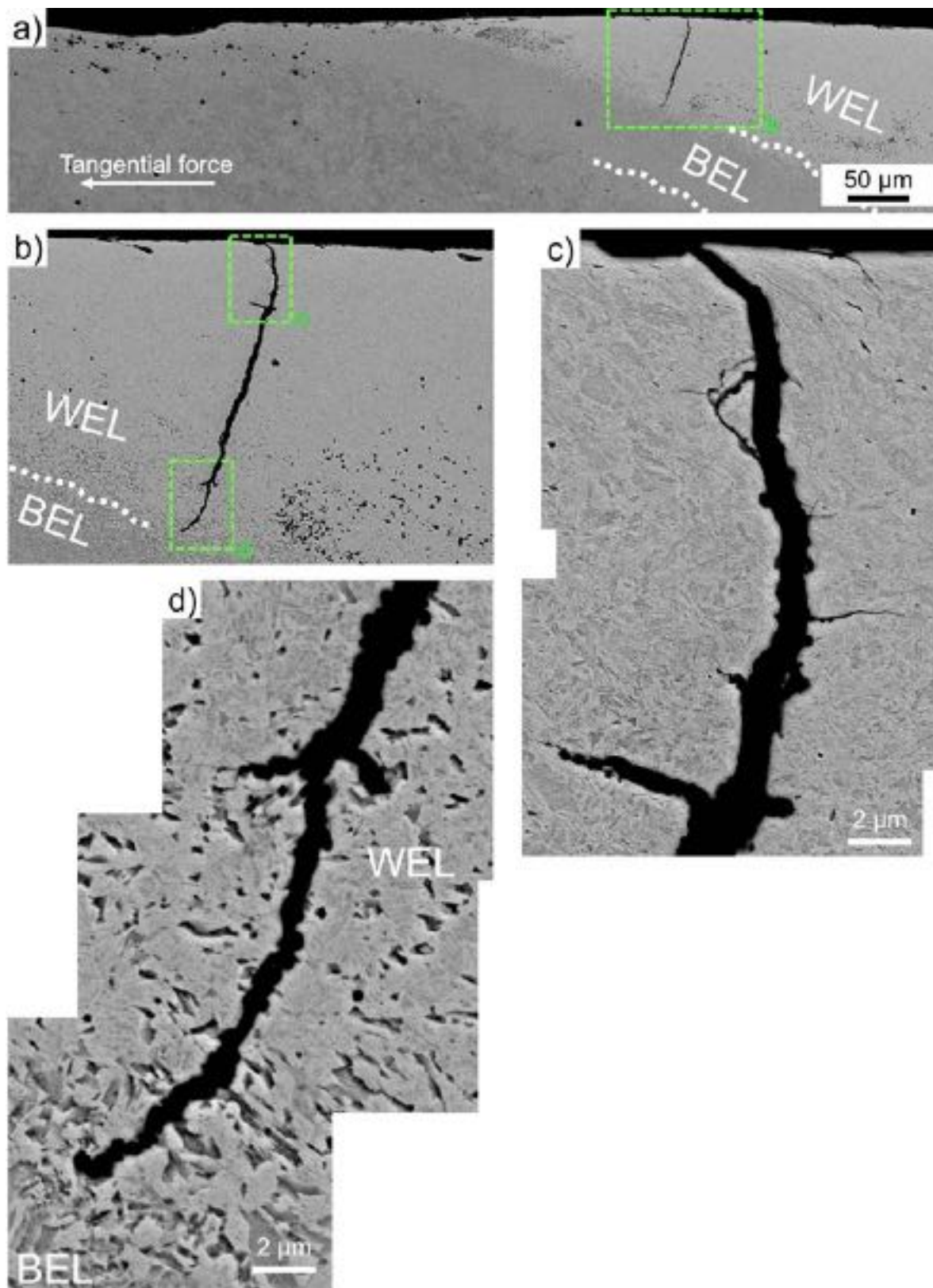


Figure 10: BE images of the leading edge of the SSL at *Stage II* are characterized by macroscopic crack initiation at the WEL with crack propagation $\sim 90^\circ$ to the surface down to the WEL/BEL interface (a), (b). The crack first propagates along the deformed martensitic microstructure (c), the crack tip is situated just in the BEL region and shows significant blunting (d).

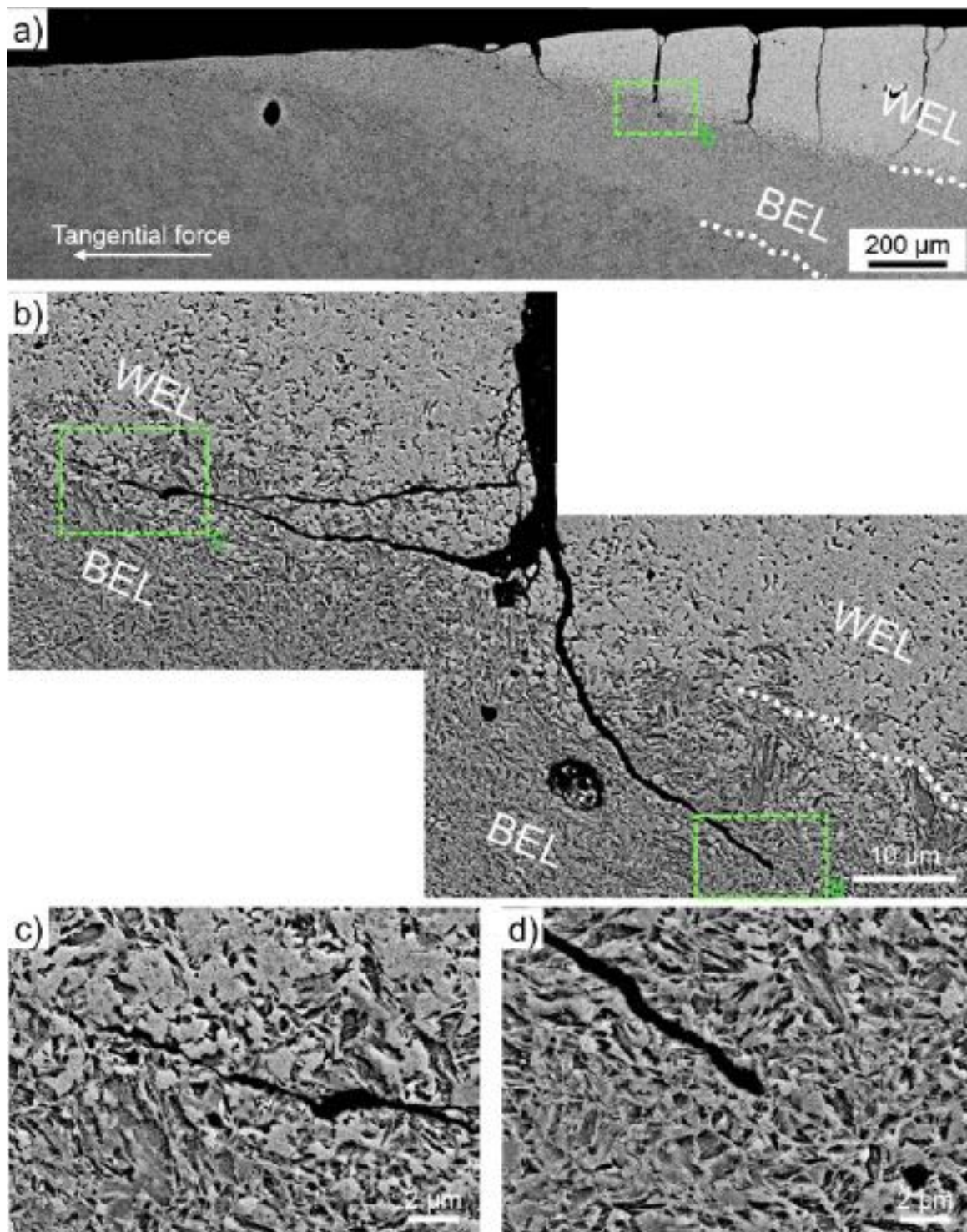


Figure 11: BE images of the leading edge of the SSL at *Stage III*: Multiple cracks are evident in the WEL next to the transition zone (a), with crack branching at the WEL/BEL interface (b). One crack branch propagates along the WEL/BEL interface in direction of the tangential force and is characterized by a sharp crack tip (c), the other propagates into the BEL showing a minor crack length and a blunt crack tip (d).

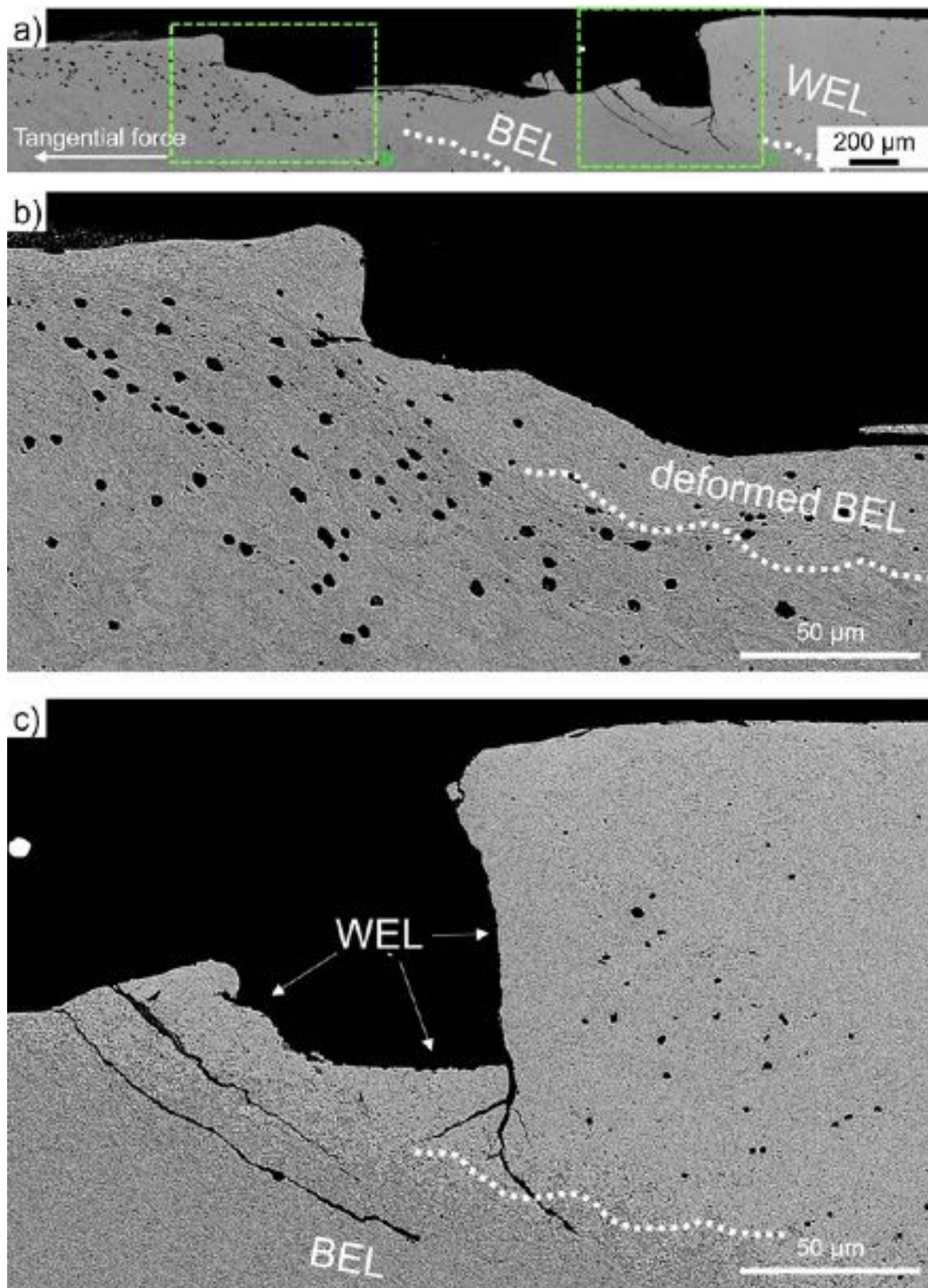


Figure 12: BE images of the leading edge of the SSL at the final stage, *Stage IV*. This stage comes up with a massive geometrical deviation on the wheel surface due to spallation of WEL fragments (a). The cracks branched at the WEL/BEL interface in Stage III merge and WEL fragments are spalled, pushed towards the direction of the tangential and normal forces against the underlying BEL and leading to a severe deformation of the BEL (b). The branched cracks propagating into the BEL are still existing, but further propagation is not expected (c).

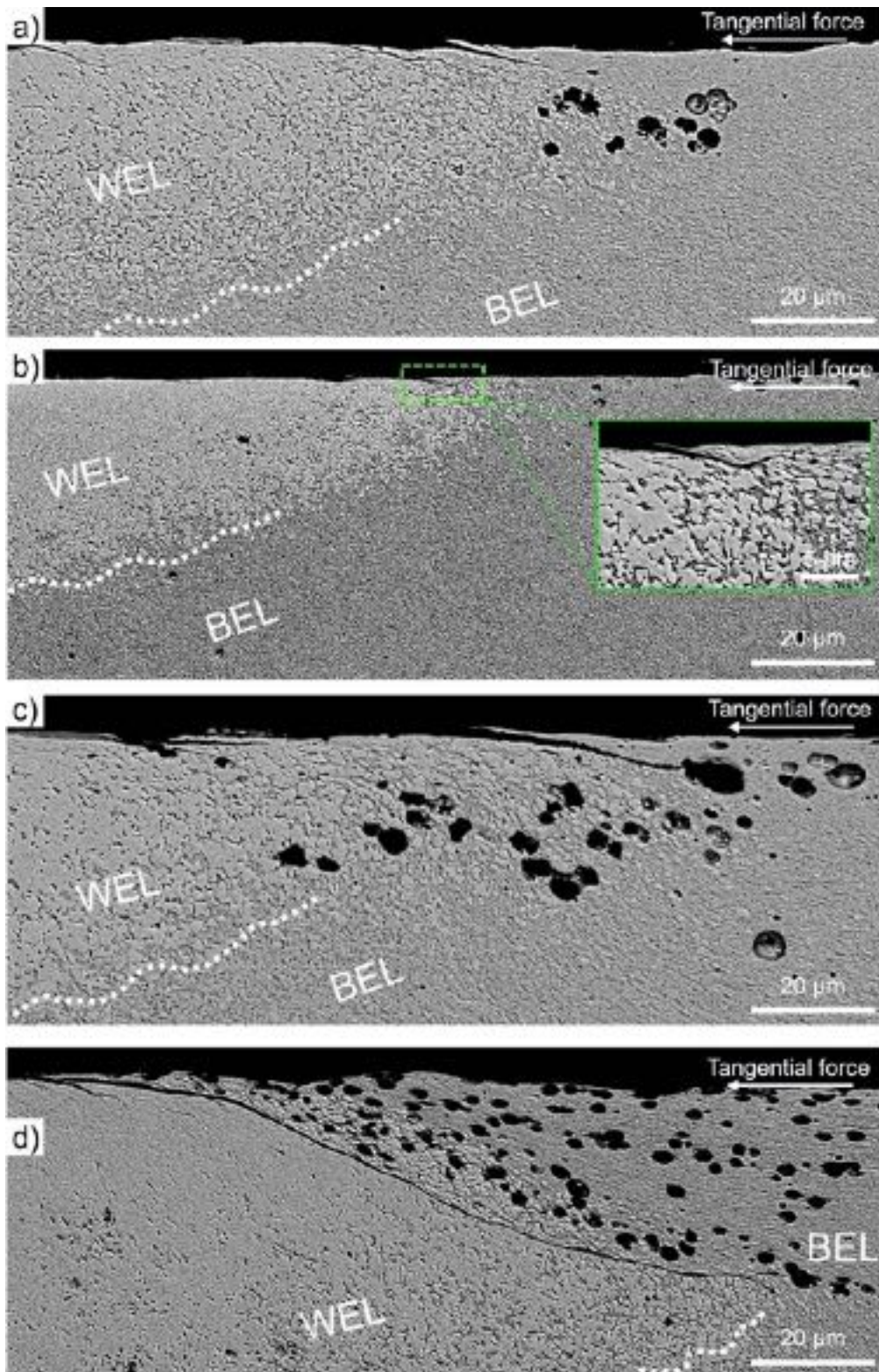


Figure 13: BE images of the trailing edges of the SSLs, which do not show critical crack initiation, but material flow of the BEL and wheel base material in the direction of the tangential force. Wear dominated micro-cracks can be identified along the WEL surface (a), propagating towards the surface in most cases (b), or stopping at cavities (c). Massive material flow leads to formation of cavities, where, in one case (d), a crack propagated along the transition to the WEL.

The change of the surface geometry at the leading edges of the SSLs for the different stages described above is shown by topographical analysis of representative samples in Figure 14. At *Stage I* and *II* (Figure 14a and b) no change within the surface can be identified. In contrast, multiple cracks can be seen at *Stage III*

(Figure 14c). Further, at *Stage IV*, a large area with massive spallation within the SSL are present (Figure 14d).

Based on the results of the analysis so far, a schematic overview of the explanatory model of fatigue crack initiation of SSLs on rail wheel materials is presented in Figure 15.

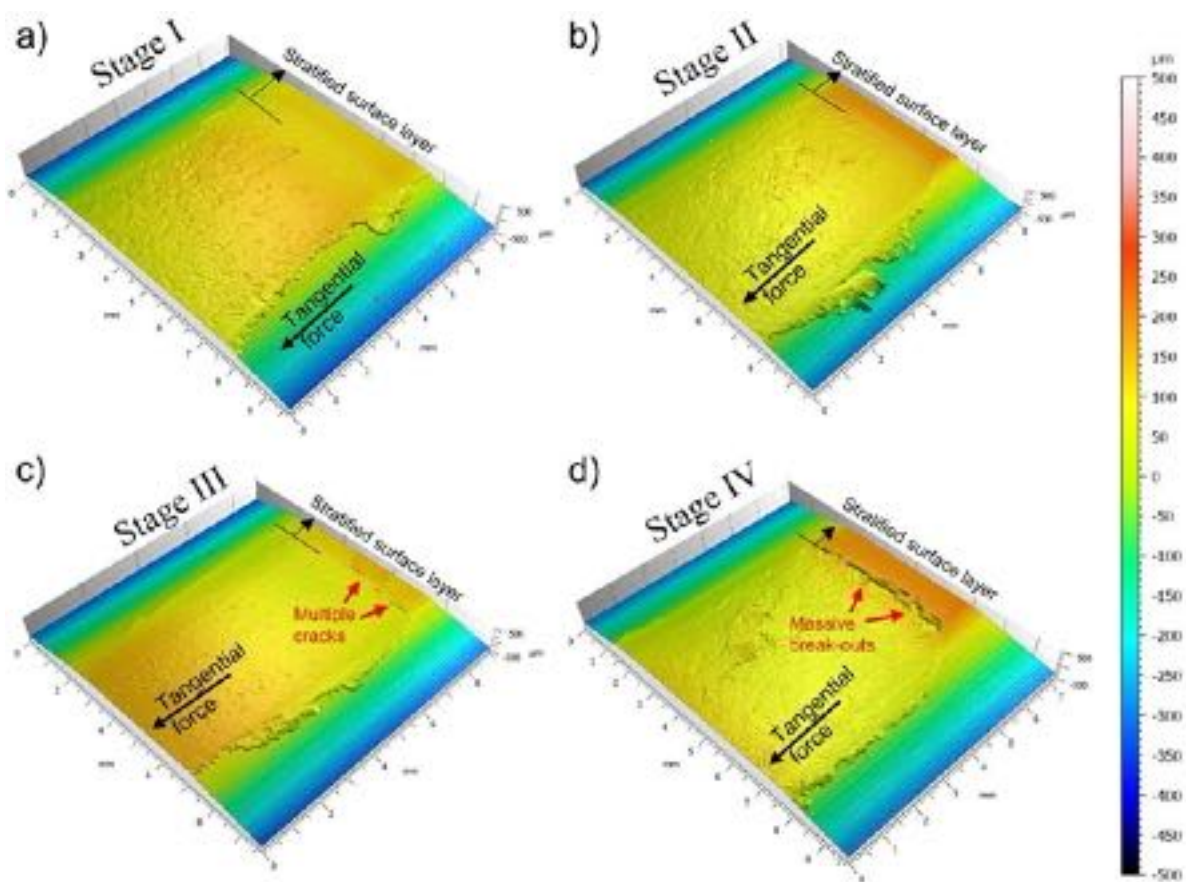


Figure 14: Topographical analysis of representative leading edges of the SSLs: *Stage I* (a) and *II* (b) do not show significant changes at the surface, in contrast, at *Stage III* (c) multiple cracks can be identified. At the final stage, *Stage IV* (d) massive spallation within the SSL can be seen, leading to significant geometrical changes of the discs.

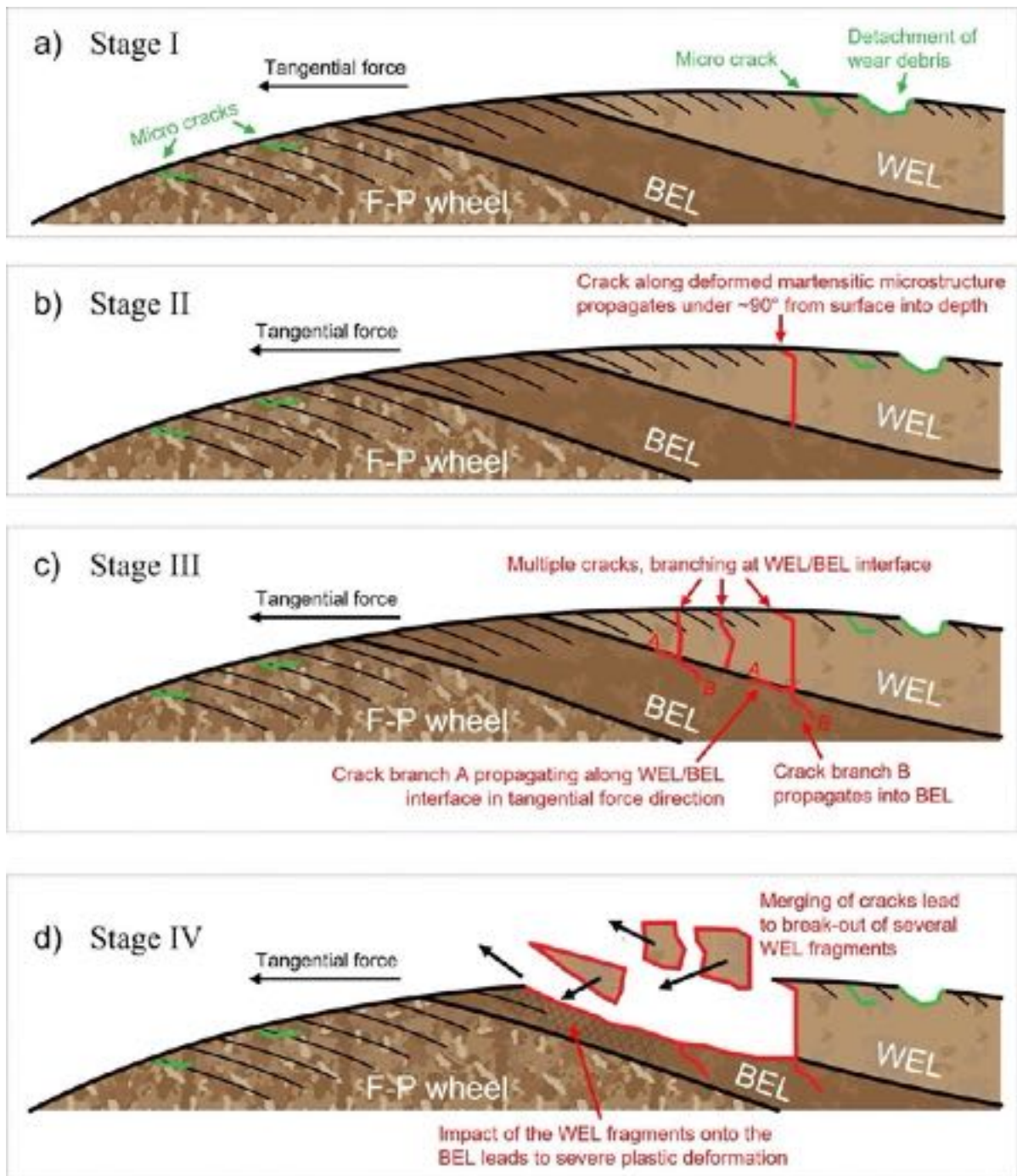


Figure 15: Explanatory model of fatigue crack initiation at the leading edges of SSLs on wheel materials: The wear dominated *Stage I* (a) shows no macroscopic crack in the transition zone of the ferritic-pearlitic wheel material (F-P wheel), to the BEL and the WEL. The depth of plastic deformation is decreasing with increasing hardness (F-P wheel \rightarrow BEL \rightarrow WEL). Micro-cracks can be observed along the disc surface, stopping, or turning towards the surface resulting in detachment of wear debris. At *Stage II* (b) a vertical crack is initiated within the WEL next to the transition zone. Initiated at the surface, the crack first propagates along the aligned martensite grains and further under $\sim 90^\circ$ from surface into depth until the WEL/BEL interface. *Stage III* is representing multiple cracks initiated within the WEL near the transition zone, with branching occurring at the WEL/BEL interface. One crack branch (A) propagates along the WEL/BEL interface in the direction of the tangential force, the other (B) in opposite direction downwards into the BEL. Finally, at *Stage IV*, the crack branches merge and fragments of the WEL break out. At least some WEL fragments get pushed against the underlying BEL, leading to a severe plastic deformation of the BEL.

4.4. Differences in fatigue crack initiation and propagation with respect to different wheel materials

Based on the results presented *Stage III* is critical for the initiation of fatigue failure of SSLs, since at this stage the smaller fatigue cracks join and result in massive spallation of WEL fragments. Clearly, a difference in degree of damage can be observed between the wheel grades ER7 and ER9 (Figure 5 and Figure 7). To understand fatigue crack morphology the evaluation of mechanical properties within the evolved layers is needed, only possible by small-scale testing methods. Therefore, distinctive regions within the SSLs of both wheel materials are further characterized by microhardness measurements (Figure 16a and b). The different regions at the cross sections around the WEL and BEL borders, Figure 16a and b, show pronounced differences in Vickers hardness. In addition to hardness, the local fracture toughness K_Q is commonly used to get a sense of potential RCF crack initiation risk in wheel and rail materials [36]–[38]. Since small-scale fracture toughness experiments would go beyond the scope of the current work, K_Q is

estimated according to [38] within this section as follows:

$$K_Q = \frac{A}{HV^B} \quad (2)$$

with microhardness HV , and fitting constants $A = 15,600 \text{ MPam}^{1/2}$ and $B = 1.0$. For easier comparison and correlation, these data are presented directly within Figure 16c. The martensitic WEL regions provide highest hardness (thus lowest K_Q) of 942 ± 18 and $998 \pm 25 \text{ HV0.01}$, see ER7-1 and ER9-1. Within these regions the crack propagates almost perpendicular from the surface towards the WEL/BEL interface, where it is deflected. There, the $HV0.01$ values are only 587 ± 9 (504 ± 8) and 754 ± 15 (533 ± 9), see ER7-2 (ER7-3) and ER9-2 (ER9-3). In general, the individual regions of ER7 are softer than the corresponding ones of ER9. This is supposed to originate on the higher carbon content of ER9, however, this is not clearly understood so far due to the controversially proposed formation mechanisms of BELs. If we use the common estimation of fracture toughness through the inverse relation with hardness mentioned above, results suggest the lowest fracture toughness within the WEL and a trend of higher fracture toughness values for SSL regions of the ER7 wheel material.

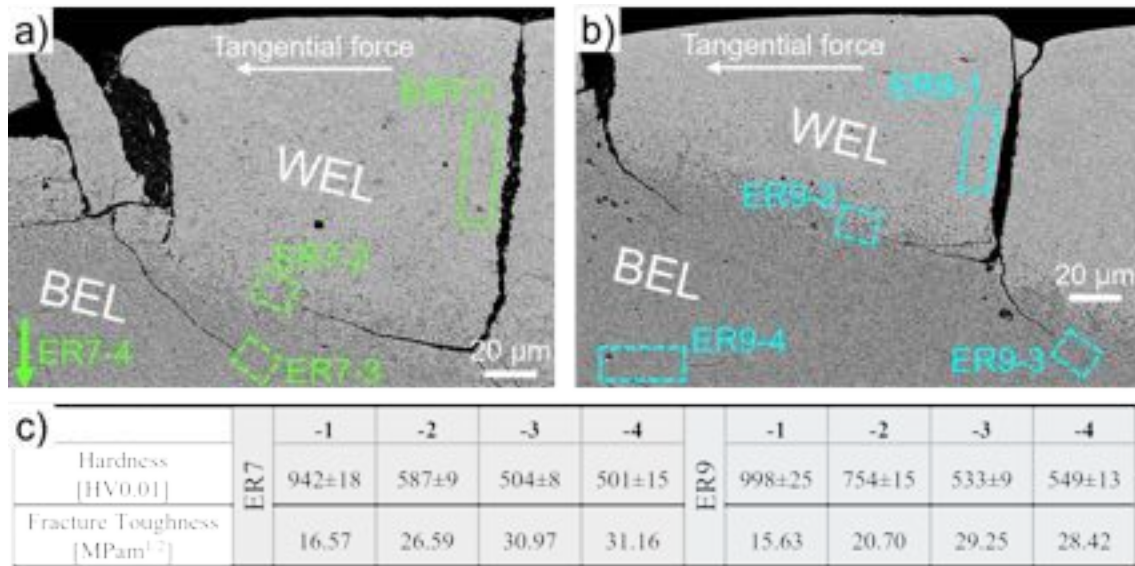


Figure 16: Microhardness measurements are conducted in specific regions at the leading edge of SSL at *Stage III* on the (a) ER7 wheel steel, and (b) ER9 wheel steel. The obtained hardness values and the estimated local fracture toughness values are given in (c).

4. Discussion

The major drawback when investigating wheel and rail samples from the field is their unknown loading history. But for detailed fatigue investigations, well-defined and known conditions are needed to draw reasonable conclusions. Therefore, the wheel and rail sample materials were well-defined treated with the help of a twin disc tribometer in our laboratory. The conditions of the field operations are mimicked by a mechanical load (to deform the material) followed by two thermal loads, which finally form WEL and BEL layers (being similar to the field samples). These disc samples were afterwards mechanically treated to initiate fatigue damages.

Due to surface inhomogeneities as a result of the first mechanical loading, the laser parameters, based on our previous work [14], were slightly changed for having a pre-defined output power. This guarantees the targeted surface temperature based on a comparable coefficient of absorption for the wheel steel samples within this work. Thus, the first thermal load (T1) was performed with a laser energy of $P = 4 \text{ kW}$ (which corresponds to an energy input of $\sim 3.5 \text{ Ws/mm}^2$), resulting in an estimated surface temperature of $\sim 930^\circ\text{C}$. This is in the range of possible temperatures reached for wheel–rail contacts [17] and above the austenitization temperature of the wheel steels. Initial trials showed that only a second thermal load (T2) with less laser energy compared to the first leads to the

formation of a BEL layer. The selected laser power of $P = 3.2$ kW induced a pronounced BEL consisting of tempered martensite microstructure underneath the martensitic WEL. This is in accordance with one proposed formation mechanism of BEL (Route 2) by Kumar et al. [28]. Further, the microstructure of the BEL created in the current work corresponds to the tempered martensite stated in [29] and former works from the authors [39], [40]. In contrast, the presented approach to create SSLs contradicts the proposed formation mechanism by Messadi et al. [30] where a single thermal loading is suggested to create a martensitic WEL with a bainitic BEL underneath.

The novel experimental approach of combining twin disc testing and surface laser treatment was successful in creating plastic shear deformation and WEL and BEL layers at the surface, as well as crack initiation and crack propagation in good correlation with reports from field samples [41]. The results obtained here are in agreement with results reported in literature using a twin disc tribometer to investigate the crack behavior of WELs, either created by rolling-sliding friction tests [22], [42] or laser discrete quenching (LDQ) [43], [44] on rail materials. Seo et al. [22] reported two types of cracks, one between the WEL and the undeformed area underneath, the other at the center of the WEL. The

branching observed at the end of the WEL resembles the branching at the WEL/BEL interface at *Stage III* within our work. The vertical strip-shape LDQ tested in the work of Ding et al. [43] also reveals similarities to the laser surface treatments of our work. Crack initiation and propagation with large angles could be observed in the edge of the quenching region, explained by the high hardness of the martensite and the relatively low strength and less supporting effect of the underlying material due to decreasing thickness at the edges. Crack branching at the end of the WEL was shown, where cracks either propagate into the substrate or along the boundary [43]. Studies with respect to crack initiation in the presence of WELs were commonly published on rail samples from field, as shown by Steenbergen et al. [8] and Al-Juboori et al. [45], where the cracks initiate at the transition zone of the WEL and the rail material. Especially the border regions of the WEL to the base material or the BEL are sensitive regions for the crack propagation, as our results show. The sudden change in microhardness causes the cracks (running from the WEL regions) to deflect and branch, which consumes energy and would be an advantage to reduce the crack propagation. But this unfortunately also lead to chipping-off of some WEL or BEL material (Figure 9). Our results about the branching characteristics of the cracks at the

boundaries of the WEL to the underlying rail material are in agreement with reports of Pereira et al. [46], about RCF on ex-service rails with detected WELs. They actually suggested that the microstructural heterogeneity promotes the change in crack growth directions. Österle et al. [47] further showed that within the WEL regions on rails high compressive residual stresses are present, which originate from phase transformations and the connected volume expansion. Additionally, Lian et al. [48] proposed (based on FE-modelling) that residual stresses within the WEL also change due to multiple train passages (thus loading changes). Earlier, the same authors highlighted (also based on numerical models) that when the wheel passes from the rail matrix to the WEL, the normal contact stress sharply increases [49], contributing to the crack initiation observed in the wheel materials here, where the most critical cracks (largest ones) are present within the WEL itself. Due to a volume reduction during tempering of martensite, high residual stresses build up, promoting fatigue crack initiation [50]. Although the tempered martensite may correspond to the BEL of our study, the fatigue crack initiation is different. Additionally to the crack initiation at the borders of the WEL, Li et al. [27] and Messadi et al. [30] also showed that cracks are initiated within the BEL of SSLs on rails. This can be due to the

higher loads present during real field operations and additional dynamic effects. However, our studies ensure defined loading parameters (mechanical and thermal) in both for the formation of the SSLs and the fatigue testing. This paves the way for future systematic studies, where different influencing parameters can be studied and fundamental knowledge about RCF in the presence of SSLs can be gained. In terms of influencing parameters, the material properties play a crucial role with respect to fatigue crack initiation and propagation. In this study, two wheel materials, ER7 and ER9, are investigated with equal preceding heat treatment. Results indicate clear differences in their crack propagation and deflection, compare [Figure 5](#) and [Figure 7](#). The sensitivity for crack initiation and propagation of the ER9 wheel material can be rationalized with their typically higher microhardness values, [Figure 16](#). However, determination of further mechanical properties such as fatigue strength is hampered due to the small scale of the evolved layers. Thus, efforts have been made by applying small-scale testing techniques to evaluate the local fracture toughness with high spatial resolution of wheel and rail materials [36]–[38], [51]. To not exceed the framework within the current study, a common estimation of the local fracture toughness was used, showing a good comparability to

results conducted for samples from the field. Moreover, findings in the presented work will act as a useful reference to future microstructural and micro-mechanical characterizations of SSLs on wheel and rail near-surface microstructures and their fatigue crack morphologies.

5. Conclusions

The main conclusions of the presented study on fatigue crack initiation of SSLs (WEL+BEL) on different wheel materials created by defined mechanical and thermal loads are:

- The established laboratory approach to create reproducible SSLs on wheel steels shows a good comparability to wheels from field. The combination of a twin disc tribometer and laser surface treatments mimics an SSL with defined mechanical and thermal loading parameters.
- The fatigue tests of the SSLs show different degrees of fatigue crack initiation and propagation exclusively on the leading edge of the SSL.
- The material ER9 (higher microhardness and lower estimated local fracture toughness in the surrounding areas of the identified cracks) showed more extensive

fatigue crack initiation and propagation.

The results obtained, allow to derive an explanatory four-stage model of fatigue crack initiation at the leading edges of the SSLs. Within *Stage I* no fatigue cracks initiate, but wear-related micro-cracks along the WEL surface. At *Stage II* a macroscopic crack initiates in the WEL next to the transition to the deformed wheel material, propagating $\sim 90^\circ$ to the surface towards the WEL/BEL interface. *Stage III* is dominated by multiple crack initiation (analogous to *Stage II*), which further branch at the WEL/BEL interface. One crack-branch propagates along the WEL/BEL interface in the direction of the tangential force, the other in the opposite direction downwards into the BEL at a slower crack growth rate. In *Stage IV*, several crack-branches grow together, causing significant spallation of material above them. The trailing edges of the SSLs do not show fatigue crack formation, which is explained by the supporting effect of the underlying material and the plastic material flow towards the SSL in tangential force direction.

The presented systematic study of SSLs created under defined mechanical and thermal loads points out their relation to fatigue crack initiation and propagation of rail wheels in service.

Acknowledgments

This project has received funding from the Shift2Rail Joint Undertaking (JU) under grant agreement No 101012456. The JU receives support from the European Union's Horizon 2020 research and innovation program and the Shift2Rail JU members other than the Union. In addition, this work was funded by the "Austrian COMET-Program" (project InTribology1, no. 872176) via the Austrian Research Promotion Agency (FFG) and the federal states of Niederösterreich and Vorarlberg and was carried out within the "Excellence Centre of Tribology" (AC2T research GmbH). This study was done in cooperation

with Virtual Vehicle Research GmbH in Graz, Austria. The authors would like to acknowledge the financial support within the COMET K2 Competence Centers for Excellent Technologies from the Austrian Federal Ministry for Climate Action (BMK), the Austrian Federal Ministry for Digital and Economic Affairs (BMDW), the Province of Styria (Dept. 12) and the Styrian Business Promotion Agency (SFG). The Austrian Research Promotion Agency (FFG) has been authorized for the programme management. The authors acknowledge the TU Wien Bibliothek for financial support through its Open Access Funding Program.

References

- [1] R. Andersson, J. Ahlström, E. Kabo, F. Larsson, and A. Ekberg, 'Numerical investigation of crack initiation in rails and wheels affected by martensite spots', *International Journal of Fatigue*, vol. 114, pp. 238–251, 2018, doi: 10.1016/j.ijfatigue.2018.05.023.
- [2] A. Ekberg, B. Åkesson, and E. Kabo, 'Wheel/rail rolling contact fatigue – Probe, predict, prevent', *Wear*, vol. 314, no. 1–2, pp. 2–12, 2014, doi: 10.1016/j.wear.2013.12.004.
- [3] A. Ekberg and E. Kabo, 'Fatigue of railway wheels and rails under rolling contact and thermal loading—an overview', *Wear*, vol. 258, no. 7–8, pp. 1288–1300, 2005, doi: 10.1016/j.wear.2004.03.039.
- [4] S. Y. Zhang *et al.*, 'Rail rolling contact fatigue formation and evolution with surface defects', *International Journal of Fatigue*, vol. 158, p. 106762, 2022, doi: 10.1016/j.ijfatigue.2022.106762.
- [5] Y. Liu, B. Stratman, and S. Mahadevan, 'Fatigue crack initiation life prediction of railroad wheels', *International Journal of Fatigue*, vol. 28, no. 7, pp. 747–756, 2006, doi: 10.1016/j.ijfatigue.2005.09.007.
- [6] D. F. C. Peixoto and P. M. S. T. de Castro, 'Fatigue crack growth of a railway wheel', *Engineering Failure Analysis*, vol. 82, pp. 420–434, 2017, doi: 10.1016/j.engfailanal.2017.07.036.
- [7] S. L. Grassie, 'Studs and squats: The evolving story', *Wear*, vol. 366–367, pp. 194–199, 2016, doi: 10.1016/j.wear.2016.03.021.
- [8] M. Steenbergen, 'Squat formation and rolling contact fatigue in curved rail track', *Engineering Fracture Mechanics*, vol. 143, pp. 80–96, 2015, doi: 10.1016/j.engfracmech.2015.05.060.
- [9] M. Steenbergen, 'On the genesis of squat-type defects on rails – Toward a unified explanation', *Wear*, vol. 478–479, p. 203906, 2021, doi: 10.1016/j.wear.2021.203906.
- [10] S. L. Grassie, 'Squats and squat-type defects in rails: the understanding to date', *Proceedings of the Institution of Mechanical Engineers, Part F: Journal of Rail and Rapid Transit*, vol. 226, no. 3, pp. 235–242, 2012, doi: 10.1177/0954409711422189.
- [11] S. L. Grassie, D. I. Fletcher, E. A. Gallardo Hernandez, and P. Summers, 'Studs: a squat-type defect in rails', *Proceedings of the Institution of Mechanical Engineers, Part F: Journal of Rail and Rapid Transit*, vol. 226, no. 3, pp. 243–256, 2012, doi: 10.1177/0954409711421462.
- [12] B. Hieu Nguyen, A. Al-Juboori, H. Zhu, Q. Zhu, H. Li, and K. Tieu, 'Formation Mechanism and Evolution of White Etching Layers on Different Rail Grades', *International Journal of Fatigue*, p. 107100, 2022, doi: 10.1016/j.ijfatigue.2022.107100.

- [13] A. Al-Juboori *et al.*, ‘Characterisation of White Etching Layers formed on rails subjected to different traffic conditions’, *Wear*, vol. 436–437, p. 202998, 2019, doi: 10.1016/j.wear.2019.202998.
- [14] M. Freisinger *et al.*, ‘Comparative study on the influence of initial deformation and temperature of thermally induced white etching layers on rail wheels’, *Tribology International*, vol. 177, p. 107990, 2023, doi: 10.1016/j.triboint.2022.107990.
- [15] R. Pan, Y. Chen, H. Lan, S. E. and R. Ren, ‘Investigation into the evolution of tribological white etching layers’, *Materials Characterization*, vol. 190, p. 112076, 2022, doi: 10.1016/j.matchar.2022.112076.
- [16] R. I. Carroll and J. H. Beynon, ‘Rolling contact fatigue of white etching layer: Part 1 Crack morphology’, *Wear*, vol. 262, pp. 1253–1266, 2007, doi: 10.1016/j.wear.2007.01.003.
- [17] C. Bernsteiner *et al.*, ‘Simulation and experiment based investigations of squat formation mechanisms’, *Wear*, vol. 440–441, p. 203093, 2019, doi: 10.1016/j.wear.2019.203093.
- [18] R. Pan, R. Ren, C. Chen, and X. Zhao, ‘The microstructure analysis of white etching layer on treads of rails’, *Engineering Failure Analysis*, vol. 82, pp. 39–46, 2017, doi: 10.1016/j.engfailanal.2017.06.018.
- [19] M. Farjoo, W. Daniel, and P. A. Meehan, ‘Modelling a squat form crack on a rail laid on an elastic foundation’, *Engineering Fracture Mechanics*, vol. 85, pp. 47–58, 2012, doi: 10.1016/j.engfracmech.2012.02.004.
- [20] Q. Lian *et al.*, ‘Crack propagation behavior in white etching layer on rail steel surface’, *Engineering Failure Analysis*, vol. 104, pp. 816–829, 2019, doi: 10.1016/j.engfailanal.2019.06.067.
- [21] S. Pal, W. J. T. Daniel, and M. Farjoo, ‘Early stages of rail squat formation and the role of a white etching layer’, *International Journal of Fatigue*, vol. 52, pp. 144–156, 2013, doi: 10.1016/j.ijfatigue.2013.02.016.
- [22] J. Seo, S. Kwon, H. Jun, and D. Lee, ‘Numerical stress analysis and rolling contact fatigue of White Etching Layer on rail steel’, *International Journal of Fatigue*, vol. 33, no. 2, pp. 203–211, 2011, doi: 10.1016/j.ijfatigue.2010.08.007.
- [23] R. Deuce, ‘Wheel Tread Damage - An Elementary Guide’, Bombardier Transportation GmbH, Netphen, Germany, Technical Report, 2007.
- [24] C. Liu *et al.*, ‘Formation mechanism for the white etching microstructure in the subsurface of the failure pearlite wheel steel’, *Wear*, vol. 494–495, p. 204243, 2022, doi: 10.1016/j.wear.2022.204243.
- [25] Y. M. Zhang, Z. M. Xiao, and M. Fan, ‘Fatigue Investigation on Railway Wheel Steel with White Etching Layer’, *Int J Steel Struct*, vol. 20, no. 1, pp. 80–88, 2020, doi: 10.1007/s13296-019-00271-x.
- [26] T. Kato, A. Sugeta, and E. Nakayama, ‘Investigation of influence of white layer geometry on spalling property in railway wheel steel’, *Wear*, vol. 271, no. 1–2, pp. 400–407, 2011, doi: 10.1016/j.wear.2010.10.024.
- [27] S. Li, J. Wu, R. H. Petrov, Z. Li, R. Dollevoet, and J. Sietsma, ‘“Brown etching layer”: A possible new insight into the crack initiation of rolling contact fatigue in rail steels?’, *Engineering Failure Analysis*, vol. 66, pp. 8–18, 2016, doi: 10.1016/j.engfailanal.2016.03.019.
- [28] A. Kumar, G. Agarwal, R. Petrov, S. Goto, J. Sietsma, and M. Herbig, ‘Microstructural evolution of white and brown etching layers in pearlitic rail steels’, *Acta Materialia*, vol. 171, pp. 48–64, 2019, doi: 10.1016/j.actamat.2019.04.012.
- [29] P.-Y. Tung, X. Zhou, L. Morsdorf, and M. Herbig, ‘Formation mechanism of brown etching layers in pearlitic rail steel’, *Materialia*, vol. 26, p. 101625, 2022, doi: 10.1016/j.mtla.2022.101625.
- [30] M. Messaadi and M. Steenbergen, ‘Stratified surface layers on rails’, *Wear*, vol. 414–415, pp. 151–162, 2018, doi: 10.1016/j.wear.2018.07.019.
- [31] J. Ahlstrom and B. Karlsson, ‘Microstructural evaluation and interpretation of the mechanically and thermally affected zone under railway wheel flats’, *Wear*, p. 14, 1999.
- [32] G Lagerberg and J. A., ‘Influence of grain boundaries on the behaviour of carbon and nitrogen in α -iron’, *ACTA METALLURGICA*, vol. 3, no. 3, pp. 236–244, 1955.
- [33] ‘EN 13262:2004+A2:2011: Railway applications - Wheelsets and bogies - Wheels - Product requirements’.
- [34] J. Herian and K. Aniolek, ‘Abrasive wear of railway sections of steel with a different pearlite morphology in railroad switches’, *Journal of Achievements of Materials and Manufacturing Engineering*, vol. 43, 2010.
- [35] M. Diener and A. Ghidini, ‘Fracture Toughness: A Quality Index for Railway Solid Wheels’, *Matls. Perf. Charact.*, vol. 3, no. 3, p. 20130047, 2014, doi: 10.1520/MPC20130047.
- [36] A. Kumar *et al.*, ‘In situ study on fracture behaviour of white etching layers formed on rails’, *Acta Materialia*, vol. 180, pp. 60–72, 2019, doi: 10.1016/j.actamat.2019.08.060.
- [37] M. Freisinger, L. Zauner, R. Hahn, H. Riedl, and P. H. Mayrhofer, ‘In-situ micro-cantilever bending studies of a white etching layer thermally induced on rail wheels’, *Materials Science and Engineering: A*, vol. 869, p. 144805, 2023, doi: 10.1016/j.msea.2023.144805.
- [38] A. K. Saxena, A. Kumar, M. Herbig, S. Brinckmann, G. Dehm, and C. Kirchlechner, ‘Micro fracture investigations of white etching layers’, *Materials & Design*, vol. 180, p. 107892, 2019, doi: 10.1016/j.matdes.2019.107892.
- [39] M. Freisinger, H. Rojacz, A. Trausmuth, and P. H. Mayrhofer, ‘Severe Plastic Deformed Zones and White Etching Layers Formed During Service of Railway Wheels’, *Metallogr. Microstruct. Anal.*, 2023, doi: 10.1007/s13632-023-00967-x.
- [40] M. Freisinger and A. Trausmuth, ‘Microstructural characterization of near-surface microstructures on rail wheels in service – an insight into “stratified surface layers”’, *Open Res Europe*, vol. 3, p. 73, 2023, doi: 10.12688/openreseurope.15881.1.
- [41] N. Fantecelle Strey, A. Bavaresco Rezende, R. da Silva Miranda, S. Tamara da Fonseca, P. R. Mei, and C. Scandian, ‘Comparison of rolling contact fatigue damage between railway wheels and twin-disc test specimens’, *Tribology International*, vol. 160, p. 107037, 2021, doi: 10.1016/j.triboint.2021.107037.

- [42] Y. Zhou, J. Mo, Z. Cai, C. Deng, J. Peng, and M. Zhu, ‘Third-body and crack behavior in white etching layer induced by sliding–rolling friction’, *Tribology International*, vol. 140, p. 105882, 2019, doi: 10.1016/j.triboint.2019.105882.
- [43] H. H. Ding *et al.*, ‘Investigation on the rolling wear and damage properties of laser discrete quenched rail material with different quenching shapes and patterns’, *Surface and Coatings Technology*, vol. 378, p. 124991, 2019, doi: 10.1016/j.surfcoat.2019.124991.
- [44] X. Cao, L. B. Shi, Z. B. Cai, Q. Y. Liu, Z. R. Zhou, and W. J. Wang, ‘Investigation on the microstructure and damage characteristics of wheel and rail materials subject to laser dispersed quenching’, *Applied Surface Science*, vol. 450, pp. 468–483, 2018, doi: 10.1016/j.apsusc.2018.04.210.
- [45] A. Al-Juboori *et al.*, ‘Squat formation and the occurrence of two distinct classes of white etching layer on the surface of rail steel’, *International Journal of Fatigue*, vol. 104, pp. 52–60, 2017, doi: 10.1016/j.ijfatigue.2017.07.005.
- [46] J. I. Pereira, G. Tressia, E. J. Kina, A. Sinatora, and R. M. Souza, ‘Analysis of subsurface layer formation on a pearlitic rail under heavy haul conditions: Spalling characterization’, *Engineering Failure Analysis*, vol. 130, p. 105549, 2021, doi: 10.1016/j.engfailanal.2021.105549.
- [47] W. Österle, H. Rooch, A. Pyzalla, and L. Wang, ‘Investigation of white etching layers on rails by optical microscopy, electron microscopy, X-ray and synchrotron X-ray diffraction’, *Materials Science and Engineering: A*, vol. 303, no. 1–2, pp. 150–157, 2001, doi: 10.1016/S0921-5093(00)01842-6.
- [48] Q. Lian *et al.*, ‘Evolution of thermally induced white etching layer at rail surface during multiple wheel/train passages’, *International Journal of Fatigue*, vol. 159, p. 106799, 2022, doi: 10.1016/j.ijfatigue.2022.106799.
- [49] Q. Lian, G. Deng, H. Zhu, H. Li, X. Wang, and Z. Liu, ‘Influence of white etching layer on rolling contact behavior at wheel-rail interface’, *Friction*, vol. 8, no. 6, pp. 1178–1196, 2020, doi: 10.1007/s40544-020-0388-x.
- [50] A. Esmaili, J. Ahlström, B. Andersson, and M. Ekh, ‘Modelling of cyclic plasticity and phase transformations during repeated local heating events in rail and wheel steels’, *International Journal of Fatigue*, vol. 151, p. 106361, 2021, doi: 10.1016/j.ijfatigue.2021.106361.
- [51] M. Freisinger, A. Trausmuth, R. Hahn, and E. Badisch, ‘Influence of the evolution of near-surface rail wheel microstructure on crack initiation by micro-bending investigations’, *Proceedings of the Institution of Mechanical Engineers, Part F: Journal of Rail and Rapid Transit*, p. 09544097231191550, 2023, doi: 10.1177/09544097231191550.